

# Conjugated Microporous Polymers For Heterogeneous Catalysis



The  
University  
Of  
Sheffield.

Supakorn Tantisriyanurak

*A thesis submitted to the University of Sheffield in partial fulfilment to the  
requirements for the degree of Doctor of Philosophy*

March 2021



# Contents

	Page
Contents	i
List of Figures	viii
List of Schemes	xx
List of Tables	xxii
Abstract	xxiv
List of Publications	xxvi
Acknowledgements	xxvii
List of Abbreviations	xxviii
<b>Chapter 1 Introduction and Background</b>	<b>1</b>
1.1 Synthesis of different types of porous organic materials	2
1.1.1 Hyper-cross-linked polymers (HCPs)	2
(a) Post-crosslinking polymer precursors	3
(b) Direct one-step polycondensation of functional monomers	4
(c) Crosslinking by external crosslinkers	7
1.1.2 Polymers of intrinsic microporosity (PIMs)	8
1.1.3 Covalent organic frameworks (COFs)	9
1.1.4 Conjugated microporous polymers (CMPs)	14
1.1.5 Covalent triazine frameworks (CTFs)	17
1.1.6 Porous aromatic frameworks (PAFs)	18
1.1.7 Extrinsic porous molecules	19
1.1.8 Porous organic cages	20

1.2 Conjugated microporous polymers (CMPs) for heterogeneous catalysis	22
1.2.1 CMPs incorporating transition-metal catalysts	22
1.2.2 CMPs for heterogeneous organocatalysis	26
1.2.3 CMPs for heterogeneous photocatalysis	29
1.3 Thesis Aim	35
1.3.1 Synthesis part	35
1.3.2 Catalytic activity part	35
1.4 References	36
<b>Chapter 2 Methods</b>	<b>41</b>
2.1 Characterisation techniques	41
2.1.1 Nitrogen gas adsorption and desorption isotherm	41
2.1.2 $^1\text{H}$ - $^{13}\text{C}$ cross-polarisation magic angle spinning (CP/MAS)	41
2.1.3 $^1\text{H}$ NMR and $^{13}\text{C}$ Nuclear magnetic resonance (NMR) spectroscopy	42
2.1.4 Fourier transform infrared (FTIR) spectroscopy	42
2.1.5 Elemental analysis (EA)	42
2.1.6 Thermogravimetric analysis (TGA)	42
2.1.7 Particle size analysis	42
2.2 Gas sorption theory	43
2.2.1 Langmuir model	44
2.2.2 BET theory	46
2.2.3 Isotherm shapes	47
2.2.4 Adsorption hysteresis	51
2.3 References	53

<b>Chapter 3 Synthesis and Characterisation of Functionalised</b>	<b>54</b>
<b>Pyrylium Based CMPs</b>	
3.1 Introduction	54
3.2 The reactions used to prepare CMPs in this work	57
3.2.1 Mechanism of Sonogashira reaction	57
3.2.2 Mechanism of Yamamoto coupling	58
3.2.3 Mechanism of oxidative coupling	59
3.3 Aims of the chapter	61
3.4 Experimental	61
3.4.1 Materials	61
3.4.2 Synthesis of pyrylium monomers	62
3.4.3 Synthesis of functionalised pyrylium based CMPs <i>via</i> Sonogashira coupling	65
3.4.4 Synthesis of pyrylium CMP <i>via</i> Yamamoto coupling	66
3.4.5 Synthesis of pyrylium CMP <i>via</i> oxidative coupling	66
3.5 Results and discussion	67
3.5.1 Characterisation of pyrylium monomers	67
3.5.2 Mechanism of pyrylium formation	70
3.5.3 Synthesis and characterisation of pyrylium based CMPs	71
(a) Elemental analysis (EA)	71
(b) FTIR of the synthesised polymers	75
(c) <sup>13</sup> C CP/MAS NMR	77
(d) Gas sorption isotherms	79
(e) TGA of the synthesised polymers	84
(f) UV-Vis spectrophotometry of the synthesised monomers	86

and polymers	
3.6 Conclusions	90
3.7 References	91
3.8 Appendices	95
3.8.1 FTIR spectra of alkyne monomers	95
3.8.2 NMR spectra of the synthesised pyrylium monomers	96
3.8.3 Mass spectra of the synthesised pyrylium monomers	108
<b>Chapter 4 Pyrylium Based Conjugated Microporous Polymers for Catalytic Oxidation of Thioanisole Using Hydrogen Peroxide as an Oxidant</b>	<b>114</b>
4.1 Introduction	114
4.2 Aims of the chapter	116
4.3 Experimental	116
4.3.1 Materials	116
4.3.2 Thioanisole oxidation using H <sub>2</sub> O <sub>2</sub> as an oxidant and pyrylium CMPs as catalysts	117
4.4 Results and discussion	117
4.4.1 Effect of polymer structure on thioanisole oxidation using H <sub>2</sub> O <sub>2</sub> as an oxidant	117
4.4.2 Effect of reaction time on thioanisole oxidation using H <sub>2</sub> O <sub>2</sub> as an oxidant	121
4.4.3 Effect of amount of H <sub>2</sub> O <sub>2</sub> on thioanisole oxidation	123
4.4.4 Effect of reaction temperature on thioanisole oxidation using H <sub>2</sub> O <sub>2</sub> as an oxidant	125
4.4.5 Control reactions	127

4.4.6	Reusability test	128
4.4.7	Plausible reaction mechanism	131
4.5	Conclusions	136
4.6	References	137
4.7	Appendices	140
4.7.1	Particle size analysis of the synthesised CMPs	140
<b>Chapter 5 Synthesis and Characterisation of Bromophenol Blue and Bromocresol Green Dyes Incorporated Conjugated Microporous Polymers</b>		<b>143</b>
5.1	Introduction	143
5.2	Aims of the chapter	145
5.3	Experimental	146
5.3.1	Materials	146
5.3.2	Synthesis of BB and BG based CMPs <i>via</i> Sonogashira – Hagihara cross coupling	146
5.3.3	Sulfonation of BB and BG CMPs	147
5.3.4	Determination of acidity of the synthesised materials	147
5.4	Results and discussion	147
5.4.1	Elemental analysis (EA)	148
5.4.2	FTIR	150
5.4.3	<sup>13</sup> C CP/MAS NMR Spectroscopy	152
5.4.4	Nitrogen adsorption and desorption isotherms	153
5.4.5	Thermogravimetric analysis (TGA)	157
5.4.6	Determination of acidity of the synthesised materials	159
5.5	Conclusions	160

5.6	References	160
5.7	Appendices	163
5.7.1	FTIR spectra of monomers and HCl-CMPs	163
5.7.2	<sup>13</sup> C NMR of monomers used in this work	165
<b>Chapter 6 Biodiesel Production form Free Fatty Acids and Vegetable</b>		<b>167</b>
<b>Oils Using Acid Functionalised CMPs</b>		
6.1	Introduction	167
6.2	Aims of the chapter	173
6.3	Experimental	173
6.3.1	Materials	173
6.3.2	Esterification of free fatty acids (FFAs) and transesterification of different vegetable oils with methanol	173
6.3.3	Reusability study	174
6.4	Results and discussion	176
6.4.1	Effect of polymer structures on esterification of free fatty acids (FFAs)	176
6.4.2	Effect of reaction time on esterification of FFAs	179
6.4.3	Effect of different FFAs and reaction temperature on biodiesel production	180
6.4.4	Transesterification of vegetable oil using different polymers as an acid catalyst	182
6.4.5	Effect of catalyst loading on transesterification of vegetable oil	183
6.4.6	Transesterification of various vegetable oils using different sulfonated polymers as a catalyst	184
6.4.7	Reusability study	185

6.5 Conclusions	188
6.6 References	188
6.7 Appendices	191
6.7.1 $^1\text{H}$ NMR spectra of FFAs, vegetable oils and methyl ester products	191
6.7.2 Particle size analysis of the synthesised polymers	203
<b>Chapter 7 Conclusions and Future Work</b>	<b>206</b>
7.1 Conclusions	206
7.2 Future work	208
7.3 References	211

# List of Figures

	Page
<b>Chapter 1 Introduction and Background</b>	
<b>Figure 1.1</b> Hyper-cross-linking process scheme	4
<b>Figure 1.2</b> Monomers used for the synthesis of the hyper-cross-linked polymers	5
<b>Figure 1.3</b> (a) The scheme of Scholl coupling reaction, (b) the Scholl coupling polymer network from triphenylbenzene monomers, (c) other monomers or co-monomers used for the synthesis of hyper-cross-linked polymer networks with various functionalities	6
<b>Figure 1.4</b> Synthetic pathway to create knitted polymer network and aromatic building blocks; (a) benzene, methylbenzene, chlorobenzene and phenol, (b) biphenyl, and (c) triphenylbenzene	8
<b>Figure 1.5</b> The synthesis pathway of PIMs 1–6. Reagents and conditions: $K_2CO_3$ , DMF, 60–120 °C	9
<b>Figure 1.6</b> (a) condensation of boronic acids with diols (b) self-condensation of boronic acids and (c) condensation of amines with aldehydes	10
<b>Figure 1.7</b> Structures of (A) COF-1 and (B) COF-5, grey, orange and red spheres represent carbon, boron, and oxygen, respectively	11
<b>Figure 1.8</b> Preparation of COF-1, COF-5, COF-6, COF-8, COF-10, COF-102 and COF-103 <i>via</i> condensation reactions	12
<b>Figure 1.9</b> Preparation of COFs using Schiff-base chemistry	13

<b>Figure 1.10</b> (A) Synthetic pathway of ILCOF-1; (B) scanning electron micrograph of the synthesised materials, and (C) space-filling representation of the resulting 2D network; carbon (grey), nitrogen (blue), hydrogen was omitted for clarity	14
<b>Figure 1.11</b> Synthetic approaches to luminescent CMPs based pyrene	16
<b>Figure 1.12</b> Synthesis of <i>p</i> -PPF and <i>m</i> -PPF via Suzuki-Miyaura coupling reaction	17
<b>Figure 1.13</b> Reaction scheme of cyclotrimerisation of 1,4-dicyanobenzene leading to the formation of a 2D framework with 1.5 nm channels	18
<b>Figure 1.14</b> Synthesis of PAF-3 and PAF-4 via Yamamoto coupling	19
<b>Figure 1.15</b> Preparation of extrinsic porous material from triptycene trisbenzimidazolone	20
<b>Figure 1.16</b> a) The one-step condensation reaction of triptycene tetraol with triboric acid to the cuboctahedral [12+8] cages. b) The structure of the cuboctahedral cage with an outer diameter (3.99 nm), maximum inner diameter (3.03 nm), and open quadric windows of 1.52 nm. Edges of the cuboctahedral geometry are highlighted in red	21
<b>Figure 1.17</b> Synthesis of the bipyridine-containing CMPs and post modification of the CMP precursors with the Re complex	24
<b>Figure 1.18</b> Synthesis of (a) Ir and Rh loaded CMPs and (b) Cplr based CMPs via direct Songogashira cross coupling	25
<b>Figure 1.19</b> Synthesis of BNPPA CMPs. Conditions: i) [Pd(PPh <sub>3</sub> ) <sub>4</sub> ], K <sub>2</sub> CO <sub>3</sub> , THF/H <sub>2</sub> O, 80 °C; ii) a) BBr <sub>3</sub> , CH <sub>2</sub> Cl <sub>2</sub> , b) poly(4-vinyl pyridine),	28

POCl<sub>3</sub>, CH<sub>2</sub>Cl<sub>2</sub>; iii) THF, 1 M HCl, RT; iv) FeCl<sub>3</sub>, toluene, acetonitrile; v) aqueous HCl

**Figure 1.20** Reusability study of polymer 7 for asymmetric hydrogenation of 3-phenyl-2H-1,4-benzoxazine (red is % enantioselectivity, blue is % conversion) 29

**Figure 1.21** Synthesis of Ru(bipy)<sub>3</sub><sup>2+</sup>-based cross-linked polymers *via* oxidative coupling 31

**Figure 1.22** The synthesis scheme of eosin Y dye incorporated porous organic polymers (EY-POPs) *via* Sonogashira-Hagihara cross-coupling reaction 33

**Figure 1.23** The structures of the obtained polymers with their applications of C-3 formylation and thiocyanation of indoles 34

## Chapter 2 Methods

**Figure 2.1** Illustration of gas adsorption theory 44

**Figure 2.2** IUPAC isotherm classifications from 1985 48

**Figure 2.3** Refined IUPAC isotherm classifications as of 2015 50

**Figure 2.4** Observed hysteresis loops as classified by IUPAC 52

## Chapter 3 Synthesis and Characterisation of Functionalised

### Pyrylium Based CMPs

**Figure 3.1** IR spectra of the synthesised pyrylium monomers 69

**Figure 3.2** IR spectra of the synthesised (a) pyrylium CMPs derived from TEB, (b) DEB synthesised *via* Sonogashira coupling and (c) pyrylium CMPs synthesised *via* Yamamoto and oxidative couplings 76

**Figure 3.3** <sup>13</sup>C CP/MAS NMR spectra of (a) PYR+TEB, PYR+DEB and PYR CMP Yamamoto compared with solution <sup>13</sup>C NMR of *p*-Br-pyrylium 78

monomer, (b) *m*-PYR+TEB and *m*-PYR+DEB compared with solution <sup>13</sup>C NMR of *m*-Br-pyrylium monomer, (c) Me-PYR+TEB and Me-PYR+DEB compared with solution <sup>13</sup>C NMR of *m*-Br-*p*-Me-pyrylium monomer, (d) MeO-PYR+TEB and MeO-PYR+DEB compared with solution <sup>13</sup>C NMR of *m*-Br-*p*-MeO-pyrylium monomer, (e) F-PYR+TEB and F-PYR+DEB compared with solution <sup>13</sup>C NMR of *m*-Br-*p*-F-pyrylium monomer and (f) PYR CMP Oxidative compared with <sup>13</sup>C NMR of biphenyl pyrylium monomer. (\* denotes spinning sideband)

**Figure 3.4** Nitrogen gas sorption isotherms of (a) pyrylium CMPs derived from TEB, (b) DEB, pore size distributions of (c) pyrylium CMPs derived from TEB and (d) DEB, cumulative pore volume of (e) pyrylium CMPs derived from TEB and (f) DEB synthesised *via* Sonogashira-Hagihara cross-coupling 81

**Figure 3.5** (a) Nitrogen gas sorption isotherms, (b) pore size distributions and (c) cumulative pore volume of pyrylium CMPs synthesised *via* Yamamoto and oxidative couplings 83

**Figure 3.6** Thermo gravimetric analysis of (a) TEB, (b) DEB based pyrylium CMPs synthesised from Sonogashira reaction and (c) obtained from Yamamoto and oxidative couplings 85

**Figure 3.7** UV-visible spectra of (a) the synthesised pyrylium monomers and (b) alkyne monomers in acetonitrile. 87

**Figure 3.8** Solid state UV-visible spectra of the pyrylium CMPs synthesised *via* (a) Sonogashira-Hagihara cross-coupling and (b) Yamamoto and oxidative couplings. 87

<b>Figure 3.9</b> Tauc plots of the pyrylium based polymers synthesised <i>via</i> (a) Sonogashira reaction and (b) Yamamoto and oxidative coupling reactions	88
<b>Figure A3.1</b> FTIR spectra of alkyne monomers	95
<b>Figure A3.2</b> $^1\text{H}$ NMR spectrum of 2,4,6-tris(4-bromophenyl) pyrylium tetrafluoroborate	96
<b>Figure A3.3</b> $^{13}\text{C}$ NMR spectrum of 2,4,6-tris(4-bromophenyl) pyrylium tetrafluoroborate	96
<b>Figure A3.4</b> $^{11}\text{B}$ NMR spectrum of 2,4,6-tris(4-bromophenyl) pyrylium tetrafluoroborate	97
<b>Figure A3.5</b> $^{19}\text{F}$ NMR spectrum of 2,4,6-tris(4-bromophenyl) pyrylium tetrafluoroborate	97
<b>Figure A3.6</b> $^1\text{H}$ NMR spectrum of 2,4,6-tris(3-bromophenyl) pyrylium tetrafluoroborate	98
<b>Figure A3.7</b> $^{13}\text{C}$ NMR spectrum of 2,4,6-tris(3-bromophenyl) pyrylium tetrafluoroborate	98
<b>Figure A3.8</b> $^{11}\text{B}$ NMR spectrum of 2,4,6-tris(3-bromophenyl) pyrylium tetrafluoroborate	99
<b>Figure A3.9</b> $^{19}\text{F}$ NMR spectrum of 2,4,6-tris(3-bromophenyl) pyrylium tetrafluoroborate	99
<b>Figure A3.10</b> $^1\text{H}$ NMR spectrum of 2,4,6-tris(3-bromo, 4-methylphenyl) pyrylium tetrafluoroborate	100
<b>Figure A3.11</b> $^{13}\text{C}$ NMR spectrum of 2,4,6-tris(3-bromo, 4-methylphenyl) pyrylium tetrafluoroborate	100
<b>Figure A3.12</b> $^{11}\text{B}$ NMR spectrum of 2,4,6-tris(3-bromo, 4-methylphenyl) pyrylium tetrafluoroborate	101

<b>Figure A3.13</b> $^{19}\text{F}$ NMR spectrum of 2,4,6-tris(3-bromo, 4-methylphenyl) pyrylium tetrafluoroborate	101
<b>Figure A3.14</b> $^1\text{H}$ NMR spectrum of 2,4,6-tris(3-bromo, 4-methoxyphenyl) pyrylium tetrafluoroborate	102
<b>Figure A3.15</b> $^{13}\text{C}$ NMR spectrum of 2,4,6-tris(3-bromo, 4-methoxyphenyl) pyrylium tetrafluoroborate	102
<b>Figure A3.16</b> $^{11}\text{B}$ NMR spectrum of 2,4,6-tris(3-bromo, 4-methoxyphenyl) pyrylium tetrafluoroborate	103
<b>Figure A3.17</b> $^{19}\text{F}$ NMR spectrum of 2,4,6-tris(3-bromo, 4-methoxyphenyl) pyrylium tetrafluoroborate	103
<b>Figure A3.18</b> $^1\text{H}$ NMR spectrum of 2,4,6-tris(3-bromo, 4-fluorophenyl) pyrylium tetrafluoroborate	104
<b>Figure A3.19</b> $^{13}\text{C}$ NMR spectrum of 2,4,6-tris(3-bromo, 4-fluorophenyl) pyrylium tetrafluoroborate	104
<b>Figure A3.20</b> $^{11}\text{B}$ NMR spectrum of 2,4,6-tris(3-bromo, 4-fluorophenyl) pyrylium tetrafluoroborate	105
<b>Figure A3.21</b> $^{19}\text{F}$ NMR spectrum of 2,4,6-tris(3-bromo, 4-fluorophenyl) pyrylium tetrafluoroborate	105
<b>Figure A3.22</b> $^1\text{H}$ NMR spectrum of 2,4,6-tris(biphenyl) pyrylium tetrafluoroborate	106
<b>Figure A3.23</b> $^{13}\text{C}$ NMR spectrum of 2,4,6-tris(biphenyl) pyrylium tetrafluoroborate	106
<b>Figure A3.24</b> $^{11}\text{B}$ NMR spectrum of 2,4,6-tris(biphenyl) pyrylium tetrafluoroborate	107

<b>Figure A3.25</b> $^{19}\text{F}$ NMR spectrum of 2,4,6-tris(biphenyl) pyrylium tetrafluoroborate	107
<b>Figure A3.26</b> Mass spectrum of 2,4,6-tris(4-bromophenyl) pyrylium tetrafluoroborate (wide)	108
<b>Figure A3.27</b> Mass spectrum of 2,4,6-tris(4-bromophenyl) pyrylium tetrafluoroborate (zoom in)	108
<b>Figure A3.28</b> Mass spectrum of 2,4,6-tris(3-bromophenyl) pyrylium tetrafluoroborate (wide)	109
<b>Figure A3.29</b> Mass spectrum of 2,4,6-tris(3-bromophenyl) pyrylium tetrafluoroborate (zoom in)	109
<b>Figure A3.30</b> Mass spectrum of 2,4,6-tris(3-bromo, 4-methylphenyl) pyrylium tetrafluoroborate (wide)	110
<b>Figure A3.31</b> Mass spectrum of 2,4,6-tris(3-bromo, 4-methylphenyl) pyrylium tetrafluoroborate (zoom in)	110
<b>Figure A3.32</b> Mass spectrum of 2,4,6-tris(3-bromo, 4-methoxyphenyl) pyrylium tetrafluoroborate (wide)	111
<b>Figure A3.33</b> Mass spectrum of 2,4,6-tris(3-bromo, 4-methoxyphenyl) pyrylium tetrafluoroborate (zoom in)	111
<b>Figure A3.34</b> Mass spectrum of 2,4,6-tris(3-bromo, 4-fluorophenyl) pyrylium tetrafluoroborate (wide)	112
<b>Figure A3.35</b> Mass spectrum of 2,4,6-tris(3-bromo, 4-fluorophenyl) pyrylium tetrafluoroborate (zoom in)	112
<b>Figure A3.36</b> Mass spectrum of 2,4,6-tris(biphenyl) pyrylium tetrafluoroborate	113

## **Chapter 4 Pyrylium Based Conjugated Microporous Polymers for Catalytic Oxidation of Thioanisole Using Hydrogen Peroxide as an Oxidant**

- Figure 4.1** Effect of different polymer structure on thioanisole oxidation using H<sub>2</sub>O<sub>2</sub> as an oxidant. (Condition: 1 mmol of thioanisole, 1.5 mmol of H<sub>2</sub>O<sub>2</sub> and 3 mL of acetonitrile using 30 mg of catalyst at 50 °C for 24h) 120
- Figure 4.2** % Conversion of thioanisole oxidation with different polymers at different reaction times. (Condition: 1 mmol of thioanisole, 1.5 mmol of H<sub>2</sub>O<sub>2</sub> and 3 mL of acetonitrile using 30 mg of catalyst at 50 °C) 122
- Figure 4.3** Selectivity of sulfoxide product using different polymers at different times. (Condition: 1 mmol of thioanisole, 1.5 mmol of H<sub>2</sub>O<sub>2</sub> and 3 mL of acetonitrile using 30 mg of catalyst at 50 °C) 123
- Figure 4.4** Effect of H<sub>2</sub>O<sub>2</sub> concentration on conversion of thioanisole oxidation (Condition: 1 mmol of thioanisole and 3 mL of acetonitrile using 30 mg of F-PYR+DEB at 50 °C) 124
- Figure 4.5** Effect of H<sub>2</sub>O<sub>2</sub> concentration on selectivity of sulfoxide product (Condition: 1 mmol of thioanisole and 3 mL of acetonitrile using 30 mg of F-PYR+DEB at 50 °C) 125
- Figure 4.6** Effect of temperature on the conversion of thioanisole oxidation (Condition: 1 mmol of thioanisole, 3 mmol of H<sub>2</sub>O<sub>2</sub> and 3 mL of acetonitrile using 30 mg of F-PYR+DEB) 126
- Figure 4.7** Effect of temperature on the selectivity of sulfoxide product. (Condition: 1 mmol of thioanisole, 3 mmol of H<sub>2</sub>O<sub>2</sub> and 3 mL of acetonitrile using 30 mg of F-PYR+DEB) 127
- Figure 4.8** TGA of fresh and 6 time reused F-Pyr+DEB catalyst 130

<b>Figure 4.9</b> FTIR spectra of fresh, 6 <sup>th</sup> time reused and H <sub>2</sub> O <sub>2</sub> treated F-Pyr+DEB. (* denotes carbonyl peak at 1738 cm <sup>-1</sup> )	131
<b>Figure 4.10</b> Effect of reactive oxygen scavengers on thioanisole oxidation (Condition: 1 mmol of sulphide, 3 mmol of H <sub>2</sub> O <sub>2</sub> , 3 mmol of scavenger, 3 mL of acetonitrile at 60 °C for 32 h)	134
<b>Figure A4.1</b> The particle size distributions of the synthesised pyrylium CMPs.	141
<b>Figure A4.2</b> The optical micrographs of the obtained pyrylium CMPs.	142
<b>Chapter 5 Synthesis and Characterisation of Bromophenol Blue and Bromocresol Green Dyes Incorporated Conjugated Microporous Polymers</b>	
<b>Figure 5.1</b> IR spectra of as-synthesised and sulfonated CMPs ((a) from 400-4000 cm <sup>-1</sup> and (b) 1800-4000 cm <sup>-1</sup> )	151
<b>Figure 5.2</b> <sup>13</sup> C CP/MAS spectra of the as-synthesised CMPs and sulfonated CMPs	153
<b>Figure 5.3</b> (a) Nitrogen gas sorption isotherms (filled is adsorption and emptied is desorption) of the synthesised CMPs and (b) the sulfonated CMPs, (c) pore size distribution of the synthesised CMPs and (d) the sulfonated CMPs. The isotherms were offset by 100 cm <sup>3</sup> /g and 0.5 cm <sup>3</sup> /g for pore size distribution	156
<b>Figure 5.4</b> (a) Nitrogen sorption isotherms (filled is adsorption and emptied is desorption) of HCl treated CMPs and (b) pore size distributions of HCl treated CMPs	157
<b>Figure 5.5</b> TGA graphs of (a) non-functionalised CMPs and sulfonated CMPs and (b) HCl treated CMPs	158

<b>Figure 5.6</b> Relationship between acidity and sulphur contents of the synthesised CMPs	159
<b>Figure A5.1</b> IR spectra of the monomers used in this study	163
<b>Figure A5.2</b> IR spectra of HCl treated BB and BG CMPs	164
<b>Figure A5.3</b> $^{13}\text{C}$ NMR of bromophenol blue (BB) and bromocresol green (BG) in $\text{D}_2\text{O}$	165
<b>Figure A5.4</b> $^{13}\text{C}$ NMR of 1,3,5-triethynylbenzene (TEB) and 1,4-diethynylbenzene (DEB) in <i>d</i> -chloroform	166
<b>Chapter 6 Biodiesel Production form Free Fatty Acids and Vegetable Oils Using Acid Functionalised CMPs</b>	
<b>Figure 6.1</b> Effect of reaction time on esterification of FFAs using different catalysts	179
<b>Figure 6.2</b> Esterification of different FFAs using different polymers at (a) 60 °C for 6h and (b) 25 °C for 24h, (c) %conversion and (d) %yield of transesterification of various vegetable oils using different polymers	181
<b>Figure 6.3</b> Effect of catalyst loading on transesterification of vegetable oil	184
<b>Figure 6.4</b> Reusability test of s-BB+DEB catalyst	186
<b>Figure 6.5</b> TGA of the fresh s-BB+DEB catalyst and reused s-BB+DEB	187
<b>Figure 6.6</b> FTIR spectra of the fresh s-BB+DEB catalyst and reused s-BB+DEB	187
<b>Figure A6.1</b> $^1\text{H}$ -NMR spectrum of lauric acid in $\text{CDCl}_3$	191
<b>Figure A6.2</b> $^1\text{H}$ -NMR spectrum of methyl ester of lauric acid in $\text{CDCl}_3$	191
<b>Figure A6.3</b> $^1\text{H}$ -NMR spectrum of myristic acid in $\text{CDCl}_3$	192
<b>Figure A6.4</b> $^1\text{H}$ -NMR spectrum of methyl ester of myristic acid in $\text{CDCl}_3$	192
<b>Figure A6.5</b> $^1\text{H}$ -NMR spectrum of palmitic acid in $\text{CDCl}_3$	193

<b>Figure A6.6</b>	<sup>1</sup> H-NMR spectrum of methyl ester of palmitic acid in CDCl <sub>3</sub>	193
<b>Figure A6.7</b>	<sup>1</sup> H-NMR spectrum of stearic acid in CDCl <sub>3</sub>	194
<b>Figure A6.8</b>	<sup>1</sup> H-NMR spectrum of methyl ester of stearic acid in CDCl <sub>3</sub>	194
<b>Figure A6.9</b>	<sup>1</sup> H-NMR spectrum of oleic acid in CDCl <sub>3</sub>	195
<b>Figure A6.10</b>	<sup>1</sup> H-NMR spectrum of methyl ester of oleic acid in CDCl <sub>3</sub>	195
<b>Figure A6.11</b>	<sup>1</sup> H-NMR spectrum of adipic acid in CDCl <sub>3</sub>	196
<b>Figure A6.12</b>	<sup>1</sup> H-NMR spectrum of methyl ester of adipic acid in CDCl <sub>3</sub>	196
<b>Figure A6.13</b>	<sup>1</sup> H-NMR spectrum of sebacic acid in CDCl <sub>3</sub>	197
<b>Figure A6.14</b>	<sup>1</sup> H-NMR spectrum of methyl ester of sebacic acid in CDCl <sub>3</sub>	197
<b>Figure A6.15</b>	<sup>1</sup> H-NMR spectrum of coconut oil in CDCl <sub>3</sub>	198
<b>Figure A6.16</b>	<sup>1</sup> H-NMR spectrum of transesterification of coconut oil using s-BB+DEB at 60 °C for 24 h in CDCl <sub>3</sub>	198
<b>Figure A6.17</b>	<sup>1</sup> H-NMR spectrum of sunflower oil in CDCl <sub>3</sub>	199
<b>Figure A6.18</b>	<sup>1</sup> H-NMR spectrum of transesterification of sunflower oil using s-BB+DEB at 60 °C for 24 h in CDCl <sub>3</sub>	199
<b>Figure A6.19</b>	<sup>1</sup> H-NMR spectrum of sesame oil in CDCl <sub>3</sub>	200
<b>Figure A6.20</b>	<sup>1</sup> H-NMR spectrum of transesterification of sesame oil using s-BB+DEB at 60 °C for 24 h in CDCl <sub>3</sub>	200
<b>Figure A6.21</b>	<sup>1</sup> H-NMR spectrum of rapeseed oil in CDCl <sub>3</sub>	201
<b>Figure A6.22</b>	<sup>1</sup> H-NMR spectrum of transesterification of rapeseed oil using s-BB+DEB at 60 °C for 24 h in CDCl <sub>3</sub>	201
<b>Figure A6.23</b>	<sup>1</sup> H-NMR spectrum of used sunflower oil in CDCl <sub>3</sub>	202
<b>Figure A6.24</b>	<sup>1</sup> H-NMR spectrum of transesterification of used sunflower oil using s-BB+DEB at 60 °C for 24 h in CDCl <sub>3</sub>	202

<b>Figure A6.25</b> The particle size distributions of the as synthesised polymers.	203
<b>Figure A6.26</b> The particle size distributions of the HCl treated polymers.	204
<b>Figure A6.27</b> The particle size distributions of the sulfonated polymers.	204
<b>Figure A6.28</b> The optical micrographs of the synthesised polymers.	205

# List of Schemes

	Page
<b>Chapter 3 Synthesis and Characterisation of Functionalised</b>	
<b>Pyrylium Based CMPs</b>	
<b>Scheme 3.1</b> Structures of 2,5,6-triphenylpyrylium tetrafluoroborate synthesised by Martiny <i>et al.</i>	55
<b>Scheme 3.2</b> Mechanism of Sonogashira reaction	58
<b>Scheme 3.3</b> Mechanism of Yamamoto coupling	59
<b>Scheme 3.4</b> Mechanisms of oxidative coupling	60
<b>Scheme 3.5</b> Synthesis of pyrylium monomers	63
<b>Scheme 3.6</b> Reversible ring opening of pyrylium cation to pent-2-ene-1,5-dione	68
<b>Scheme 3.7</b> Mechanism of 2,4,6-tris (4-bromo) pyrylium tetrafluoroborate synthesis	71
<b>Scheme 3.8</b> Synthesis of pyrylium based CMPs <i>via</i> Sonogashira coupling	72
<b>Scheme 3.9</b> Synthesis of pyrylium CMP <i>via</i> Yamamoto coupling	73
<b>Scheme 3.10</b> Synthesis of pyrylium CMP <i>via</i> oxidative coupling	74
<b>Chapter 4 Pyrylium Based Conjugated Microporous Polymers for Catalytic Oxidation of Thioanisole Using Hydrogen Peroxide as an Oxidant</b>	
<b>Scheme 4.1</b> oxidation of thioether to sulfoxide and sulfone products	115
<b>Scheme 4.2</b> The structure of pyrylium based CMPs studied in this work	119
<b>Scheme 4.3</b> Formation of reactive oxygen species from H <sub>2</sub> O <sub>2</sub>	132

<b>Scheme 4.4</b> Scavenging processes of ROSs by (a) t-butanol, (b) $\alpha$ -tocopherol and (c) benzoquinone	133
<b>Scheme 4.5</b> The plausible mechanism of thioanisole oxidation catalysed by pyrylium CMPs <i>via</i> a perhydroxyl radical transfer pathway	135
<b>Chapter 5 Synthesis and Characterisation of Bromophenol Blue and Bromocresol Green Dyes Incorporated Conjugated Microporous Polymers</b>	
<b>Scheme 5.1</b> Structure of bromophenol blue sodium salt (R = H) and bromocresol green sodium salt (R = CH <sub>3</sub> )	143
<b>Scheme 5.2</b> Synthesis of BB and BG based CMPs <i>via</i> Sonogashira reaction and post modification of the synthesised CMPs with chlorosulfonic acid	150
<b>Chapter 6 Biodiesel Production form Free Fatty Acids and Vegetable Oils Using Acid Functionalised CMPs</b>	
<b>Scheme 6.1</b> Biodiesel production <i>via</i> transesterification of triglyceride and alcohol	168
<b>Scheme 6.2</b> Saponification of FFA with alkaline catalyst	169
<b>Scheme 6.3</b> Hydrolysis of triglyceride to diglyceride and FFA	169
<b>Scheme 6.4</b> Esterification of FFA to fatty acid ester using acid catalyst	170
<b>Scheme 6.5</b> Synthesis of phenol and bisphenol A based HCPs <i>via</i> Friedel-Craft alkylation and post-functionalisation with chlorosulfonic acid	171
<b>Chapter 7 Conclusions and Future Work</b>	
<b>Scheme 7.1</b> Synthesis of D-A type CMPs <i>via</i> Sonogashira coupling	209
<b>Scheme 7.2</b> Synthesis of D-A molecule and oxidative coupling of the D-A molecule to form D-A type CMP	210

# List of Tables

	Page
<b>Chapter 1 Introduction and Background</b>	
<b>Table 1.1</b> Reductive amination with heterogeneous CplR based CMPs	26
<b>Chapter 3 Synthesis and Characterisation of Functionalised Pyrylium Based CMPs</b>	
<b>Table 3.1</b> Yields and Elemental analysis of the synthesised polymers	74
<b>Table 3.2</b> BET surface areas ( $S_{\text{BET}}$ ), micropore volumes, total pore volumes and ratio of micropores of the synthesised polymers and monomers	84
<b>Table 3.3</b> Bandgap energy ( $E_g$ ) of the synthesised monomers and polymers	89
<b>Chapter 4 Pyrylium Based Conjugated Microporous Polymers for Catalytic Oxidation of Thioanisole Using Hydrogen Peroxide as an Oxidant</b>	
<b>Table 4.1</b> Controls reactions of thioanisole oxidation	128
<b>Table 4.2</b> Reusability test	129
<b>Table A4.1</b> The particle sizes of the synthesised pyrylium based CMPs	140
<b>Chapter 5 Synthesis and characterisation of bromophenol blue and bromocresol green dyes incorporated conjugated microporous polymers</b>	
<b>Table 5.1</b> Elemental analysis of the synthesised polymers	149
<b>Table 5.2</b> BET surface areas, total pore volumes, sulphur contents and acidity of the synthesised CMPs	155

## **Chapter 6 Biodiesel Production from Free Fatty Acids and Vegetable Oils Using Acid Functionalised CMPs**

<b>Table 6.1</b> Chemical formula and structure of free fatty acids (FFAs) used in this work	175
<b>Table 6.2</b> Effect of different catalysts on esterification of FFAs	178
<b>Table 6.3</b> Transesterification of coconut oil with methanol using various catalysts	183
<b>Table A6.1</b> The particle size of the synthesised polymers	203

## Abstract

Conjugated microporous polymers (CMPs) are a type of amorphous porous organic polymers (POPs) with extended  $\pi$  conjugation system in polymer backbones. The CMPs usually have a high surface area ( $> 1000 \text{ m}^2/\text{g}$ ) and micropores (pore width  $< 2 \text{ nm}$ ). Moreover, they also have high thermal and chemical stability due to covalent bond linkages. The applications of CMPs include gas separation, adsorption of gases and molecules, energy storage, catalysis and more. In this work, new types of CMPs were prepared by various synthetic methods including Sonogashira, Yamamoto and oxidative couplings and characterised by  $^{13}\text{C}$  Cross-Polarisation Magic-Angle-Spinning (CP/MAS) NMR, FTIR, gas sorption, UV-visible spectroscopy, elemental analysis and thermogravimetric analysis (TGA) to confirm the structures, porosity, light absorption and thermal stability of the materials. A series of functionalised pyrylium based CMPs was successfully synthesised and showed high surface areas up to  $721 \text{ m}^2/\text{g}$  with pore sizes in a range of micropore to mesopore. The materials were investigated for use as heterogeneous catalysts in the oxidation of thioanisole and showed a high catalytic activity of 99% conversion and 94% selectivity of sulfoxide product at the optimum condition. The catalysts were able to be reused up to 6 times however the catalytic activity decreased after multiple uses. Bromophenol blue and bromocresol green based CMPs were also successfully prepared and they exhibited high surface areas up to  $747 \text{ m}^2/\text{g}$ . The synthesised CMPs were chemically post-modified with chlorosulfonic acid in order to increase acidity of the materials. The acid functionalised CMPs were used as catalysts for biodiesel production *via* esterification of free fatty acids (FFAs) and transesterification of vegetable oils. The sulfonated

CMPs can produce more than 90% of biodiesel product and can be recycled up to 4 cycles with just 10% activity loss.

## List of Publications

Parts of this thesis have been published in the following peer reviewed journal:

- (1) Acid Functionalized Conjugated Microporous Polymers as a Reusable Catalyst for Biodiesel Production

**Tantisriyanurak, S.**, Duguid, H. N., Peattie, L., Dawson, R. *ACS Appl.*

*Polym. Mater.* 2020, 2, 3908–3915.

Other papers published:

- (2) Porous Silica-Pillared MXenes with Controllable Interlayer Distances for Long-Life Na-Ion Batteries

Maughan, P. A., Seymour, V. R., Bernardo-Gavito, R., Kelly, D. J., Shao, S.,

**Tantisriyanurak, S.**, Dawson, R., Haigh, S. J., Young, R. J., Tapia-Ruiz, N.,

Bimbo, N. *Langmuir* 2020, 36, 4370-4382.

## Acknowledgements

First of all, I would like to thank Dr. Robert Dawson, my supervisor for his support throughout my PhD. Rob is always supportive and kind to me. I am really happy that I have worked with him. I would also like to thank Dr. Arosha Karunathilake, Dr. Alex James, Xuefeng Qi, Shaobo Du and all past and current members of Dawson group for all their help without them working in the lab must be lonely and difficult.

I am grateful to all academic, technical and administrative staffs of the Department of Chemistry, University of Sheffield for their kind support especially the staffs of NMR service, mass spectrometry and elemental analysis for running numerous samples for me and Weinstein group for giving me access to spectrophotometers.

I would like to thank all my friends for joy and fun that we had together especially Dr. Mon, my long-time friend for her help since the first day I moved to Sheffield. My thanks also go to my ex house mates, Dr. Sine, Dr. Tee, Tim and Tao for always making me feel like home.

I would like to acknowledge the Development and Promotion of Science and Technology Talents Project (DPST) for giving me such a great opportunity to study abroad and financial support from undergraduate to PhD. Without this scholarship, I would not be able to fulfil my dream and none of this work would have been possible.

Finally, I would like to thank my family for their love, motivation and financial support. You are always there for me no matter what.

## List of Abbreviations

1D	One Dimensional
2D	Two Dimensional
3D	Three Dimensional
ATR	Attenuated Total Reflectance
BB	Bromophenol Blue
BCMA	Bis(chloromethyl) anthracene
BCMBP	4,4'-Bis(chloromethyl)biphenyl
BDD	Benzodithiophenedione
BET	Brunauer-Emmett-Teller
BG	Bromocresol Green
BNPPA	1,1'-Binaphthalene-2,2'-diyl hydrogenphosphate
Bpy	Bipyridine
CMPs	Conjugated Microporous Polymers
COD	1,5-Cyclooctadiene
COFs	Covalent Organic Frameworks
CP/MAS	Cross-Polarisation Magic Angle Spinning
CTFs	Covalent Triazine Frameworks
DCM	Dichloromethane
DCX	Dichloroxylene
DEB	1,4-Diethynylbenzene
DMAc	N,N-Dimethylacetamide
DMF	N,N-Dimethylformamide

DVB	Divinylbenzene
EA	Elemental Analysis
$E_g$	Band Gap Energy
$E_{red}$	Reduction Potential
Et <sub>3</sub> N	Triethylamine
FAMEs	Fatty Acid Methyl Esters
FDA	Formaldehyde Dimethyl Acetal
FFAs	Free Fatty Acids
FTIR	Fourier Transform Infrared
GC-MS	Gas Chromatography Coupled with Mass Spectrometry
HCPs	Hyper-Cross-Linked Polymers
HHTP	2,3,6,7,10,11-Hexahydroxytriphenylene
HOMO	Highest Occupied Molecular Orbital
HPLC	High Performance Liquid Chromatography
ICP-OES	Inductively Coupled Plasma-Optical Emission Spectroscopy
ICT	Intramolecular Charge Transfer
IUPAC	International Union of Pure and Applied Chemistry
LUMO	Lowest Unoccupied Molecular Orbital
MCDE	Monochlorodimethyl ether
MeOH	Methanol
MOFs	Metal-Organic Frameworks
NL-DFT	Non-Local Density Functional Theory
NMR	Nuclear Magnetic Resonance
PAFs	Porous Aromatic Frameworks

PIMs	Polymers of Intrinsic Microporosity
polyVBC–DVB	Vinylbenzyl chloride–divinylbenzene copolymers
PYR	Pyrylium
ROMP	Ring Opening Metathesis Polymerisation
ROs	Reactive Oxygen Species
S <sub>BET</sub>	BET Surface Area
SCE	Standard Calomel Electrode
TCD	Thermal Conductivity Detector
TCMM	Tris-(chloromethyl)-mesitylene
T <sub>dec</sub>	Decomposition Temperature
TEB	1,3,5-Triethynylbenzene
TFA	Trifluoroacetic Acid
TFMS	Trifluoromethanesulfonic Acid
TGA	Thermogravimetric Analysis
THF	Tetrahydrofuran
TMS	Tetramethylsilane
TPPM	Two-pulse Phase Modulation
VBC	Vinyl Benzyl Chloride
V <sub>micro</sub>	Micropore Volume
V <sub>total</sub>	Total Pore Volume
λ <sub>max</sub>	Maximum Wavelength

# Chapter 1

## Introduction and Background

A porous medium or porous material can be described as any materials (usually solid) containing void spaces which are not occupied by the main framework of atoms that make up the structure of the solid.<sup>1</sup> The presence of pores in the materials gives rise to low density and high surface area.<sup>2</sup> Porous materials have been widely studied due to their numerous applications such as in (heterogeneous) catalysis, separations, sensors, and chromatography. According to IUPAC classification, porous materials can be categorised into three types depending on their pore sizes; microporous materials (pore diameter less than 2 nm), mesoporous materials (pore diameter between 2 nm and 50 nm) and macroporous materials (pore diameter greater than 50 nm)<sup>3</sup>. Besides their pore size classification, porous materials can also be classified by their elemental structures. For example, inorganic porous materials can be prepared from both pure metals and metal oxides such as metal foams, silicas ( $\text{SiO}_2$ ), pillared clays which are metal oxides intercalated between layers of clays and zeolites which are microporous aluminosilicate<sup>4-6</sup>. Inorganic-organic hybrid porous materials e.g. metal-organic frameworks (MOFs), contain metal ions or metal clusters linked together by organic molecules (linkers)<sup>7</sup> while porous organic materials consist of organic moieties. Examples include covalent organic frameworks (COFs), conjugated microporous polymers (CMPs), hyper-cross-linked polymers (HCPs) and polymers of intrinsic microporosity (PIMs)<sup>8</sup>.

Inorganic porous materials such as zeolites have high surface area, uniform and interconnected pores with accessible pore volume, high adsorption capacity, ion

exchange ability and shape/size selectivity that make them useful materials for various applications such as adsorption and heterogeneous catalysis.<sup>9</sup> However, zeolites suffer from deactivation by irreversible adsorption of heavy secondary products or pore blockage and their poor accessibility of large molecules due to microporosity.<sup>10</sup> MOFs, inorganic-organic hybrid materials also have numerous advantages such as high surface area, high porosity, tunable chemical structure, flexible and multifunctional properties. Nevertheless, they have some drawbacks including high fabrication costs, poor selectivity, low capacity, and poor recyclability.<sup>11</sup>

Porous organic materials have been recently developed and utilised in various applications such as gas storage, separations, and catalysis due to the ease of property tuning by introducing organic functionalities. Some classes of porous organic material also possess extended  $\pi$  conjugated bonds combined with the high surface area, excellent thermal stability, reusability, water tolerance and metal free synthesis<sup>8,12-14</sup>. In this work, we focus on the synthesis of organic porous materials and their application as heterogeneous catalysts. There are various types of organic porous materials, and a wide range of synthesis methods have been used to prepare these materials as discussed below.

## **1.1 Synthesis of different types of porous organic materials**

### **1.1.1 Hyper-Cross-Linked Polymers (HCPs)**

HCPs are organic polymers that possess an amorphous structure and microporosity leading to very high surface areas up to 2440 m<sup>2</sup>/g<sup>15</sup> and low densities e.g. 1.28 g/cm<sup>3</sup> for *p*-dichloroxylylene (DCX) based HCP.<sup>16</sup> They can be synthesised using various chemistries such as Friedel-Crafts alkylation, Scholl coupling, and self-condensation, which rapidly form covalent linkages resulting in a high degree of cross-

linking polymers with porosity. Due to the ability to use cheap reagents and a straightforward approach, it can be accessible to scale-up and be of use in industrial processes. Moreover, various kinds of aromatic monomers can be employed to create specific pore structures and functionalities which suit particular applications such as gas adsorption and storage, water treatment, catalysis, etc.<sup>17–19</sup> HCPs are prepared by following three main methods;

### 1.1.1 (a) Post-crosslinking polymer precursors

This process consists of two essential steps as shown in Figure 1.1: (1) polymer precursors are entirely dissolved and swelled in a solvent. In this step, the polymer chains are separated from each other and surrounded by solvent. (2) The polymer chains are crosslinked using internal cross-linkers which are polymer itself containing chloromethyl groups undergoing self-condensation such as vinylbenzyl chloride–divinylbenzene copolymers (polyVBC–DVB) or external cross-linkers that are additional electrophiles such as monochlorodimethyl ether (MCDE), tris-(chloromethyl)-mesitylene (TCMM) and formaldehyde dimethyl acetal (FDA) resulting in an interlinked porous polymer.<sup>17,18,20</sup> Davankov *et al.*, first synthesised hyper-cross-linked polystyrene from linear polystyrene and different cross-linkers like monochlorodimethyl ether and *p*-xylylenedichloride.<sup>21–23</sup> The synthesised hyper-cross-linked polymers showed impressive surface areas at 1106 m<sup>2</sup>/g<sup>21</sup> and 956 m<sup>2</sup>/g,<sup>23</sup> respectively. In 2006, Ahn *et al.* studied the synthesis of hyper-cross-linked polydivinylbenzene (DVB)-vinyl benzyl chloride (VBC) and the maximum obtained surface area was 2090 m<sup>2</sup>/g<sup>24</sup>. Li *et al.* reported the effect of DVB content in a polymer precursor on the pore size of hyper-cross-linked poly(divinylbenzene-co-vinyl benzyl chloride). They found that the pore size could be adjusted by increasing the amount of DVB resulting in higher micropore volume.<sup>25</sup>

The most important benefit of this method is to use commercially available polymeric precursors for post-crosslinking. However, this method still has some limitations. First, the synthesis of polymer precursors is time-consuming and limited monomers like styrene are used to suit both radical polymerisation and Friedel-Crafts alkylation.<sup>17</sup>

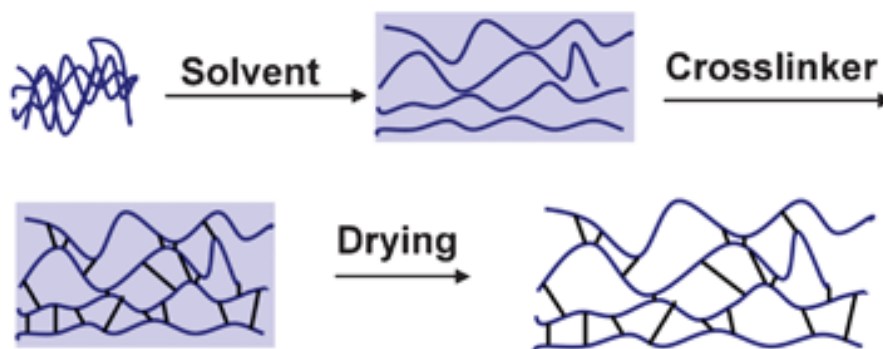


**Figure 1.1 Hyper-cross-linking process scheme.**<sup>20</sup>

### 1.1.1 (b) Direct one-step polycondensation of functional monomers

Cooper and co-workers investigated the self-condensation of monomers or internal crosslinkers.<sup>16,26</sup> In this work, a series of hyper-cross-linked polymers was obtained from three bis(chloromethyl) aromatic building blocks; dichloroxylylene (DCX), 4,4'-bis(chloromethyl)biphenyl (BCMBP), and bis(chloromethyl) anthracene (BCMA) (as shown in Figure 1.2); using a simple one-pot condensation polymerisation process. With Lewis acid catalysts, chloromethyl groups readily react with adjacent phenyl rings to form rigid methylene linkages between each building block. The synthesised materials exhibited microporosity and high surface areas up to 1874, 1391, and 921 m<sup>2</sup>/g for BCMBP, DCX and BCMA monomers, respectively under the same conditions. Moreover, copolymerisation of DCX and BCMA at 1 : 3 molar ratio resulted in a higher surface area of 1924 m<sup>2</sup>/g.

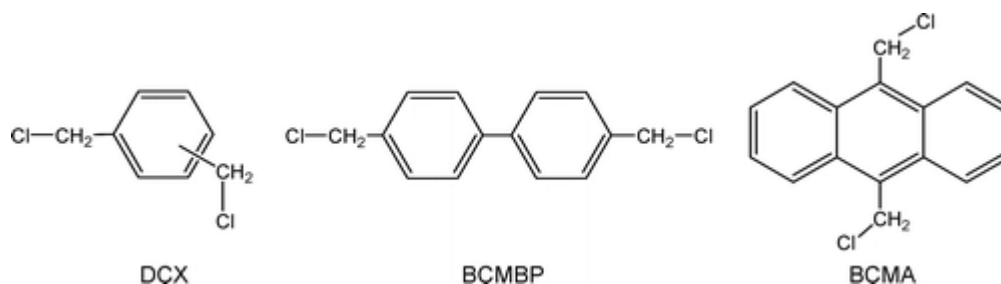


**Figure 1.2 Monomers used for the synthesis of the hyper-cross-linked polymers.**<sup>26</sup>

In 2014, Tan and co-workers employed a Scholl coupling reaction as a cost-effective way for the synthesis of microporous polymers by eliminating two hydrogen atoms from adjacent phenyl rings and forming a new aryl-aryl bond in the presence of  $\text{AlCl}_3$  catalyst (Figure 1.3).<sup>17,27,28</sup> Because no external bridges are built, extended  $\pi$  conjugation could be achieved leading to high catalytic activity. Moreover, monomers with various functionalities could be used in this reaction, such as electron-rich molecules (anisole, benzylamine) or electron deficient molecules (tetraphenylporphyrin), acidic (benzoic acid) or alkaline (bipyridine) monomers, an aryl ring (triphenylbenzene), fused ring molecules (naphthalene, anthracene, pyrene) or a heterocyclic ring (pyrrole). With various functional monomers, the polymers could be employed in a wide range of applications including gas storage, heterogeneous catalysis, luminescence and semiconductors. The polymer networks prepared from triphenylbenzene copolymerised with the alkaline monomer; pyrrole showed the highest BET surface area of  $1421 \text{ m}^2/\text{g}$  with the most elevated  $\text{CO}_2$  uptake up to 20 wt. % at 1 bar and 273 K while the homopolymer synthesised from triphenylbenzene exhibited a surface area of  $1254 \text{ m}^2/\text{g}$  and lowered  $\text{CO}_2$  absorption of 18.0 wt. %. However, the polymer network obtained from triphenylbenzene copolymerised benzoic acid showed the lowest  $\text{CO}_2$  of 13.7 wt. %. The results indicated that the basic functional groups play a more critical role in the  $\text{CO}_2$  uptake. Also, the polymer

networks synthesised from fused aromatic rings; naphthalene and pyrene showed lower surface areas of 822 and 636 m<sup>2</sup>/g, respectively.

Nonetheless, the significant disadvantage of the Scholl coupling reaction is a generation of hydrogen chloride which is toxic to humans and the environment.

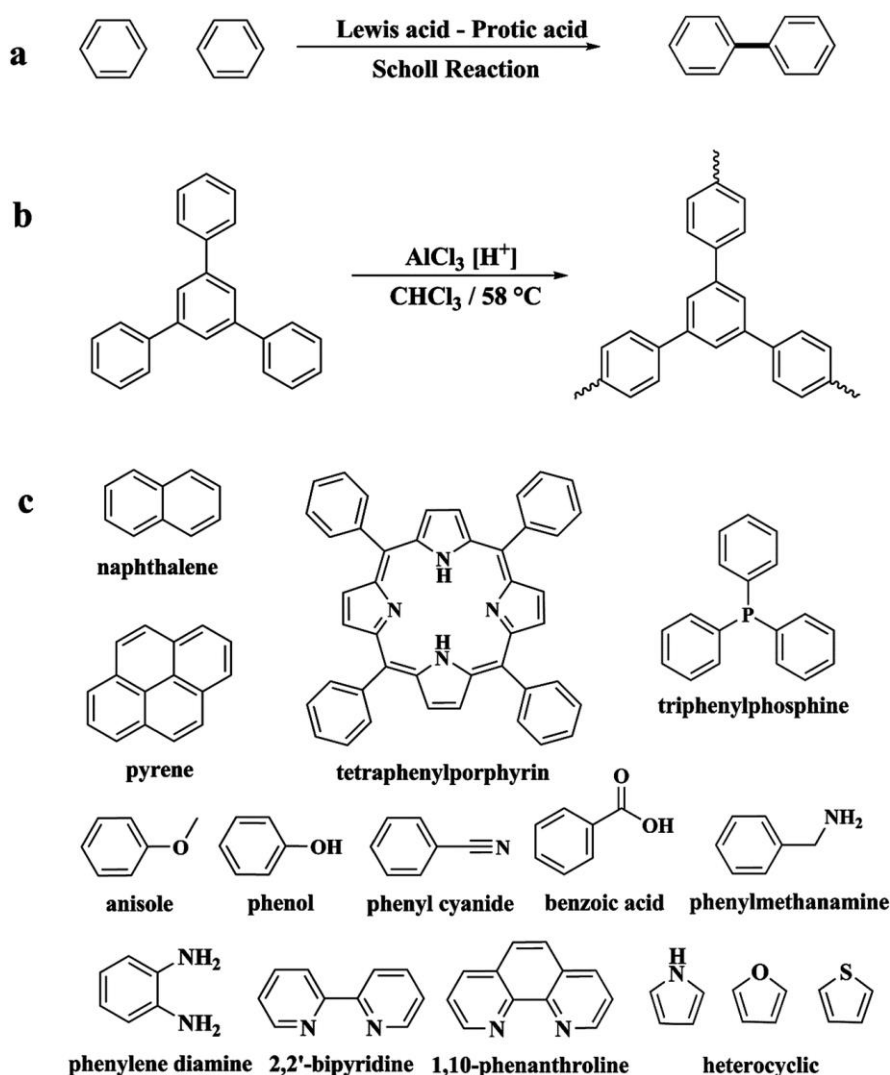


**Figure 1.3** (a) The general scheme of the Scholl coupling reaction, (b) the Scholl coupling polymer network from triphenylbenzene monomers, (c) other monomers or co-monomers used for the synthesis of hyper-cross-linked polymer networks with various functionalities.<sup>17</sup>

### 1.1.1 (c) Crosslinking by external crosslinkers

Tan and co-workers introduced the “knitting” strategy in 2011.<sup>29</sup> Formaldehyde dimethyl acetal (FDA) was used as an external crosslinker to link aromatic compounds with methylene linkages using anhydrous  $\text{FeCl}_3$  catalysed Friedel-Crafts reaction as shown in Figure 1.4. Several aromatic monomers, such as benzene, biphenyl, triphenylbenzene, methylbenzene, chlorobenzene, and phenol, were directly knitted by FDA resulting in predominantly microporous networks and a high surface area. Varying the ratio between external crosslinkers and monomers affects the crosslinking degree, so pore structures and surface areas could be tuneable. The surface area of the polymer network synthesised from 3:1 molar ratio of benzene and FDA was 1391  $\text{m}^2/\text{g}$ , which was higher than that of the 1:1 molar ratio network (897  $\text{m}^2/\text{g}$ ). Furthermore, different monomers could be used to adjust the functionality of polymer networks. By introducing phenol into the knitted polymer networks, it exhibited higher  $\text{CO}_2$  uptake of 9.4 wt. % at 1 bar and 273 K than the biphenyl networks (6.9 wt.%). It could be explained that the hydroxyl group increased the interaction with  $\text{CO}_2$ .

Beside high efficiency, versatility and flexibility of this synthesis method, the advantages of this approach are the use of inexpensive reagents and mild reaction conditions.

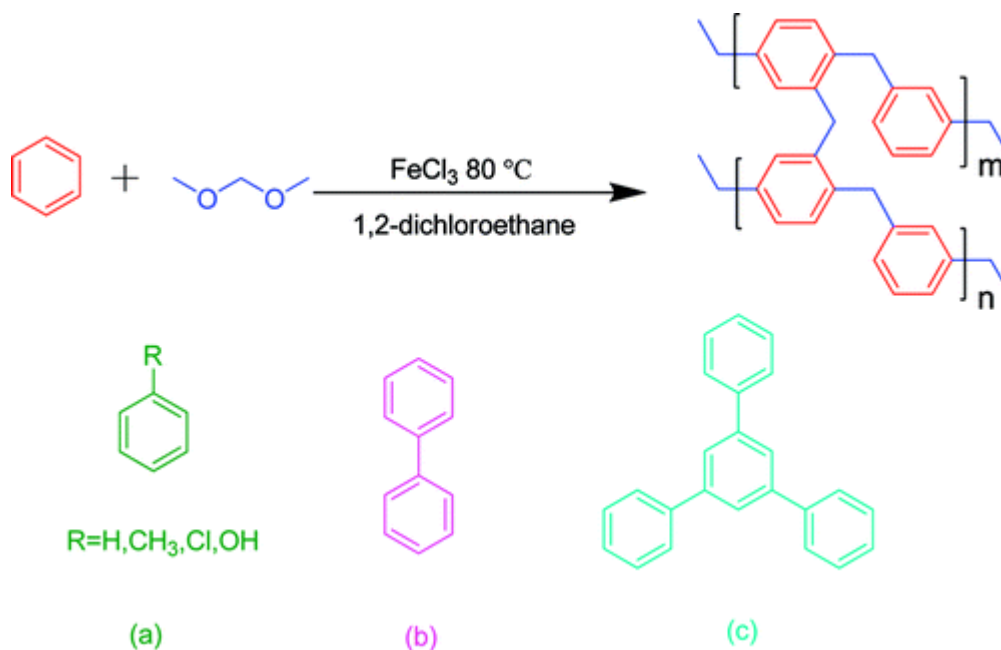


**Figure 1.4 Synthetic pathway to create knitted polymer network and aromatic building blocks; (a) benzene, methylbenzene, chlorobenzene and phenol, (b) biphenyl, and (c) triphenylbenzene.<sup>29</sup>**

### **1.1.2 Polymers of Intrinsic Microporosity (PIMs)**

PIMs are rigid linear polymer chains (often ladder type polymers) which contain a site of contortion (such as a rigid tetrahedral C) in the backbone resulting in the inefficient packing of the polymer chain in the solid state. This leads to the introduction of microporosity and high surface areas into the materials. Due to the potential to make linear structures, they can be soluble and can be cast to form membranes which are further utilised for gas separation.<sup>30</sup>

According to Budd and co-workers,<sup>31</sup> they discovered a series of PIMs (PIM1-6) synthesised from tetrol monomers A1-A3 with appropriate fluorine-containing molecules B1-B3 to form dibenzodioxane linkages as shown in Figure 1.5. PIM1-3 were made from monomer A1 with monomers B1-3, while PIM4-5 were prepared from monomer A2 and monomers B1-2, respectively. All synthesised PIMs were soluble in

polar aprotic solvents (e.g. tetrahydrofuran (THF) and dimethylacetamide (DMAc)), except PIM6 (prepared from A3 and B2) that was soluble only in acidic solvents (e.g. trifluoroacetic acid (TFA)). The synthesised polymers also showed high surface areas varied from 430 to 850 m<sup>2</sup>/g.

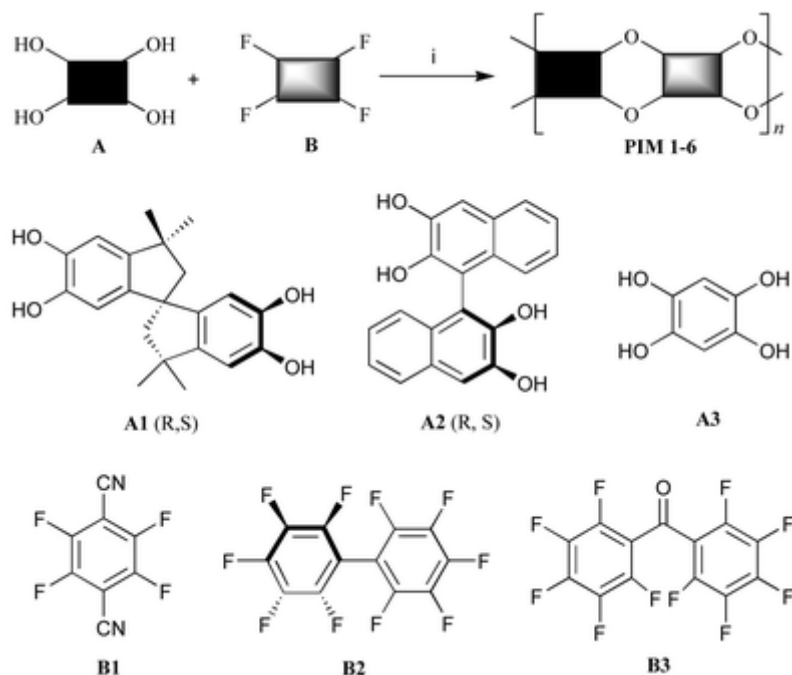


**Figure 1.5** The synthesis pathway of PIMs 1–6. Reagents and conditions: K<sub>2</sub>CO<sub>3</sub>, DMF, 60–120 °C.<sup>31</sup>

### 1.1.3 Covalent Organic Frameworks (COFs)

COFs are crystalline porous polymer networks where the monomers are linked by covalent bonds. The polymerisation reactions used to synthesise these materials are reversible and hence thermodynamically controlled resulting in low energy crystalline structures (c.f. kinetically controlled HCPs and CMPs).<sup>18</sup> COFs can be synthesised by various chemical reactions e.g. the condensation of boronic acids with diols to form boroxine rings, self-condensation of boronic acids, and the condensation of amines with aldehydes to form imine linkages as shown in Figure 1.6(a) to (c),<sup>8</sup>

respectively. Due to the diversity of building blocks employed in COFs synthesis, they can be used in many applications including gas storage and adsorption, catalysis, and energy storage.

In 2005, the first COFs were reported by Yaghi and co-workers.<sup>32</sup> COF-1 and COF-5 were prepared by the self-condensation reaction of 1,4-benzenediboronic acid to form boroxine anhydride and the co-condensation reaction of the 1,4-benzenediboronic acid with 2,3,6,7,10,11-hexahydroxytriphenylene to form boronate ester linkages, respectively. 1,4-dibenzenediboronic acid was partially dissolved in the chosen solvent to slow down condensation reaction leading to the nucleation and growth of crystalline COFs. From their results, COF-1 showed a staggered structure with a surface area of 711 m<sup>2</sup>/g while COF-5 exhibited an eclipsed structure with a higher surface area of 1592 m<sup>2</sup>/g as shown in Figure 1.7.

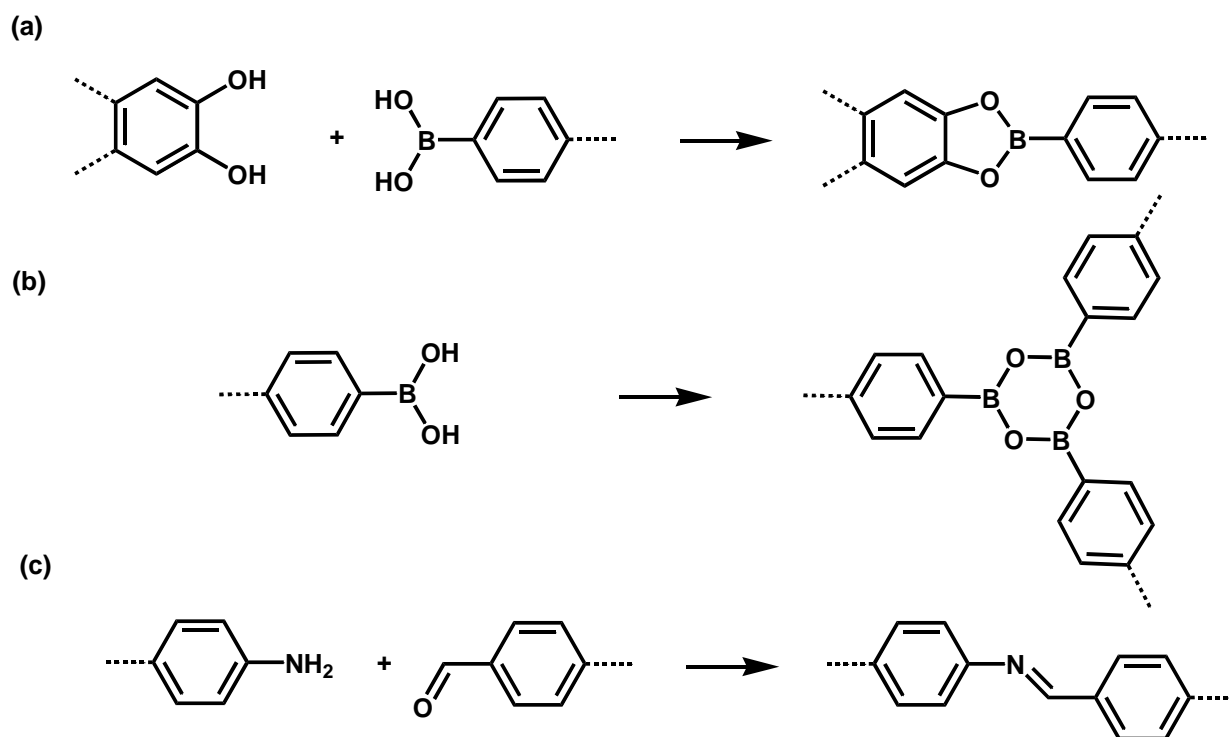
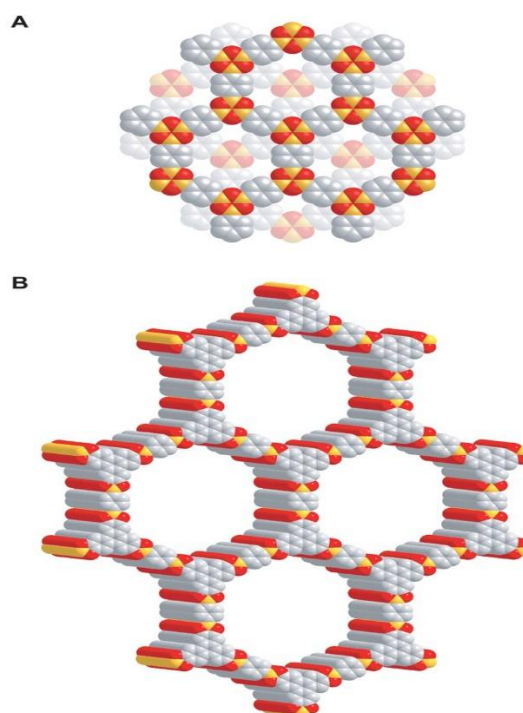


Figure 1.6 (a) condensation of boronic acids with diols (b) self-condensation of

boronic acids and (c) condensation of amines with aldehydes.<sup>8</sup>



**Figure 1.7 Structures of (A) COF-1 and (B) COF-5, grey, orange and red spheres represent carbon, boron, and oxygen, respectively.<sup>32</sup>**

COF-1 and COF-6 have 2D structures with 1D small pores; COF-5, COF-8, and COF-10 possess 2D structures with large 1D pores.; and COF-102 and COF-103 have 3D structures with 3D medium sized pores. These materials were prepared from various building blocks using the condensation of different boronic acids with 2,3,6,7,10,11-hexahydroxytriphenylene (HHTP) and self-condensation of boronic acids as shown in Figure 1.8.<sup>33</sup>

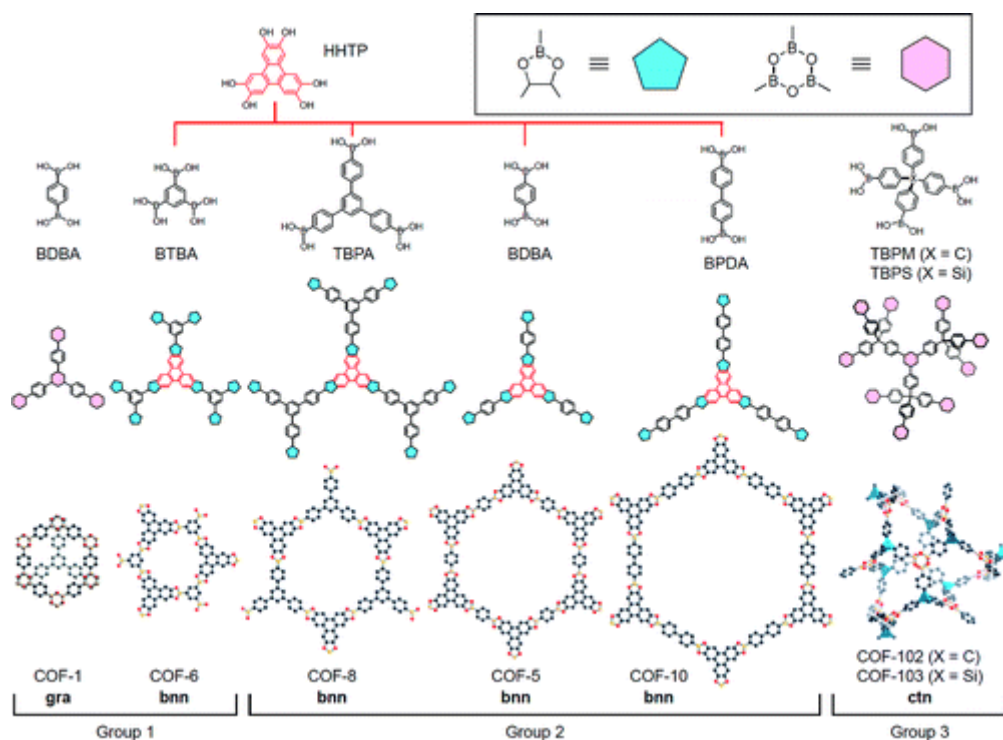


**Figure 1.8 Preparation of COF-1, COF-5, COF-6, COF-8, COF-10, COF-102 and COF-103 via condensation reactions.**<sup>33</sup>

In addition, COFs can be prepared *via* Schiff-base reactions as shown in Figure 1.9.<sup>34</sup> The condensation reactions of amines with aldehydes to form imine linkages have been widely used to synthesise COFs. The reaction conditions for this reaction are to use mixtures of mesitylene/dioxane/acetic acid or combinations of the dioxane-acetic acid aqueous solution or n-butanol/1,2-dichlorobenzene/3M acetic acid. Acetic acid has been the commonly chosen as a catalyst for this reaction.<sup>34</sup> For instance, a high surface area ( $S_{\text{BET}}=2723 \text{ m}^2/\text{g}$ ) mesoporous imine linked COF (ILCOF-1) with 2D structure has been synthesised using tetrakis(*p*-formylphenyl)pyrene and 1,4-*p*-phenylenediamine as precursors as shown in Figure 1.10.<sup>35</sup>

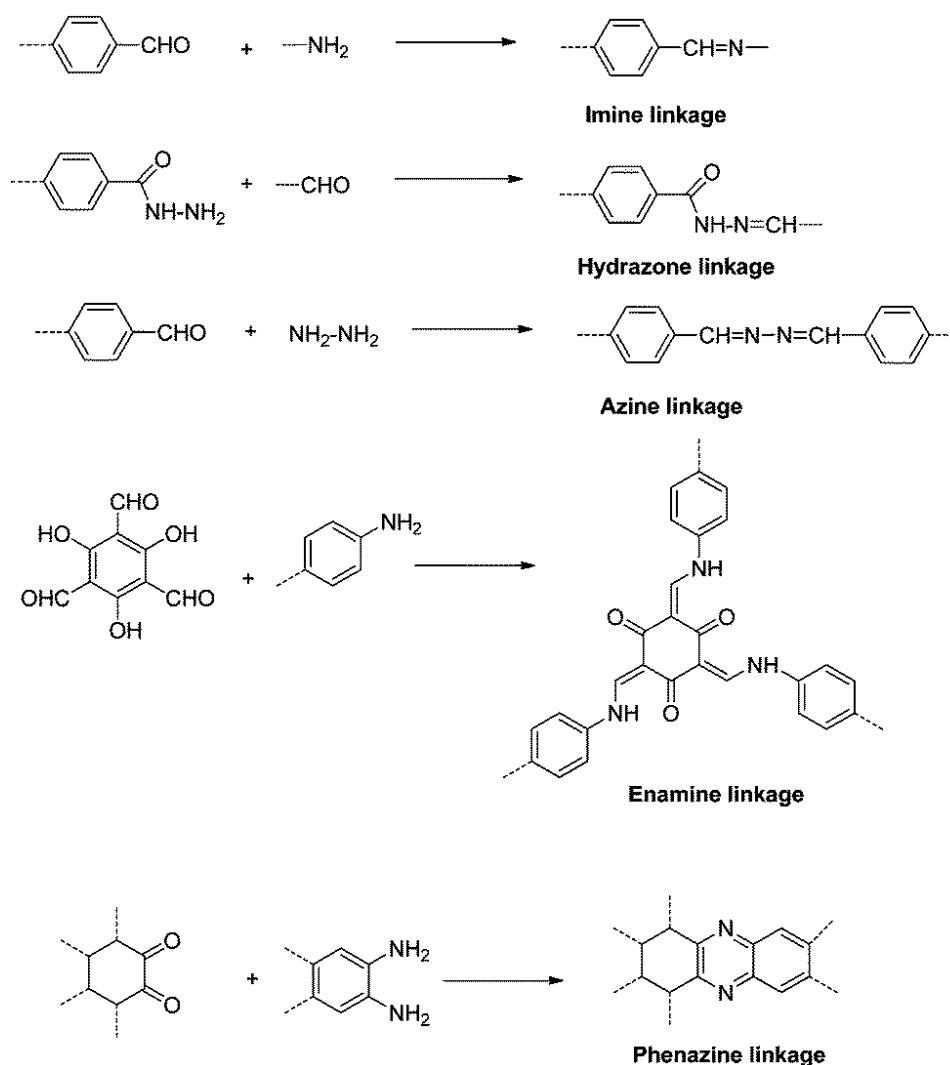


**Figure 1.9 Preparation of COFs using Schiff-base chemistry.**<sup>34</sup>

In 2011, Yaghi and co-workers prepared hydrazone linked COF-42 and COF-43 by the condensation of 2,5-diethoxyterephthalohydrazide with 1,3,5-triformylbenzene or 1,3,5-tris(4-formylphenyl)benzene. The synthesised materials showed extended 2D porous networks with high crystallinity, excellent chemical and thermal stabilities as well as permanent porosity.<sup>36</sup>

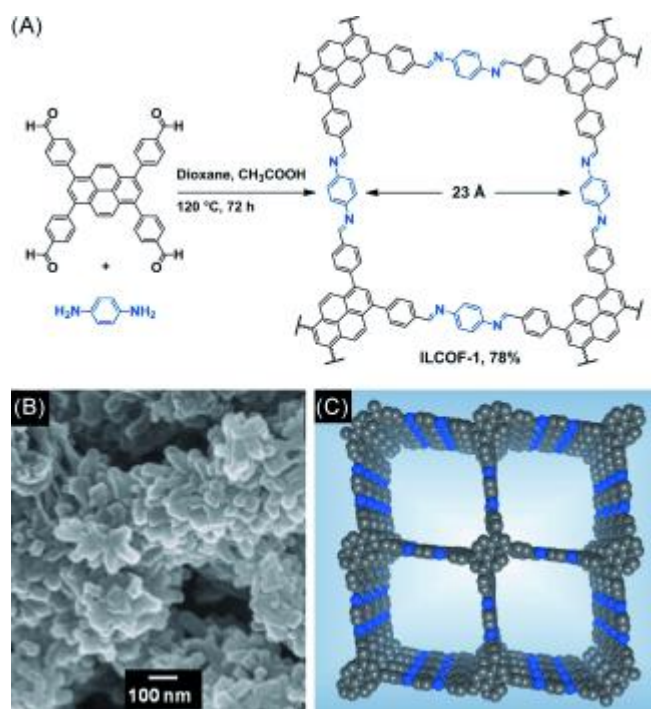


**Figure 1.10 (A) Synthetic pathway of ILCOF-1; (B) scanning electron micrograph of the synthesised materials, and (C) space-filling representation of the resulting 2D network; carbon (grey), nitrogen (blue), hydrogen was omitted for clarity.<sup>35</sup>**

#### **1.1.4 Conjugated Microporous Polymers (CMPs)**

CMPs are organic porous polymers that contain  $\pi$ -conjugated systems with permanent microporous structure. CMPs can be synthesised from various chemical reactions and monomers resulting in a variety of CMPs that have multiple structures and specific functionality.<sup>37</sup> Because of the free rotation of  $\sigma$  bonds formed between monomer molecules, these materials are amorphous.<sup>18</sup> The Cooper group reported the first CMPs in 2007,<sup>38</sup> which were synthesised using the Sonogashira-Hagihara cross coupling reaction of alkyne and halogen building blocks to form a series of poly(aryleneethynylene) networks, namely CMP-1, CMP-2, CMP-3 and CMP-4. CMP-1 and CMP-2 were synthesised using 1,3,5-triethynylbenzene with 1,4-diiodobenzene

and 4,4'-diiododiphenyl, respectively while CMP-3 and CMP-4 were prepared from 1,4-diethynylbenzene with 1,3,5-tris(4'-iodophenyl)benzene and 1,3,5-tribromobenzene, respectively. All the synthesised CMP materials are microporous with surface areas from 522 to 834 m<sup>2</sup>/g. They also exhibited high thermal stability  $T_{dec} > 400$  °C and were insoluble in all common organic solvents and chemically stable in acids and bases. A combination of an extended conjugated system and porosity of the CMPs makes the materials useful for chemical, electrical and optical applications. Take CMP-1 as an example; it showed photoluminescence at  $\lambda_{max} = 500-550$  nm. In 2011, the Cooper group also reported the synthesis of CMPs based on pyrene monomers *via* Ni-catalysed Yamamoto reactions as shown in Figure 1.11. The obtained materials were both microporous and highly luminescent.<sup>39</sup> They found that by introducing different comonomers and by varying the monomer distribution, the emission colour and bandgap could be tuned. The synthesised materials possessed high surface areas in the range of 303-1508 m<sup>2</sup>/g with a statistical monomer distribution. The homocoupled polymer network, YPy showed the lowest bandgap energy due to the most extended conjugation length in the system. The synthesised polymers showed the blue-shifted emission from YPy, YDPPy and YDBPy, respectively because the fluorescence band red shifts as a function of the number of pyrene units. Alternative monomer distribution SDBPy could be created by using Suzuki copolymerization of tetrabromopyrene and 1,4-benzene diboronic acid. The result showed that SDBPy gave narrower green emission band centred at 530 nm while YDBPy exhibited a broader, green emission spectrum with two central peaks centred at 545 and 582 nm. It indicates that the electronic structure and therefore the band gap could be possibly tuned in CMP networks by selective choice of comonomer.

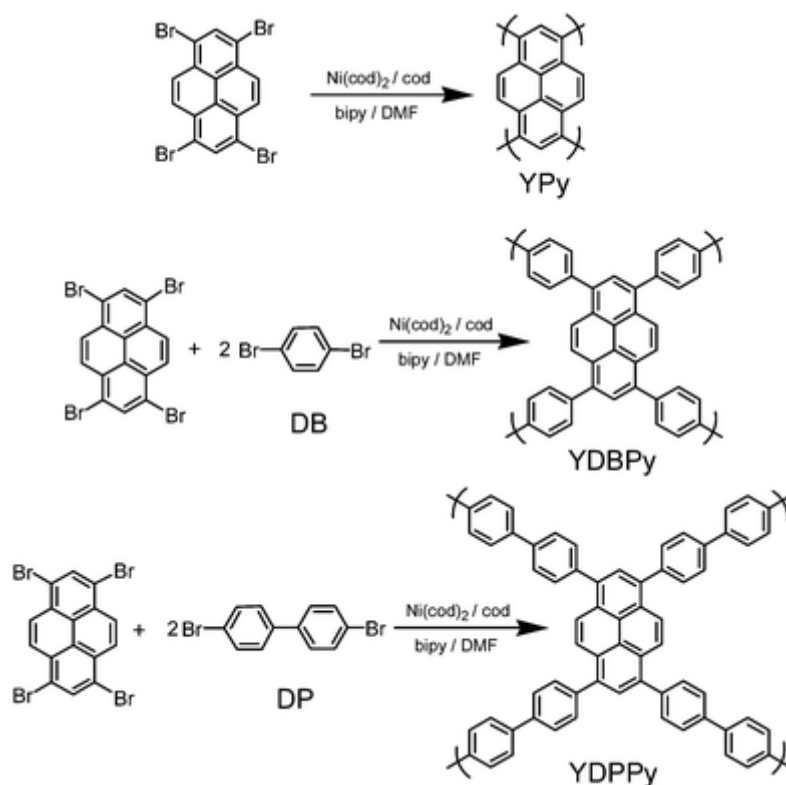


**Figure 1.11 Synthetic approaches to luminescent CMPs based pyrene.**<sup>39</sup>

The Suzuki-Miyaura coupling reaction was used to synthesise extended phenylene based microporous polymers employing *para*- and *meta*-1,3,5-triphenyltribromide as monomers as shown in Figure 1.12. The resulting materials showed 3D amorphous structures with surface areas of 269 (pore volume = 0.20 cm<sup>3</sup>/g) and 229 m<sup>2</sup>/g (pore volume = 0.15 cm<sup>3</sup>/g) for *p*-PPF and *m*-PPF, respectively. The more twisted geometry of a *meta*-directing monomer compared to *para*-building block gave a more dense structure resulting in the smaller pore volume of *m*-PPF<sup>40</sup>.

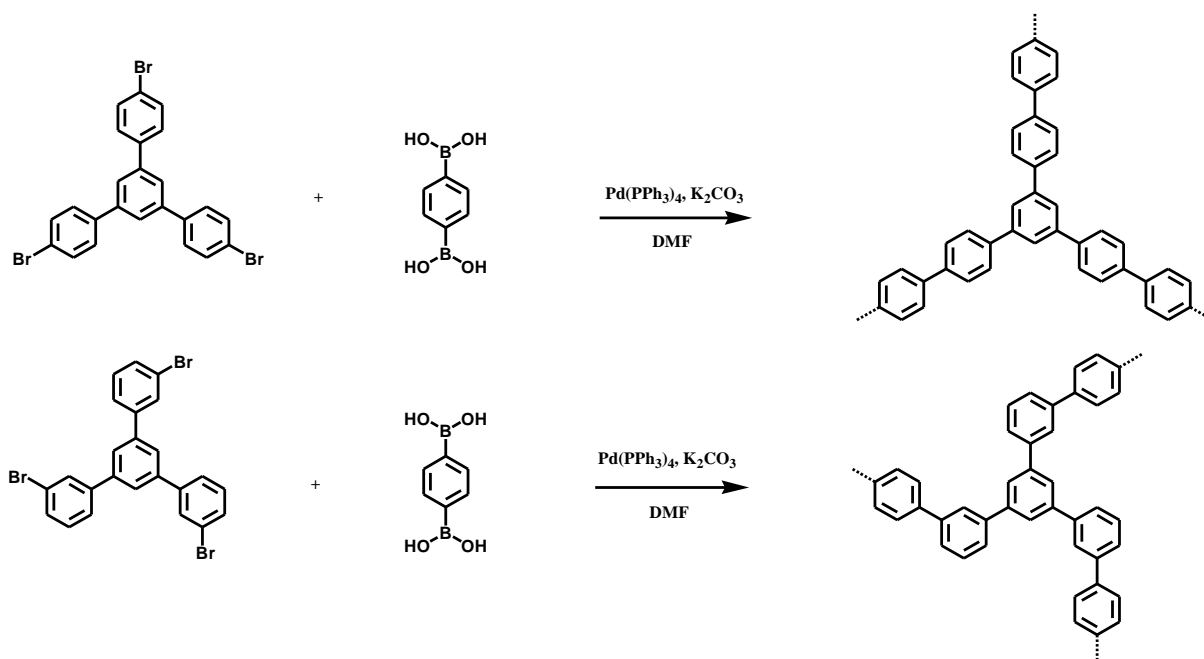


**Figure 1.12 Synthesis of *p*-PPF and *m*-PPF via Suzuki-Miyaura coupling reaction.<sup>40</sup>**

### **1.1.5 Covalent Triazine Frameworks (CTFs)**

The CTF networks were firstly reported by Thomas *et al.* in 2008.<sup>41</sup> They are synthesised by nitrile cyclotrimerisation to form triazine rings. CFT-1 was prepared from 1,4-dicyanobenzene using ZnCl<sub>2</sub> as a catalyst at 400 °C under ionothermal conditions as shown in Figure 1.13. It showed crystallinity and microporosity with a high surface area of 791 m<sup>2</sup>/g. However, the produced triazine-based polymer networks were amorphous when different building blocks and monomer: catalyst ratios were used. Also, reaction temperature and time can affect the structures and properties of CTFs.<sup>42</sup> The surface area of CTF produced from 1,4-dicyanobenzene increased significantly from 920 m<sup>2</sup>/g to 3270 m<sup>2</sup>/g when the reaction temperature was held at 400 °C for 20 h and then increased to 600 °C for 96 h. The result can be explained by increasing the reaction temperature, also the mesoporosity of the synthesised polymer networks. The significant drawbacks of ionothermal reaction are

long reaction time, high temperature and the need for  $\text{ZnCl}_2$  catalyst separation at the end of the reaction.<sup>43</sup> To solve these problems, Cooper and co-workers introduced trifluoromethanesulfonic acid (TFMS) as a catalyst for synthesis of triazine-based polymer networks under both room temperature and microwave assisted conditions. The results showed that the synthesised materials exhibited impressive BET surface areas higher than  $1100 \text{ m}^2/\text{g}$ . Moreover, the mild synthetic routes allow incorporation of functional groups that are intolerant to high temperature methods.<sup>43</sup>

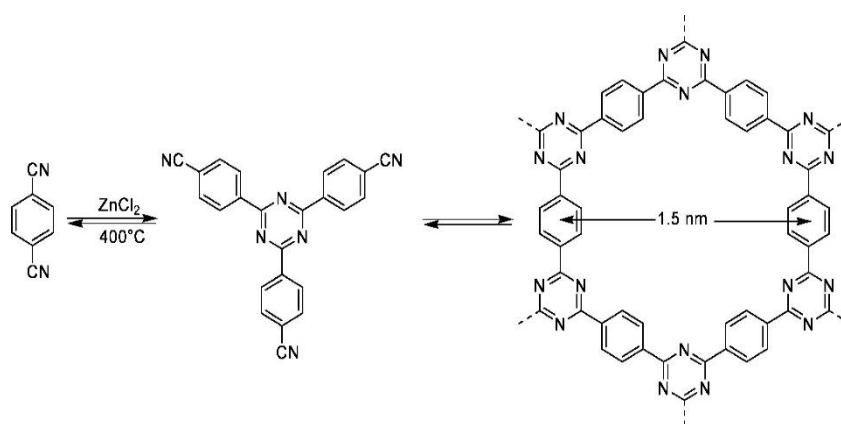


**Figure 1.13 Reaction scheme of cyclotrimerisation of 1,4-dicyanobenzene leading to the formation of a 2D framework with 1.5 nm channels.<sup>42</sup>**

### **1.1.6 Porous Aromatic Frameworks (PAFs)**

PAFs are porous organic frameworks containing rigid aromatic building blocks linked by covalent bonds leading to the high surface area and exceptional stability.<sup>44</sup> In 2009, Ben and co-workers firstly reported synthesis a long-range ordered PAF with diamondoid (dia) topology namely PAF-1.<sup>45</sup> They prepared it from tetrakis(4-bromophenyl)methane building block using nickel catalysed Yamamoto coupling reaction. The resulted PAF-1 showed extremely high BET surface area up to  $5640 \text{ m}^2/\text{g}$ , superhydrophobic property and excellent stability with high  $\text{CO}_2$  uptake ( $1300 \text{ mg/g}$  at  $298 \text{ K}$ ,  $40 \text{ bar}$ ) as well as benzene and toluene uptakes at room temperature<sup>45</sup>.

In the following two years, Ben and co-workers also adopted Yamamoto coupling for the synthesis of PAF-3 and PAF-4 using tetrakis(4-bromophenyl)silane and tetrakis(4-bromophenyl)germane as monomers, respectively as shown in Figure 1.14. The synthesised polymer networks were found to have high surface areas (PAF-3, 2932 m<sup>2</sup>/g and PAF-4, 2246 m<sup>2</sup>/g) and excellent selectivity for the adsorption of gases (PAF-3 CO<sub>2</sub>/N<sub>2</sub> selectivity, 87/1 and CH<sub>4</sub>/N<sub>2</sub> selectivity, 30/1 at 1 bar and 273 K). The high selective adsorption of greenhouse gas of PAFs can be potentially applied to solve greenhouse gases pollutant problems.<sup>46</sup>

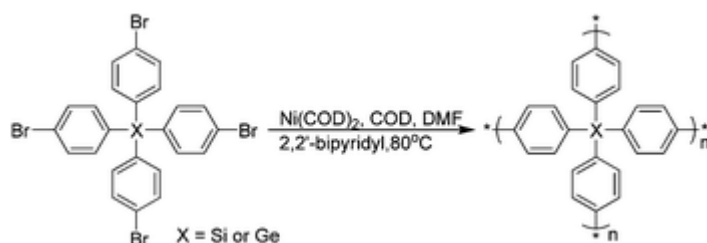


**Figure 1.14 Synthesis of PAF-3 and PAF-4 via Yamamoto coupling.**<sup>46</sup>

### **1.1.7 Extrinsic Porous Molecules**

Most porous materials such as zeolites, COFs, MOFs and amorphous porous organic materials are extended networks. Recently, a relatively new type of porous material which consists of discrete organic molecules can be divided into 2 subtypes; intrinsic and extrinsic porous molecules. Intrinsic porous molecules exhibit porosity caused by intramolecular voids and porosity is ingrained with the molecules. In contrast, extrinsic porous molecules are formed by an inefficient packing of molecules that caused porosity (outside of molecules).<sup>18</sup> Hexagonal molecular crystals of tris-*o*-phenylenedioxycyclotriphosphazene formed *via* van der Waals interaction were reported by Sozzani *et al.*, in 2005. The nanoporous crystals showed good CO<sub>2</sub> and CH<sub>4</sub> storage at 12wt.% and 2.4wt% at 195 K and 1 atm.<sup>47</sup> In 2012, Mastalerz *et al.*,

reported the synthesis of extrinsic porous material by the self-assembly of triptycene trisbenzimidazolone *via* H bondings (Figure 1.15).<sup>48</sup> The results showed that the prepared material gave a high surface area of 2796 m<sup>2</sup>/g and selective adsorption of CO<sub>2</sub> (15.9wt.%) over CH<sub>4</sub> (1.5wt.%) at 273 K and 1 bar.

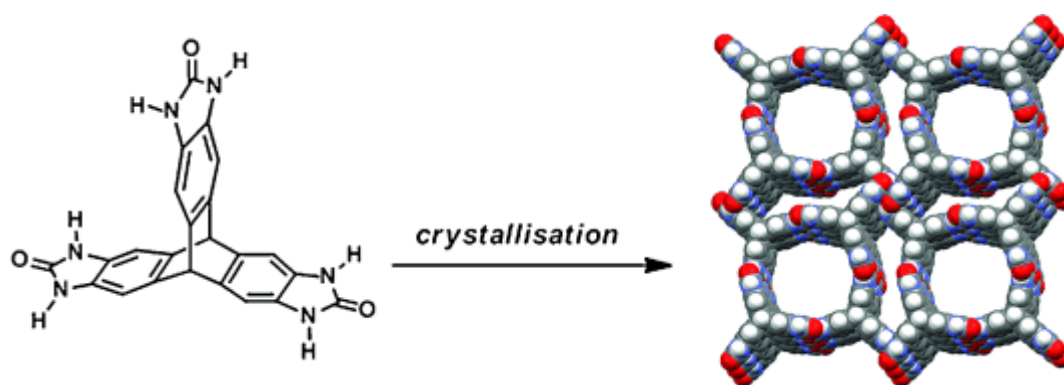


**Figure 1.15 Preparation of extrinsic porous material from triptycene trisbenzimidazolone.**<sup>48</sup>

### 1.1.8 Porous Organic Cages

Porous organic cages are a fairly new type of porous material, and they have some different properties from extended porous frameworks, such as solution processability. Porous organic cages with extrinsic porosity can be produced from molecules that pack inefficiently due to rigid structures of the molecules or directional intermolecular interactions such as hydrogen bonding. In contrast, intrinsic porous organic cages are synthesised by molecules with permanent voids inside a rigid structure.<sup>49</sup> Zhang and co-workers reported a permanent mesoporous organic cage from twelve triptycene tetraol molecules and eight triboric acid molecules *via* boronic ester formation as shown in Figure 1.16. The material displayed an extremely high surface area of 3758 m<sup>2</sup>/g with a pore diameter of 2.3 nm.<sup>50</sup> Jiang *et al.*, reported a propeller-shaped [2+3] organic cage prepared *via* the condensation of 1,3,5-tri(4-formylphenyl)benzene with 1,5-pentanediamine. The synthesised material has 1-D



In this work, we mainly focus on conjugated porous polymers (CMPs) for heterogeneous catalysis. Different catalysts derived from CMPs such as transition metal incorporated CMPs, CMP organocatalysts, CMP photocatalysts are discussed in the following part 1.2.

## **1.2 Conjugated Microporous Polymers (CMPs) for Heterogeneous Catalysis**

CMPs have been widely used as heterogeneous catalysts for various organic reactions over the past decade. Catalytically active molecules can be directly incorporated into the polymer networks either as part of the polymer backbone, as pendant groups or as supports for metal nanoparticles to produce heterogeneous CMP catalysts. The high surface area of CMPs provides high loading of active sites with a homogeneous distribution throughout the network which make CMPs highly active heterogeneous catalysts. In comparison with other porous materials such as metal-organic frameworks (MOFs) and covalent organic frameworks (COFs), CMPs often possess higher chemical and thermal stability which enhances their suitability for reuse. Moreover, CMPs are insoluble in common solvents, bases and acids, so it is easy to separate and reuse them multiple times which is more environmentally friendly and cost effective. CMPs for heterogeneous catalysis can be categorised into 3 different classes based on their applications for either: CMPs for heterogeneous transition-metal catalysis, organocatalysis and photocatalysis.<sup>53</sup>

### **1.2.1 CMPs incorporating transition-metal catalysts**

Transition-metal catalysts, particularly organometallic catalysts have been extensively utilised in homogeneous catalysis including asymmetric hydrogenation reactions catalysed by Rh, Ru, or Ir complexes, asymmetric epoxidation and dihydroxylation reactions catalysed by Ti or Os complexes, olefin metathesis reactions

using Ru or Mo organometallic compounds as catalysts; and Pd-catalysed cross-coupling reactions.<sup>54</sup> However, most of homogeneous transition-metal catalysts are expensive and difficult to be isolated from products and then recycled. Incorporation of transition metals with specific functional groups in CMPs enables the catalysts to be recyclable due to the insolubility and high physicochemical stability of the CMPs.<sup>53</sup>

Cooper and co-workers reported preparation of transition metal such as rhenium (Re), rhodium (Rh) and iridium (Ir) incorporated conjugated microporous polymers.<sup>55</sup> The obtained materials can be prepared by post-synthetic modification of bipyridine-functionalised CMPs with a metal complex or by direct Sonogashira-Hagihara cross-coupling of a halogenated metal complex with alkyne linkers such as 1,3,5-triethynylbenzene and 1,4-diethynylbenzene as shown in Figure 1.17 and 1.18, respectively. In Figure 1.17, 5,5-dibromo-2,2'-bipyridine and 1,4-dibromobenzene were co-polymerised with 1,3,5-triethynylbenzene by varying the feed ratios of bipyridine monomer from 10 to 50% to yield CMP-(Bpy)<sub>x</sub> where x = 10, 20, 50%. A CMP without bipyridine was also synthesised as a control. The synthesised pyridine CMPs showed high surface areas from 664 to 859 m<sup>2</sup>/g. After [Re(CO)<sub>5</sub>Cl] was coordinated to the pyridine ligand in the networks, the surface areas dropped compared with the precursor CMPs due to a combination of partial pore filling and additional mass. The FTIR spectra of the networks showed additional peaks after modification with the Re complex at 2020, 1920 and 1885 cm<sup>-1</sup> corresponding to the carbonyl ligands of the metal complex. Inductively coupled plasma-optical emission spectroscopy (ICP-OES) was also employed to determine the amount of metal loading in the CMP networks and the metal incorporation saturated at around 15% w/w. The non-pyridine CMP was also treated with the Re complex and no Re was detected.

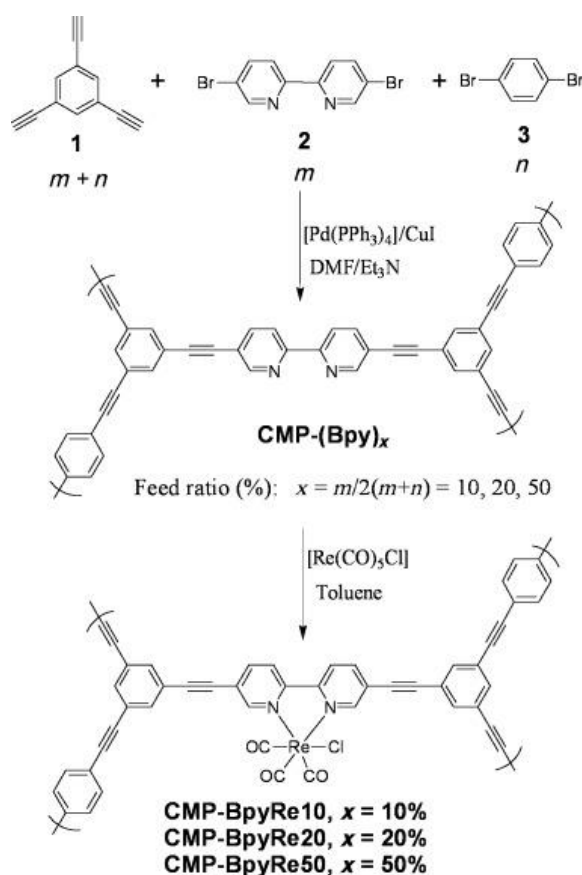


**Figure 1.17** Synthesis of the bipyridine-containing CMPs and post modification of the CMP precursors with the Re complex.<sup>55</sup>

Ir and Rh complexes were also incorporated into CMP networks by reacting tetrabromo metal complexes (Figure 1.18, 5a and 5b) with either 1,3,5-triethynylbenzene or 1,4-dithynylbenzene *via* direct Sonogashira-cross coupling to yield IrCMP-1, IrCMP-2, RhCMP-1 and RhCMP-2 with surface areas of 507, 721, 423 and 556 m<sup>2</sup>/g, respectively. CMPs based on cyclometalated Ir complex were synthesised by co-polymerisation of different ratio (x) of the halogenated Ir complex (6) with 1,4-dibromobenzene and 1,3,5-triethynylbenzene to yield CMP-CpIr with x = 5, 10, 50%; the surface areas were 864, 698 and 469 m<sup>2</sup>/g, respectively.

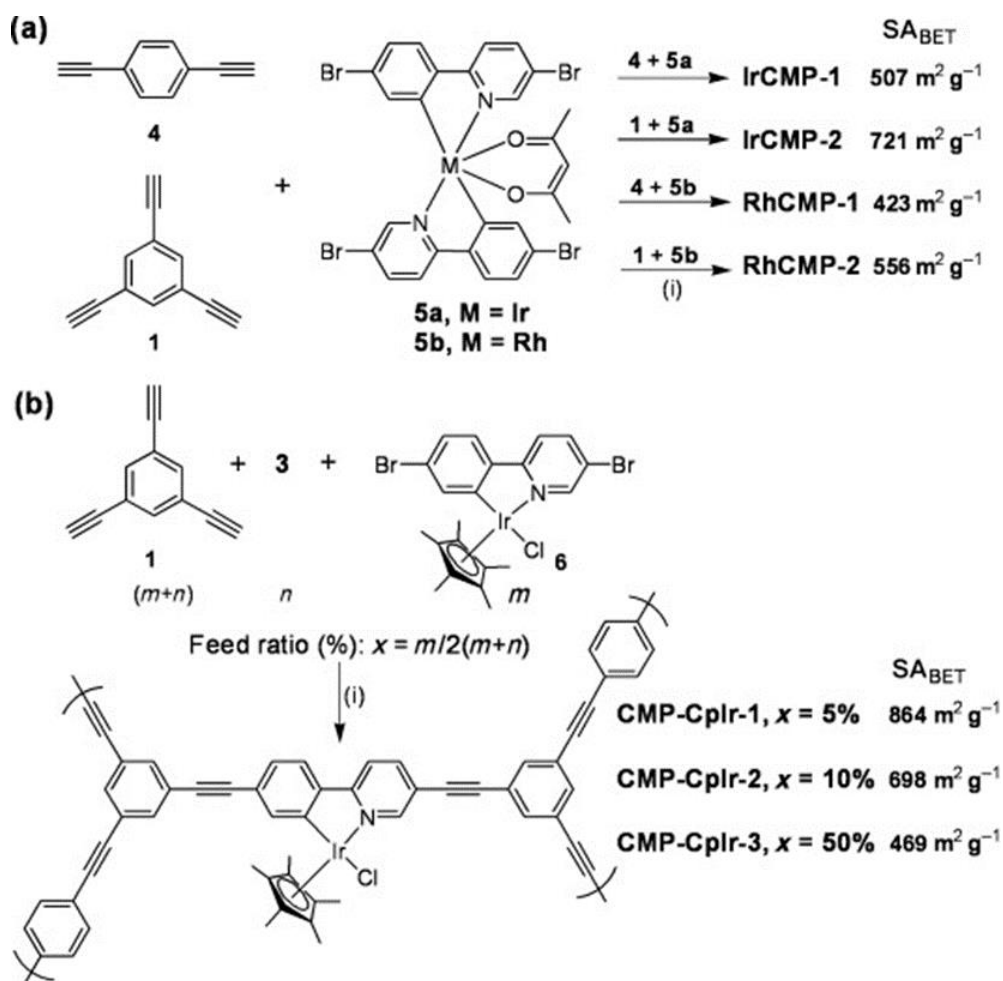


**Figure 1.18 Synthesis of (a) Ir and Rh loaded CMPs and (b) CplR based CMPs via direct Songogashira cross coupling.<sup>55</sup>**

CplR based CMPs were used as heterogeneous catalysts for reductive amination. The CMP-CplR-3 which has the highest Ir content in the network showed the highest activity up to 96% conversion which was comparable with the homogeneous catalyst (97%), so CMP-CplR-3 was selected as an optimum catalyst and it was applied to different substrates with product yields from 86 to 95%. The CMP-CplR-3 was reused, however; %conversion dropped to 51% after 3<sup>rd</sup> cycle probably due to metal leaching.

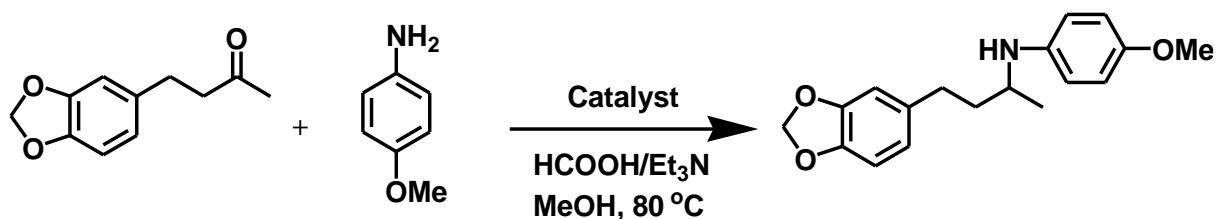


**Table 1.1** Reductive amination with heterogeneous Cplr based CMPs<sup>(a)</sup> 55

Entry	Catalyst	x (mol%) <sup>(b)</sup>	Time (h)	Conversion (%) <sup>(c)</sup>
1	Monomer 6	1	5	97
2	CMP-Cplr-1	1	5	51
3	CMP-Cplr-2	1	5	37
4	CMP-Cplr-3	1	5	96

(a) reaction conditions: ketone (0.5 mmol), amine (0.6 mmol), HCOOH/Et<sub>3</sub>N (2.5:1 molar) = 0.5 mL, MeOH (3 mL); (b) the molar ratio of iridium to ketone monomer; (c) determined by <sup>1</sup>H NMR based on ketone monomer.

### 1.2.2 CMPs for heterogeneous organocatalysis

Organocatalysis has been extensively applied in synthetic organic chemistry. The organocatalyst can be achiral or chiral and composes of non-metallic elements, typically C, H, N, S, and P. Organocatalysts are metal-free avoiding the use of toxic, moisture and air sensitive and expensive transition metal catalysts, hence organocatalysis is not only more sustainable but can also be more cost-effective. Types of organocatalysts include Lewis bases, Lewis acids, Brønsted bases, and Brønsted acids.<sup>56</sup> However, homogeneous organocatalysts still possess many of the disadvantages of traditional homogeneous metal catalysts such as their difficulty to be recycled. Therefore, the immobilisation of the catalysts with inorganic or organic

supports can improve the reusability of the catalysts. Organocatalysts embedded in CMP networks can be easily constructed by reacting catalytic active molecules with organic linkers *via* condensation reactions to form insoluble solid catalysts which can be simply separated and recycled. The incorporation of organic catalyst into CMP framework also provides additional benefits such as superior catalytic activity, porosity, high surface area and physicochemical stability.<sup>53</sup>

1,1'-binaphthalene-2,2'-diol (binol) based CMPs have been studied as reusable heterogeneous catalysts for asymmetric hydrogenation by Thomas and Blechert research groups.<sup>57</sup> 1,1'-binaphthalene-2,2'-diyl hydrogenphosphate (BNPPA) with 9-anthracenyl as bulky groups in 3,3'-positions was chosen as a starting tecton. A 3-thiophenyl group was introduced at 10-position of the anthracene units as coupling points to produce monomer 1. However, the phosphoric monomer 1 was not suitable for oxidative coupling reaction due to the poor solubility of the monomer, so the BNPPA chloride (monomer 5) which has better solubility was reacted with  $\text{FeCl}_3$  *via* oxidative coupling to form polymer 6. Then, polymer 6 was hydrolysed using aqueous hydrochloric acid and then washed with ethanol, THF and  $\text{CHCl}_3$  to give polymer 7 as shown in Figure 1.19. The Polymer 7 was characterised with nitrogen sorption method and it exhibited microporous characteristic with BET surface area at  $386 \text{ m}^2/\text{g}$  which can provide good accessibility of the catalytically active sites.

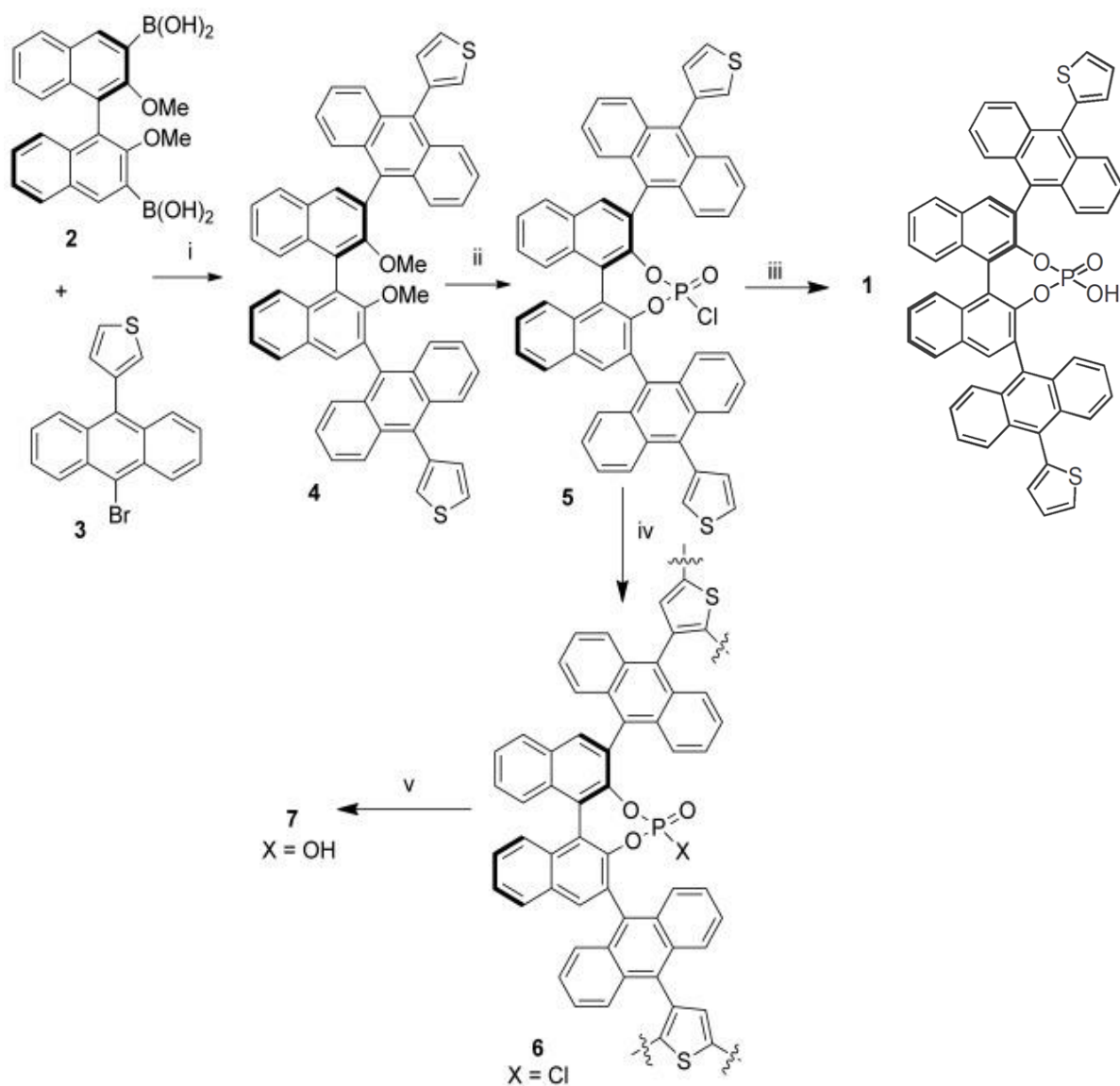


**Figure 1.19 Synthesis of BNPPA CMPs. Conditions: i)  $[\text{Pd}(\text{PPh}_3)_4]$ ,  $\text{K}_2\text{CO}_3$ , THF/ $\text{H}_2\text{O}$ ,  $80\text{ }^\circ\text{C}$ ; ii) a)  $\text{BBr}_3$ ,  $\text{CH}_2\text{Cl}_2$ , b) poly(4-vinyl pyridine),  $\text{POCl}_3$ ,  $\text{CH}_2\text{Cl}_2$ ; iii) THF,  $1\text{ M HCl}$ , RT; iv)  $\text{FeCl}_3$ , toluene, acetonitrile; v) aqueous HCl.<sup>57</sup>**

The synthesised polymer network **7** was used as a heterogeneous catalyst for asymmetric hydrogenation of 3-phenyl-2*H*-1,4-benzoxazine and it was compared with monomer **1** and commercially available (*R*)-3,3'-bis(9-anthracenyl)-1,1'-binaphthyl-2,2'-diyl hydrogenphosphate. All catalysts showed high conversions up to 99% with

98% (S) enantioselectivity for which is more selective than the commercial compound (95%) and comparable with monomer 1 (99%). The kinetic study of heterogeneous catalyst 7 was found to be as fast as with homogeneous catalyst 1 owing to the microporous nature and high surface area of heterogeneous catalyst and the reactions were completed within 2 h with 5mol% of the monomer 1 or with the same weight percentage of polymer 7. The polymer 7 was reused for 10 times and it did not show any loss in %conversion and %enantioselectivity as shown in Figure 1.20.

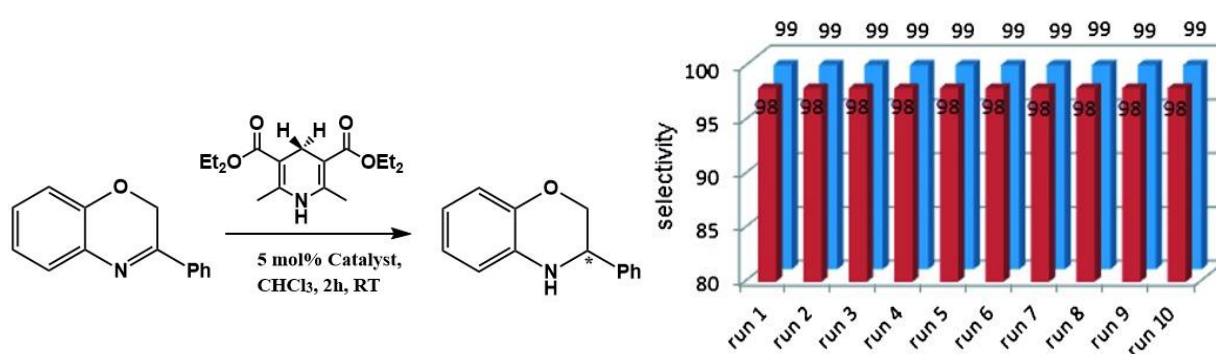


**Figure 1.20** Reusability study of polymer 7 for asymmetric hydrogenation of 3-phenyl-2H-1,4-benzoxazine (red is % enantioselectivity, blue is % conversion).<sup>57</sup>

### 1.2.3 CMPs for heterogeneous photocatalysis

CMPs have been extensively studied in the field of heterogeneous photocatalysis due to potentially versatile electronic and photophysical properties resulting from the extended  $\pi$ -conjugation system in the networks. The main advantages of CMPs are flexible tuning of the absorbance and bandgap by using various choices of monomers and synthesis methods and they are also recyclable due to high physicochemical stability. Furthermore, CMPs exhibit stronger light harvesting abilities than their monomeric counterparts, a key feature for photocatalytic performance. A great number of CMPs including organometallic and organic networks have been synthesised and used as heterogeneous photocatalysts.<sup>53</sup>

Ru(bipy)<sub>3</sub><sup>2+</sup>-based CMPs have been synthesised *via* oxidative homocoupling reactions of tetra(ethynyl) derivatives of Ru(bpy)<sub>3</sub><sup>2+</sup> (with the alkynyl groups located at 4,4'- or 5,5'- positions of two substituted bipyridines) as shown in Figure 1.21.<sup>58</sup> The synthesised polymers contained high loading of Ru contents at 89.6- 91.0 wt % respectively, which can enhance visible light absorption and also increase reactivity of the catalyst. The polymers showed BET surface areas from 15-198 m<sup>2</sup>/g which are relatively low for CMPs due to the presence of the bulky groups of the [Ru(bpy)<sub>3</sub>]<sup>2+</sup> complexes in the polymer networks. The polymers also exhibited red shift when compared with homogeneous catalyst and the broad absorption bands with relatively long excited state lifetimes which can make them good candidates as heterogeneous photocatalysts. The synthesised CMPs were tested as catalysts for the aza-Henry reaction, aerobic oxidative coupling of amine and dehalogenation of benzyl bromoacetate. The aza-Henry reaction was performed at room temperature with 0.2 mol % ratio catalyst for 8 h with a 26 W fluorescent lamp and they showed high conversions more than 90% with reusability up to 4 cycles without significant decrease in catalytic activity. The polymers also showed higher conversion than the homogeneous catalyst analogue which can be polymerised under light and cannot be used as control homogeneous catalysts. The crosslinked polymers also showed high conversion up to 99% for photocatalytic aerobic oxidative coupling reactions and they also gave high %yield of the benzyl acetate product (86-92%) for photocatalytic dehalogenation of benzylbromoacetate. The catalysts were also reused for both reactions and they showed no significant decrease in conversions and yields.

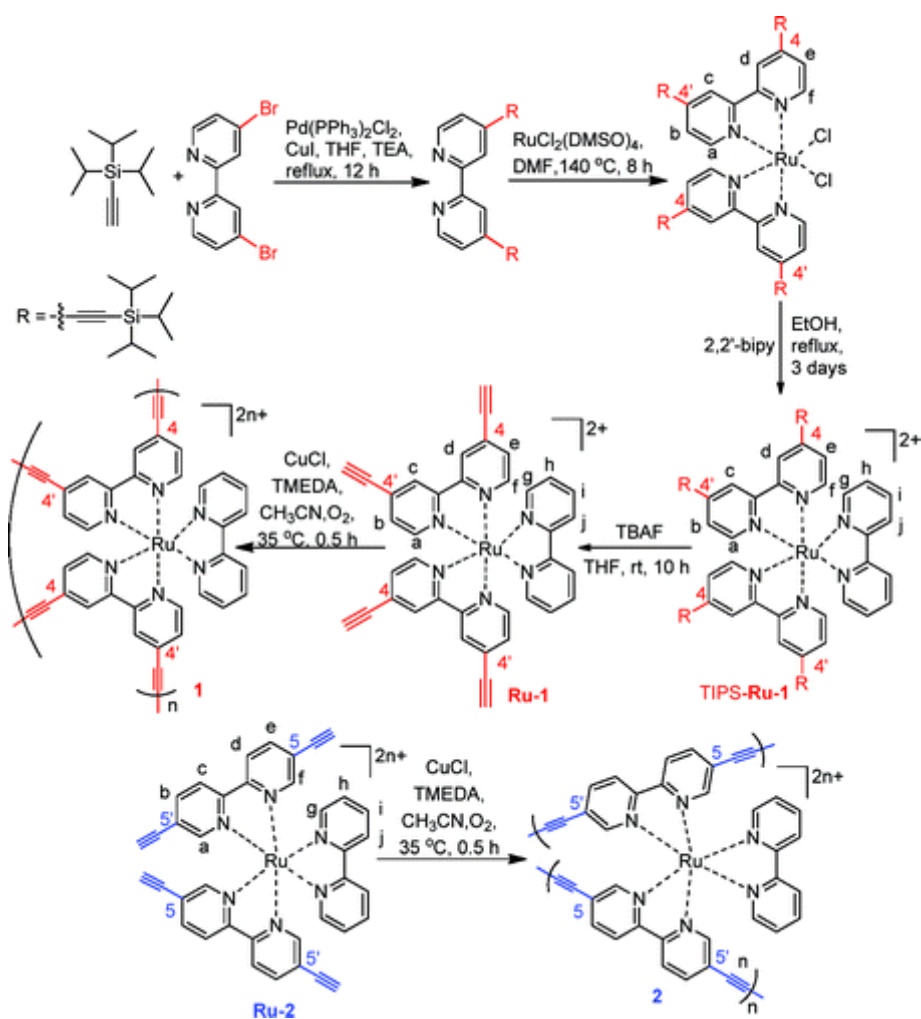


**Figure 1.21** Synthesis of Ru(bipy)<sub>3</sub><sup>2+</sup>-based cross-linked polymers *via* oxidative coupling.<sup>58</sup>

Organic dyes such as methylene blue, Eosin Y, triphenylpyrylium and acridinium have been used for organic photoredox catalysts due to their high reactivity that outperforms their inorganic and organometallic counterparts with relatively lower cost and wide availability.<sup>59</sup> In 2013, Jiang and co-workers studied the incorporation of rose bengal dye into conjugated microporous polymer networks by Sonogashira-Hagihara cross coupling reaction.<sup>60</sup> The synthesised materials exhibited high surface areas of more than 800 m<sup>2</sup>/g with high chemical and thermal stabilities. The

synthesised polymers were also tested as catalysts for the aza-Henry reaction using 60W white light or natural sunlight and showed impressive %conversions of more than 97%. The rose bengal based CMPs were reused for 10 cycles without a significant drop in %conversion. Similar work was reported in 2017 by Wang *et al.*<sup>13</sup> They included Eosin Y dye into porous organic polymer networks using Sonogashira-Hagihara reaction as shown in Figure 1.22. The resulting materials showed high surface areas of 587 and 718 m<sup>2</sup>/g for EY-POP-1 and EY-POP-2, respectively. The EY-POP-1 exhibited excellent photocatalytic activity for the aza-Henry reaction under 14W light bulb or natural sunlight, which resulted in high % conversions more than 90%. The synthesised EY-POP-1 showed excellent reusability up to 12 cycles without significant loss in %yield of the reaction product.

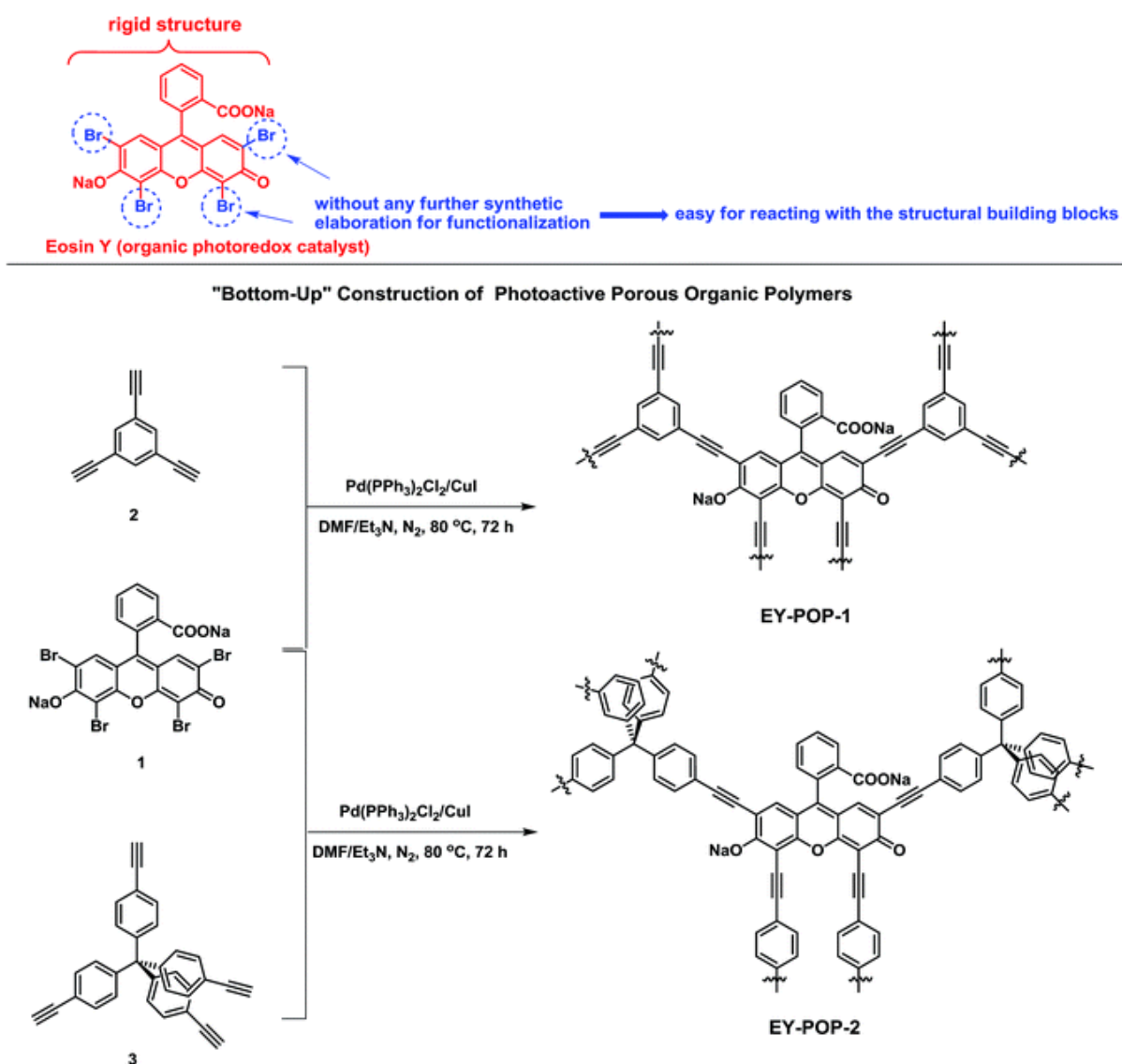


**Figure 1.22** The synthesis scheme of eosin Y dye incorporated porous organic polymers (EY-POPs) *via* Sonogashira-Hagihara cross-coupling reaction.<sup>13</sup>

Zhang and co-workers<sup>3</sup> reported a series of carbazole-based CMPs with tunable redox potentials and their photocatalytic study of C-3 formylation and thiocyanation of indoles as shown in Figure 1.23. The CMPs were synthesised by Friedel–Crafts reaction using FeCl<sub>3</sub> as a catalyst and the redox properties can be tuned by changing a core from 1,4-dibenzyl, 1,3,5-tribenzyl, or 1,3,5-triazin-2,4,6-triyl. The obtained CMPs showed high surface areas (978-1717 m<sup>2</sup>/g), visible light absorptions, and tunable semiconductor-range band gaps. The bandgaps were 2.14, 2.29, and 2.08 eV

and HOMO levels were 1.26, 1.42, and 1.19 V for CMP-CSU5, CMP-CSU6, and CMP-CSU7, respectively and all polymers showed LUMO levels lower than -0.86 V which was negative enough to reduce oxygen into the active species  $O_2^{\cdot-}$ . With the highest oxidative capability, CMP-CSU6 derived from 1,3,5-tri(9*H*-carbazol-9-yl)benzene showed the highest efficiency for C-3 formylation and thiocyanation of indoles at room temperature. The synthesised catalysts can be easily recovered and reused at least five times without decay in catalytic activity, suggesting good recyclability.<sup>61</sup>

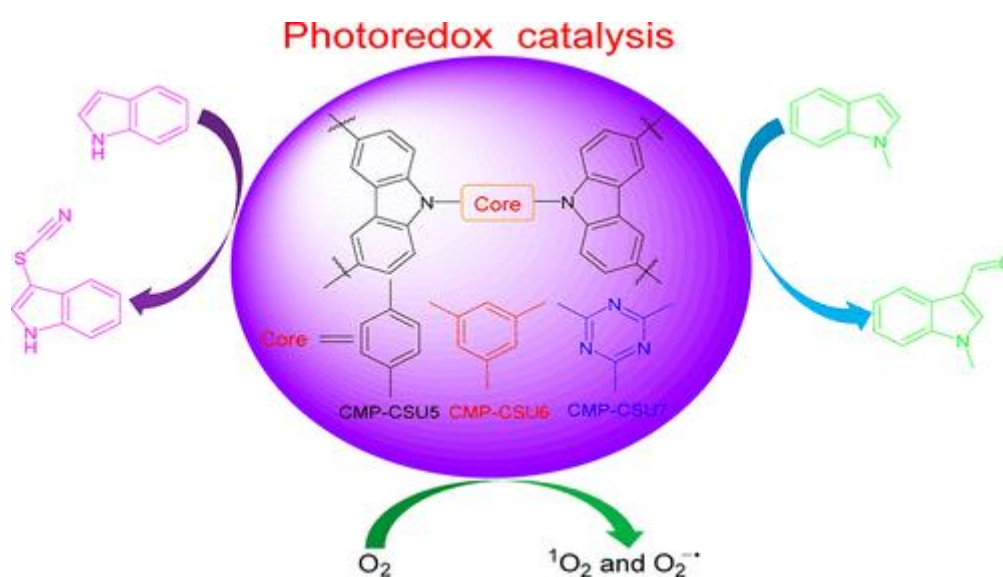


**Figure 1.23** The structures of the obtained polymers with their applications of C-3 formylation and thiocyanation of indoles.<sup>61</sup>

### 1.3 Thesis Aims

The aims of this thesis are to prepare microporous polymers using various organic monomers and different synthesis methods and to perform metal free heterogeneous catalysis.

#### **1.3.1 Synthesis Part**

(a) To synthesise a range of different functionalised triphenylpyrylium compounds and use them as catalytic active monomers to synthesise microporous polymers.

(b) To prepare different functionalised pyrylium based microporous polymers by different synthetic methods, such as different types of coupling reactions; Sonogashira, Yamamoto and oxidative coupling reactions.

(c) To incorporate bromophenol blue and bromocresol green dyes into microporous polymer networks using Sonogashira cross coupling chemistry and post-synthetic modification with chlorosulfonic acid.

(d) To fully characterise all synthesised microporous polymers with various characterisation methods such as nitrogen gas sorptions, solid state NMR, FTIR, solid state UV-Vis spectroscopies, elemental analysis and thermogravimetric analysis (TGA).

#### **1.3.2 Catalytic Activity Part**

(a) To perform thioanisole oxidation using functionalised pyrylium CMPs as heterogeneous catalysts and reusability study.

(b) To investigate biodiesel production using functionalised bromophenol blue and bromocresol green based CMPs and recyclability test of the synthesised catalyst.

## 1.4 References

- 1 J. T. Culp, in *Novel Materials for Carbon Dioxide Mitigation Technology*, Elsevier, 2015, pp. 149–176.
- 2 K. Nishiyabu, in *Handbook of Metal Injection Molding*, Elsevier Inc., 2012, pp. 349–390.
- 3 B. D. Zdravkov, J. J. Cermák, M. Sefara and J. Janků, *CEJC*, 2007, **5**, 385–395.
- 4 C. J. Brinker, *Curr. Opin. Solid State Mater. Sci.*, 1996, **1**, 798–805.
- 5 H. Nakajima, *Proc. Japan Acad. Ser. B*, 2010, **86**, 884–899.
- 6 H. Zheng, F. Gao and V. Valtchev, *J. Mater. Chem. A*, 2016, **4**, 16756–16770.
- 7 J. L. C. Rowsell and O. M. Yaghi, *Microporous Mesoporous Mater.*, 2004, **73**, 3–14.
- 8 R. Dawson, A. I. Cooper and D. J. Adams, *Prog. Polym. Sci.*, 2012, **37**, 530–563.
- 9 A. Chica, *ISRN Chem. Eng.*, 2013, **2013**, 1–19.
- 10 G. Perot and M. Guisnet, *J. Mol. Catal.*, 1990, **61**, 173–196.
- 11 K. Vikrant, V. Kumar, K. H. Kim and D. Kukkar, *J. Mater. Chem. A*, 2017, **5**, 22877–22896.
- 12 N. Chaoui, M. Trunk, R. Dawson, J. Schmidt and A. Thomas, *Chem. Soc. Rev.*, 2017, **46**, 3302–3321.
- 13 C.-A. A. Wang, Y.-W. W. Li, X.-L. L. Cheng, J.-P. P. Zhang and Y.-F. F. Han, *RSC Adv.*, 2017, **7**, 408–414.

- 14 T. A. Makal, J.-R. Li, W. Lu and H.-C. Zhou, *Chem. Soc. Rev.*, 2012, **41**, 7761–7779.
- 15 Q. Chen, D. P. Liu, J. H. Zhu and B. H. Han, *Macromolecules*, 2014, **47**, 5926–5931.
- 16 C. D. Wood, B. Tan, A. Trewin, H. Niu, D. Bradshaw, M. J. Rosseinsky, Y. Z. Khimyak, N. L. Campbell, R. Kirk, E. Stöckel and A. I. Cooper, *Chem. Mater.*, 2007, **19**, 2034–2048.
- 17 L. Tan and B. Tan, *Chem. Soc. Rev.*, 2017, **46**, 3322–3356.
- 18 S. Das, P. Heasman, T. Ben and S. Qiu, *Chem. Rev.*, 2017, **117**, 1515–1563.
- 19 R. T. Woodward, A. Jobbe-Duval, S. Marchesini, D. B. Anthony, C. Petit and A. Bismarck, *Polymer (Guildf.)*, 2017, **115**, 146–153.
- 20 J. Germain, J. M. J. Fréchet and F. Svec, *J. Mater. Chem.*, 2007, **17**, 4989–4997.
- 21 R. Joseph, W. T. Ford, S. Zhang, M. P. Tsyurupa, A. V. Pastukhov and V. A. Davankov, *J. Polym. Sci. Part A Polym. Chem.*, 1997, **35**, 695–701.
- 22 V. A. Davankov, M. M. Ilyin, M. P. Tsyurupa, G. I. Timofeeva and L. V. Dubrovina, *Macromolecules*, 1996, **29**, 8398–8403.
- 23 V. A. Davankov, S. V. Rogoshin and M. P. Tsyurupa, *J. Polym. Sci. Polym. Symp.*, 2007, **47**, 95–101.
- 24 J.-H. Ahn, J.-E. Jang, C.-G. Oh, S.-K. Ihm, J. Cortez and D. C. Sherrington, *Macromolecules*, 2006, **39**, 627–632.
- 25 B. Li, R. Gong, Y. Luo and B. Tan, *Soft Matter*, 2011, **7**, 10910–10916.

- 26 C. D. Wood, B. Tan, A. Trewin, F. Su, M. J. Rosseinsky, D. Bradshaw, Y. Sun, L. Zhou and A. I. Cooper, *Adv. Mater.*, 2008, **20**, 1916–1921.
- 27 B. Li, Z. Guan, X. Yang, W. D. Wang, W. D. Wang, I. Hussain, K. Song, B. Tan and T. Li, *J. Mater. Chem. A*, 2014, **2**, 11930–11939.
- 28 M. Grzybowski, K. Skonieczny, H. Butenschön, D. T. Gryko, H. Butenschön and D. T. Gryko, *Angew. Chemie Int. Ed.*, 2013, **52**, 9900–9930.
- 29 B. Li, R. Gong, W. Wang, X. Huang, W. Zhang, H. Li, C. Hu and B. Tan, *Macromolecules*, 2011, **44**, 2410–2414.
- 30 P. M. Budd, N. B. McKeown and D. Fritsch, *Macromol. Symp.*, 2006, **245–246**, 403–405.
- 31 P. M. Budd, B. S. Ghanem, S. Makhseed, N. B. McKeown, K. J. Msayib and C. E. Tattershall, *Chem. Commun.*, 2004, **0**, 230–231.
- 32 A. P. Côté, A. I. Benin, N. W. Ockwig, M. O’Keeffe, A. J. Matzger and O. M. Yaghi, *Science*, 2005, **310**, 1166–1170.
- 33 H. Furukawa and O. M. Yaghi, *J. Am. Chem. Soc.*, 2009, **131**, 8875–8883.
- 34 J. L. Segura, M. J. Mancheño and F. Zamora, *Chem. Soc. Rev.*, 2016, **45**, 5635–5671.
- 35 M. G. Rabbani, A. K. Sekizkardes, Z. Kahveci, T. E. Reich, R. Ding and H. M. El-Kaderi, *Chem. - A Eur. J.*, 2013, **19**, 3324–3328.
- 36 F. J. Uribe-Romo, C. J. Doonan, H. Furukawa, K. Oisaki and O. M. Yaghi, *J. Am. Chem. Soc.*, 2011, **133**, 11478–11481.
- 37 Y. Xu, S. Jin, H. Xu, A. Nagai and D. Jiang, *Chem. Soc. Rev.*, 2013, **42**, 8012–

- 8031.
- 38 J.-X. Jiang, F. Su, A. Trewin, C. D. Wood, N. L. Campbell, H. Niu, C. Dickinson, A. Y. Ganin, M. J. Rosseinsky, Y. Z. Khimyak and A. I. Cooper, *Angew. Chemie*, 2007, **119**, 8728–8732.
- 39 J.-X. X. Jiang, A. Trewin, D. J. Adams and A. I. Cooper, *Chem. Sci.*, 2011, **2**, 1777–1781.
- 40 K. V. Rao, S. Mohapatra, C. Kulkarni, T. K. Maji and S. J. George, *J. Mater. Chem.*, 2011, **21**, 12958–12963.
- 41 P. Kuhn, M. Antonietti and A. Thomas, *Angew. Chemie Int. Ed.*, 2008, **47**, 3450–3453.
- 42 P. Kuhn, A. Forget, D. Su, A. Thomas and M. Antonietti, *J. Am. Chem. Soc.*, 2008, **130**, 13333–13337.
- 43 S. Ren, M. J. Bojdys, R. Dawson, A. Laybourn, Y. Z. Khimyak, D. J. Adams and A. I. Cooper, *Adv. Mater.*, 2012, **24**, 2357–2361.
- 44 T. Ben and S. Qiu, *CrystEngComm*, 2013, **15**, 17–26.
- 45 T. Ben, H. Ren, S. Ma, D. Cao, J. Lan, X. Jing, W. Wang, J. Xu, F. Deng, J. M. Simmons, S. Qiu and G. Zhu, *Angew. Chemie*, 2009, **121**, 9621–9624.
- 46 T. Ben, C. Pei, D. Zhang, J. Xu, F. Deng, X. Jing and S. Qiu, *Energy Environ. Sci.*, 2011, **4**, 3991–3999.
- 47 P. Sozzani, S. Bracco, A. Comotti, L. Ferretti and R. Simonutti, *Angew. Chemie Int. Ed.*, 2005, **44**, 1816–1820.
- 48 M. Mastalerz and I. M. Oppel, *Angew. Chemie Int. Ed.*, 2012, **51**, 5252–5255.

- 49 T. Hasell and A. I. Cooper, *Nat. Rev. Mater.*, 2016, **1**, 16053.
- 50 G. Zhang, O. Presly, F. White, I. M. Oppel and M. Mastalerz, *Angew. Chemie Int. Ed.*, 2014, **53**, 1516–1520.
- 51 S. Jiang, J. Bacsa, X. Wu, J. T. A. Jones, R. Dawson, A. Trewin, D. J. Adams and A. I. Cooper, *Chem. Commun.*, 2011, **47**, 8919–8921.
- 52 T. Hasell, M. A. Little, S. Y. Chong, M. Schmidtman, M. E. Briggs, V. Santolini, K. E. Jelfs and A. I. Cooper, *Nanoscale*, 2017, **9**, 6783–6790.
- 53 Y.-B. Zhou and Z.-P. Zhan, *Chem. - An Asian J.*, 2018, **13**, 9–19.
- 54 Q.-L. Zhou, *Angew. Chemie Int. Ed.*, 2016, **55**, 5352–5353.
- 55 J.-X. Jiang, C. Wang, A. Laybourn, T. Hasell, R. Clowes, Y. Z. Khimyak, J. Xiao, S. J. Higgins, D. J. Adams and A. I. Cooper, *Angew. Chemie Int. Ed.*, 2011, **50**, 1072–1075.
- 56 I. R. Shaikh, *J. Catal.*, 2014, **2014**, 402860.
- 57 D. S. Kundu, J. Schmidt, C. Bleschke, A. Thomas and S. Blechert, *Angew. Chemie Int. Ed.*, 2012, **51**, 5456–5459.
- 58 J. L. Wang, C. Wang, K. E. Dekrafft and W. Lin, *ACS Catal.*, 2012, **2**, 417–424.
- 59 D. A. Nicewicz and T. M. Nguyen, *ACS Catal.*, 2014, **4**, 355–360.
- 60 J. X. Jiang, Y. Li, X. Wu, J. Xiao, D. J. Adams and A. I. Cooper, *Macromolecules*, 2013, **46**, 8779–8783.
- 61 W. Zhang, J. Tang, W. Yu, Q. Huang, Y. Fu, G. Kuang, C. Pan and G. Yu, *ACS Catal.*, 2018, **8**, 8084–8091.

## Chapter 2

### Methods

#### 2.1 Characterisation Techniques

##### **2.1.1 Nitrogen gas adsorption and desorption isotherm**

Nitrogen gas sorption isotherms were acquired by a Micromeritics ASAP 2020Plus analyser using high purity gases at 77 K. All samples (ca. 0.1 g) were degassed at 120 °C under dynamic vacuum prior to analysis to remove any adsorbed molecules such as water and volatile molecules which can be trapped inside the pores leading to lower adsorption of analysis gas resulting in the lower surface areas of materials than it should be. Surface areas were calculated using the Brunauer-Emmett-Teller (BET) method over a relative pressure range of 0.01–0.15 P/P<sub>0</sub>. Differential pore sizes were calculated using the NL-DFT method.

##### **2.1.2 <sup>1</sup>H–<sup>13</sup>C cross-polarisation magic angle spinning (CP/MAS)**

The synthesised polymers were filled into 4 mm zirconia rotors before analysed with a Bruker Avance III HD spectrometer at 125.76 MHz (500.13 MHz <sup>1</sup>H) at a MAS rate of 10.0 kHz. The <sup>1</sup>H π/2 pulse was 3.4 μs, and two-pulse phase modulation (TPPM) decoupling was used during the acquisition. The Hartmann–Hahn condition was set using hexamethylbenzene. The spectra were measured using a contact time of 2.0 ms. The relaxation delay D<sub>1</sub> for each sample was individually determined from the proton T<sub>1</sub> measurement (D<sub>1</sub> = 5 × T<sub>1</sub>). Data was collected until sufficient signal-to-noise was obtained, typically greater than 256 scans. The chemical shift values are referred to that of TMS.

### **2.1.3 $^1\text{H}$ NMR and $^{13}\text{C}$ Nuclear magnetic resonance (NMR) spectroscopy**

Solution state NMR were performed using Bruker AV 400MHz. Samples were dissolved in deuterated solvents and filtered by cotton wool prior analysis at room temperature.

### **2.1.4 Fourier transform infrared (FTIR) spectroscopy**

FTIR was performed using a PerkinElmer Spectrum 100. Samples were analysed with a diamond ATR accessory or were mixed with KBr and pressed into a disk before being measured in transmission mode.

### **2.1.5 Elemental analysis (EA)**

EA was obtained using Elementar Vario MICRO Cube CHN/S analyser by burning a sample in a stream of oxygen. Combustion products were passed through a copper tube to remove excess oxygen and reduce  $\text{NO}_x$  to  $\text{N}_2$  before separated with a Thermal Programmed Desorption column and detected by a thermal conductivity detector (TCD). Halogen analysis was performed using the Schöniger flask combustion method and a titration was used to determine the amount of required element.

### **2.1.6 Thermogravimetric analysis (TGA)**

TGA was performed using PE Pyris. Approximately 5 mg of material was pyrolysed under a nitrogen atmosphere from room temperature to 800 °C using 10 °C/min heating rate.

### **2.1.7 Particle size analysis**

Particle size of the synthesised materials was determined using an optical microscope. The photographs of the polymers were taken using a SuperEyes camera and the photos were analysed using ImageJ. The particle size of the polymers was determined by comparing with a scale.

## 2.2 Gas sorption theory

Gas sorption is the most important method used to determine the pore structure, size, volume and surface area over a wide range of porous materials.

Gases (sorbates) can interact with the solid (sorbent) by 2 different mechanisms. The interactions can either be strong (chemisorption) resulting in chemical bond formation or they can be weak (physisorption) which involves only weak Van der Waals interactions. In most instances, surface area, pore size and volume of porous materials can be determined using physisorption of nitrogen gas with a solid sample at 77 K.

Gas adsorption can be divided into 4 stages based on an increase in a number of gas molecules adsorbed on a solid sorbent when increasing gas pressure as shown in Figure 2.1.

Stage 1: At low pressure, isolated sites on the surface of solid begin to adsorb gas molecules.

Stage 2: When the gas pressure increases, the solid surface is covered by adsorbed molecules to form a monolayer.

Stage 3: Further increasing gas pressure results in the beginning of multi-layer coverage. Smaller pores in the sample will fill first.

Stage 4: A further increase in the gas pressure will cause full coverage of the solid sample and fill all the pores.

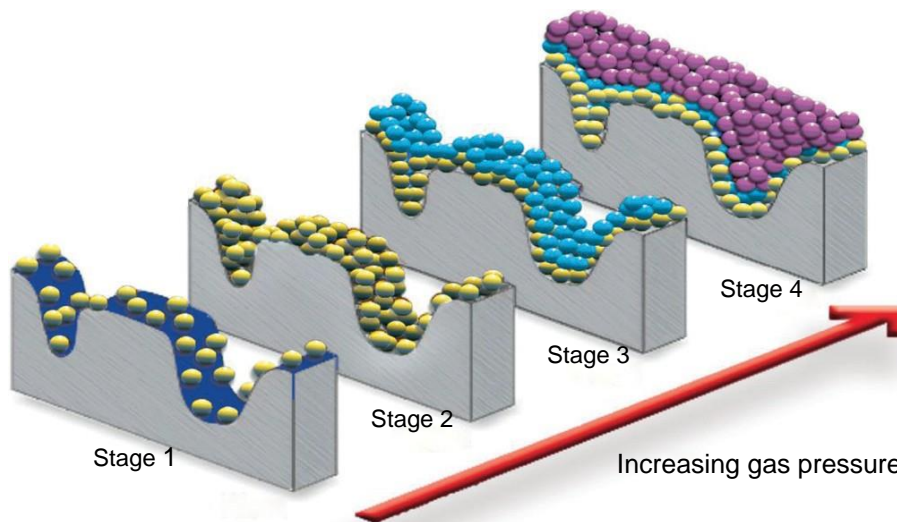


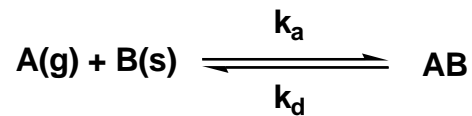
**Figure 2.1** Illustration of gas adsorption theory.<sup>1</sup>

Over the years, many adsorption theories have been developed. In this chapter, the Langmuir and Brunauer-Emmett-Teller (BET) models are common theories that are widely applied in porous material research and these 2 models will be discussed.

### **2.2.1 Langmuir Model**

The Langmuir adsorption isotherm is a theory used to explain the equilibrium between adsorbate and adsorbent system based on following assumptions<sup>2</sup>:

1. Gas molecules behave ideally. There is an equilibrium between adsorbed gaseous molecules and the free gaseous molecules.
2. There is only one monolayer formed.
3. All sites on the surface are equivalent (homogeneous).
4. There is no interaction between adsorbate molecules.
5. An adsorbed molecule does not migrate and the enthalpy of adsorption is constant.



where: A(g) is unadsorbed gas molecule,

B(s) is an unoccupied solid surface

AB is an adsorbed gas molecule on a solid surface site.

$k_a$  and  $k_d$  represent rates constants of the adsorption and desorption, respectively.

Based on the kinetic model of adsorption-desorption process,

$$\text{Rate of adsorption: } k_a P(N-n)$$

$$\text{Rate of desorption: } k_d n$$

Where P is pressure of adsorbate

N is total number of adsorption sites

n is number of occupied sites

At equilibrium, the rates of adsorption and desorption are equal.

$$k_a P(N-n) = k_d n$$

The equilibrium constant,  $K_{eq} = k_a/k_d$

$$K_{eq} = n/P(N-n) = \exp(-\Delta H^0/RT)$$

Where  $\Delta H^0$  is heat of adsorption at temperature T and standard pressure  $P_{ST}$

The fraction of the adsorption sites occupied ( $\theta$ ) is

$$\theta = n/N$$

So, it can be written as

$$\theta = K_{eq}P/(1+K_{eq}P)$$

This is well known as the Langmuir adsorption equation.

For gas sorption theory, this equation can be written in terms of volume of gas adsorbed by a sorbent.

$$\theta = V_{\text{ads}} / V_{\text{mono}}$$

where  $V_{\text{ads}}$  is the volume of gas adsorbed

$V_{\text{mono}}$  is the amount of gas adsorbed corresponding to monolayer coverage.

So, the Langmuir equation can be rearranged in linear form as

$$P/V_{\text{ads}} = P/V_{\text{mono}} + 1/(KV_{\text{mono}})$$

If we were to then plot a graph of  $P/V_{\text{ads}}$  vs  $P$  will give a linear line where the slope is equal to  $1 / V_{\text{mono}}$  and the intercept  $1 / KV_{\text{mono}}$ .

The Langmuir surface area ( $SA_{\text{lang}}$ ) can be determined by this following equation

$$SA_{\text{lang}} = V_{\text{mono}} \times A$$

Where  $A$  is the area of one molecule

### **2.2.2 BET Theory**

Langmuir isotherm provides a simple explanation of gas adsorption which is valid at low pressure, but it becomes inaccurate at the higher pressure because more than one adsorbate molecule can adsorb to each site on a solid surface at low temperature. In 1938, Stephen Brunauer, Paul Hugh Emmett and Edward Teller published their gas adsorption theory that allows for multiple adsorbate molecules to adsorb on each solid site. The BET theory is based on these assumptions:<sup>3</sup>

1. Gas molecules behave ideally
2. There is multilayer adsorption formed
3. Each adsorbed gas molecule provides a site for the adsorption of the molecule in the next layer above it and the second and higher layers are assumed to be liquid like. The adsorption of first layer is controlled by heat of adsorption ( $\Delta H_A$ ) while the subsequent layers are controlled by heat of liquification ( $\Delta H_L$ ).

4. The sites on the surface are equivalent.
5. There is no interaction between adsorbate molecules and they are immobilised

The overall equation for BET theory is

$$\frac{P}{V(P_0 - P)} = \frac{1}{V_m C} + \frac{(C-1)P}{V_m C P_0}$$

Where V is volume of adsorbed vapor at STP.

$V_m$  is monolayer capacity at STP.

P is partial pressure of the adsorbate.

$P_0$  is saturation vapor pressure of the adsorbate.

$$C = e^{(\Delta H_A - \Delta H_L)/RT}$$

To calculate the BET surface area ( $S_{BET}$ ), a plot of  $P/[V(P_0 - P)]$  against  $P/P_0$  will give a straight line over a relative pressure range of between 0.05 – 0.35.

Where Slope (S) =  $(C-1)/(V_m C)$

Intercept (I) =  $1/V_m C$

Then  $V_m = 1/(S+I)$

$S_{BET} = V_m K / \text{sample weight}$

Where  $K = N_A A / M_v$

$N_A$  = Avogadro's number ( $6.02 \times 10^{23} \text{ mol}^{-1}$ )

A = area per molecule ( $1.62 \text{ nm}^2$  for  $N_2$  at 77K)

$M_v$  = volume per mole of gas

### **2.2.3 Isotherm Shapes**

According to IUPAC (1985), isotherms can be divided into 6 different shapes as shown in Figure 2.2.<sup>4</sup>

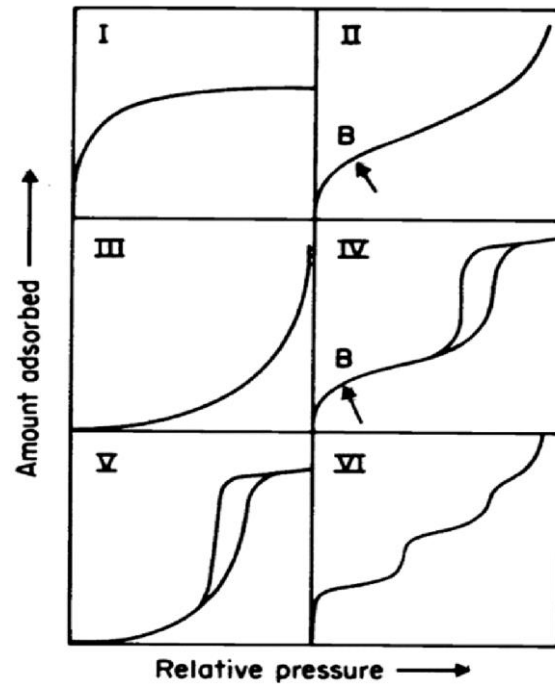


**Figure 2.2** IUPAC isotherm classifications from 1985.<sup>4</sup>

Firstly, the reversible type I isotherm shows steep uptake at low pressure which is a characteristic of microporous materials with relatively low external surfaces. The limiting uptake is controlled by accessible micropore volume instead of the internal surface area. The examples of materials that give type I isotherms include activated carbons, molecular sieves, zeolites and some porous oxides.

The reversible type II isotherm illustrates unrestricted monolayer-multilayer adsorption. Point B is the stage that monolayer adsorption is complete and multilayer adsorption is about to start. This isotherm is normally obtained for a non-porous or macroporous material.

The reversible type III isotherm which is convex to the x axis (relative pressure;  $P/P_0$ ) is rare. It can be observed in some systems such as nitrogen on polyethylene. The interaction between adsorbate molecules is stronger than adsorbate-adsorbent interaction for this type of isotherm.

Next, the type IV isotherm is quite similar to the type II isotherm which shows monolayer-multilayer adsorption at the initial stage. The distinction of type IV isotherm is the hysteresis loops caused by capillary condensation in mesopores and the plateau indicating limiting uptake at high  $P/P_0$ .

The type V isotherm is also uncommon like type III isotherm. It shows convex curve to the x axis similar to type III but has the hysteresis loop. This type of isotherm is associated with the weak interaction between adsorbate and adsorbent.

Finally, the type VI isotherm shows stepwise multilayer adsorption on a uniform nonporous surface. The height of each step corresponds to the monolayer capacity for each adsorbed layer. The example material showing type VI isotherm is graphite carbon black which adsorbs argon or krypton at 77K.

As porous material research is broadly developing and various new isotherms have been published, in 2015, IUPAC has revised the types of isotherms as shown in Figure 2.3.<sup>5</sup>

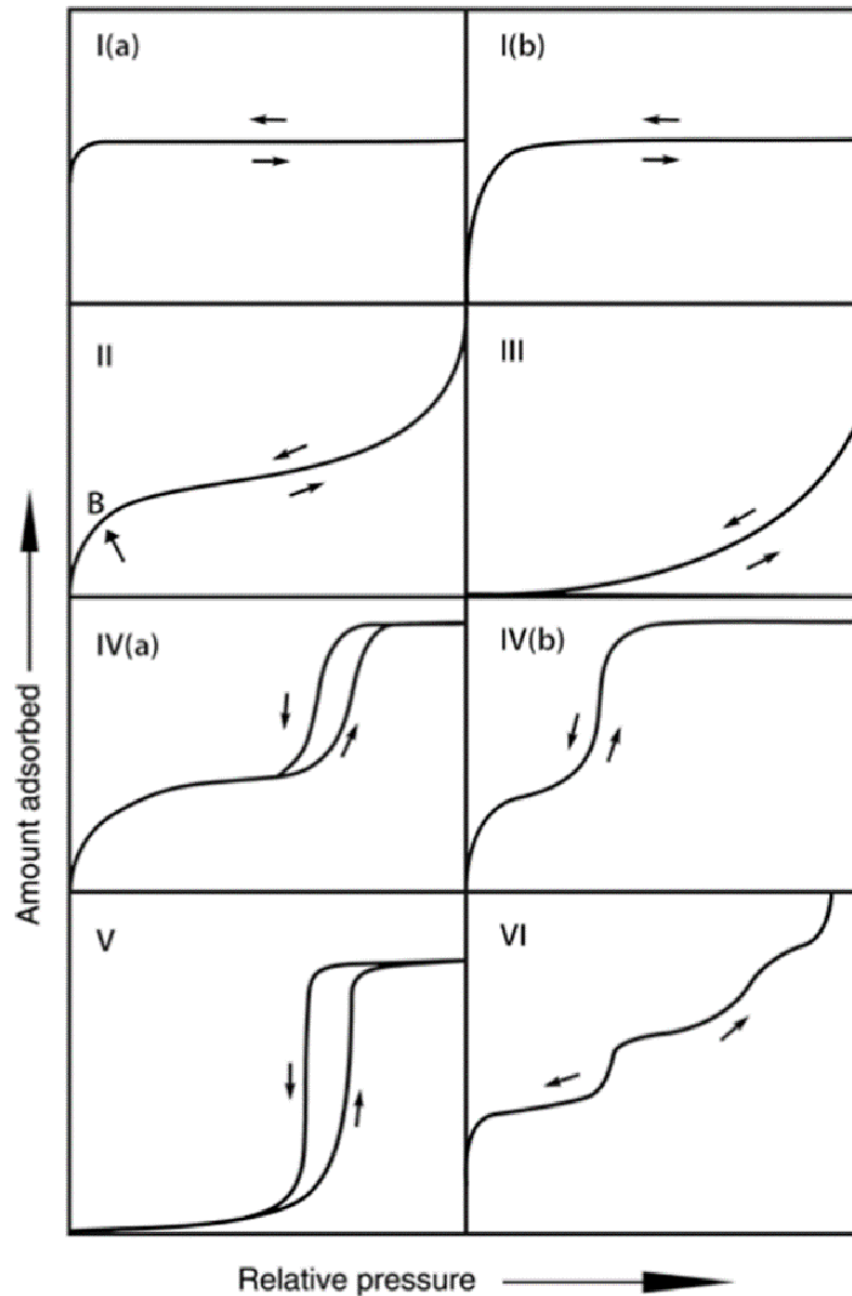


**Figure 2.3** Refined IUPAC isotherm classifications as of 2015.<sup>5</sup>

In the 2015 version, the type I and IV isotherms have been updated while the others remained the same. The type I isotherm has been divided into two different categories; a type I(a) which is given by microporous materials with mainly narrow pore sizes (pore widths less than 1 nm) and a type I(b) which is given by microporous materials with broader pore size distributions from wider micropores to narrow

mesopores (pore widths less than 2.5 nm). The type I(a) shows steeper uptake at the low pressure compared to the type I(b) due to more adsorbent-adsorptive interactions in narrow micropores.

Likewise, the type IV has also been categorised into two different types namely type IV(a) and type IV(b). The type IV(a) isotherm has a noticeably large hysteresis loop resulting from capillary condensation in mesoporous materials which have pore width greater than 4 nm for nitrogen and argon adsorption in cylindrical pores at 77 K and 87 K, respectively while the completely reversible type IV(b) isotherm is given by smaller mesopores.

#### **2.2.4 Adsorption Hysteresis**

Hysteresis loops are generally associated with capillary condensation. The hysteresis loops can be various shapes based on pore structures as shown in Figure 2.4.<sup>4,5</sup>

The type H1 loops are found in materials which have ordered mesopores with narrow pore size distribution e.g., MCM-41, MCM-48, SBA-15. Type H1 hysteresis has also been observed in networks of ink-bottle pores where the width of the neck size distribution is similar to the width of the pore/cavity size distribution.

The type H2 loops which can be divided into 2 types; H2(a) and H2(b) are given by more complex pore structure. H2(a) can be ascribed to pore-blocking/percolation in a narrow range of pore necks. H2(a) loops can be found in many silica gels, some porous glasses, and some ordered mesoporous silicas (SBA-16 and KIT-5). Likewise, H2(b) loops are also related to pore blocking but with much larger size distribution of neck widths.

The type H3 loops which have type II adsorption branch are given by non-rigid aggregates of plate-like particles (e.g. certain clays) but also if the pore network consists of macropores which are not entirely filled with pore condensate.

The type H4 loops are similar to H3 but the adsorption branch is mixed between type I and II. The steep uptake at very low relative pressure associates with the filling of micropores. H4 loops can be observed in aggregated crystals of zeolites, some mesoporous zeolites, and micro-mesoporous carbons.

The type H5 loops, which are rare are related to certain pore structures containing both open and partially blocked mesopores such as plugged hexagonal templated silicas.

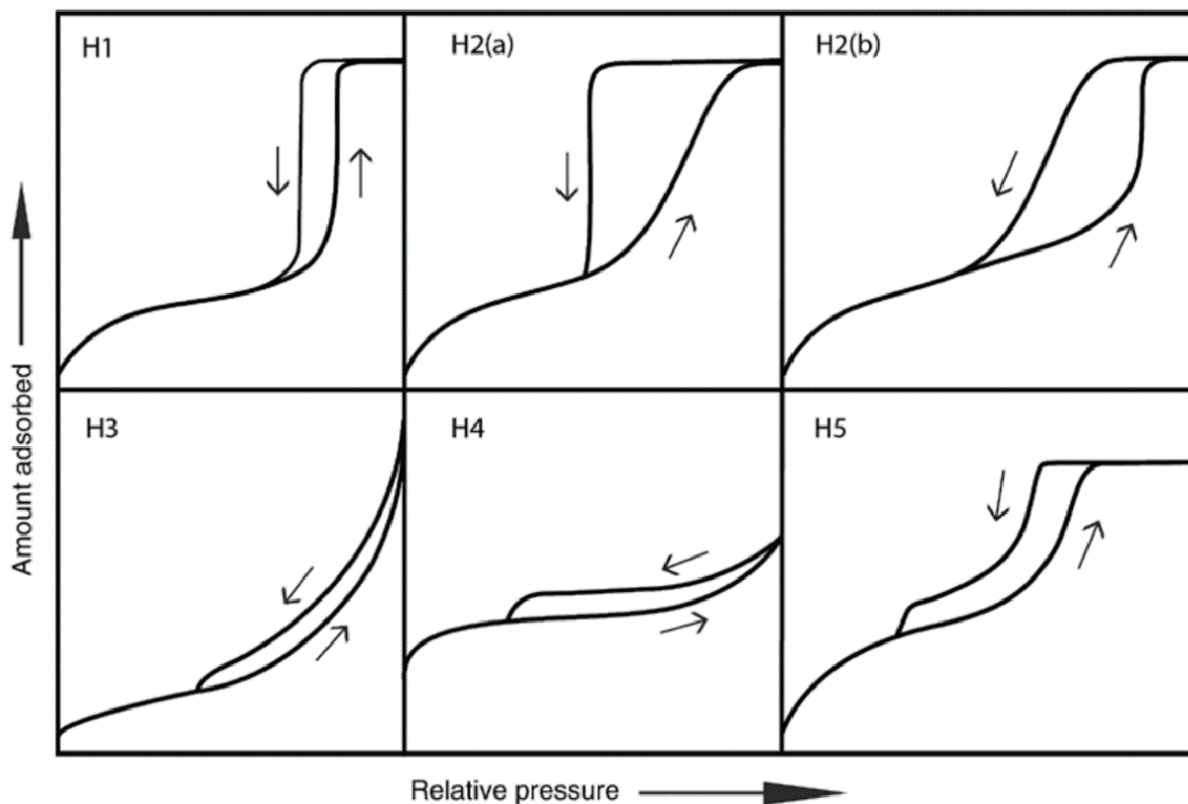


**Figure 2.4** Observed hysteresis loops as classified by IUPAC.<sup>4,5</sup>

## 2.3 References

- 1 Z. Chen, T. Bai and Z. Pan, *Coal Prod. Process. Technol.*, 2015, 79–100.
- 2 I. Langmuir, *J. Am. Chem. Soc.*, 1916, **38**, 2221–2295.
- 3 S. Brunauer, P. H. Emmett and E. Teller, *J. Am. Chem. Soc.*, 1938, **60**, 309–319.
- 4 K. S. W. Sing, D. H. Everett, R. A. W. Haul, L. Moscou, R. A. Pierotti, J. Rouquerol and T. Siemieniowska, *Pure Appl. Chem.*, 1985, **57**, 603–619.
- 5 M. Thommes, K. Kaneko, A. V. Neimark, J. P. Olivier, F. Rodriguez-Reinoso, J. Rouquerol and K. S. W. Sing, *Pure Appl. Chem.*, 2015, **87**, 1051–1069.

## Chapter 3

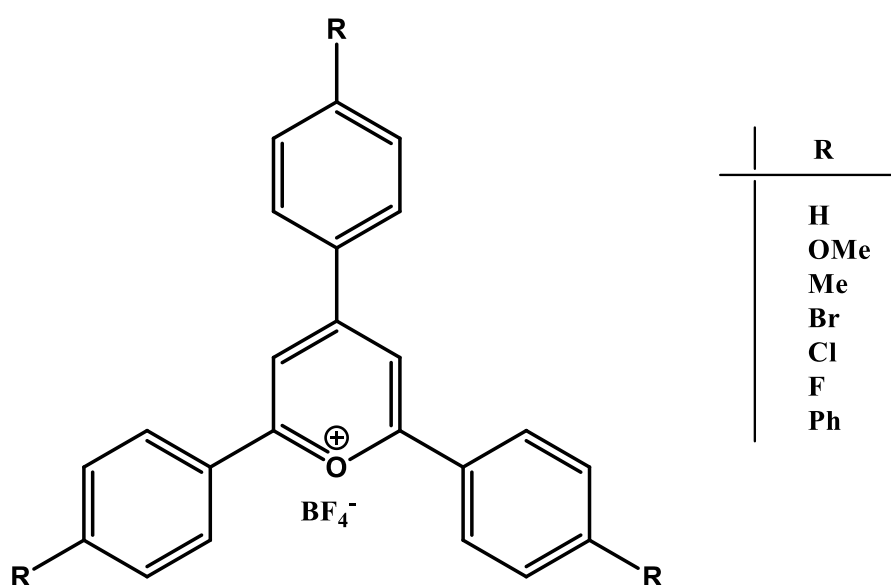
# Synthesis of Functionalised Pyrylium Based CMPs

### 3.1 Introduction

Recently, organocatalyst dyes such as eosin Y, rose bengal, BODIPY have been incorporated into conjugated microporous polymers (CMPs) and they were used as high efficient and reusable heterogeneous catalysts for various organic reactions.<sup>1-4</sup> Jiang and co-workers studied the incorporation of rose bengal dye into conjugated microporous polymer networks using the Sonogashira-Hagihara cross-coupling reaction with a tris/bis-alkyne.<sup>1</sup> The synthesised materials exhibited high surface areas of more than 800 m<sup>2</sup>/g with high chemical and thermal stabilities. The synthesised polymers were also tested as catalysts for the photocatalytic aza-Henry reaction and showed impressive %conversions which were more than 97% and the polymer can be reused up to 10 times. Similar work was reported in 2017 by Wang et al.<sup>2</sup> They included Eosin Y dye into porous organic polymer networks using Sonogashira-Hagihara reaction. The resulted materials showed high surface areas of 587 and 718 m<sup>2</sup>/g for EY-POP-1 and EY-POP-2, respectively. The EY-POP-1 exhibited excellent catalytic activity for the aza-Henry reaction which resulted in high % conversions of more than 90% and it was highly stable catalyst which can be recycled up to 12 cycles.

BODIPY embedded conjugated microporous networks synthesised *via* Sonogashira reaction was reported with a moderate surface area of 299 m<sup>2</sup>/g and it was used as a heterogeneous catalyst for thioanisole oxidation under visible light. It showed 4 times higher reaction rate than the homogeneous catalyst and it can be reused 2 times.<sup>4</sup>

Triarylpyrylium compounds have been widely studied as homogeneous photocatalysts due to their excellent catalytic properties. According to Martiny *et al.*, a series of triarylpyrylium tetrafluoroborate was synthesised (Scheme 3.1), and the electrochemical and photophysical properties were also be examined.<sup>5</sup> 2,4,6-triphenyl pyrylium (TPT<sup>+</sup>) showed an oxidation potential at 2.53 V while the triphenyl pyrylium with various aryl groups substitution exhibited oxidation potential (TPT<sup>+/•</sup>/TPT<sup>•</sup>) in the range of 1.98 to 2.53 V. Moreover, the synthesised pyrylium salts showed  $\lambda_{\max}$  from 465 to 550 nm and band gap energy from 2.25 to 2.66 eV.<sup>5</sup> They have been used as a catalyst for various organic reactions such as diene cyclisation-endoperoxidation with product yields up to 79%,<sup>6</sup> [2+2] cycloaddition reactions,<sup>7</sup> rearrangements with high yields of products from 56 to 99% at ambient temperature,<sup>8</sup> and metal-free ring opening metathesis polymerisation (ROMP).<sup>9</sup>



**Scheme 3.1** Structures of 2,5,6-triphenylpyrylium tetrafluoroborate synthesised by Martiny *et al.*<sup>5</sup>

In 2017, Wang and co-workers reported metal free visible light promoted [2+2+2] cyclisation of alkynes with nitriles to pyridines using pyrylium salts as

photoredox catalysts at room temperature.<sup>10</sup> They found that the substituted groups on the triarylpyrylium salts plays a more important role on the photocatalytic activity than counter anions. They also found that thiapyrylium which the oxygen on the pyrylium is replaced by sulphur showed no improvement in catalytic activity. The electron withdrawing such as F and Cl substituted on pyrylium salts exhibited higher activity than those with electron donating groups such as methoxy (MeO) and methyl (Me). Cl substituted pyrylium showed the highest catalytic activity and possessed highest oxidation potential at 2.3 V which is higher than the oxidation potential of alkyne at 2.163 V.

Despite the high catalytic activity of pyrylium compounds, they have poor reusability due to the low stability and difficulty to separate from the reaction. To improve the recyclability of the catalysts, the tribromophenyl pyryliums with various substituents synthesised *via* cyclisation of benzaldehydes and acetophenones are polymerised with alkyne monomers *via* Sonogashira-Hagihara coupling to form pyrylium based CMPs which have a high surface area and high stability as well as are insoluble in common solvents making it easy to be separated and reused after catalysing reactions. The pyrylium based CMPs are also synthesised by oxidative and Yamamoto couplings to compare with networks obtained from Sonogashira reaction. The synthesised materials are characterised by <sup>13</sup>C CP/MAS NMR, N<sub>2</sub> gas sorption, fourier-transform infrared spectroscopy (FTIR), solid state UV-Vis spectrophotometry, elemental analysis (EA) and thermogravimetric analysis (TGA). The effect of substituents on physicochemical and photo properties will be discussed in this chapter. The catalytic activity study of the synthesised polymers will be discussed in the next chapters.

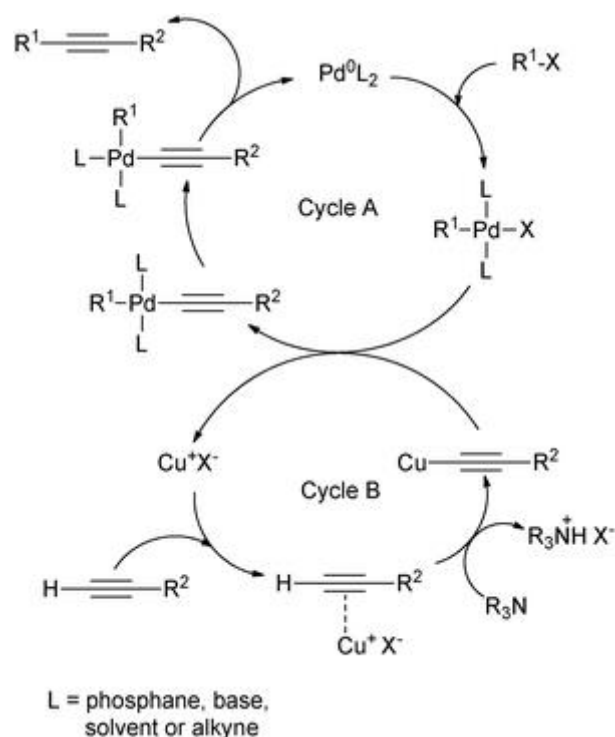
### 3.2 The reactions used to prepare CMPs in this work

The reaction mechanism of the reactions used to synthesise the CMPs are shown in the following paragraphs.

#### **3.2.1 Mechanism of Sonogashira reaction**

The Sonogashira reaction occurs *via* two independent catalytic cycles which are Pd-cycle (cycle A) and Cu-cycle (cycle B) as shown in Scheme 3.2. The reactive  $\text{Pd}^0\text{L}_2$  such as  $\text{Pd}(\text{PPh}_3)_4$  undergoes oxidative addition of arylhalide ( $\text{R}^1\text{-X}$ ) to form a  $[\text{Pd}(\text{II})\text{R}^1\text{L}_2\text{X}]$  which is a rate limiting step of the Sonogashira reaction.  $[\text{Pd}(\text{II})\text{R}^1\text{L}_2\text{X}]$  is then transformed into a  $[\text{Pd}(\text{II})\text{L}_2\text{R}^1(\text{C}\equiv\text{CR}^2)]$  by transmetalation with a copper acetylide ( $\text{Cu}\text{-}\equiv\text{-R}^2$ ) which is formed in Cu-Cycle. After that,  $[\text{Pd}(\text{II})\text{L}_2\text{R}^1(\text{C}\equiv\text{CR}^2)]$  goes through *cis/trans*-isomerisation then reductive elimination to the final alkyne product ( $\text{R}^1\text{-}\equiv\text{-R}^2$ ) and regenerating the  $\text{Pd}^0\text{L}_2$  active specie.

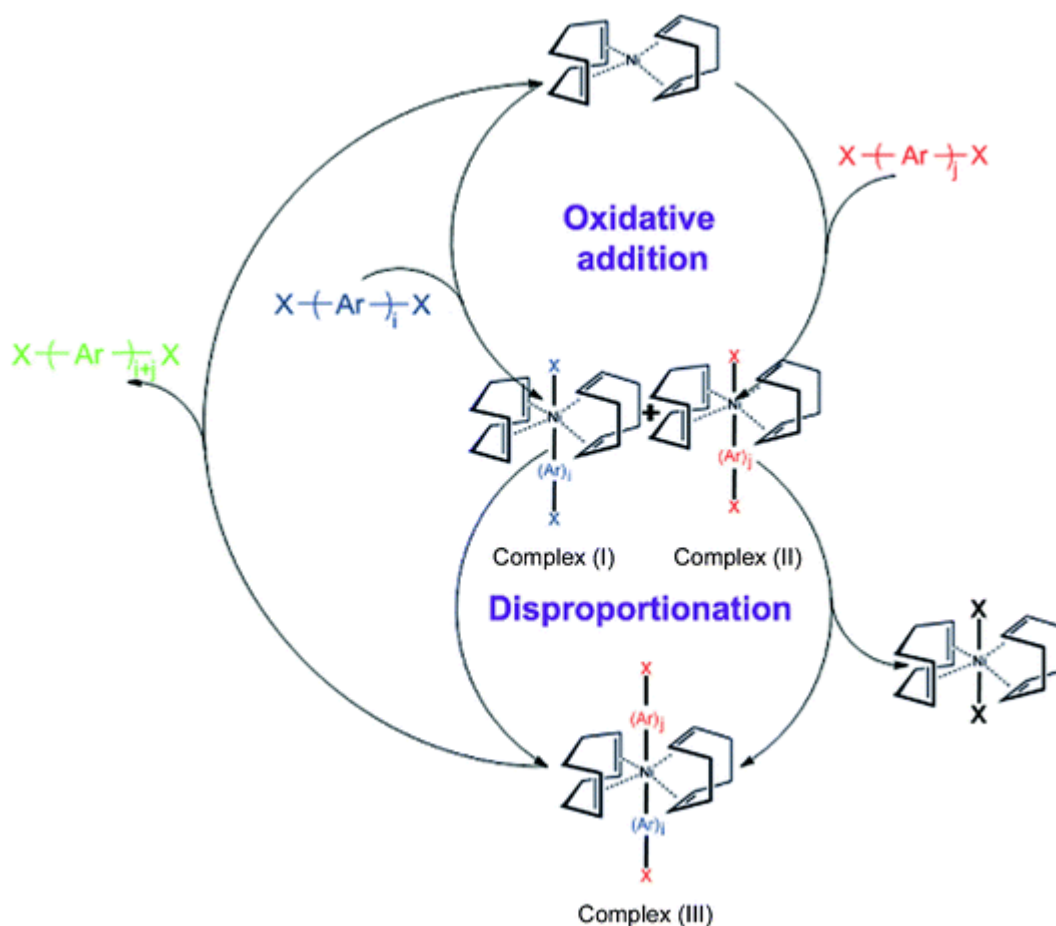
For cycle B,  $\text{H-C}\equiv\text{-R}^2$  reacts with copper halide to form a  $\pi$ -alkynecopper complex which makes the alkyne terminal proton more acidic and then the complex reacts with an amine base to form a copper acetylide ( $\text{Cu}\text{-}\equiv\text{-R}^2$ ) which then participates in cycle A and ammonium salt.<sup>11</sup>



**Scheme 3.2** Mechanism of Sonogashira reaction.<sup>11</sup>

### **3.2.2 Mechanism of Yamamoto coupling**

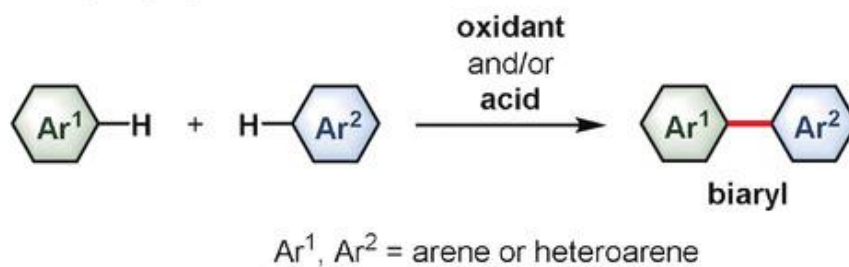
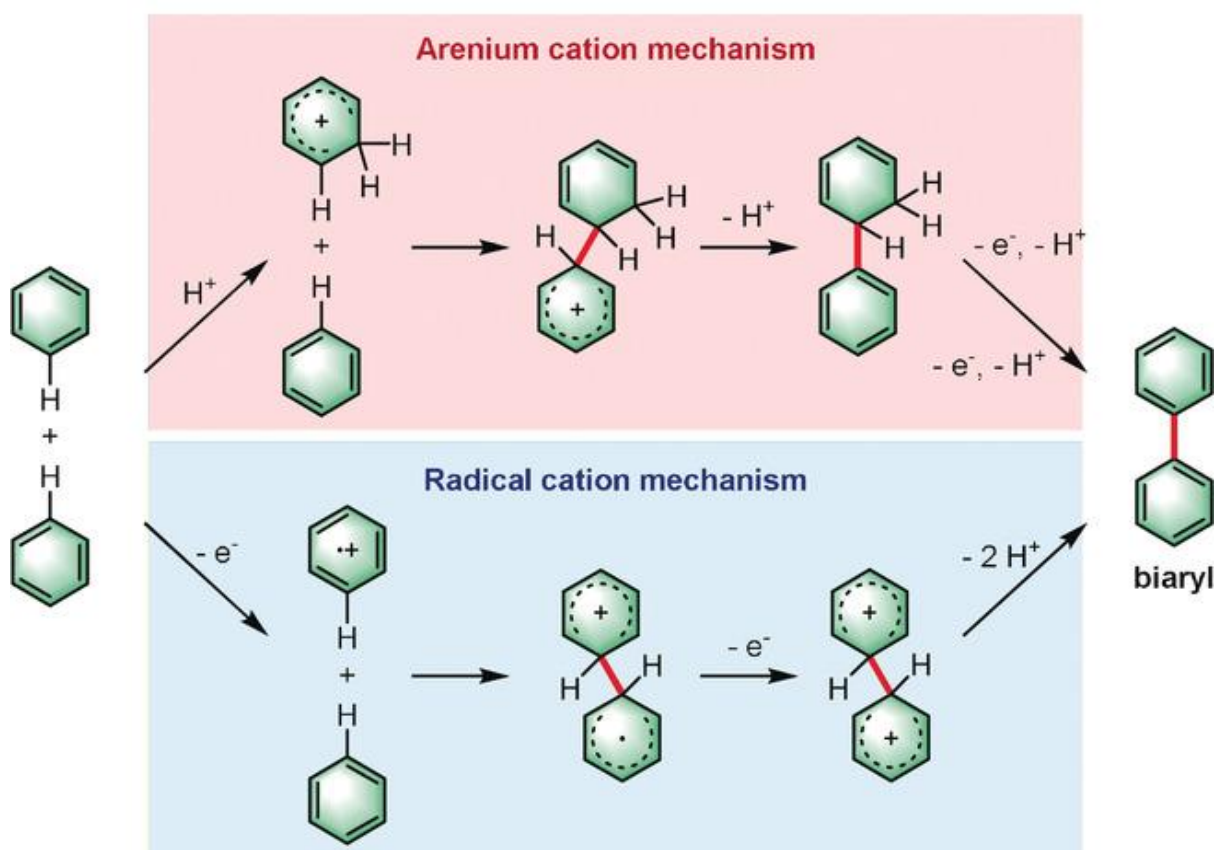
The Yamamoto coupling is aryl-aryl coupling of halogen compounds using stoichiometric amounts of bis(1,5-cyclooctadiene)nickel(0) ( $\text{Ni}(\text{COD})_2$ ). The reaction firstly involves the oxidative addition of halogen monomers to  $\text{Ni}(\text{COD})_2$  complex to form complex I and II (Scheme 3.3) following by disproportionation of the complex I and II to give complex III. Finally, the complex III undergoes reductive elimination to produce the aryl-aryl coupling product and regenerate  $\text{Ni}(\text{COD})_2$  catalyst.<sup>12,13</sup>



**Scheme 3.3** Mechanism of Yamamoto coupling.<sup>12</sup>

### **3.2.3 Mechanism of oxidative coupling**

The oxidative coupling can undergo 2 possible pathways; arenium cation and radical mechanisms as shown in Scheme 3.4.<sup>14</sup> The arenium cation mechanism involves the protonation of the aryl species to form an electrophilic  $\sigma$  complex following by the attack of the electrophilic species at the other aromatic to form a new C-C bond. Then, the aromatic system is regenerated by hydrogen elimination. The radical cation mechanism involves the formation of radical cation then substitution at the neutral aromatic and finally elimination of hydrogen to form the coupling product.<sup>15</sup>

**Oxidative coupling - general scheme****Alternative mechanisms****Scheme 3.4** Mechanisms of oxidative coupling.<sup>14</sup>

### 3.3 Aims of the chapter

- To synthesise and characterise functionalised pyrylium monomers with  $^1\text{H}$  and  $^{13}\text{C}$  NMR, FTIR, UV-Vis spectrophotometry, mass spectrometry and elemental analysis.
- To synthesise new pyrylium based CMPs using various synthetic methods such as Sonogashira-Hagihara cross-coupling, Yamamoto coupling and oxidative coupling.
- To characterise chemical properties of the synthesised materials with elemental analysis (EA), FTIR and  $^{13}\text{C}$  MAS NMR in order to confirm the incorporation of monomers and formation of CMPs.
- To characterise physical properties of the synthesised materials by nitrogen gas sorption, thermogravimetric analysis (TGA) and solid-state UV-Vis spectrophotometry in order to determine the surface area, pore size, thermal stability, light absorption profile and band gap of the materials.

### 3.4 Experimental

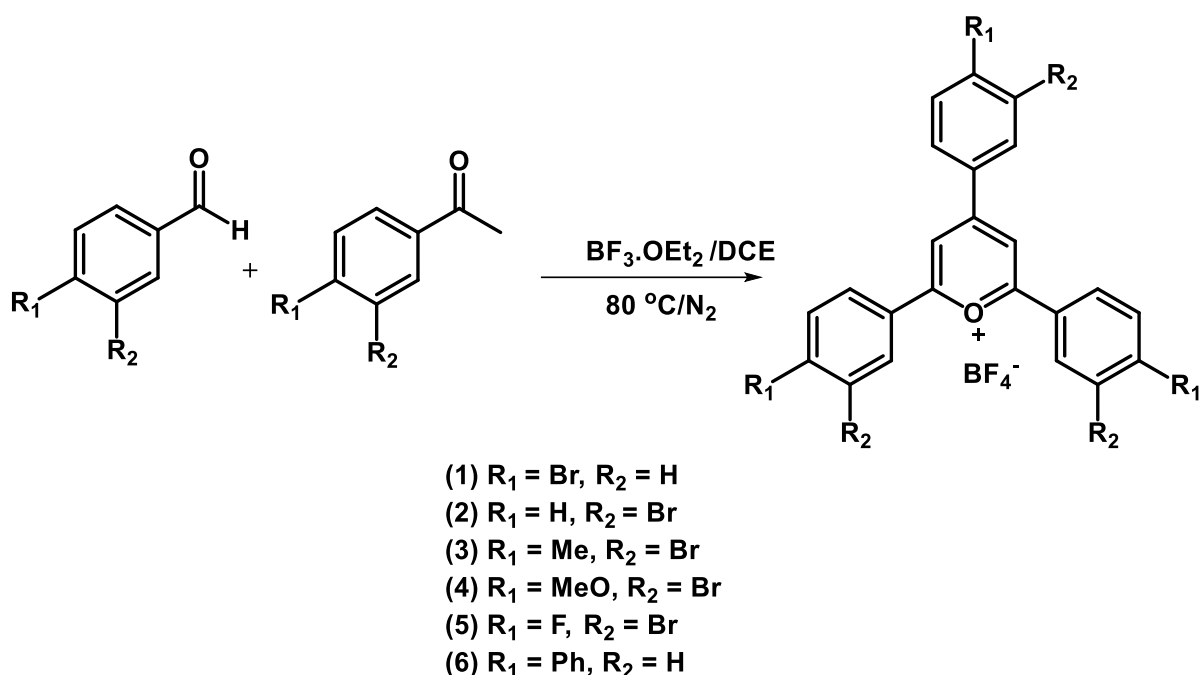
#### 3.4.1 Materials

3-Bromo-4-fluorobenzaldehyde, 3-bromo-4-methoxybenzaldehyde, 3-bromo-4-methylbenzaldehyde, biphenyl-4-carboxaldehyde, 3'-bromo-4'-fluoroacetophenone, 1-([1,1'-biphenyl]-4-yl)ethenone, 1-(3-bromo-4-methoxyphenyl)ethenone and 1-(3-bromo-4-methylphenyl)ethenone were purchased from Fluorochem. 4-Bromobenzaldehyde 3-bromobenzaldehyde, 3'-bromoacetophenone, boron trifluoride diethyl etherate, tetrakis(triphenylphosphine)palladium(0), 1,5-cyclooctadiene, aluminium chloride, 2,2'-bipyridyl, triethylamine ( $\text{Et}_3\text{N}$ , anhydrous), 1,2-dichloroethane (anhydrous) and N,N-dimethylformamide (DMF, anhydrous) were purchased from

Sigma-Aldrich. Cooper (I) iodide and 1,3,5-triethynylbenzene were obtained from Alfa Aesar. 1,4-Diethynylbenzene and bis(1,5-Cyclooctadiene)nickel(0) were bought from Acros. Methanol (HPLC), chloroform (HPLC), acetone (SLR) were purchased from Fischer Scientific. Diethyl ether (anhydrous) and tetrahydrofuran (THF) were obtained from Honeywell and VWR, respectively. Nitrogen (oxygen free) was purchased from BOC Science. All chemicals used in this work have purities over 95% and were used as received.

### **3.4.2 Synthesis of pyrylium monomers**

Bromo substituted-benzaldehyde (9.435 mmol, 1 eq.) and Br-acetophenone (18.87 mmol, 2 eq.) were added into 100 mL of two-neck round bottom flask. The flask was degassed and purged with nitrogen for 3 cycles, after which 8 mL of 1,2-dichloroethane was added by syringe. The mixture was stirred while 20.68 mmol of  $\text{BF}_3 \cdot \text{OEt}_2$  was slowly added at room temperature then refluxed under nitrogen at 80 °C for 16 h. The reaction was cooled down to room temperature and then the solution was poured into 500 mL of diethylether and stirred for 1 h. The solid product was obtained using vacuum filtration and was washed with 1L of diethylether and dried in a vacuum oven at 50 °C for 16 h. The structure of starting materials and pyrylium products are shown in Scheme 3.5.



### Scheme 3.5 Synthesis of pyrylium monomers

The monomers were characterised by  $^1\text{H}$ ,  $^{13}\text{C}$  NMR, mass spectrophotometry and elemental analysis as following. (The NMR and mass spectra are presented in appendices (Section 3.8.2 and 3.8.3))

**(1) 2,4,6-tris (4-bromophenyl) pyrylium tetrafluoroborate;** Yield = 36.6%  $^1\text{H}$ -NMR (DMSO- $d_6$ )  $\delta$  (ppm) 9.21 (s, 2H), 8.56 (d,  $J = 8.7$  Hz, 3H), 8.51 (d,  $J = 8.7$  Hz, 3H), 8.04 (d,  $J = 8.4$  Hz, 3H), 8.03 (d,  $J = 8.6$  Hz, 3H).  $^{13}\text{C}$  NMR (DMSO- $d_6$ )  $\delta$  (ppm); 115.9, 128.6, 130.2, 130.7, 131.1, 131.9, 132.2, 132.3, 133.4, 164.5, 169.8. ESI-MS ( $m/z$ ) calculated for  $\text{C}_{23}\text{H}_{14}\text{O}^{79}\text{Br}_3$  [ $\text{M}^+ - \text{BF}_4$ ] 542.9, found 543.0; calculated for  $\text{C}_{23}\text{H}_{14}\text{O}^{79}\text{Br}_2^{81}\text{Br}$  [ $\text{M}^+ - \text{BF}_4$ ] 544.9, found 544.9. Elemental analysis; C 43.90 (43.61), H 2.63 (2.23), Br 36.78 (37.88); theory value is in brackets.

**(2) 2,4,6-tris (3-bromophenyl) pyrylium tetrafluoroborate;** Yield = 20.8%  $^1\text{H}$ -NMR (DMSO- $d_6$ )  $\delta$  (ppm) 9.27 (s, 2H), 8.85 (d,  $J = 8.0$  Hz, 3H), 8.63 (d,  $J = 7.3$  Hz, 1H), 8.55 (d,  $J = 7.7$  Hz, 2H), 8.09 (d,  $J = 7.9$  Hz, 3H), 7.77 (d,  $J = 9.0$  Hz, 3H).  $^{13}\text{C}$  NMR

(DMSO-*d*6)  $\delta$  (ppm) 117.3, 123.5, 123.9, 128.4, 129.8, 131.6, 131.8, 132.2, 132.5, 132.8, 135.0, 138.2, 138.3, 164.6, 169.6. ESI-MS (*m/z*) calculated for  $C_{23}H_{14}O^{79}Br_3$  [ $M^+ - BF_4$ ] 542.9, found 542.8; calculated for  $C_{23}H_{14}O^{79}Br_2^{81}Br$  [ $M^+ - BF_4$ ] 544.9, found 544.8. Elemental analysis; C 43.92 (43.61), H 2.53 (2.23), Br 35.59 (37.88).

**(3) 2,4,6-tris (3-bromo, 4-methylphenyl) pyrylium tetrafluoroborate;** Yield = 16.9%  $^1H$ -NMR (DMSO-*d*6)  $\delta$  (ppm) 9.09 (s, 2H), 8.84 (d,  $J = 1.4$  Hz, 1H), 8.76 (d,  $J = 1.6$  Hz, 2H), 8.53 (d,  $J = 7.9$  Hz, 1 H), 8.39 (d,  $J = 7.9$  Hz, 2H), 7.75 (d,  $J = 8.1$  Hz, 2H), 7.74 (d,  $J = 8.0$  Hz, 1H), 2.53 (s, 9H).  $^{13}C$  NMR (DMSO-*d*6)  $\delta$  (ppm) 23.5, 23.5, 115.4, 126.0, 126.4, 128.1, 128.8, 129.8, 132.0, 132.3, 132.6, 132.8, 133.5, 146.0, 146.5, 163.7, 168.8. ESI-MS (*m/z*) calculated for  $C_{26}H_{20}O^{79}Br_3$  [ $M^+ - BF_4$ ] 585.5, found 585.0; calculated for  $C_{23}H_{14}O^{79}Br_2^{81}Br$  [ $M^+ - BF_4$ ] 587.45, found 588.0. Elemental analysis; C 45.90 (46.23), H 3.39 (2.99), Br 32.32 (35.52).

**(4) 2,4,6-tris (3-bromo, 4-methoxyphenyl) pyrylium tetrafluoroborate;** Yield = 20.0%  $^1H$ -NMR (DMSO-*d*6)  $\delta$  (ppm) 8.84 (d,  $J = 2.2$  Hz, 1H), 8.79 (s, 2H), 8.69 (d,  $J = 2.3$  Hz, 2H), 8.60 (dd,  $J = 8.8$  Hz,  $J = 2.31$  Hz, 1H), 8.40 (dd,  $J = 8.9$  Hz,  $J = 2.2$  Hz, 2H), 7.40 (d,  $J = 9.1$  Hz, 2 H), 7.36 (d,  $J = 8.9$  Hz, 2 H), 4.08 (s, 3H), 4.06 (s, 6H).  $^{13}C$  NMR (DMSO-*d*6)  $\delta$  (ppm); 57.7, 57.8, 112.5, 112.7, 113.1, 113.6, 113.9, 122.9, 125.9, 130.6, 132.6, 133.3, 134.8, 161.0, 161.6, 167.5. ESI-MS (*m/z*) calculated for  $C_{26}H_{20}O_4^{79}Br_3$  [ $M^+ - BF_4$ ] 633.5, found 632.9; calculated for  $C_{26}H_{20}O_4^{79}Br_2^{81}Br$  [ $M^+ - BF_4$ ] 635.5, found 635.9. Elemental analysis; C 40.75 (43.16), H 3.23 (2.79), Br 29.22 (33.16).

**(5) 2,4,6-tris (3-bromo, 4-fluorophenyl) pyrylium tetrafluoroborate;** Yield = 20.9%  $^1H$ -NMR (DMSO-*d*6)  $\delta$  (ppm) 9.19 (s, 2H), 9.03 (dd,  $J = 6.5$  Hz, 1.9 Hz, 1H), 8.99 (dd,  $J = 6.8$  Hz, 1.9 Hz, 2H), 8.70 (dd,  $J = 4.2$  Hz,  $J = 2.8$ , 1H), 8.61 (dd,  $J = 4.9$  Hz, 2.2

Hz, 2H), 7.85 (d,  $J = 8.8$  Hz, 1H), 7.82 (dd,  $J = 8.6$  Hz,  $J = 2.5$  Hz, 2H).  $^{13}\text{C}$  NMR (DMSO- $d_6$ )  $\delta$  (ppm) 110.5, 110.7, 116.7, 118.7, 119.0, 127.6, 131.6, 131.7, 135.0, 136.1, 150.9, 161.4, 163.3, 164.0, 168.7. ESI-MS ( $m/z$ ) calculated for  $\text{C}_{23}\text{H}_{11}\text{OF}_3^{79}\text{Br}_3$  [ $\text{M}^+ - \text{BF}_4$ ] 597.3, found 596.7; calculated for  $\text{C}_{23}\text{H}_{11}\text{OF}_3^{79}\text{Br}_2^{81}\text{Br}$  [ $\text{M}^+ - \text{BF}_4$ ] 599.3, found 598.7. Elemental analysis; C 40.44 (40.44), H 1.95 (1.61), Br 33.52 (34.90).

**(6) 2,4,6-tris (biphenyl) pyrylium tetrafluoroborate**; Yield = 24.8%  $^1\text{H}$ -NMR (DMSO- $d_6$ )  $\delta$  (ppm) 9.22 (s, 2H), 8.76 (d,  $J = 8.7$  Hz, 2H), 8.69 (d,  $J = 8.7$  Hz, 4H), 8.12 (dd,  $J = 8.8$  Hz, 2.96 Hz, 6H), 7.92 (dd,  $J = 7.2$  Hz, 1.5 Hz, 6H), 7.59 (dd,  $J = 7.7$  Hz, 1.6 Hz, 6H), 7.53 (dd,  $J = 7.5$  Hz, 1.4 Hz, 3H).  $^{13}\text{C}$  NMR (DMSO- $d_6$ )  $\delta$  (ppm) 115.0, 127.1, 127.7, 127.8, 128.2, 128.3, 128.6, 129.5, 129.6, 129.8, 129.9, 131.4, 131.8, 138.6, 138.6, 146.6, 146.9, 164.1, 169.7. ESI-MS ( $m/z$ ) calculated for  $\text{C}_{41}\text{H}_{29}\text{O}$  [ $\text{M}^+ - \text{BF}_4$ ] 537.7, found 537.2. Elemental analysis; C 78.65 (78.86), H 5.05 (4.68).

### **3.4.3 Synthesis of functionalised pyrylium based CMPs via Sonogashira coupling**

The ratio of bromo and alkyne functional groups was fixed at 1:1.5 as the previous works showed that it gave the highest BET surface areas.<sup>16–18</sup> Bromo substituted pyrylium monomers (0.5 mmol), and either TEB (0.75 mmol) or DEB (1.125 mmol) were added into a two-neck round bottom flask along with CuI (0.079 mmol, 15 mg). The flask was degassed and backfilled with nitrogen gas for 3 cycles. Then, either 5 mL (for TEB) or 15 mL (for DEB) each of anhydrous DMF and Et<sub>3</sub>N were added and the reaction mixture was heated to 100 °C under nitrogen atmosphere. Once the reaction had reached the required temperature, Tetrakis(triphenylphosphine)palladium(0) (0.043 mmol, 50 mg) was mixed with 2 mL

of anhydrous DMF and the mixture was immediately injected as a slurry into the reaction using a wide bore syringe needle. The reaction was heated for 24 h. The resulting solid product was filtered by vacuum filtration and washed with methanol, chloroform and acetone, respectively. The washed product was further purified by Soxhlet extraction using methanol for 16 h and the obtained solid was dried under vacuum at 80 °C.

#### **3.4.4 Synthesis of pyrylium CMP via Yamamoto Coupling**

2,4,6-tris(4-bromophenyl) pyrylium tetrafluoroborate (0.35 mmol), 1.77 mmol of 1,5-Cyclooctadiene (COD), 1.83 mmol of 2,2'-bipyridyl and 1.83 mmol of bis(1,5-cyclooctadiene)nickel(0) (Ni(COD)<sub>2</sub>) were mixed with 30 mL of anhydrous DMF under nitrogen atmosphere. The mixture was then heat to 120 °C overnight. The reaction was cooled down and then poured into water and washed with methanol, chloroform, acetone and THF, respectively. The polymers were further purified by Soxhlet extraction using methanol, chloroform and THF 24 h each, respectively. The product was collected and then dried in a vacuum oven at 80 °C overnight.

#### **3.4.5 Synthesis of pyrylium CMP via oxidative Coupling**

2,4,6-tris(biphenyl) pyrylium tetrafluoroborate (1 mmol) was added in round bottom flask and degassed and purged with nitrogen for 3 cycles each. Then the anhydrous chloroform (15 mL) was added *via* syringe and 7 mmol of anhydrous AlCl<sub>3</sub> catalyst was added. The reaction was heated to 65 °C for 2 days and after cool down, the solid product was collected and washed with methanol. The obtained material was further washed with methanol using Soxhlet extraction overnight and then the product was dried for 16 h at 80 °C under vacuum.

## 3.5 Results and Discussion

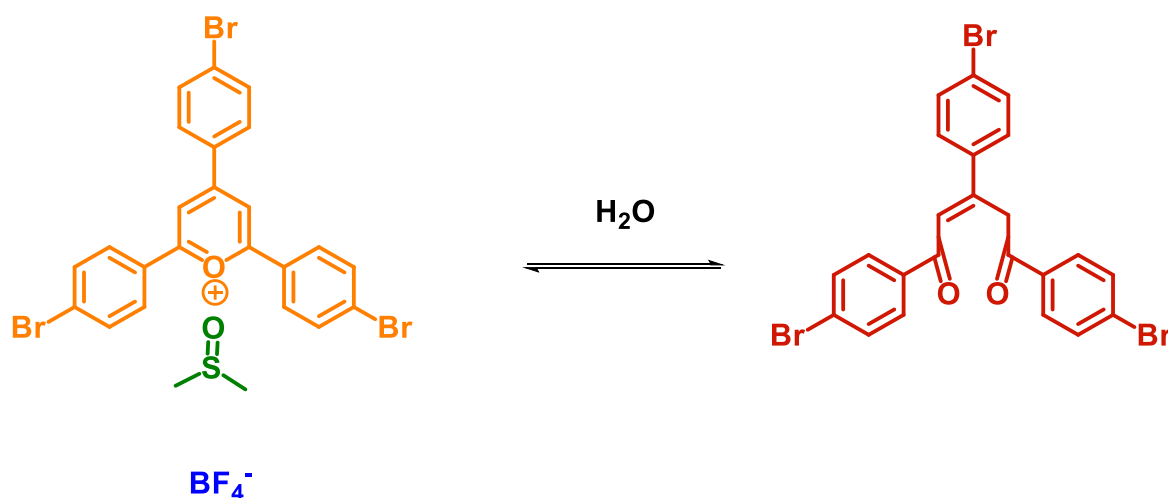
### 3.5.1 Characterisation of pyrylium monomers

The triphenylpyrylium tetrafluoroborate monomers with different substituent groups were synthesised by the cyclisation of substituted benzaldehydes and acetophenones using  $\text{BF}_3 \cdot \text{OEt}_2$  catalyst as shown in Scheme 3.5. The yields of the products ranged from 16.9 to 36.6%. The yields of compound (1) are similar with the previous works (22-32%).<sup>19,20</sup> The synthesised pyrylium monomers were chemically characterised by  $^1\text{H}$ ,  $^{13}\text{C}$ ,  $^{11}\text{B}$  and  $^{19}\text{F}$  NMR as well as mass spectrometry and elemental analysis. The characteristic peaks at 8.79 to 9.27 ppm observed in  $^1\text{H}$  NMR of different substituted pyrylium monomers correspond to 2H in the oxonium ring confirming the formation of a pyrylium. The  $^{13}\text{C}$  NMR spectra also show the peaks of carbons in pyrylium functional group at 115 ( $\text{C}_3$  and  $\text{C}_5$ ), 164 ( $\text{C}_4$ ) and 169 ppm ( $\text{C}_2$  and  $\text{C}_6$ ).<sup>19-21</sup> The pyrylium monomers show signals of  $\text{BF}_4^-$  in the  $^{11}\text{B}$  NMR at approximately -1.29 ppm and in the  $^{19}\text{F}$  NMR at around -148.3 ppm which are similar with the previous work.<sup>22</sup>

2,4,6-tris (3-bromo, 4-methylphenyl) pyrylium tetrafluoroborate (compound (3)) shows methyl proton peak at 2.53 ppm and methyl carbon peaks at 23.47 and 23.51 ppm while 2,4,6-tris (3-bromo, 4-methoxyphenyl) pyrylium tetrafluoroborate (compound (4)) shows methoxy proton peaks at 4.06 and 4.08 ppm and methoxy carbon peaks at 57.68 and 57.92 ppm. 2,4,6-tris (3-bromo, 4-fluorophenyl) pyrylium tetrafluoroborate (compound (5)) exhibits C-F signals in  $^{19}\text{F}$  NMR at 97.28, 101.16 and 106.99 ppm, respectively. The elemental analysis results are close to the calculated values which can confirm the purity of the monomers. Mass spectrometry results are

consistent with the previous work and showed  $m/z$  of pyrylium cations and only one group of peaks was found in the spectra confirming the purity of the compounds.<sup>20</sup>

The presence of water (for example in NMR solvent DMSO- $d_6$ ) leads to the reversible ring opening of pyrylium to pent-2-ene-1,5-dione which is to be expected when the pyryliums are substituted with electron withdrawing groups such as Br as shown in Scheme 3.6.<sup>23</sup> DMSO- $d_6$  can solvate pyrylium cations and split ionic aggregates. When the pyrylium cation is separated from  $\text{BF}_4^-$  anion, this results in ring opening in the presence of water which is commonly observed in high polar NMR solvents.<sup>23</sup> The methylene protons and carbon can be observed at 4.75 ppm and 42.73 ppm in  $^1\text{H}$  and  $^{13}\text{C}$  NMR, respectively. Moreover, an olefinic proton and carbon can be noticed at 7.66 and 123.23 ppm in  $^1\text{H}$  and  $^{13}\text{C}$  NMR, respectively. The dione carbons are observed at 188.9 and 196.4 ppm in  $^{13}\text{C}$  NMR.



**Scheme 3.6** Reversible ring opening of pyrylium cation to pent-2-ene-1,5-dione.<sup>23</sup>

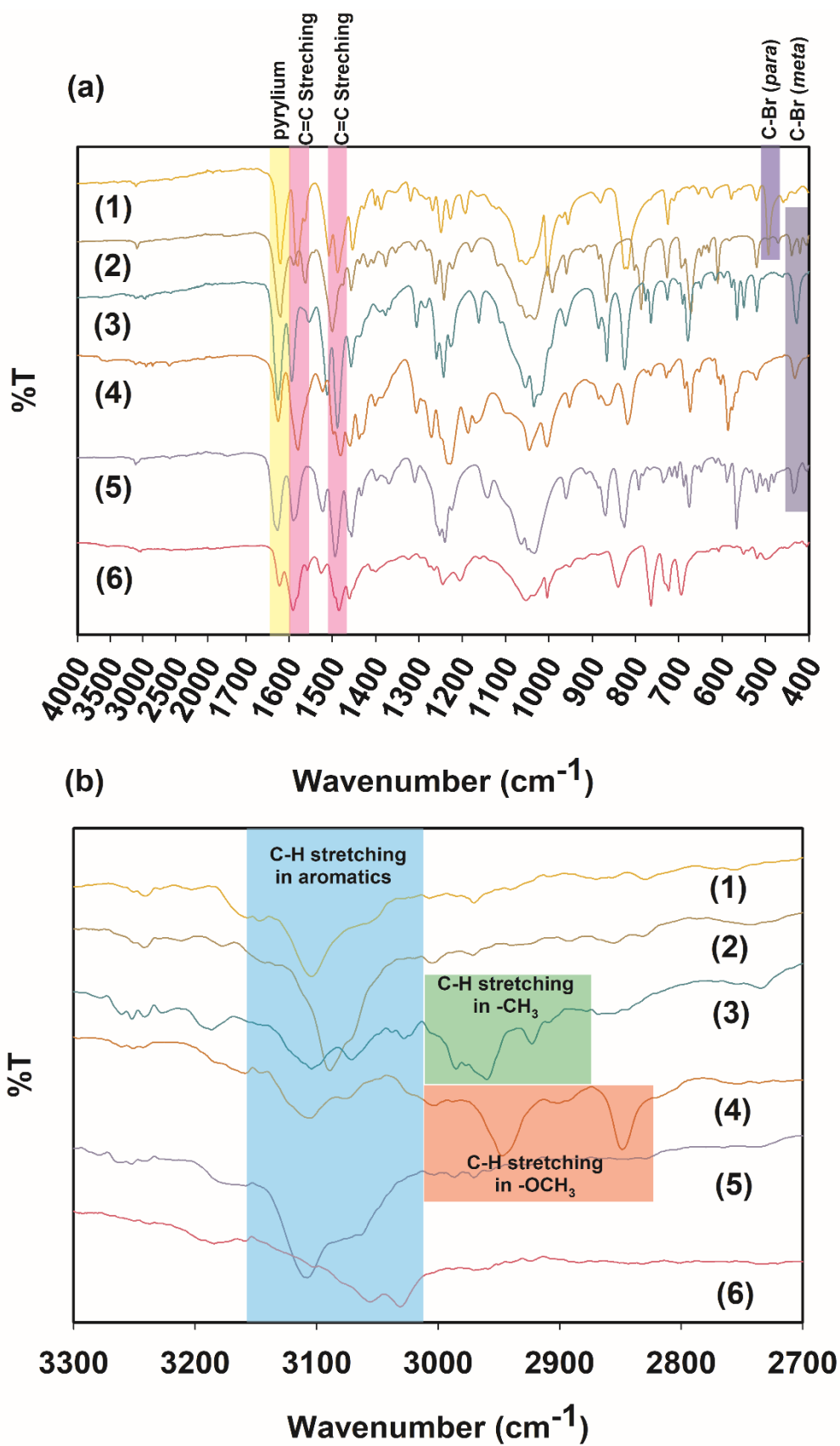
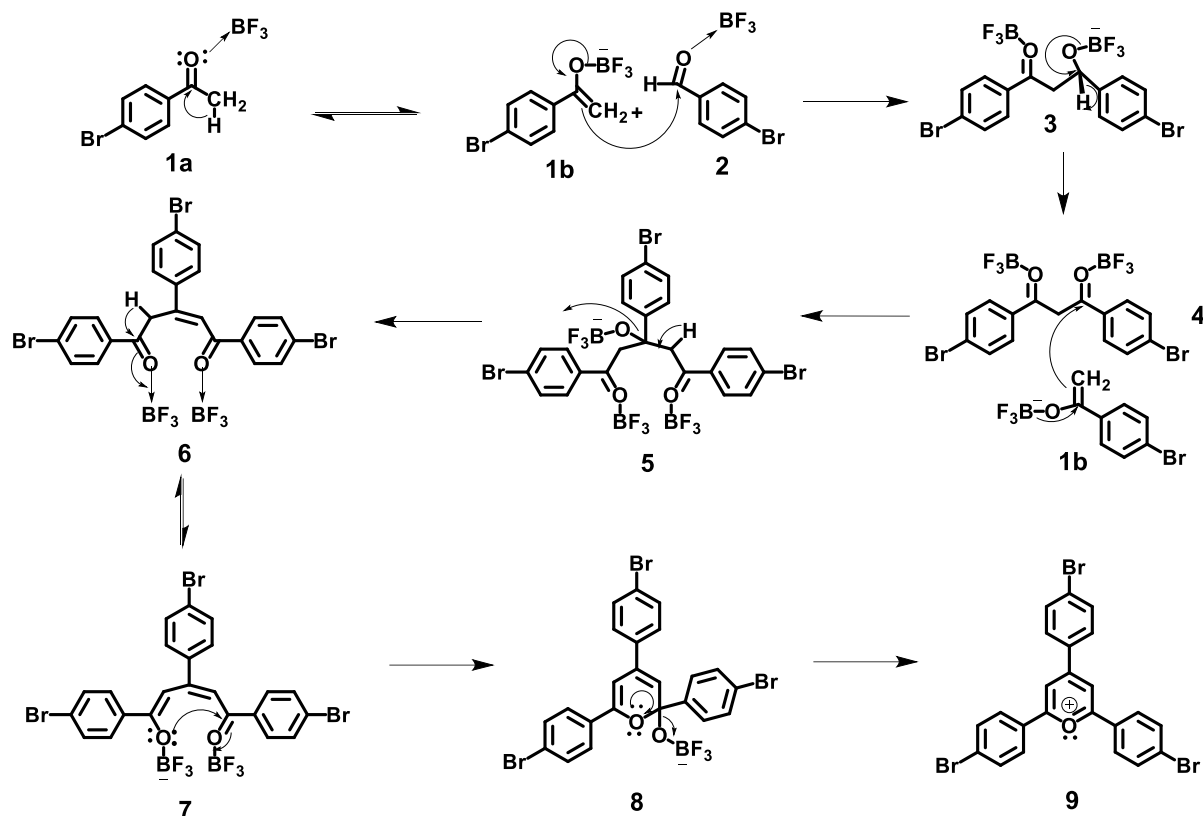


**Figure 3.1** IR spectra of the synthesised perylium monomers (a) 400-4000 and (b) 2700-3300  $\text{cm}^{-1}$ .

All synthesised monomers were characterised by FTIR and showed a characteristic pyrylium functional group peak at  $1620\text{ cm}^{-1}$  confirming that the pyrylium compounds were successfully prepared. The characteristic peaks of  $\text{BF}_4^-$  were observed at  $\sim 521, 1054, 1166\text{ cm}^{-1}$  as shown in Figure 3.1.<sup>19,21,24</sup> The C-Br peak at *para* position was detected at  $517\text{ cm}^{-1}$  (1) while *meta* C-Br peak was found at  $428\text{--}440\text{ cm}^{-1}$  (2-5).<sup>19</sup> All monomers show C=C stretching at around  $1480$  and  $1580\text{ cm}^{-1}$  and C-H stretching peaks of aromatic rings at around  $3100\text{ cm}^{-1}$ . Molecule (3) shows C-H stretching peaks at  $2965\text{--}2990\text{ cm}^{-1}$  corresponding to methyl groups while (4) shows peaks at  $2856\text{--}2948\text{ cm}^{-1}$  assigned as methoxy groups.<sup>25</sup>

### **3.5.2 Mechanism of pyrylium formation**

The proposed mechanism for pyrylium formation is illustrated in Scheme 3.7. Using 2,4,6-tris (4-bromophenyl) pyrylium tetrafluoroborate as an example, boron trifluoride etherate induces formation of keto-enol equilibrium of 4-bromoacetophenone. The enol form (1b) then undergoes nucleophilic attack at aldehyde (2) activated by  $\text{BF}_3$  followed by elimination of H and the formation of the  $\beta$ -diketone (4). The  $\beta$ -diketone then goes through a condensation with another enol form of 4-bromoacetophenone (1b) leading to the formation of the  $\beta$ -hydroxy- $\delta$ -diketone (5). The hydroxyl group is eliminated in the form of  $(\text{OBF}_3)^-$  and it results in an unsaturated  $\delta$ -diketone (6) which is then induced by  $\text{BF}_3$  to form enol form (7). The enol form undergoes internal cyclisation by elimination of a  $\text{BF}_3$  molecule and finally generates the six-membered pyrylium ring (9).<sup>20</sup>

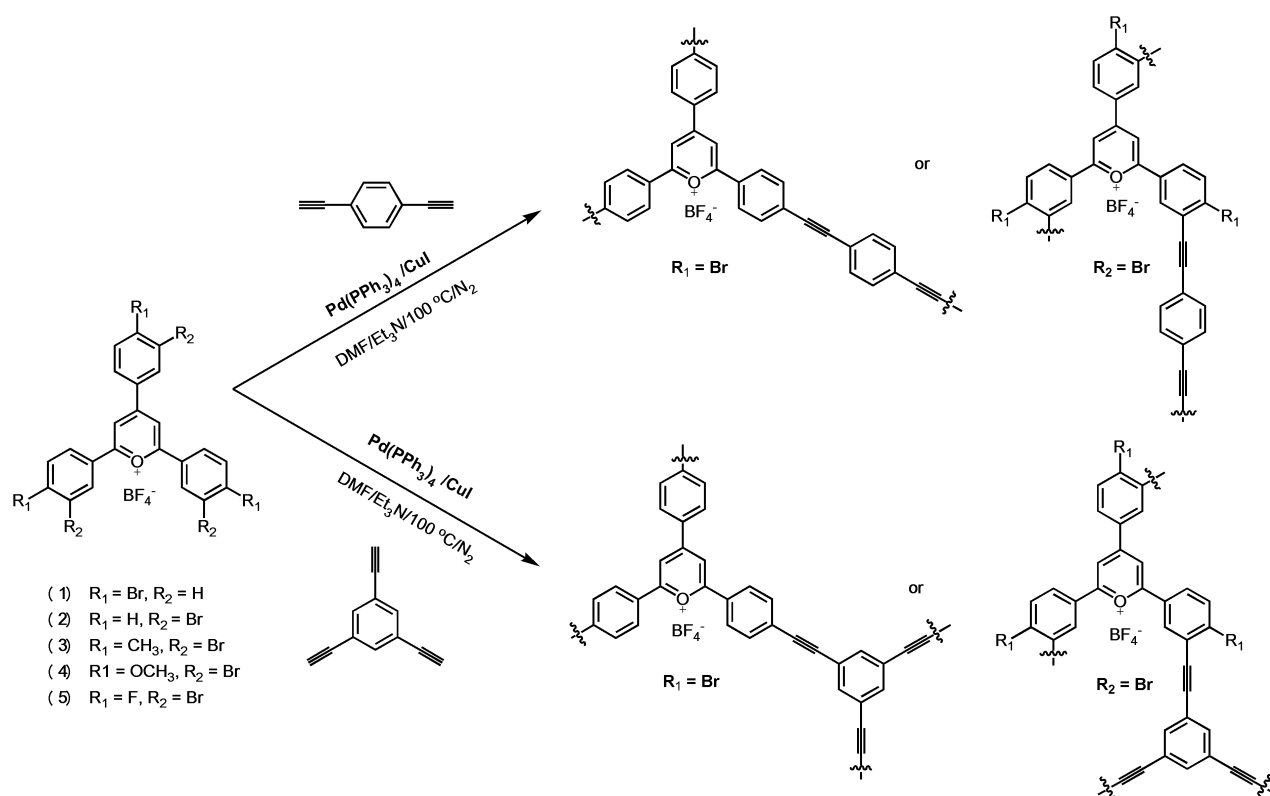


**Scheme 3.7** Mechanism of 2,4,6-tris (4-bromo) pyrylium tetrafluoroborate synthesis<sup>20</sup>

### **3.5.3 Synthesis and characterisation of pyrylium based CMPs**

#### **3.5.3 (a) Elemental analysis (EA)**

The pyrylium CMPs with different substituents were synthesised *via* Sonogashira coupling. The ratio of bromo to alkyne functional groups was 1:1.5 as it gave the highest surface areas according to previous works.<sup>16–18</sup> The prepared pyrylium monomers with various substituted groups were polymerised with either 1,3,5-triethynyl benzene (TEB) or 1,4-diethynylbenzene (DEB) as shown in Scheme 3.8.



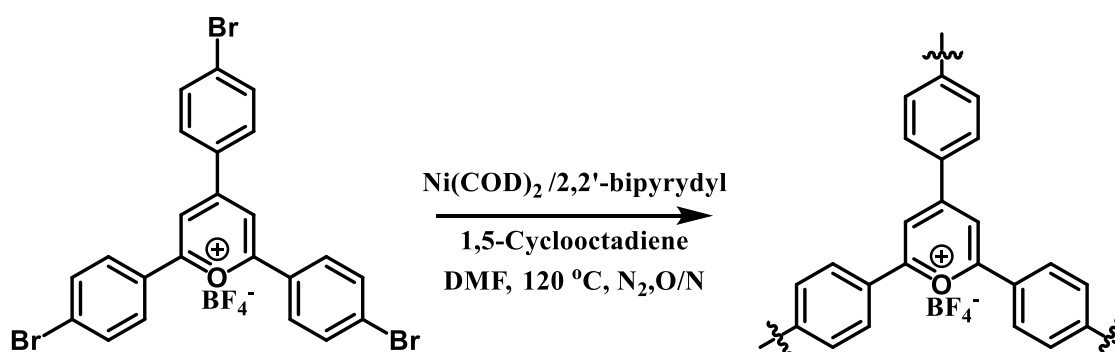
**Scheme 3.8** Synthesis of pyrylium based CMPs *via* Sonogashira coupling.

The yields and elemental analysis results of the synthesised polymers are illustrated in Table 3.2. The yields of the synthesised polymers (Table 3.1) were from 98 to 116% as is typical for CMPs.<sup>16,17,26–28</sup> The over hundred %yield might be caused from the residual monomers, catalysts, moisture and solvents trapped in the pores and the residual bromo end groups.<sup>16,17,27</sup>

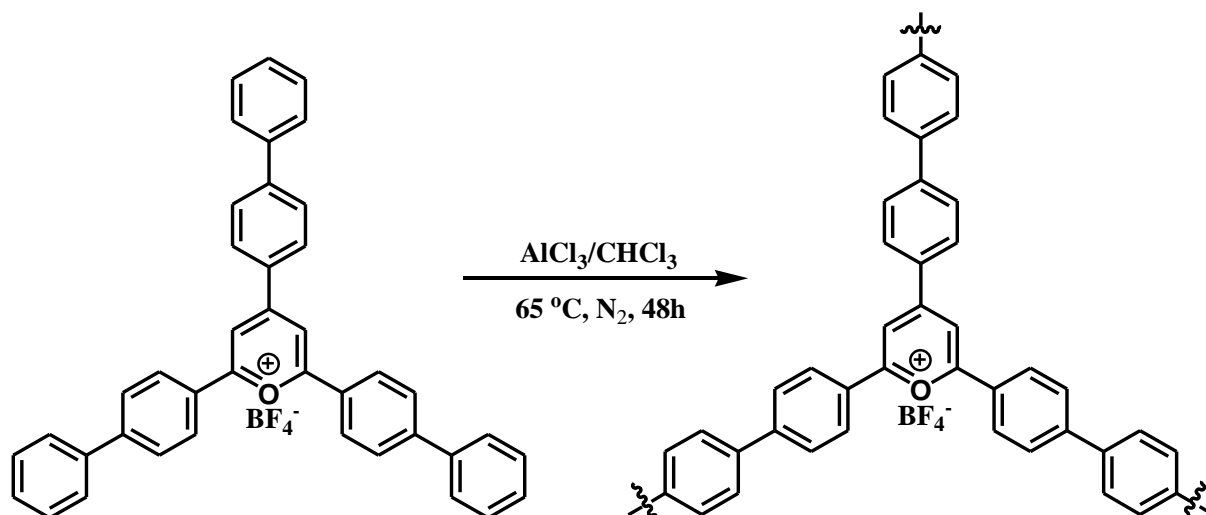
The elemental analysis results are shown in Table 3.1. The theory values are based on 1:1.5 ratio of bromine to alkyne, so it is expected that all bromine can be consumed in the reaction. However, bromine contents are higher than expected values due to incomplete reaction leading to the residual Br group at the end chains of polymers. The residual Br resulted in lower found carbon content than the theory. This is consistent with the previous work that the polymers tend to terminate with

bromine in DMF solvent.<sup>17</sup> The DEB version of the polymers possesses lower amount of bromine due to the less steric hindrance than TEB leading to more conversion of bromine monomers to polymer networks.

The pyrylium based CMP synthesised *via* Yamamoto homocoupling of bromo pyrylium monomer gave the %yield of 95 of the polymer product (Scheme 3.9) due to the lower unreacted Br end group (Table 3.1) when compared with networks synthesised from Sonogashira reaction. This is consistent with the previous work reporting that Yamamoto coupling shows the unexpected ability to eliminate bromine end group when compared with the other reactions such as Sonogashira and Suzuki cross-couplings.<sup>12</sup> The pyrylium CMP can also be prepared *via* oxidative coupling of biphenyl pyrylium monomer giving a 122 % yield of the solid product (Scheme 3.10). The excessive yield can be explained by the residual Cl (Table 3.1) associated from residual  $\text{CHCl}_3$  solvent and  $\text{AlCl}_3$  catalyst.



**Scheme 3.9** Synthesis of pyrylium CMP *via* Yamamoto coupling.



**Scheme 3.10** Synthesis of perylium CMP *via* oxidative coupling.

**Table 3.1** Yields and elemental analysis of the synthesised polymers.

Sample	%Yield	Expected (%)			Found (%)		
		C	H	Br	C	H	halogen
Pyr+TEB	116	79.63	3.75	0	75.82	3.96	9.83
Pyr+DEB	102	81.54	3.12	0	79.63	4.30	3.42
<i>m</i> -Pyr+TEB	112	79.63	3.75	0	70.35	3.55	17.62
<i>m</i> -Pyr+DEB	101	81.54	3.12	0	82.37	4.34	7.29
Me-Pyr+TEB	116	80.56	3.76	0	67.90	3.90	20.01
Me-Pyr+DEB	110	81.78	3.79	0	75.39	4.48	14.19
MeO-Pyr+TEB	109	75.07	3.51	0	70.46	4.01	11.39
MeO-Pyr+DEB	99	76.62	3.55	0	75.58	4.42	8.35
F-Pyr+TEB	107	73.73	2.34	0	69.28	3.14	12.58
F-Pyr+DEB	98	75.46	2.47	0	75.75	3.56	7.11
PYR CMP Yamamoto	95	69.73	4.32	0	52.08	4.56	1.9
PYR CMP oxidative	122	78.86	4.68	0	68.99	4.67	11.53

### 3.5.3 (b) FTIR of the synthesised polymers

The FTIR spectra of the synthesised pyrylium polymers obtained from the Sonogashira reactions (Figure 3.2(a) and (b)) were used to investigate the networks. The C-Br stretching peak at 428-517  $\text{cm}^{-1}$  (Figure 3.1) and alkyne C-H stretching peak at 3261-3281  $\text{cm}^{-1}$  (Figure A3.1) observed in monomers were not detected indicating a high conversion of monomers to polymer networks. Moreover, the appearance of a new alkyne linkage peak at 2168  $\text{cm}^{-1}$  suggests the successful formation of CMP networks.<sup>16,17,27</sup> The characteristic peak of pyrylium can be observed at 1670  $\text{cm}^{-1}$  which is closed to the peak of 1620  $\text{cm}^{-1}$  found in pyrylium monomers (Figure 3.1).<sup>19,21</sup> The pyrylium CMP networks synthesised *via* Yamamoto and oxidative couplings also showed the presence of a pyrylium peak at 1690  $\text{cm}^{-1}$  and peaks at 2855 and 2922  $\text{cm}^{-1}$  corresponding to C-H stretching in aromatic for PYR CMP synthesised *via* Yamamoto and oxidative coupling, respectively. No evidence peaks of carbonyl peaks at 1740  $\text{cm}^{-1}$  corresponding to ring opening were observed.

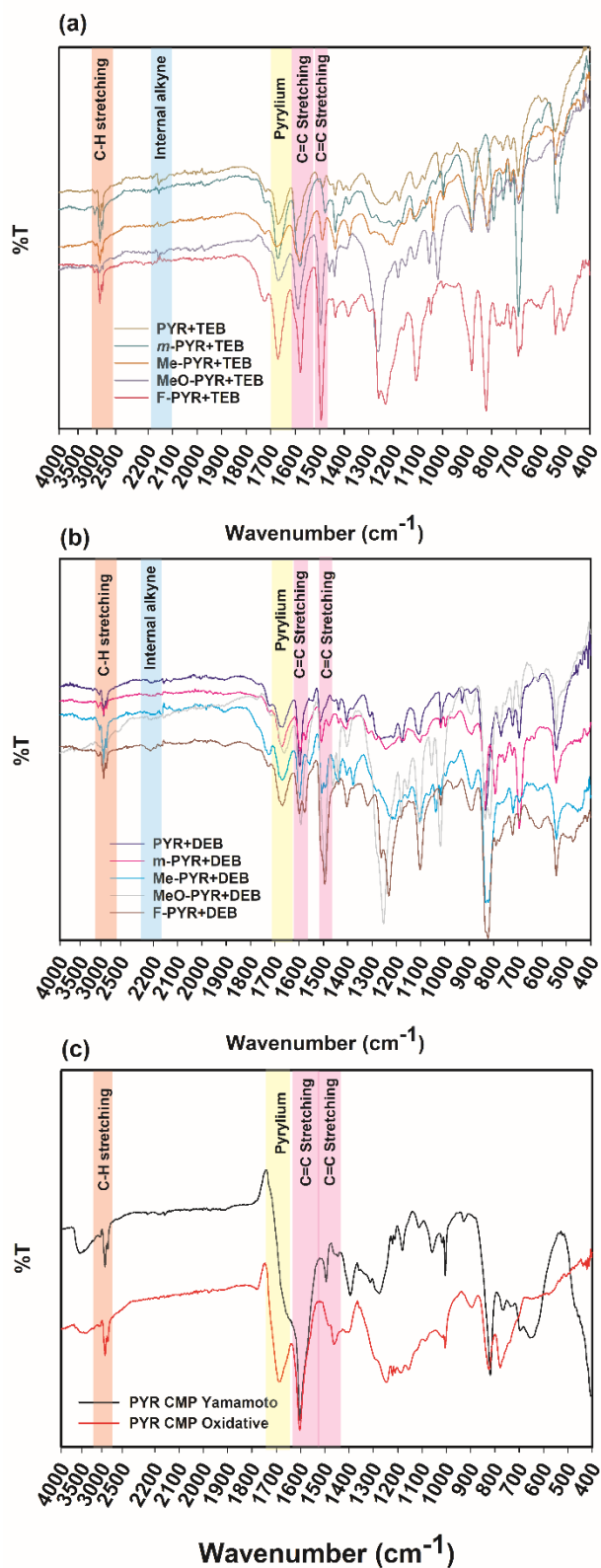


**Figure 3.2** IR spectra of the synthesised (a) pyrylium CMPs derived from TEB, (b) DEB synthesised *via* Sonogashira coupling and (c) pyrylium CMPs synthesised *via* Yamamoto and oxidative couplings.

### 3.5.3 (c) $^{13}\text{C}$ CP/MAS NMR

Further structural characterisation of the as synthesised pyrylium CMPs was achieved by  $^{13}\text{C}$  CP/MAS NMR (Figure 3.3 (a)-(e)). The peaks around 85 and 95 ppm were related to terminal ( $\text{C}_{\text{Ar}}-\text{C}\equiv\text{C}-\text{H}$ ) and quaternary alkynes ( $\text{C}_{\text{Ar}}-\text{C}\equiv\text{C}-\text{C}_{\text{Ar}}$ ), respectively. Even though the C-H stretching peak in terminal alkyne was not detected in IR, small peaks of terminal alkyne were observed by NMR especially in substituted pyrylium networks including Me, OMe and F pyrylium CMPs. This can be explained by the steric hindrance and deactivation of aryl bromide caused by electron donor substituents leading to a lower coupling of monomers to polymer networks.<sup>29</sup> The peak at 125 ppm was assigned for quaternary aromatic carbon of alkyne units and hydrogen substituted aromatic carbon of phenyl in pyrylium units. The peak at 132 was assigned for hydrogen substituted aromatic carbon in alkyne units and quaternary aromatic carbon of phenyl in pyrylium units. The methyl and methoxy pyrylium showed additional peak at 20 and 55 ppm which were related to methyl and methoxy groups, respectively. The fluoro and methoxy pyrylium also showed the peaks at approximately 160 ppm which were assigned as aromatic carbon connected with fluoro and methoxy groups, respectively while methyl pyrylium illustrated the peak at 138 assigned as methyl substituted aromatic carbon. So, this can confirm that the pyrylium monomers have been incorporated into the CMP networks.<sup>16,17,27</sup> The C-Br peaks in residual bromo end groups were overlapped in the aromatic carbon peaks except methoxy and fluoro pyrylium CMPs that showed the peaks at 106 and 114 ppm, respectively. Figure 3.3(a) and 3.3(f) show the  $^{13}\text{C}$  CP/MAS NMR spectra of pyrylium CMPs obtained by Yamamoto and oxidative couplings. The peak at 130 ppm corresponded to H substituted aromatic carbon while the peak at 142 related to quaternary aromatic carbon.

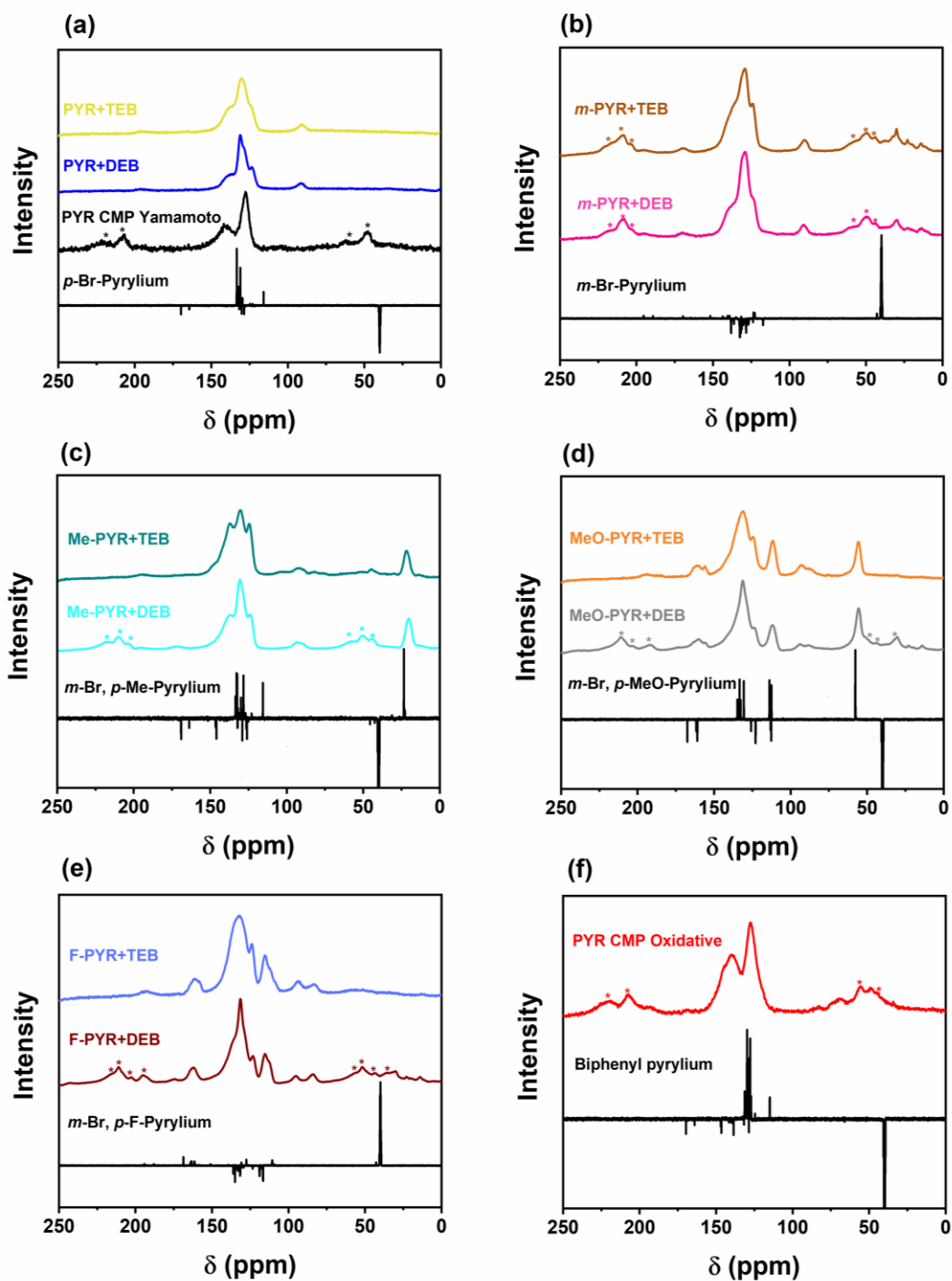


**Figure 3.3**  $^{13}\text{C}$  CP/MAS NMR spectra of (a) PYR+TEB, PYR+DEB and PYR CMP Yamamoto compared with solution  $^{13}\text{C}$  NMR of *p*-Br-pyrylium monomer, (b) *m*-PYR+TEB and *m*-PYR+DEB compared with solution  $^{13}\text{C}$  NMR of *m*-Br-pyrylium monomer, (c) Me-PYR+TEB and Me-PYR+DEB compared with solution  $^{13}\text{C}$  NMR of

*m*-Br-*p*-Me-pyrylium monomer, (d) MeO-PYR+TEB and MeO-PYR+DEB compared with solution  $^{13}\text{C}$  NMR of *m*-Br-*p*-MeO-pyrylium monomer, (e) F-PYR+TEB and F-PYR+DEB compared with solution  $^{13}\text{C}$  NMR of *m*-Br-*p*-F-pyrylium monomer and (f) PYR CMP Oxidative compared with  $^{13}\text{C}$  NMR of biphenyl pyrylium monomer. (\* denotes spinning sideband)

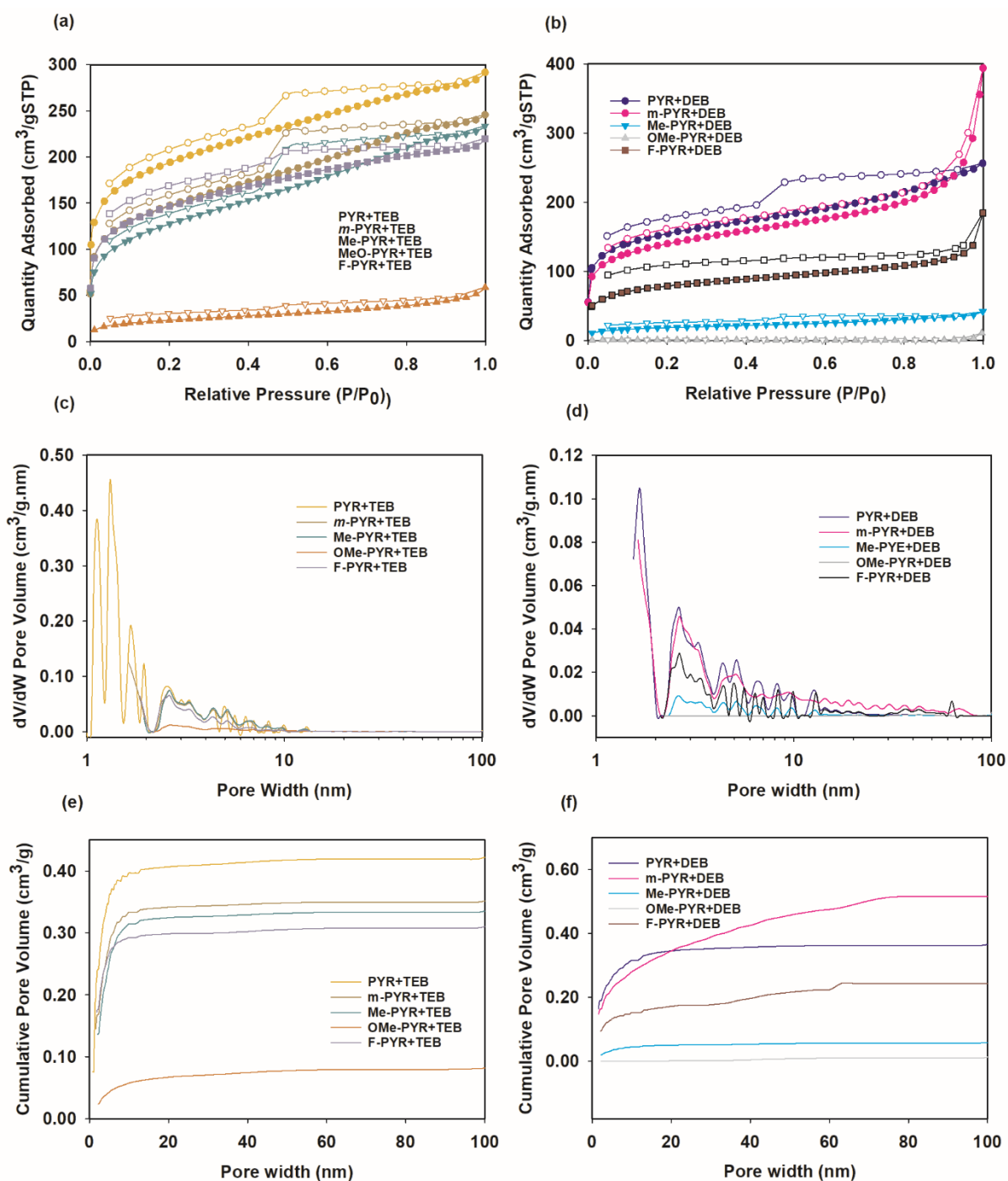
### 3.5.3 (d) Gas sorption isotherms

All pyrylium based CMPs were characterised by  $\text{N}_2$  gas adsorption and desorption method as shown in Figure 3.4. Pyr+TEB (Figure 3.4(a)) showed steep uptake at a low pressure indicating of Type I isotherm which is a characteristic of microporous materials with a high BET surface area of  $710 \text{ m}^2/\text{g}$  as shown in Table 3.2. Likewise, *m*-PYR+TEB, Me-PYR+TEB and F-PYR+TEB (Figure 3.4(a)) exhibited type I isotherms with BET surface areas from  $453\text{--}533 \text{ m}^2/\text{g}$ . The presence of hysteresis loops indicates that the materials contain mesopores. However, MeO-PYR+TEB (Figure 3.4(a)) does not show steep uptake at a low pressure indicating of no micropores with a low BET surface area of  $82 \text{ m}^2/\text{g}$ . The CMPs synthesised from DEB linker (Figure 3.4(b)) also show type I isotherm with hysteresis loops except MeO-, F- and Me-PYR+DEB, which exhibited no steep uptake at a low pressure.<sup>30,31</sup> The BET surface areas of PYR+DEB and *m*-PYR+DEB were between  $514$  and  $573 \text{ m}^2/\text{g}$  while MeO-, F- and Me-PYR+DEB showed BET surface areas from  $4$  to  $289 \text{ m}^2/\text{g}$ . The polymers derived from TEB showed higher surface areas than DEB as might be expected due to the higher connectivity and rigidity of the networks.<sup>2,32</sup> The CMPs obtained from *p*-Br-pyrylium monomer showed higher BET surface areas than those prepared from *m*-Br-pyrylium because of the lower dissociation energy of C-Br bonds leading to higher rate in oxidative addition step of Pd cycle in Sonogashira reaction. Generally, oxidative addition step can be promoted by electron withdrawing groups at

aryl halides, thus the substituted groups at *para* position (Me-, MeO- and F-) which are electron donating groups results in slower oxidative addition of aryl bromides with palladium catalyst leading to low surface area materials.<sup>29</sup> This is consistent with the <sup>13</sup>C MAS NMR that the substituted pyrylium CMPs illustrate unreacted C-Br and terminal alkyne peaks.

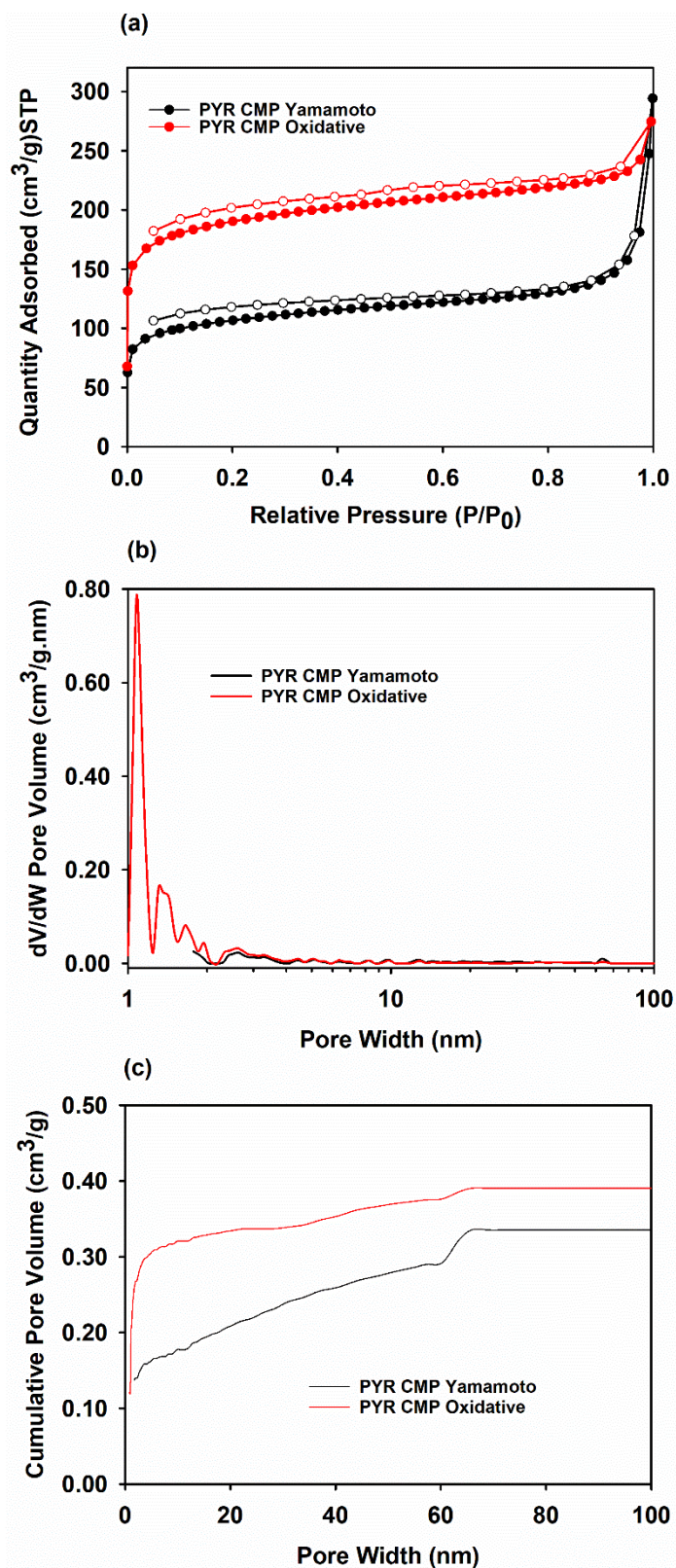
The pore size distribution of pyrylium CMPs are shown in Figure 3.4(c). All synthesised polymers obtained from TEB except for MeO-PYR+TEB exhibited main peaks at pore width less than 2 nm combined with broad peaks of mesopores from 2-10 nm, which is consistent with nitrogen gas sorption isotherms. PYR+DEB and *m*-PYR+DEB (Figure 3.4(d)) showed the main peaks at less than 2 nm confirming they were indeed microporous materials. Me- and F-PYR+DEB exhibited broad peaks in the mesopore region while the MeO-PYR+DEB illustrated no porosity, which is in agreement with the low gas uptake in nitrogen isotherms.

Figure 3.4(e) and (f) show cumulative pore volumes of the synthesised pyrylium CMPs. All TEB based polymers (Figure 3.4(e)) except for MeO-PYR+TEB exhibited high cumulative pore volumes at pore size less than 2 nm while only PYR+DEB and *m*-PYR+DEB in a DEB polymer series (Figure 3.5(f)) showed large cumulative pore volume at pore width less than 2 nm. The cumulative pore volume results were consistent with isotherms and pore size distribution results. The micropore volumes, total pore volumes, and the ratios of micropore volumes obtained from cumulative pore volumes are shown in Table 3.2 and the ratios of micropore volumes of the synthesised polymers were from 0 to 0.58.



**Figure 3.4** Nitrogen gas sorption isotherms of (a) pyrylium CMPs derived from TEB, (b) DEB, pore size distributions of (c) pyrylium CMPs derived from TEB and (d) DEB, cumulative pore volume of (e) pyrylium CMPs derived from TEB and (f) DEB synthesised *via* Sonogashira-Hagihara cross-coupling.

In addition, pyrylium based CMPs can be synthesised by various methods such as Yamamoto and oxidative couplings. Homocoupling of 2,4,6-tris(4-bromophenyl) pyrylium tetrafluoroborate *via* Yamamoto coupling gave a high surface area of 402 m<sup>2</sup>/g with type I isotherm and a hysteresis loop indicating of mixed micropores and mesopores ( $V_{\text{micro}}/V_{\text{total}} = 0.41$ ) as shown in Table 3.2 and Figure 3.5(a)-(b). Likewise, 2,4,6-tris(biphenyl) pyrylium tetrafluoroborate can be polymerised by oxidative coupling to form the pyrylium CMP with a high surface area of 721 m<sup>2</sup>/g. The material showed type I isotherm with a hysteresis loop (Figure 3.5(a)) confirming that the material possessed micropores and mesopores with 0.69 of ratio of micropore volume. Pyrylium CMP synthesised from oxidative coupling showed a main pore size at lower than 2 nm (Figure 3.5(b)) and higher cumulative pore volume contributing from mainly micropores, while the CMP obtained from Yamamoto coupling exhibited lower cumulative volume which mostly caused from mesopores and macropores as shown in Figure 3.5(c). It is worth to mention that 2,4,6-tris(4-biphenyl) pyrylium monomer gave a higher surface area material than 2,4,6-triphenyl pyrylium monomer which yielded a low surface area of 14 m<sup>2</sup>/g because the biphenyl pyrylium is more electron rich which is favour for oxidative coupling.<sup>14,15</sup> The results indicated that the pyrylium CMPs can be synthesised by various methods which gave different structures and porosities of the materials.



**Figure 3.5** (a) Nitrogen gas sorption isotherms, (b) pore size distributions and (c) cumulative pore volume of pyrylium CMPs synthesised *via* Yamamoto and oxidative couplings.

**Table 3.2** BET surface areas ( $S_{\text{BET}}$ ), micropore volumes, total pore volumes and ratio of micropores of the synthesised polymers and monomers.

Sample	$S_{\text{BET}}$ ( $\text{m}^2/\text{g}$ )	$V_{\text{micro}}$ ( $\text{cm}^3/\text{g}$ )	$V_{\text{total}}$ ( $\text{cm}^3/\text{g}$ )	$V_{\text{micro}}/V_{\text{total}}$
PYR+TEB	710 $\pm$ 1	0.24	0.42	0.57
PYE+DEB	573 $\pm$ 2	0.19	0.37	0.51
m-PYR+TEB	533 $\pm$ 2	0.17	0.35	0.49
m-PYR+DEB	514 $\pm$ 3	0.16	0.52	0.31
Me-PYR+TEB	453 $\pm$ 3	0.14	0.34	0.41
Me-PYR+DEB	67 $\pm$ 1	0.00	0.06	0.00
F-PYR+TEB	530 $\pm$ 0	0.18	0.31	0.58
F-PYR+DEB	289 $\pm$ 2	0.00	0.24	0.00
MeO-PYR+TEB	82 $\pm$ 2	0.00	0.08	0.00
MeO-PYR+DEB	4 $\pm$ 0	0.00	0.00	0.00
PYR CMP Yamamoto	402 $\pm$ 3	0.14	0.34	0.41
PYR CMP Oxidative	721 $\pm$ 0	0.27	0.39	0.69

### 3.5.3 (e) TGA of the synthesised polymers

The synthesised pyrylium CMPs were analysed by thermogravimetric analysis (TGA) to determine a thermal stability of the materials as illustrated in Figure 3.6. The obtained polymers were pyrolysed from 25 to 800 °C under nitrogen atmosphere and they exhibited high % weight residues at more than 60% indicating of a high thermal stability of the materials. The substituted groups such as F, Me and MeO contained polymers shows lower weight residues than the non-substituted ones due to the

degradation of the substituents. F-PYR CMPs seem to be the most stable substituted polymers following by Me-PYR and MeO-PYR CMPs, respectively. PYR CMP obtained from oxidative coupling showed higher thermal stability than that synthesised from Yamamoto coupling (Figure 3.6(c)). The TGA results are consistent with the BET surface areas indicating that the higher surface areas of polymers lead to higher thermal stability.

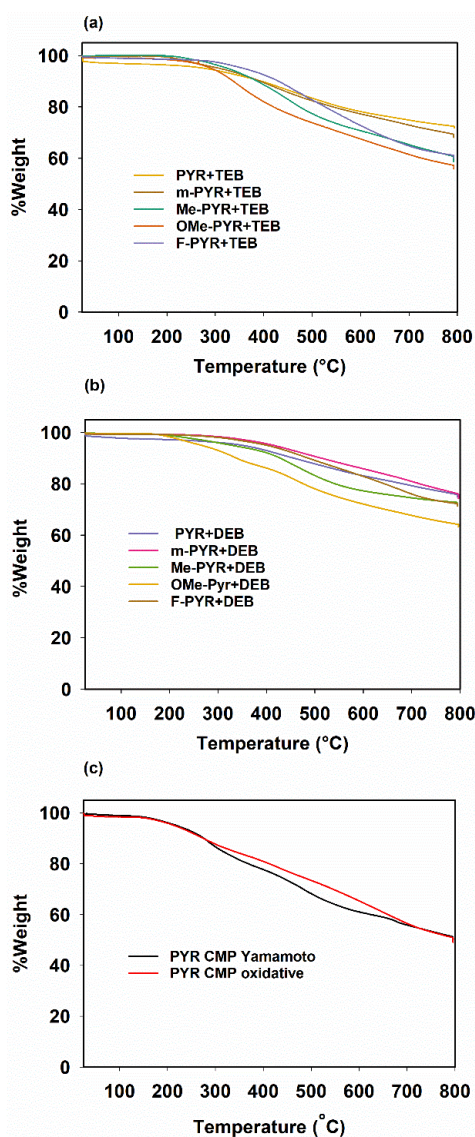


**Figure 3.6** Thermogravimetric analysis of (a) TEB, (b) DEB based pyrylium CMPs synthesised from Sonogashira reaction and (c) obtained from Yamamoto and oxidative couplings.

### 3.5.3 (f) UV-Vis spectrophotometry of the synthesised monomers and polymers

The obtained pyrylium monomers and pyrylium based CMPs have been characterised using UV-visible spectrophotometer. Pyrylium monomer exhibited 3 distinctive peaks which were a peak at ca. 274 nm relating to  $\pi$  to  $\pi^*$  from phenyl groups, ca. 354 nm corresponding to 4-phenylpyrylium chromophore and the broad peak centred at ca. 405 nm assigned to 2,6-diphenylpyrylium chromophore as shown in Figure 3.7(a).<sup>33</sup> *p*-Br-Pyrylium showed red shift to 421 nm while *m*-Br-Pyrylium displayed similar wavelength with pyrylium at 405 nm due to the less resonance at *meta* position. Likewise, *m*-Br-*p*-Me-pyrylium and *m*-Br-*p*-F show bathochromic shift to 418 and 413 nm, respectively when compared to *m*-Br-pyrylium. *m*-Br-*p*-MeO-pyrylium shows a large redshift to 455 nm due to the resonance effect of methoxy groups. Biphenyl pyrylium shows broader peaks and redshift compared with pyrylium due to the more conjugation. TEB and DEB (Figure 3.7(b)) exhibit peaks corresponding to  $\pi$  to  $\pi^*$  of benzene and alkyne at 232 and 270 nm, respectively. The higher wavelength of DEB causes by *para* substitution of alkyne rather than *meta* substitution of TEB.<sup>34</sup>

The solid state UV-Vis spectra of the synthesised polymers are shown in Figure 3.8 (a) and (b). The spectra of the pyrylium CMPs are broader and more red shifted compared to the monomers leading to lower band gap energies ( $E_g$ ) than the monomers because of the higher conjugation degree in the polymer networks which is normally observed in CMP network.<sup>35–38</sup>  $E_g$  of the monomers are calculated from the onset of the peaks while the  $E_g$  of the polymers are derived from Tauc plots as shown in Table 3.3 and Figure 3.9 (a) and (b). The pyrylium CMPs are suitable to use as a heterogeneous catalyst because they exhibit low band gaps which require lower activation energy to catalyse reactions as widely discussed in previous works.<sup>39–42</sup>

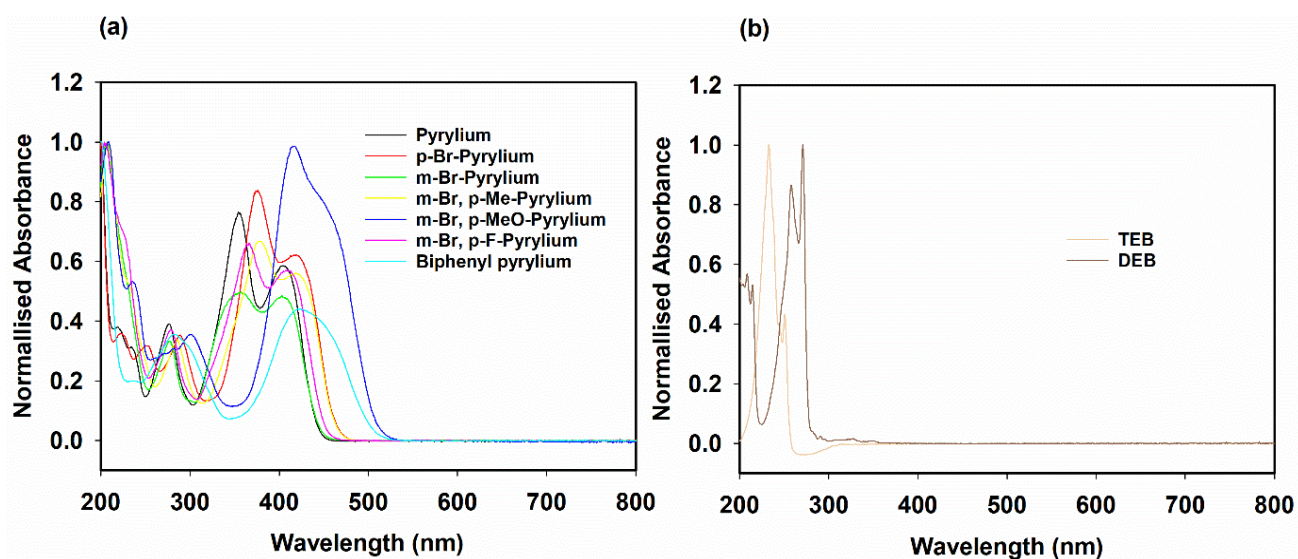


**Figure 3.7** UV-visible spectra of (a) the synthesised perylium monomers and (b) alkyne monomers in acetonitrile.

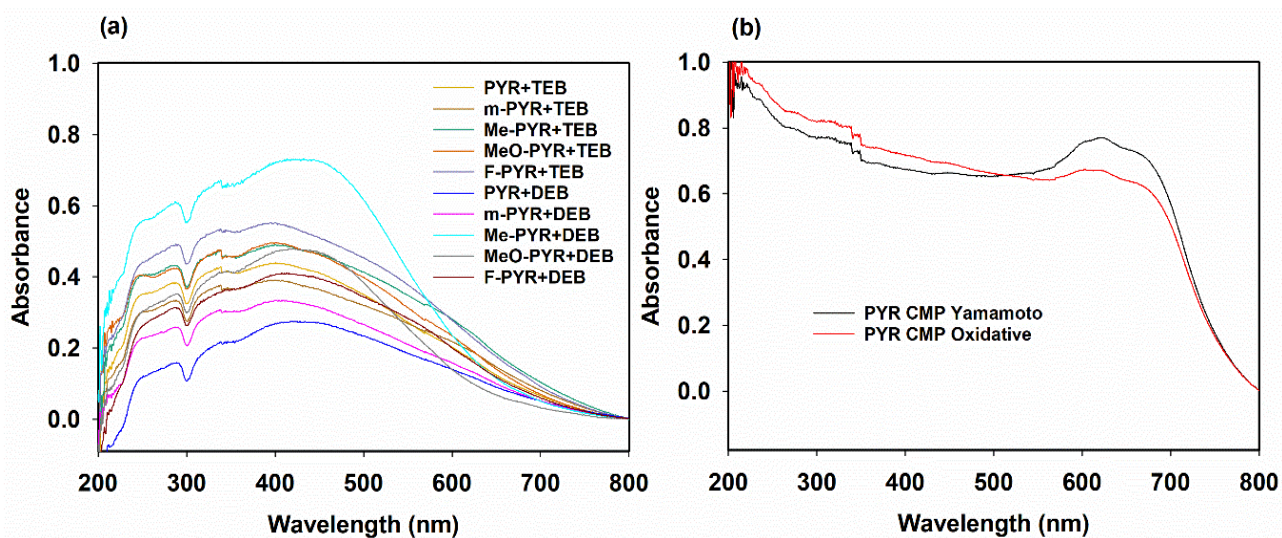


**Figure 3.8** Solid state UV-visible spectra of the perylium CMPs synthesised *via* (a) Sonogashira-Hagihara cross-coupling and (b) Yamamoto and oxidative couplings.

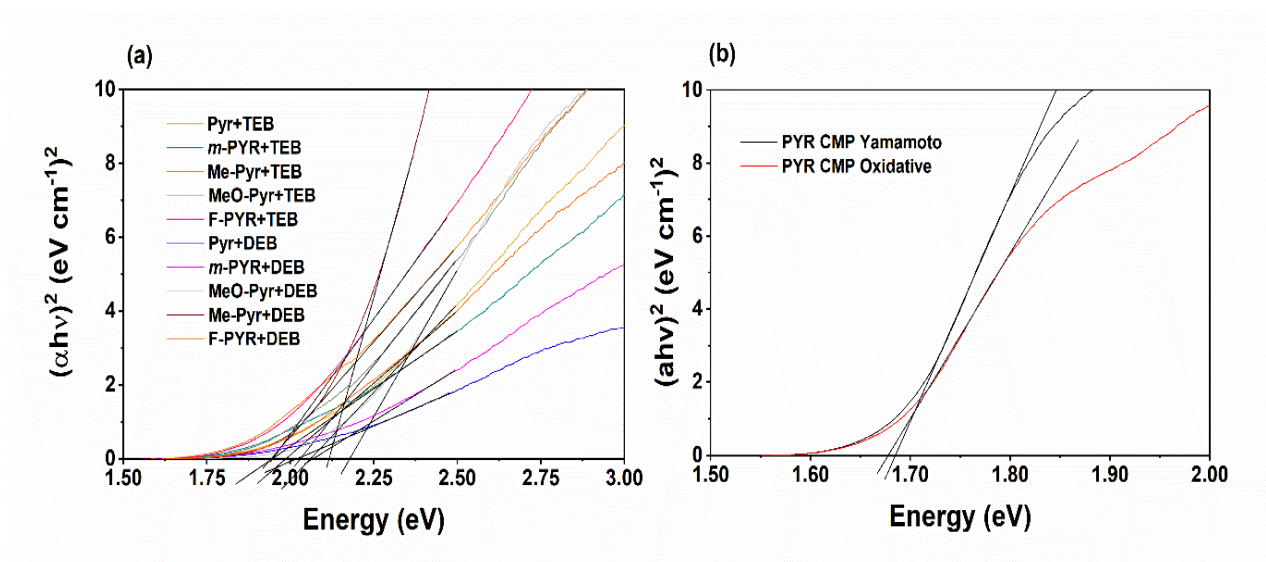


**Figure 3.9** Tauc plots of the pyrylium based polymers synthesised via (a) Sonogashira reaction and (b) Yamamoto and oxidative coupling reactions.

**Table 3.3** Bandgap energy ( $E_g$ ) of the synthesised monomers and polymers.

Sample	$E_g$ (eV)
PYR+TEB	2.06
PYE+DEB	2.02
m-PYR+TEB	1.95
m-PYR+DEB	2.07
Me-PYR+TEB	1.94
Me-PYR+DEB	2.12
F-PYR+TEB	1.95
F-PYR+DEB	1.99
MeO-PYR+TEB	2.03
MeO-PYR+DEB	2.18
PYR CMP Yamamoto	1.69
PYR CMP Oxidative	1.68
<i>p</i> -Br-pyrylium	2.67
<i>m</i> -Br-pyrylium	2.79
<i>m</i> -Br, <i>p</i> -Me-pyrylium	2.67
<i>m</i> -Br, <i>p</i> -MeO-pyrylium	2.44
<i>m</i> -Br, <i>p</i> -F-pyrylium	2.75
Biphenyl-pyrylium	2.46
TEB	4.99
DEB	4.45

### 3.6 Conclusions

The substituted 2,4,6-triphenyl pyrylium tetrafluoroborate monomers were successfully synthesised according to NMR, FTIR, EA and MS results. The obtained monomers were successfully polymerised to form CMP networks *via* Sonogashira, Yamamoto and oxidative coupling reactions confirming by FTIR and <sup>13</sup>C CP MAS NMR. The synthesised materials show high surface areas up to 721 m<sup>2</sup>/g with pore sizes in the range of micropores to mesopores. The surface area, pore size and volume can be controlled by tuning the structure of monomers and synthesis methods. The substituted networks with Me, MeO and F groups increase the steric hindrance and deactivation of arylbromide resulting in low surface areas. The synthesised polymers showed broad absorption spectra and low band gap energy due to the extended conjugation system in the CMP networks. Moreover, the synthesised CMPs showed a high thermal stability due to the strong covalent bonded networks. Due to the properties of the synthesised polymers, they could be used in many applications such as gas adsorption, energy storage and heterogeneous catalysis. In this work, pyrylium CMPs were used as a heterogeneous catalyst for oxidation of thioanisole as discussed in Chapter 4.

### 3.7 References

- 1 J. X. Jiang, Y. Li, X. Wu, J. Xiao, D. J. Adams and A. I. Cooper, *Macromolecules*, 2013, **46**, 8779–8783.
- 2 C. A. Wang, Y. W. Li, X. L. Cheng, J. P. Zhang and Y. F. Han, *RSC Adv.*, 2017, **7**, 408–414.
- 3 J. M. Tobin, J. Liu, H. Hayes, M. Demleitner, D. Ellis, V. Arrighi, Z. Xu and F. Vilela, *Polym. Chem.*, 2016, **7**, 6662–6670.
- 4 M. Liras, M. Iglesias and F. Sánchez, *Macromolecules*, 2016, **49**, 1666–1673.
- 5 M. Martiny, E. Steckhan and T. Esch, *Chem. Ber.*, 1993, **126**, 1671–1682.
- 6 N. J. Gesmundo and D. A. Nicewicz, *Beilstein J. Org. Chem.*, 2014, **10**, 1272–1281.
- 7 M. Riener and D. A. Nicewicz, *Chem. Sci.*, 2013, **4**, 2625–2629.
- 8 A. J. Perkowski, C. L. Cruz and D. A. Nicewicz, *J. Am. Chem. Soc.*, 2015, **137**, 15684–15687.
- 9 K. A. Ogawa, A. E. Goetz and A. J. Boydston, *J. Am. Chem. Soc.*, 2015, **137**, 1400–1403.
- 10 K. Wang, L. G. Meng and L. Wang, *Org. Lett.*, 2017, **19**, 1958–1961.
- 11 R. Chinchilla and C. Nájera, *Recent advances in Sonogashira reactions*, The Royal Society of Chemistry, 2011, vol. 40.
- 12 T. Ben and S. Qiu, *CrystEngComm*, 2013, **15**, 17–26.
- 13 T. Yamamoto, S. Wakabayashi and K. Osakada, *J. Organomet. Chem.*, 1992, **428**, 223–237.

- 14 M. Grzybowski, B. Sadowski, H. Butenschön and D. T. Gryko, *Angew. Chemie - Int. Ed.*, 2020, **59**, 2998–3027.
- 15 M. Grzybowski, K. Skonieczny, H. Butenschön, D. T. Gryko, H. Butenschön and D. T. Gryko, *Angew. Chemie Int. Ed.*, 2013, **52**, 9900–9930.
- 16 A. Laybourn, R. Dawson, R. Clowes, T. Hasell, A. I. Cooper, Y. Z. Khimyak and D. J. Adams, *Polym. Chem.*, 2014, **5**, 6325–6333.
- 17 R. Dawson, A. Laybourn, Y. Z. Khimyak, D. J. Adams and A. I. Cooper, *Macromolecules*, 2010, **43**, 8524–8530.
- 18 J. X. Jiang, F. Su, A. Trewin, C. D. Wood, H. Niu, J. T. A. Jones, Y. Z. Khimyak and A. I. Cooper, *J. Am. Chem. Soc.*, 2008, **130**, 7710–7720.
- 19 I. K. Spiliopoulos and J. A. Mikroyannidis, *Macromolecules*, 2002, **35**, 7254–7261.
- 20 A. M. A. M. Bello and L. P. Kotra, *Tetrahedron Lett.*, 2003, **44**, 9271–9274.
- 21 I. K. Spiliopoulos and J. A. Mikroyannidis, *J. Polym. Sci. Part A Polym. Chem.*, 2002, **40**, 682–693.
- 22 Y. Ma, Y. Pang, S. Chhabra, E. J. Reijerse, A. Schnegg, J. Niski, M. Leutzsch and J. Cornella, *Chem. - A Eur. J.*, 2020, **26**, 3738–3743.
- 23 A. Franconetti, R. Nuñez-Franco, G. de Gonzalo, J. Iglesias-Sigüenza, E. Álvarez and F. Cabrera-Escribano, *ChemPhysChem*, 2018, **19**, 327–334.
- 24 R. L. Hunt and B. S. Ault, *Spectrochim. Acta Part A Mol. Spectrosc.*, 1981, **37**, 63–69.
- 25 C. T. Fathimath Salfeena, Basavaraja, K. T. Ashitha, V. P. Kumar, S.

- Varughese, C. H. Suresh and B. S. Sasidhar, *Chem. Commun.*, 2018, **54**, 12463–12466.
- 26 S. Ren, R. Dawson, A. Laybourn, J. Jiang, Y. Khimyak, D. J. Adams and A. I. Cooper, *Polym. Chem.*, 2012, **3**, 928–934.
- 27 R. Dawson, A. Laybourn, R. Clowes, Y. Z. Khimyak, D. J. Adams and A. I. Cooper, *Macromolecules*, 2009, **42**, 8809–8816.
- 28 J. X. Jiang, F. Su, A. Trewin, C. D. Wood, N. L. Campbell, H. Niu, C. Dickinson, A. Y. Ganin, M. J. Rosseinsky, Y. Z. Khimyak and A. I. Cooper, *Angew. Chemie-International Ed.*, 2007, **46**, 8574–8578.
- 29 M. Schilz and H. Plenio, *J. Org. Chem.*, 2012, **77**, 2798–2807.
- 30 K. S. W. Sing, D. H. Everett, R. A. W. Haul, L. Moscou, R. A. Pierotti, J. Rouquerol and T. Siemieniowska, *Pure Appl. Chem.*, 1985, **57**, 603–619.
- 31 M. Thommes, K. Kaneko, A. V. Neimark, J. P. Olivier, F. Rodriguez-Reinoso, J. Rouquerol and K. S. W. Sing, *Pure Appl. Chem.*, 2015, **87**, 1051–1069.
- 32 X. Yu, Z. Yang, B. Qiu, S. Guo, P. Yang, B. Yu, H. Zhang, Y. Zhao, X. Yang, B. Han and Z. Liu, *Angew. Chemie Int. Ed.*, 2019, **58**, 632–636.
- 33 M. A. Miranda and H. Garcia, *Triphenylpyrylium Tetrafluoroborate as an Electron-Transfer Photosensitizer*, 1994, vol. 94.
- 34 A. Loibl, W. Oschmann, M. Vogler, E. A. Pidko, M. Weber, J. Wiecko and C. Müller, *Dalt. Trans.*, 2018, **47**, 9355–9366.
- 35 J.-X. X. Jiang, A. Trewin, D. J. Adams and A. I. Cooper, *Chem. Sci.*, 2011, **2**, 1777–1781.

- 36 C. P. Sen, R. G. Shrestha, L. K. Shrestha, K. Ariga and S. Valiyaveetil, *Chem. - A Eur. J.*, 2015, **21**, 17344–17354.
- 37 J. Byun and K. A. I. Zhang, *Mater. Horizons*, 2020, 7, 15–31.
- 38 Y. Xu, N. Mao, S. Feng, C. Zhang, F. Wang, Y. Chen, J. Zeng and J.-X. Jiang, *Macromol. Chem. Phys.*, 2017, **218**, 1700049.
- 39 S. Yang and H. Lee, *Nanoscale Res. Lett.*, 2017, **12**, 582.
- 40 M. A. Johar, R. A. Afzal, A. A. Alazba and U. Manzoor, *Adv. Mater. Sci. Eng.*, , DOI:10.1155/2015/934587.
- 41 H. Yan, X. Wang, M. Yao and X. Yao, *Prog. Nat. Sci. Mater. Int.*, 2013, **23**, 402–407.
- 42 A. Getsoian, Z. Zhai and A. T. Bell, *J. Am. Chem. Soc.*, 2014, **136**, 13684–13697.

### 3.8 Appendices

#### 3.8.1 FTIR spectra of alkyne monomers

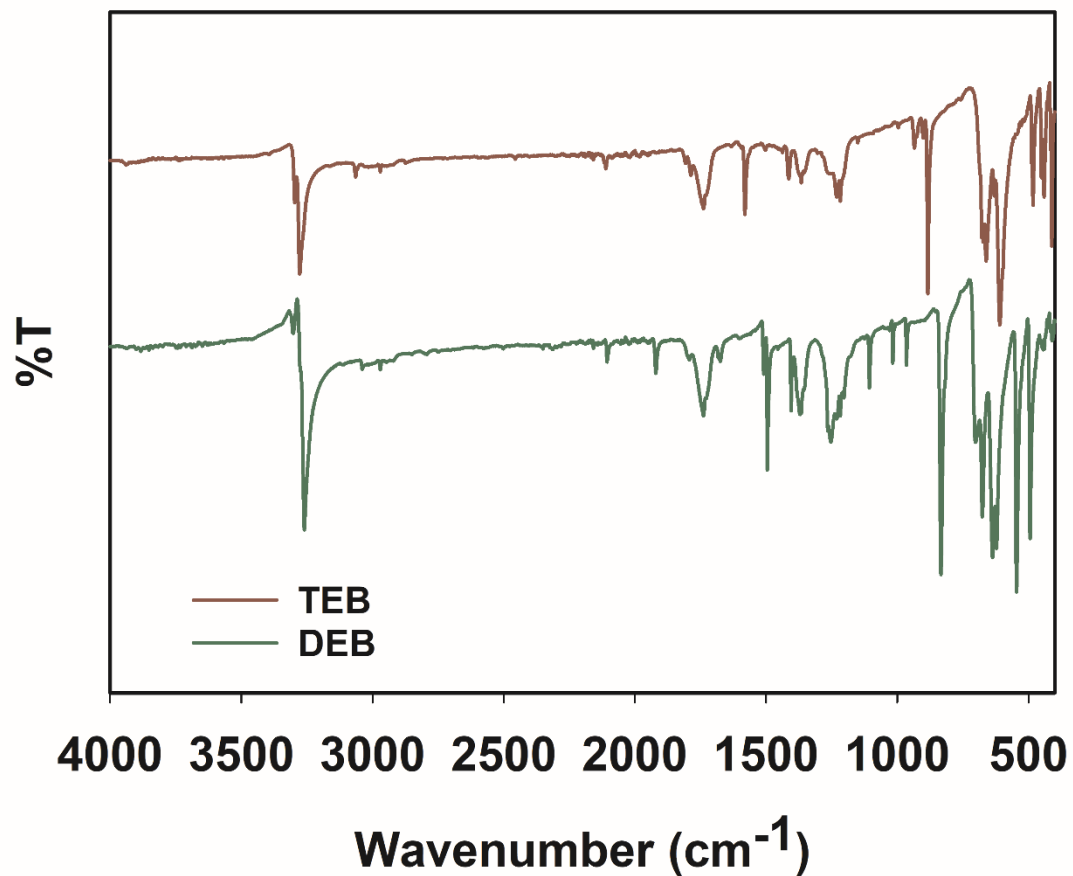
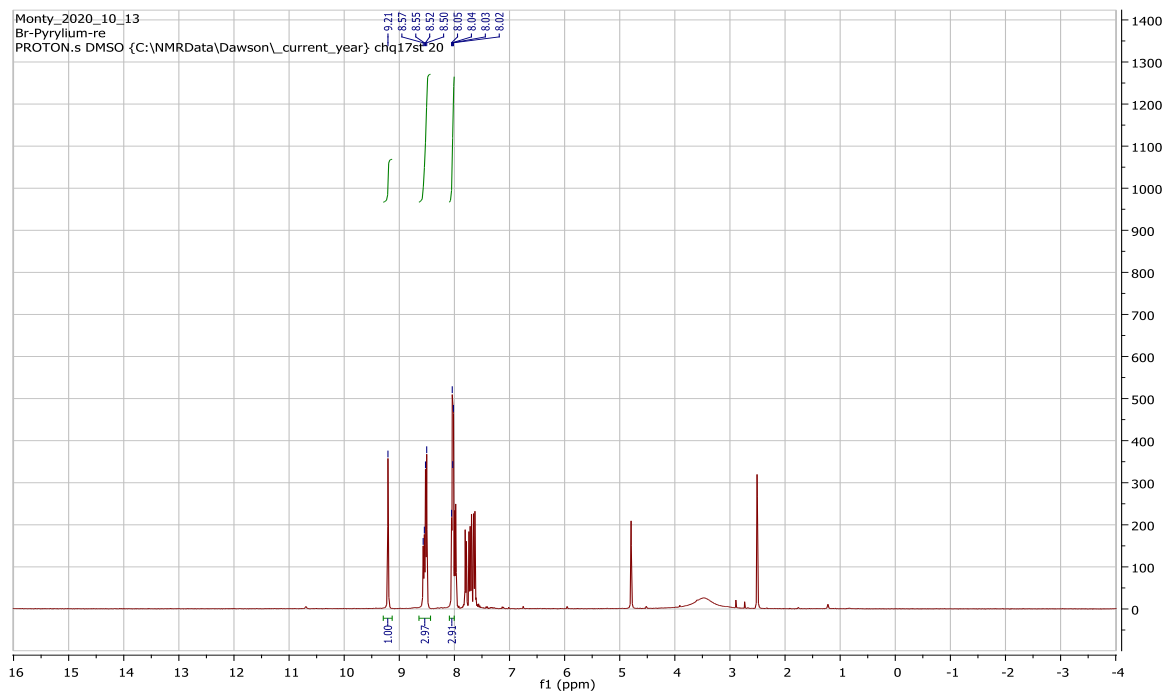
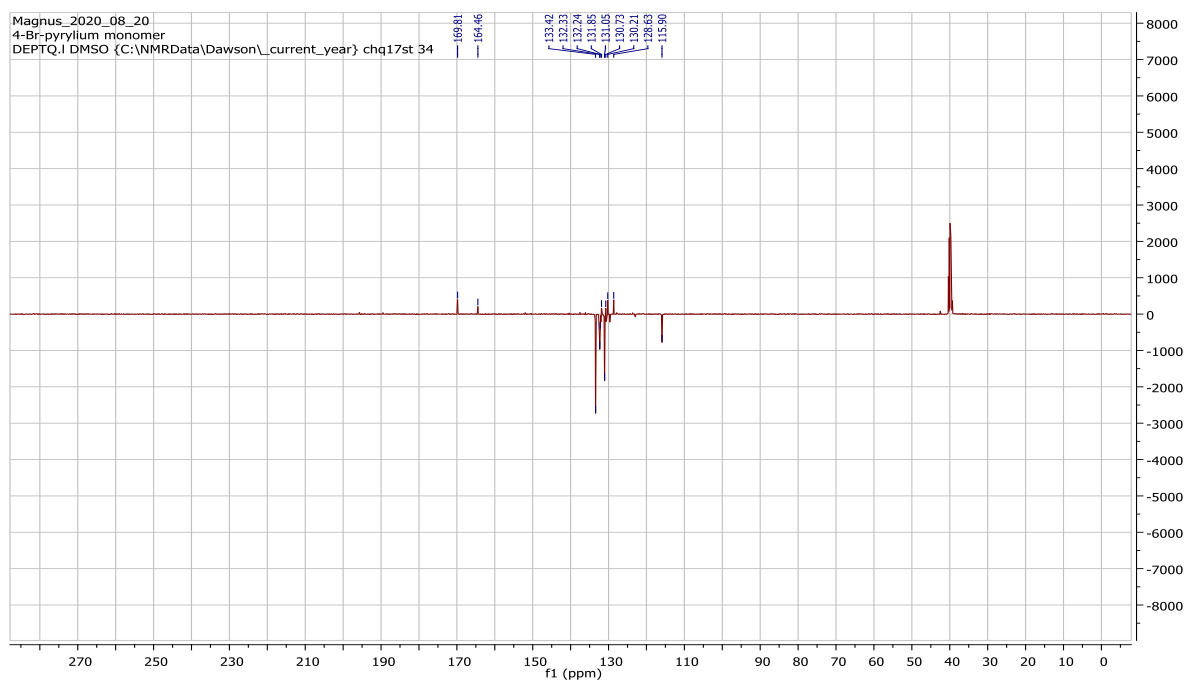


Figure A3.1 FTIR spectra of alkyne monomers.

## 3.8.2 NMR spectra of the synthesised pyrylium monomers



**Figure A3.2**  $^1\text{H}$  NMR spectrum of 2,4,6-tris(4-bromophenyl) pyrylium tetrafluoroborate.



**Figure A3.3**  $^{13}\text{C}$  NMR spectrum of 2,4,6-tris(4-bromophenyl) pyrylium tetrafluoroborate.

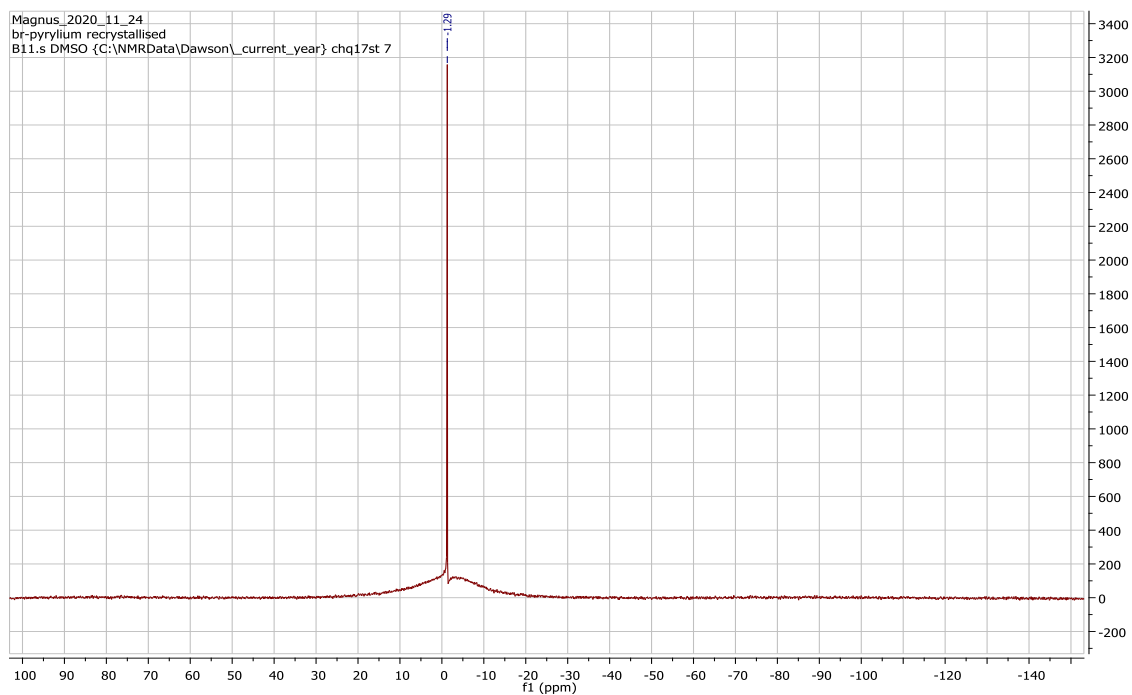


**Figure A3.4**  $^{11}\text{B}$  NMR spectrum of 2,4,6-tris(4-bromophenyl) pyrylium tetrafluoroborate.

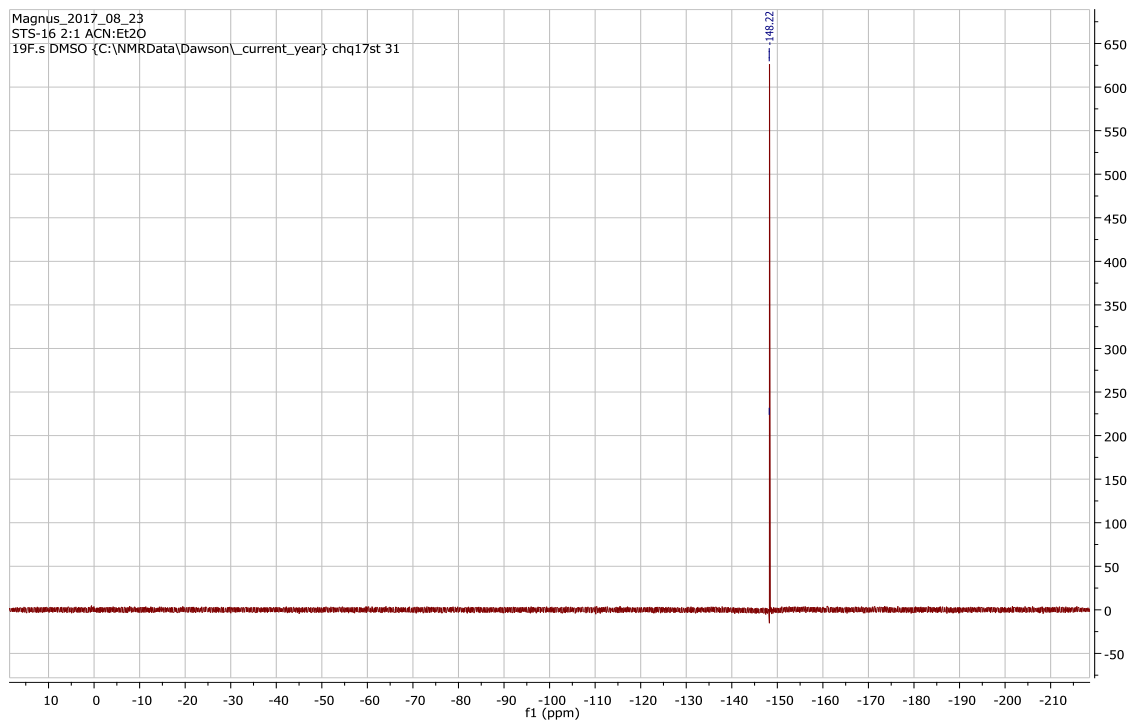


**Figure A3.5**  $^{19}\text{F}$  NMR spectrum of 2,4,6-tris(4-bromophenyl) pyrylium tetrafluoroborate.

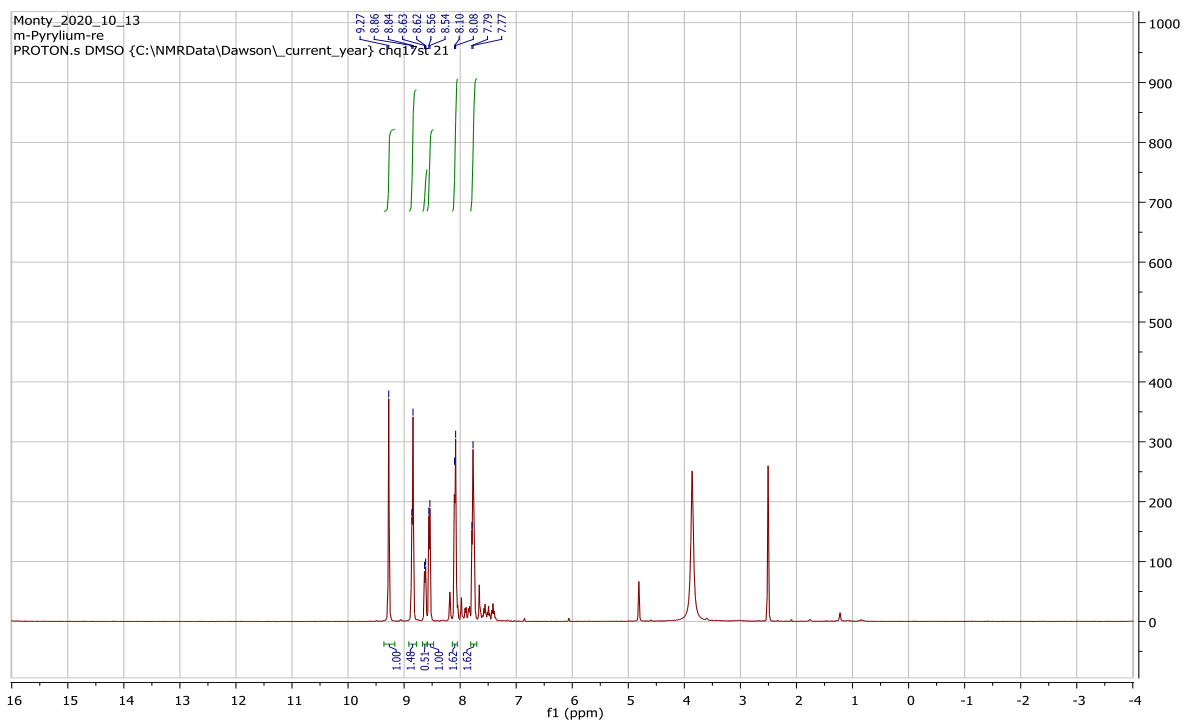


**Figure A3.6**  $^1\text{H}$  NMR spectrum of 2,4,6-tris(3-bromophenyl) pyrylium tetrafluoroborate.

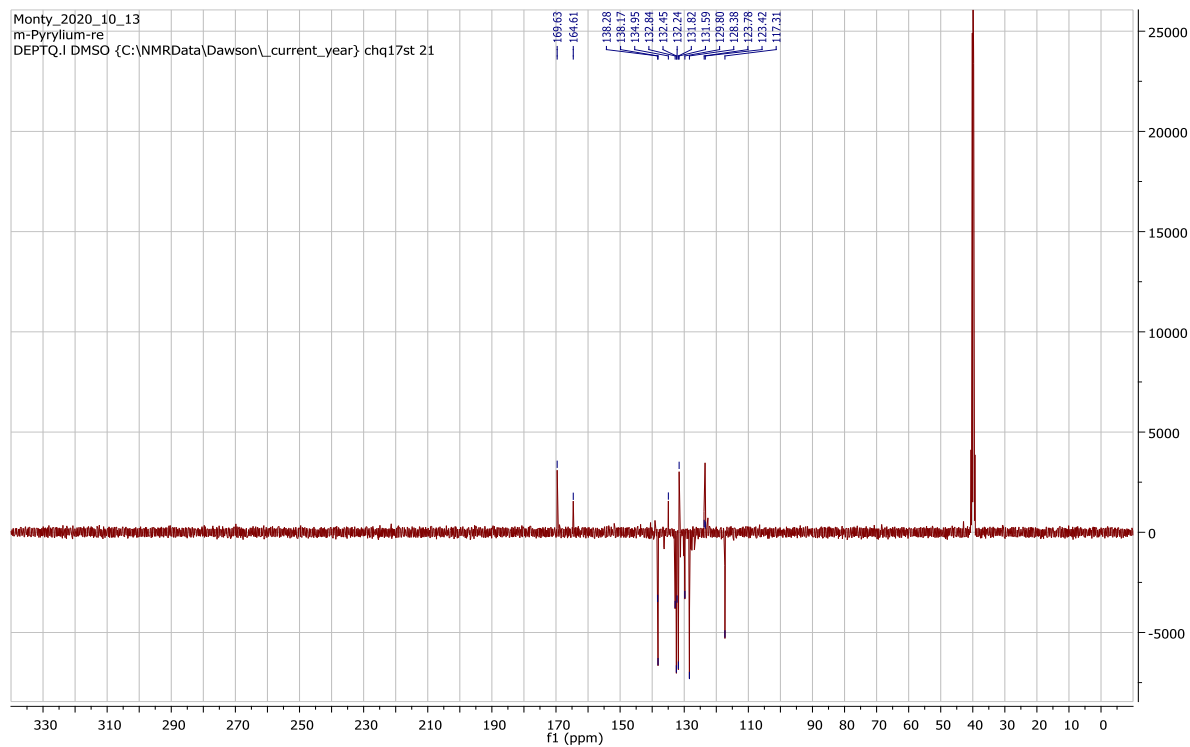


**Figure A3.7**  $^{13}\text{C}$  NMR spectrum of 2,4,6-tris(3-bromophenyl) pyrylium tetrafluoroborate.

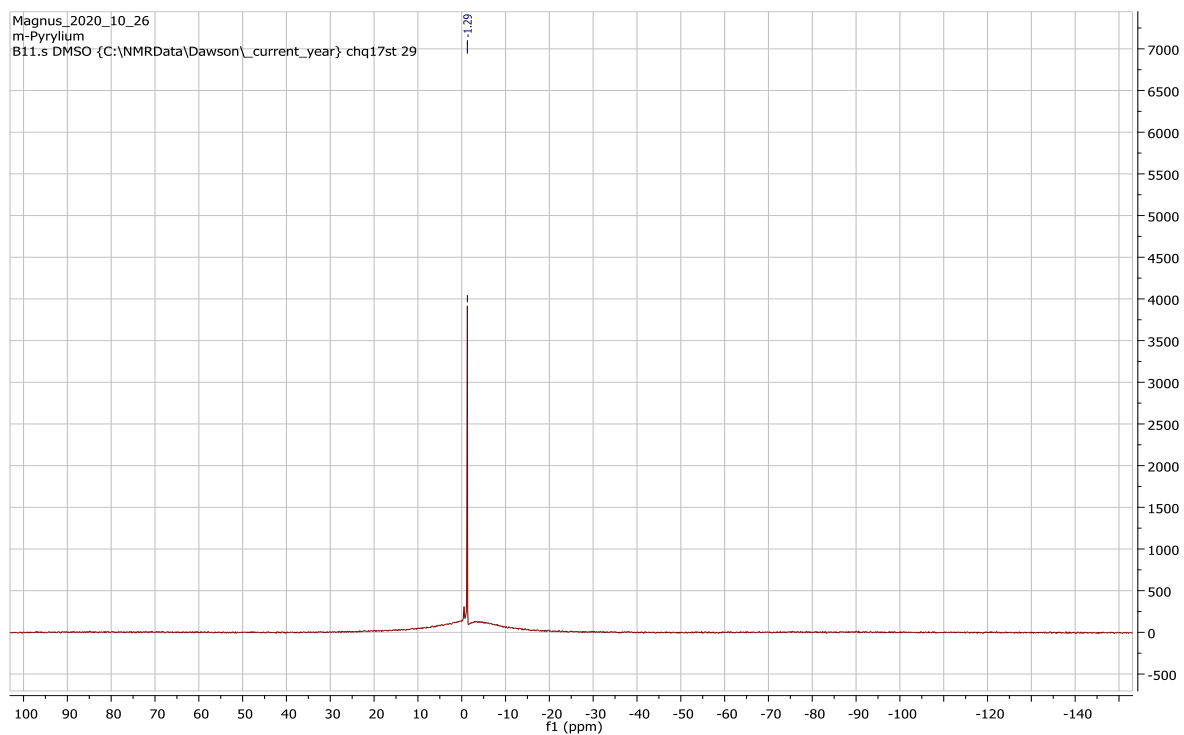


**Figure A3.8**  $^{11}\text{B}$  NMR spectrum of 2,4,6-tris(3-bromophenyl) pyrylium tetrafluoroborate.

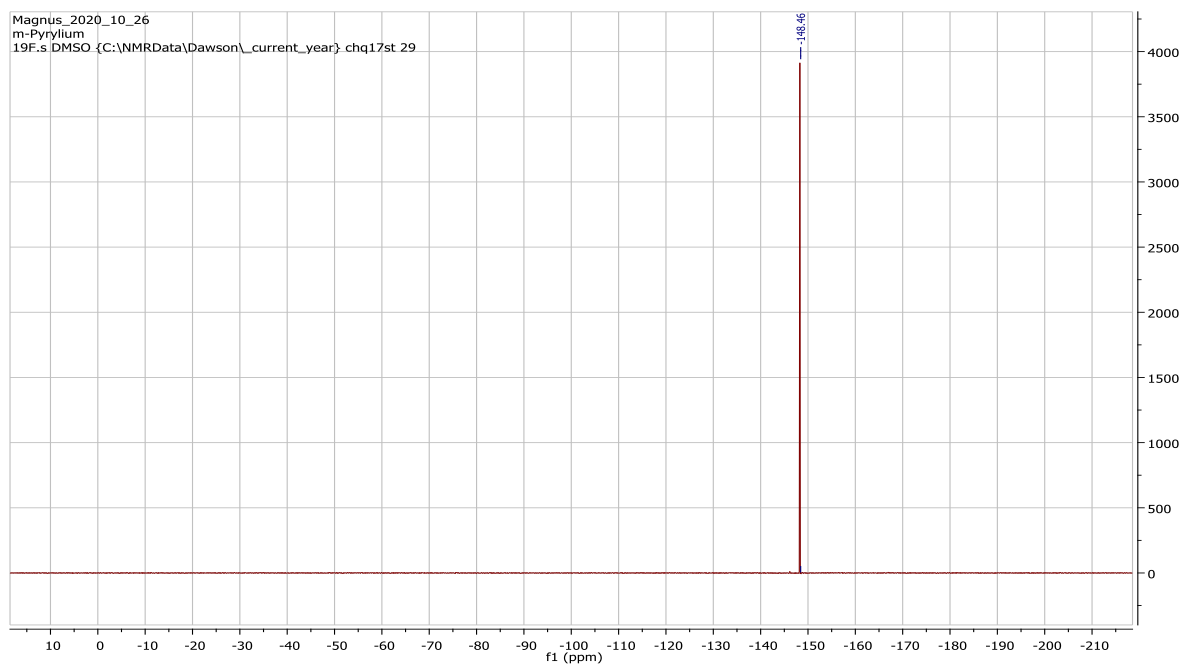


**Figure A3.9**  $^{19}\text{F}$  NMR spectrum of 2,4,6-tris(3-bromophenyl) pyrylium tetrafluoroborate.

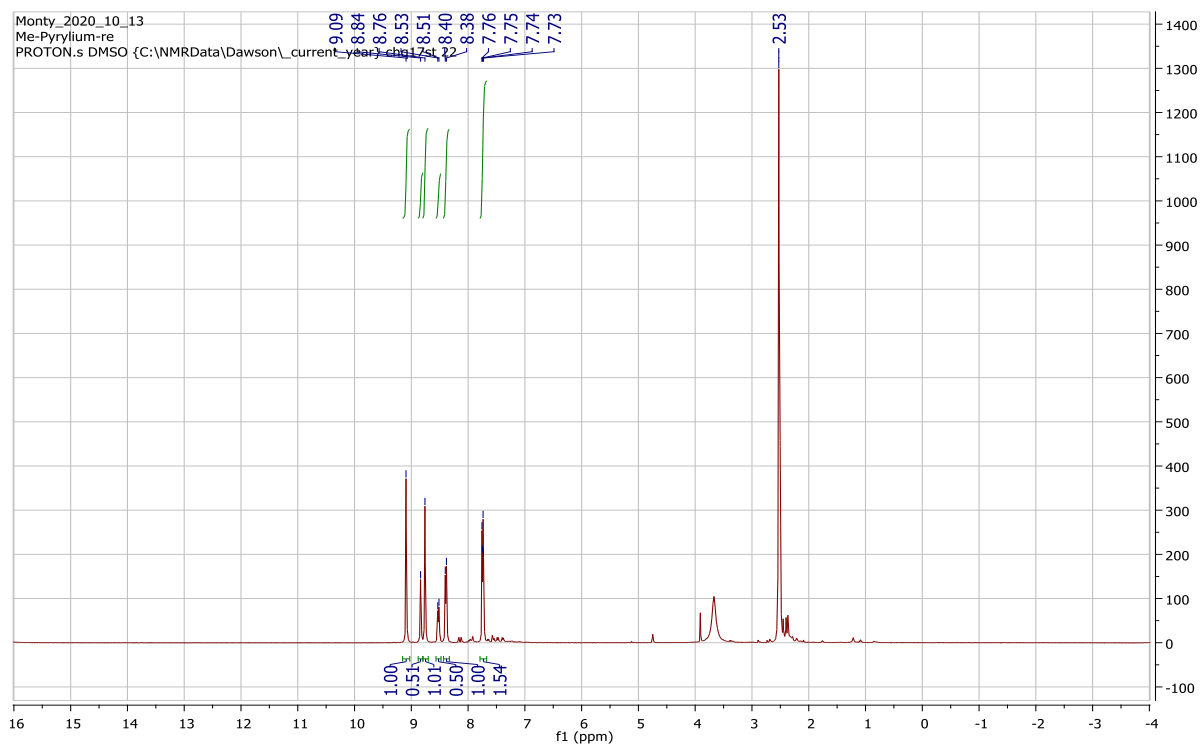


**Figure A3.10**  $^1\text{H}$  NMR spectrum of 2,4,6-tris(3-bromo, 4-methylphenyl) pyrylium tetrafluoroborate.

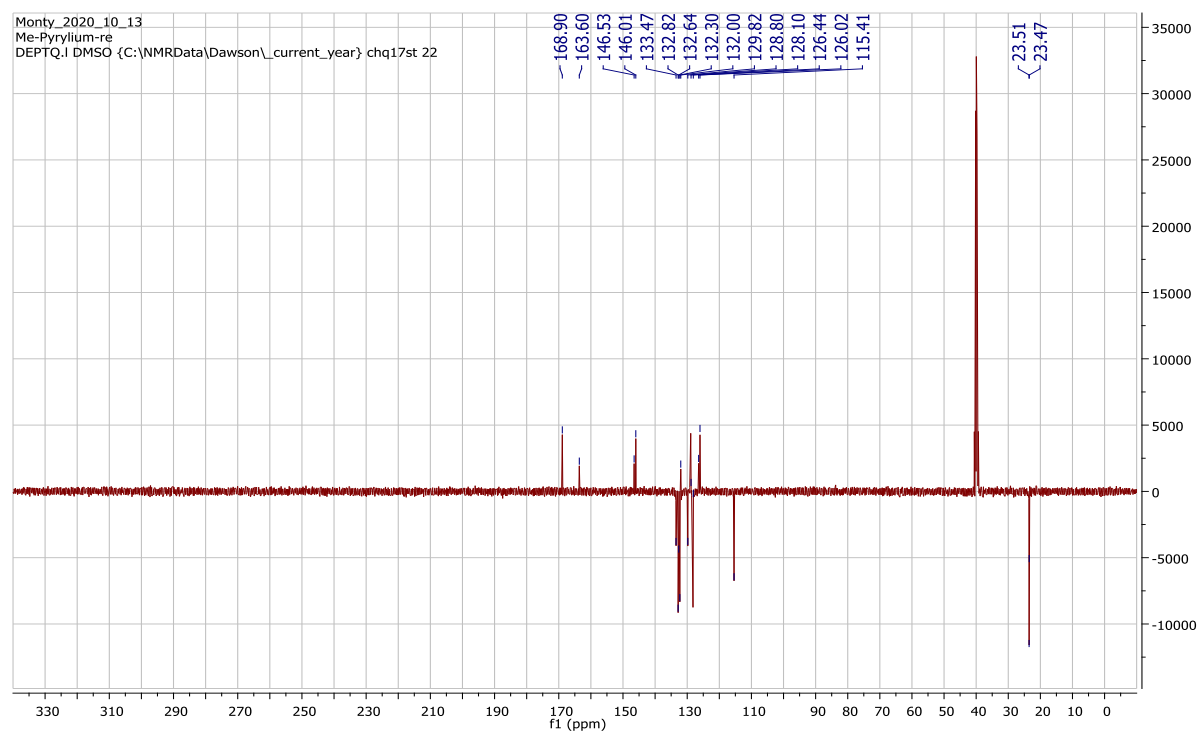


**Figure A3.11**  $^{13}\text{C}$  NMR spectrum of 2,4,6-tris(3-bromo, 4-methylphenyl) pyrylium tetrafluoroborate.

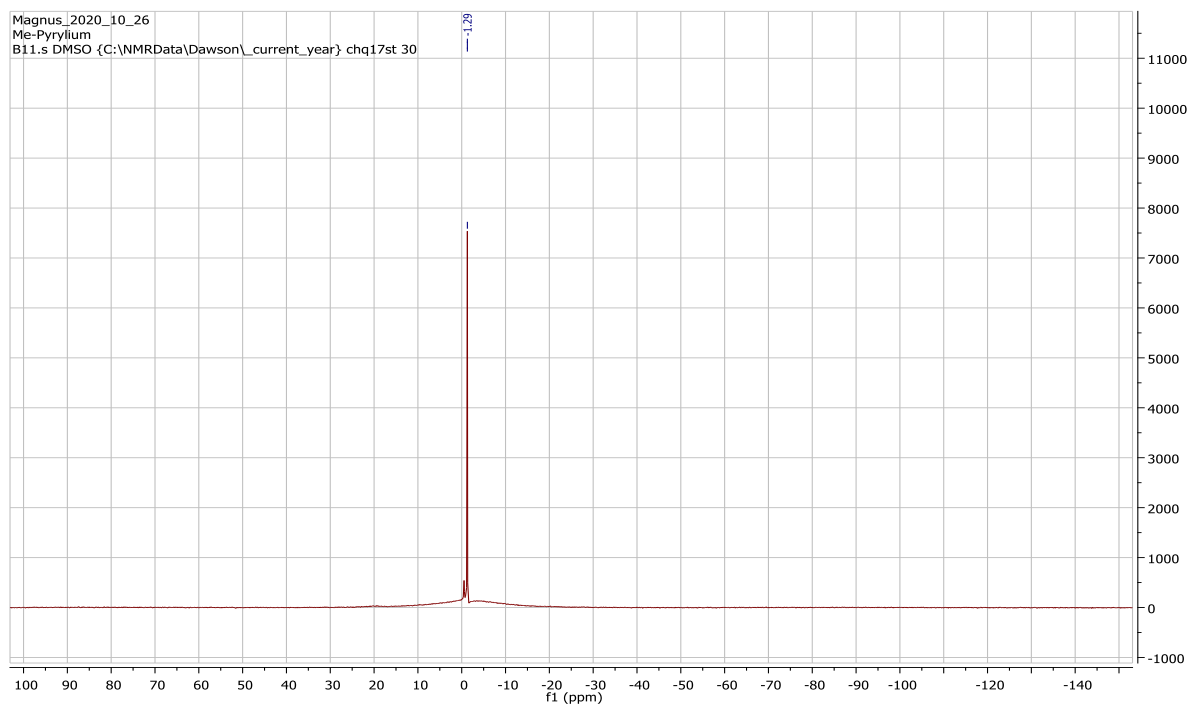


**Figure A3.12**  $^{11}\text{B}$  NMR spectrum of 2,4,6-tris(3-bromo, 4-methylphenyl) pyrylium tetrafluoroborate.

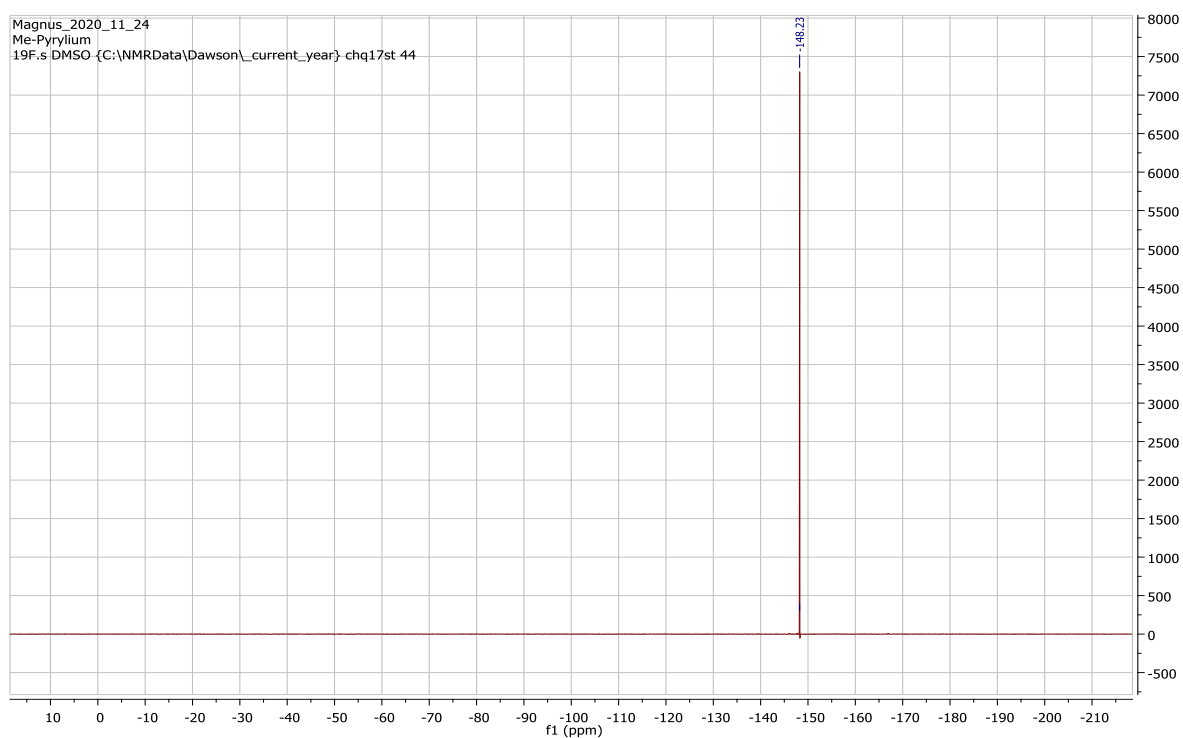


**Figure A3.13**  $^{19}\text{F}$  NMR spectrum of 2,4,6-tris(3-bromo, 4-methylphenyl) pyrylium tetrafluoroborate.

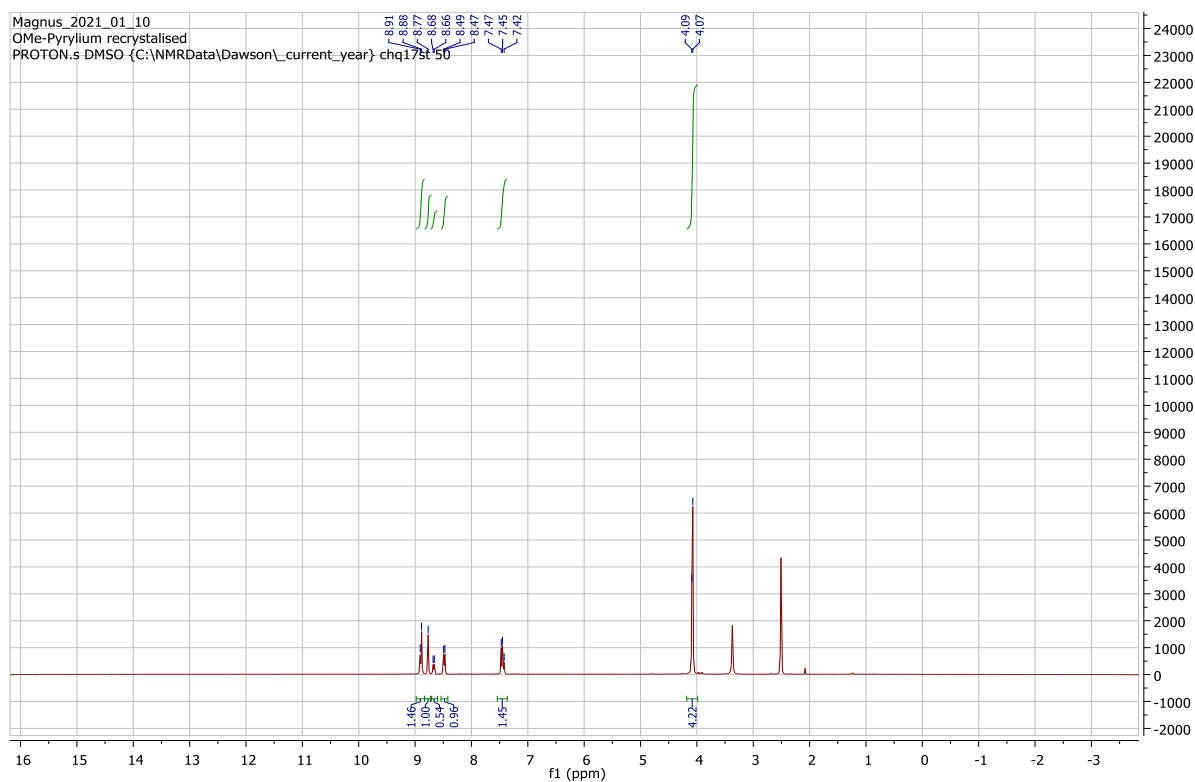


**Figure A3.14**  $^1\text{H}$  NMR spectrum of 2,4,6-tris(3-bromo, 4-methoxyphenyl) pyrylium tetrafluoroborate.

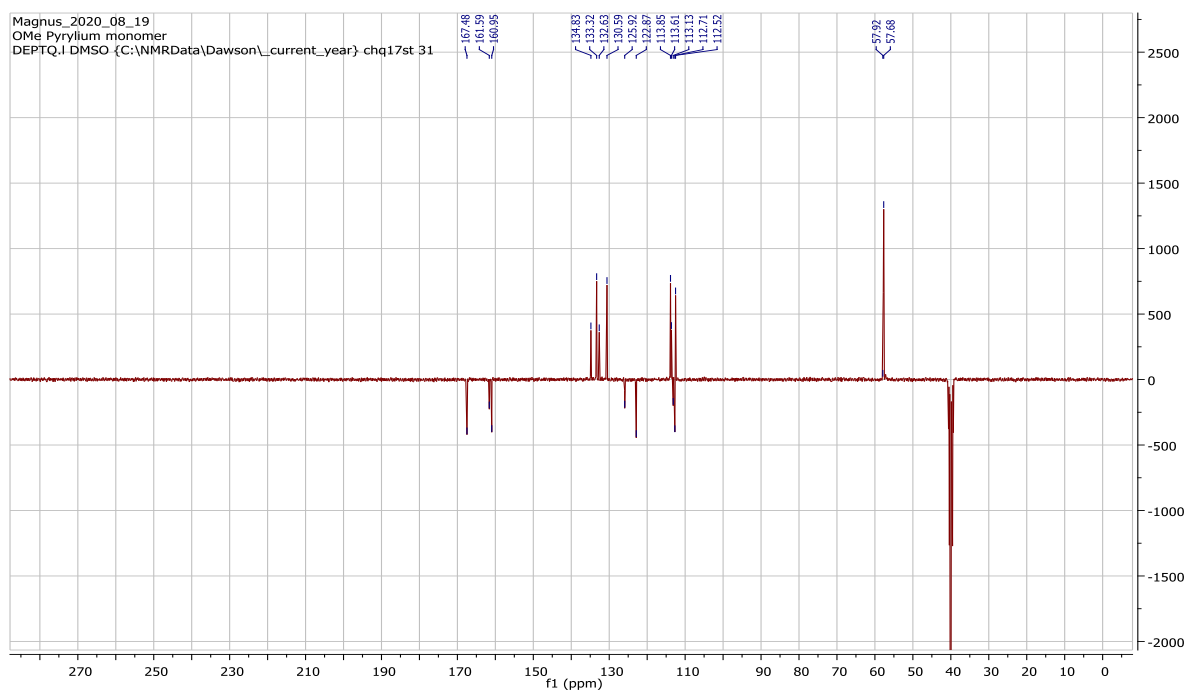


**Figure A3.15**  $^{13}\text{C}$  NMR spectrum of 2,4,6-tris(3-bromo, 4-methoxyphenyl) pyrylium tetrafluoroborate.

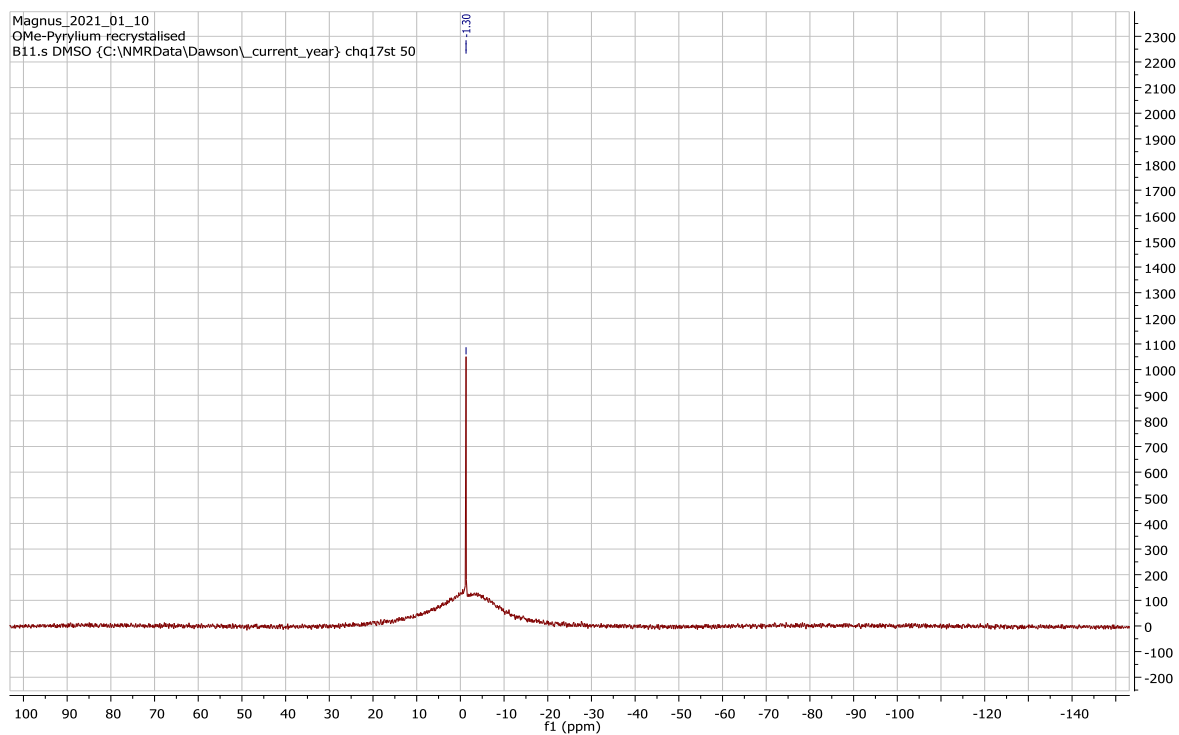


**Figure A3.16**  $^{11}\text{B}$  NMR spectrum of 2,4,6-tris(3-bromo, 4-methoxyphenyl) pyrylium tetrafluoroborate.

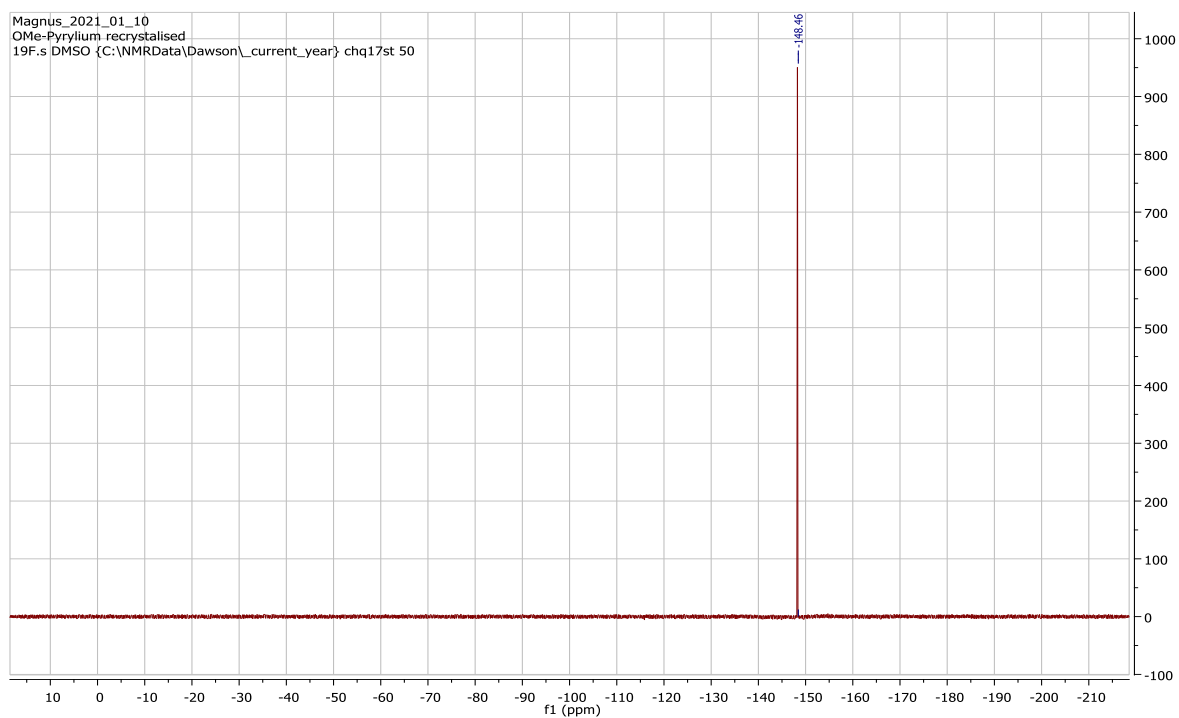


**Figure A3.17**  $^{19}\text{F}$  NMR spectrum of 2,4,6-tris(3-bromo, 4-methoxyphenyl) pyrylium tetrafluoroborate.

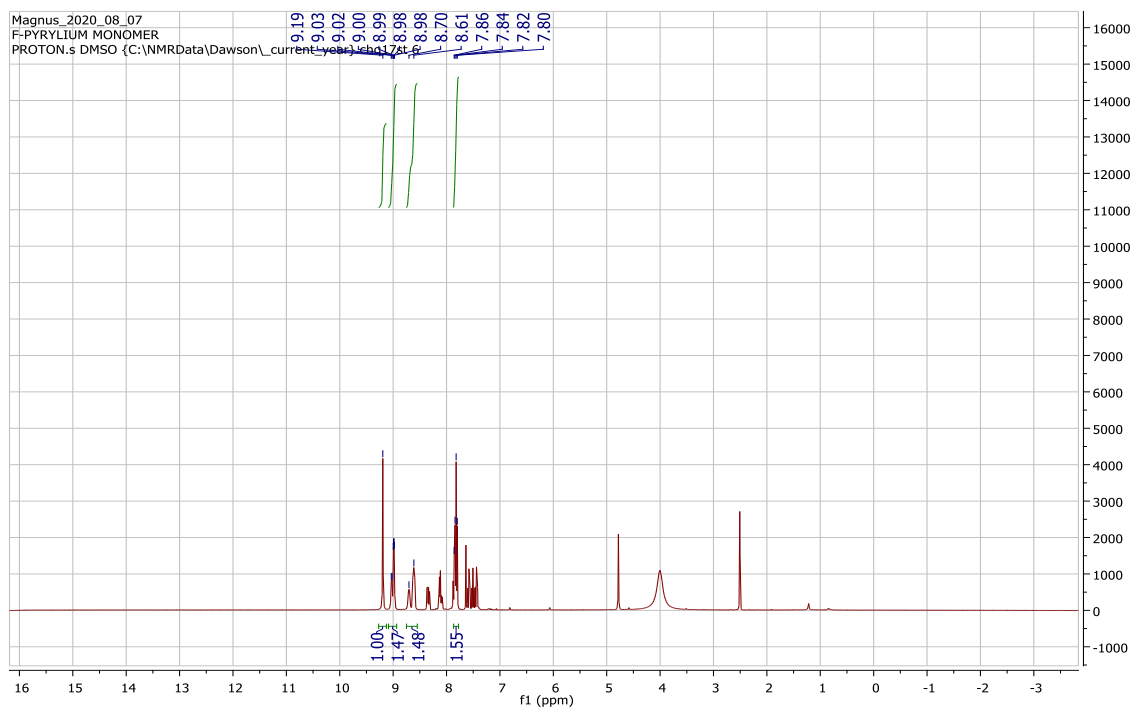


**Figure A3.18**  $^1\text{H}$  NMR spectrum of 2,4,6-tris(3-bromo, 4-fluorophenyl) pyrylium tetrafluoroborate.

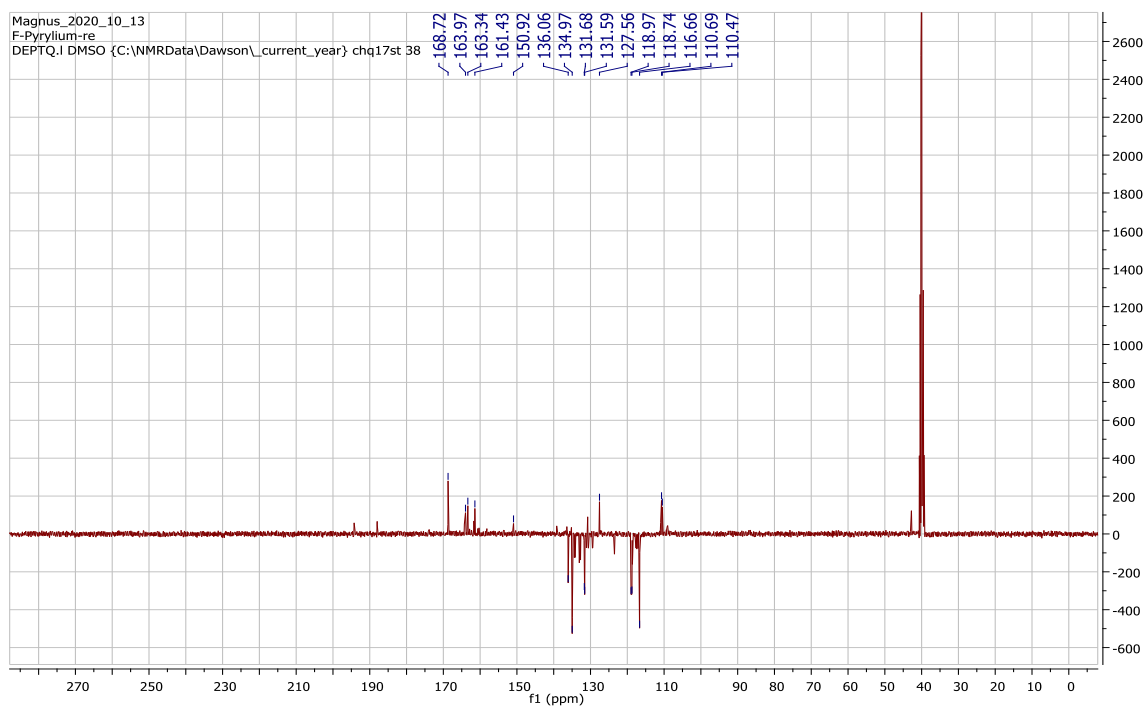


**Figure A3.19**  $^{13}\text{C}$  NMR spectrum of 2,4,6-tris(3-bromo, 4-fluorophenyl) pyrylium tetrafluoroborate.

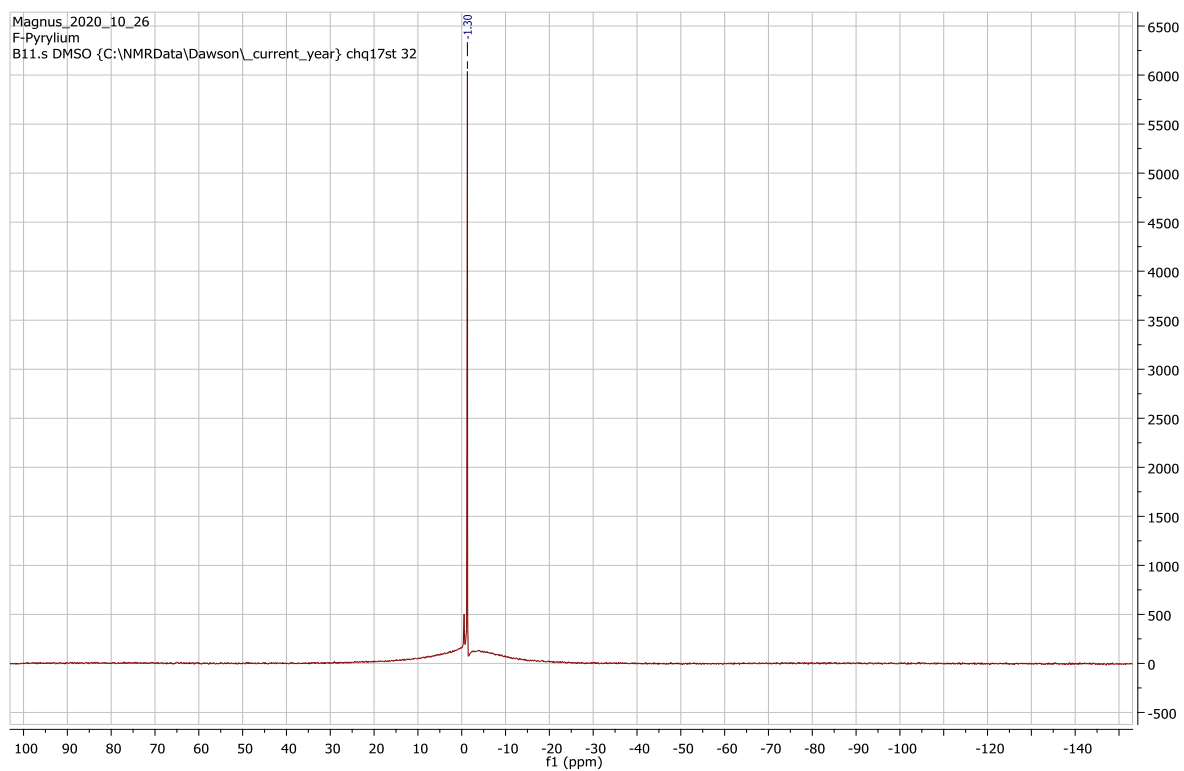


**Figure A3.20**  $^{11}\text{B}$  NMR spectrum of 2,4,6-tris(3-bromo, 4-fluorophenyl) pyrylium tetrafluoroborate.

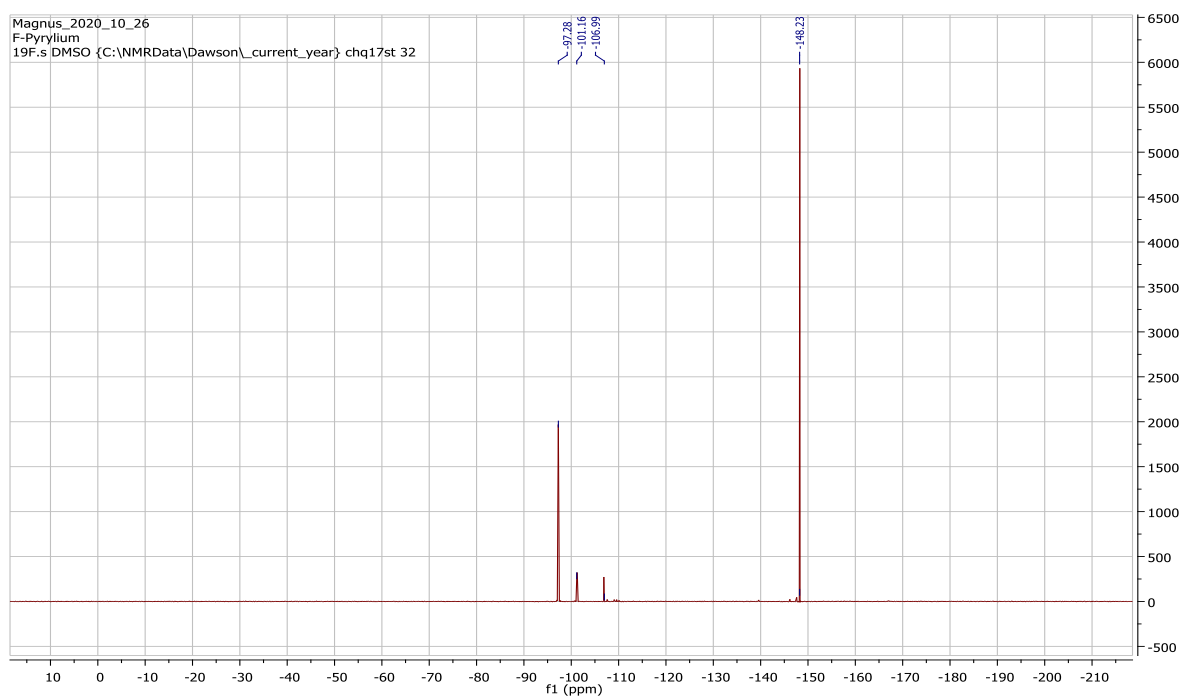


**Figure A3.21**  $^{19}\text{F}$  NMR spectrum of 2,4,6-tris(3-bromo, 4-fluorophenyl) pyrylium tetrafluoroborate.

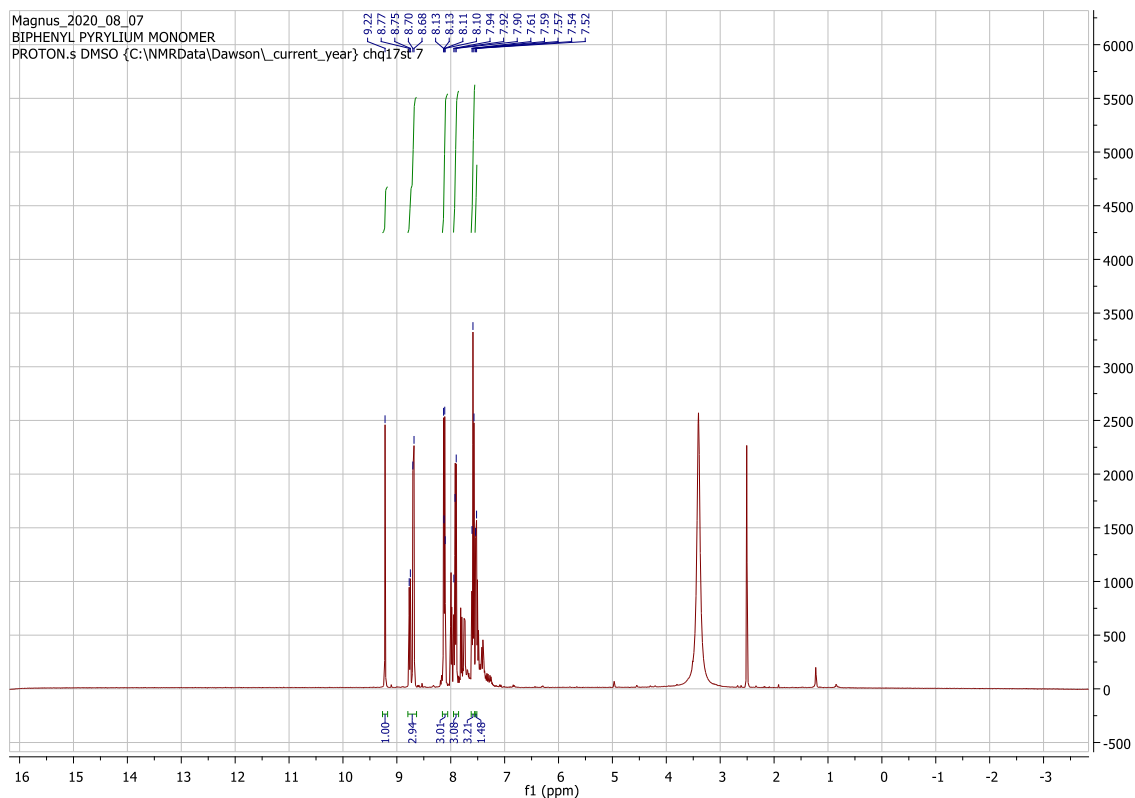


**Figure A3.22**  $^1\text{H}$  NMR spectrum of 2,4,6-tris(biphenyl) pyrylium tetrafluoroborate.

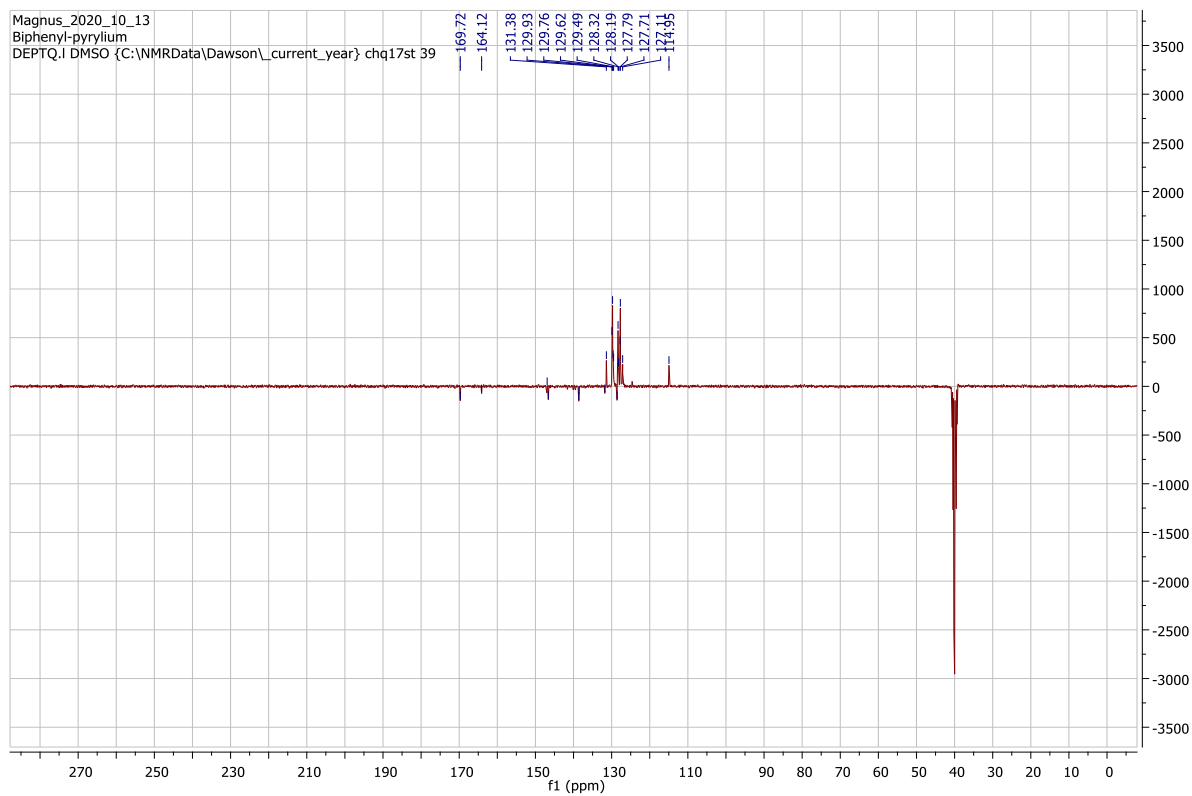


**Figure A3.23**  $^{13}\text{C}$  NMR spectrum of 2,4,6-tris(biphenyl) pyrylium tetrafluoroborate.

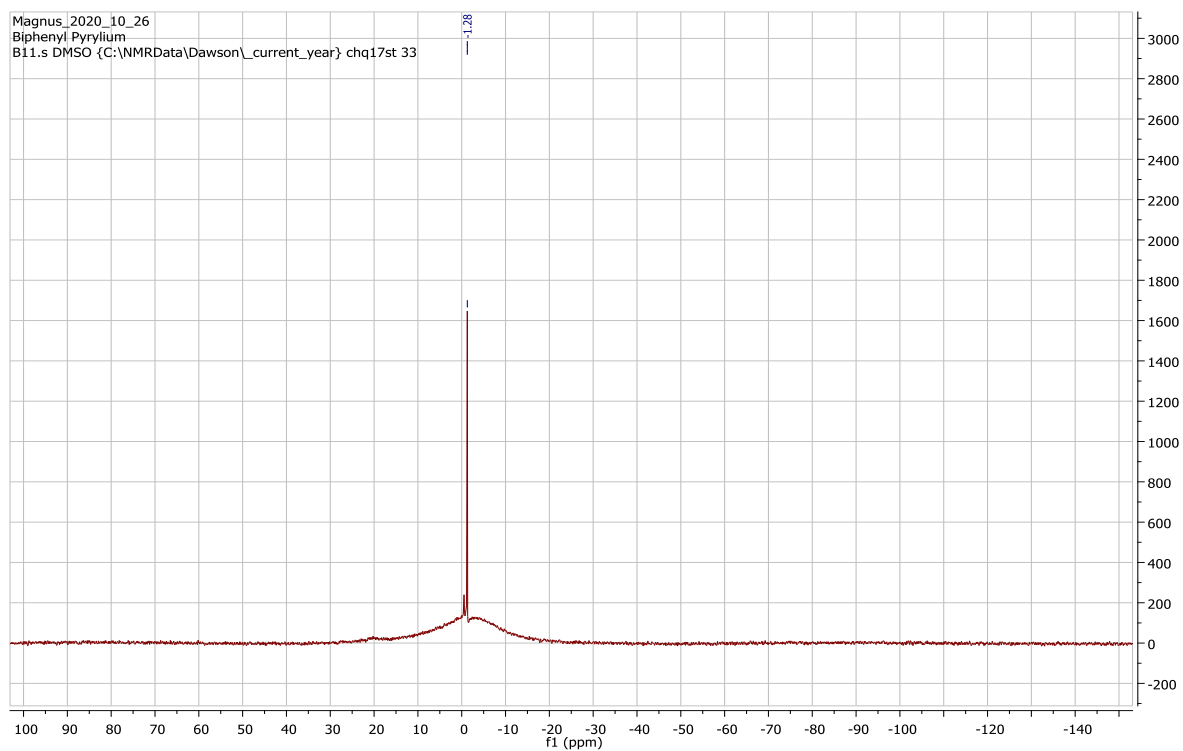


**Figure A3.24**  $^{11}\text{B}$  NMR spectrum of 2,4,6-tris(biphenyl) pyrylium tetrafluoroborate.

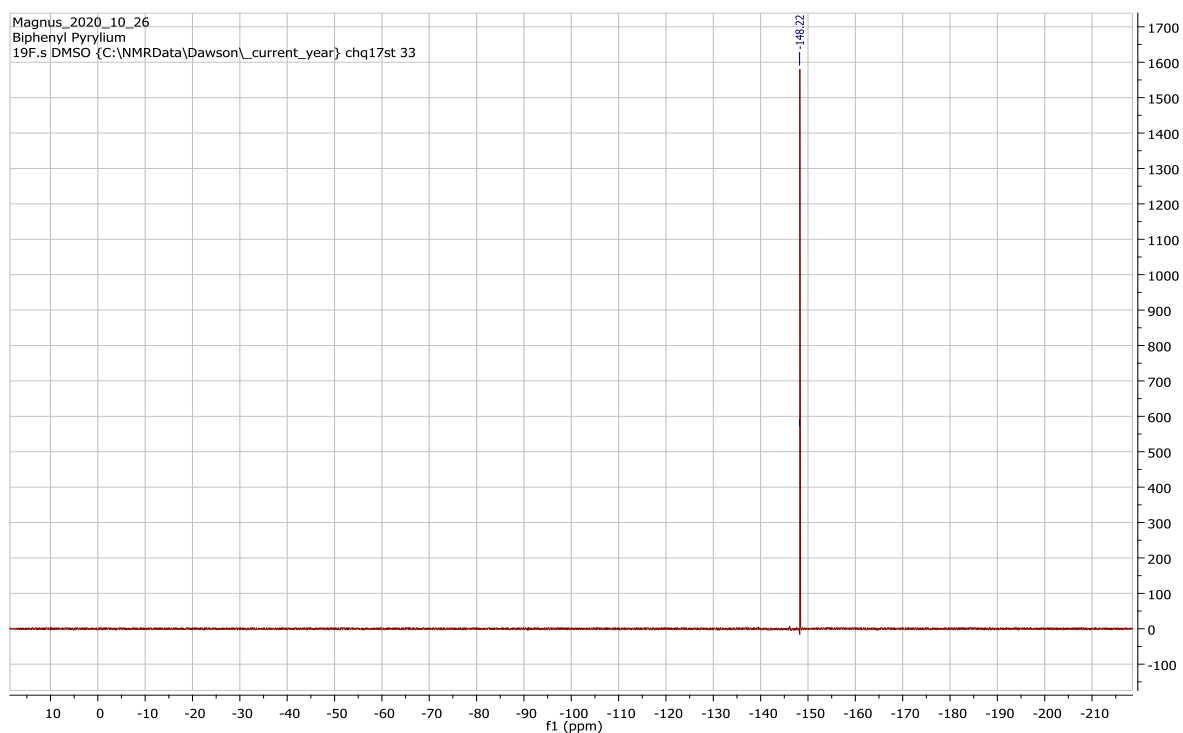


**Figure A3.25**  $^{19}\text{F}$  NMR spectrum of 2,4,6-tris(biphenyl) pyrylium tetrafluoroborate.

### 3.8.3 Mass spectra of the synthesised pyrylium monomers

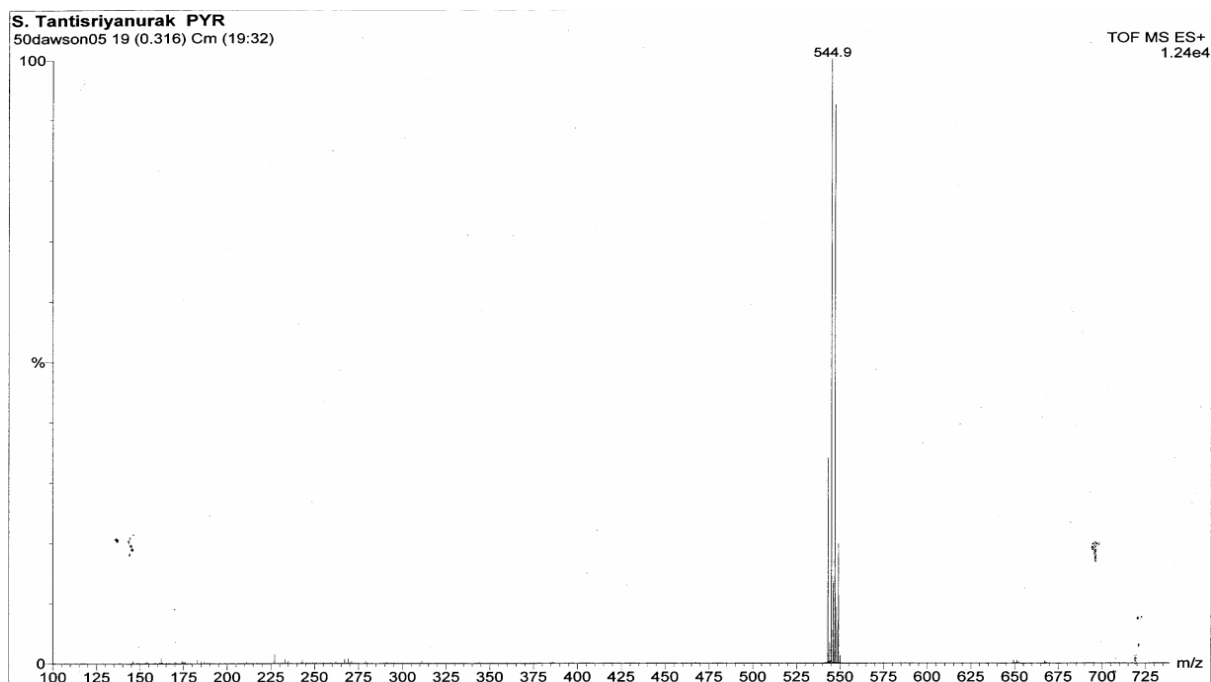


**Figure A3.26** Mass spectrum of 2,4,6-tris(4-bromophenyl) pyrylium tetrafluoroborate (wide).

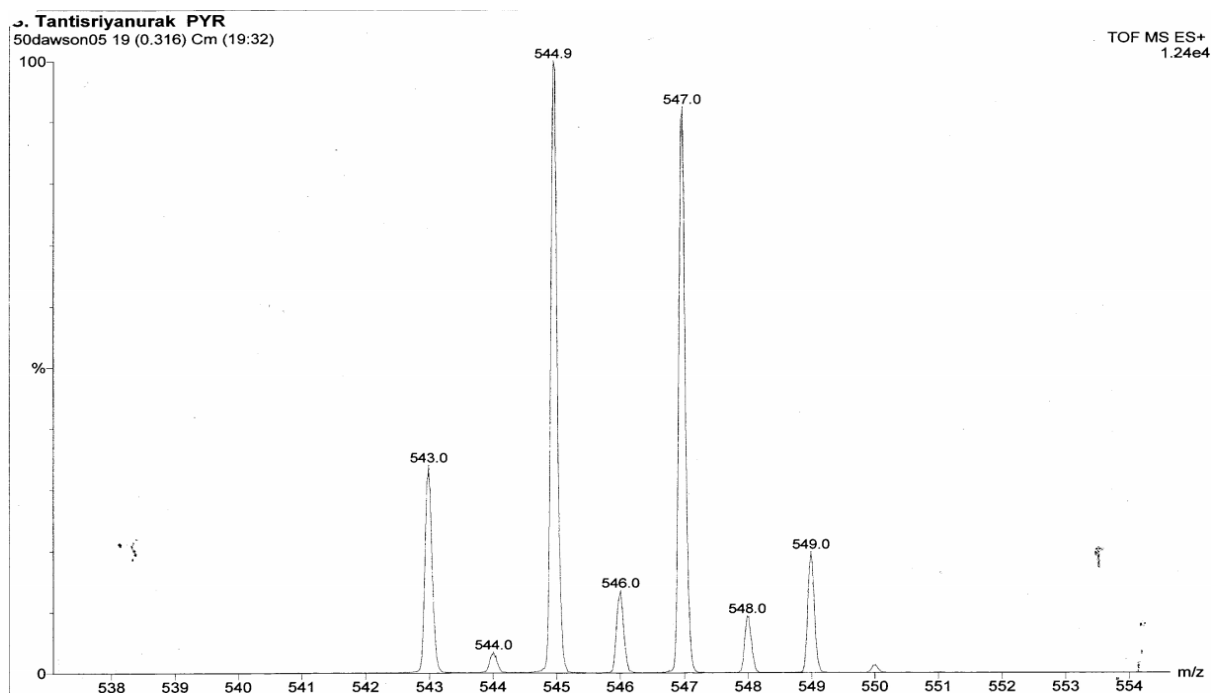


**Figure A3.27** Mass spectrum of 2,4,6-tris(4-bromophenyl) pyrylium tetrafluoroborate (zoom in).

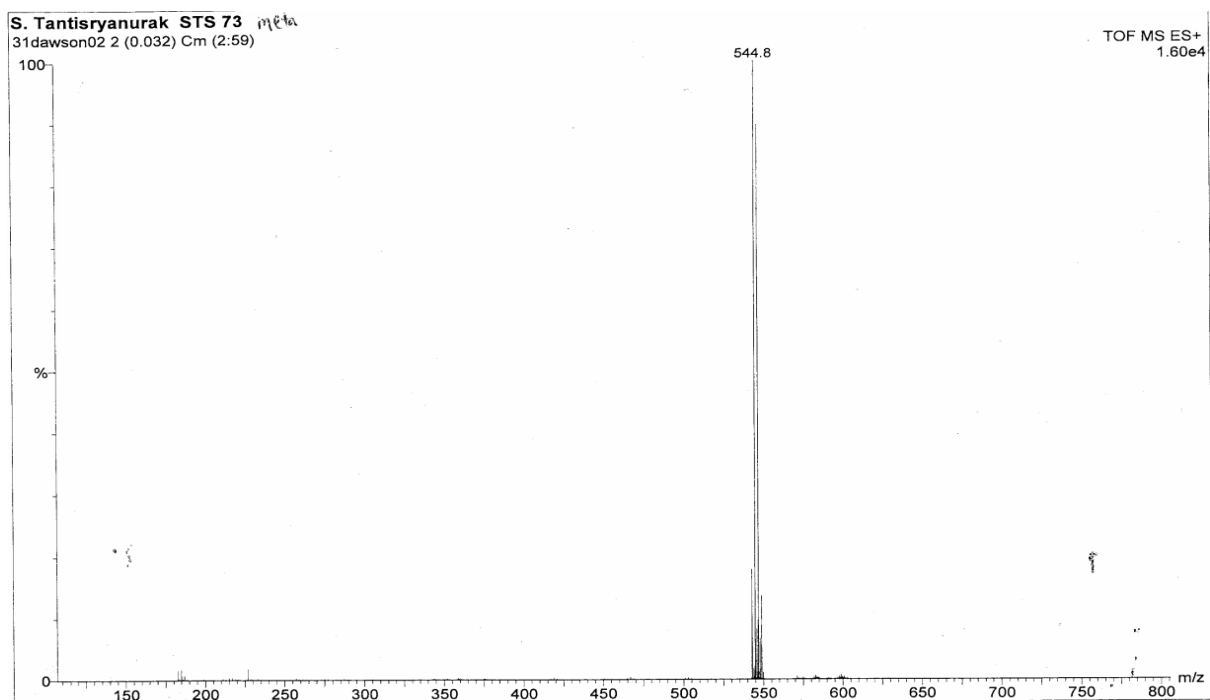


**Figure A3.28** Mass spectrum of 2,4,6-tris(3-bromophenyl) pyrylium tetrafluoroborate (wide).

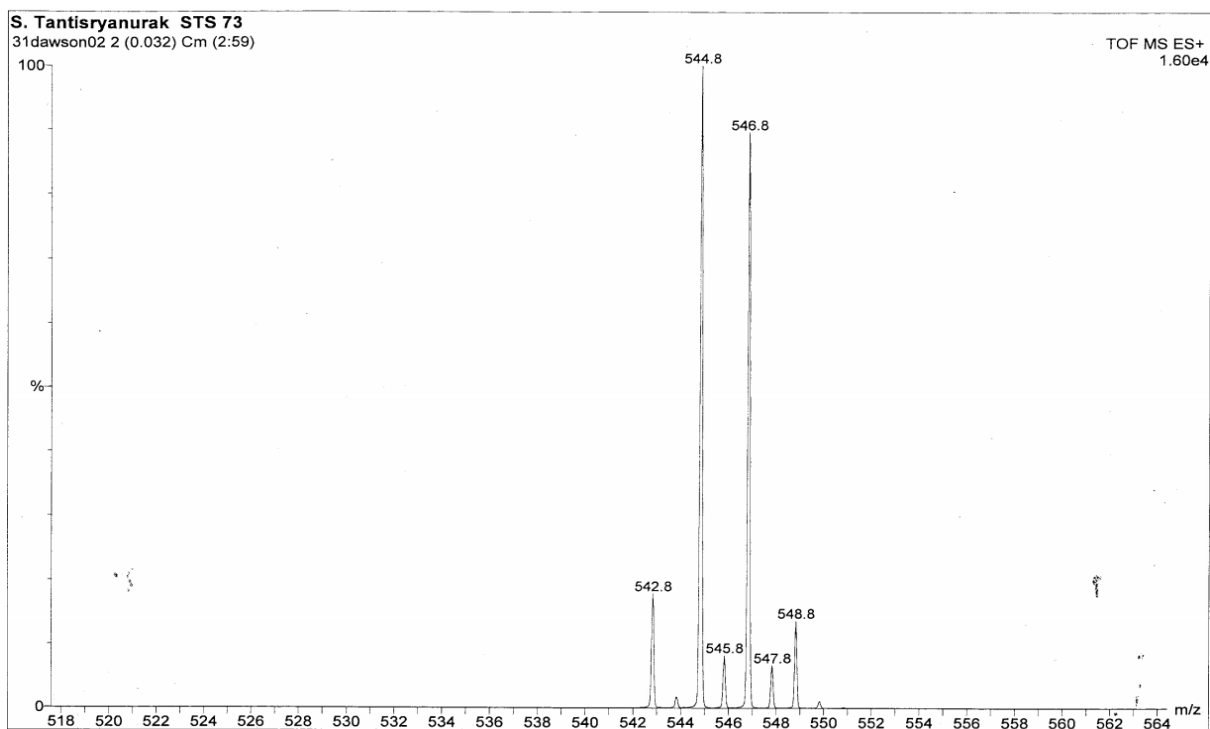


**Figure A3.29** Mass spectrum of 2,4,6-tris(3-bromophenyl) pyrylium tetrafluoroborate (zoom in).

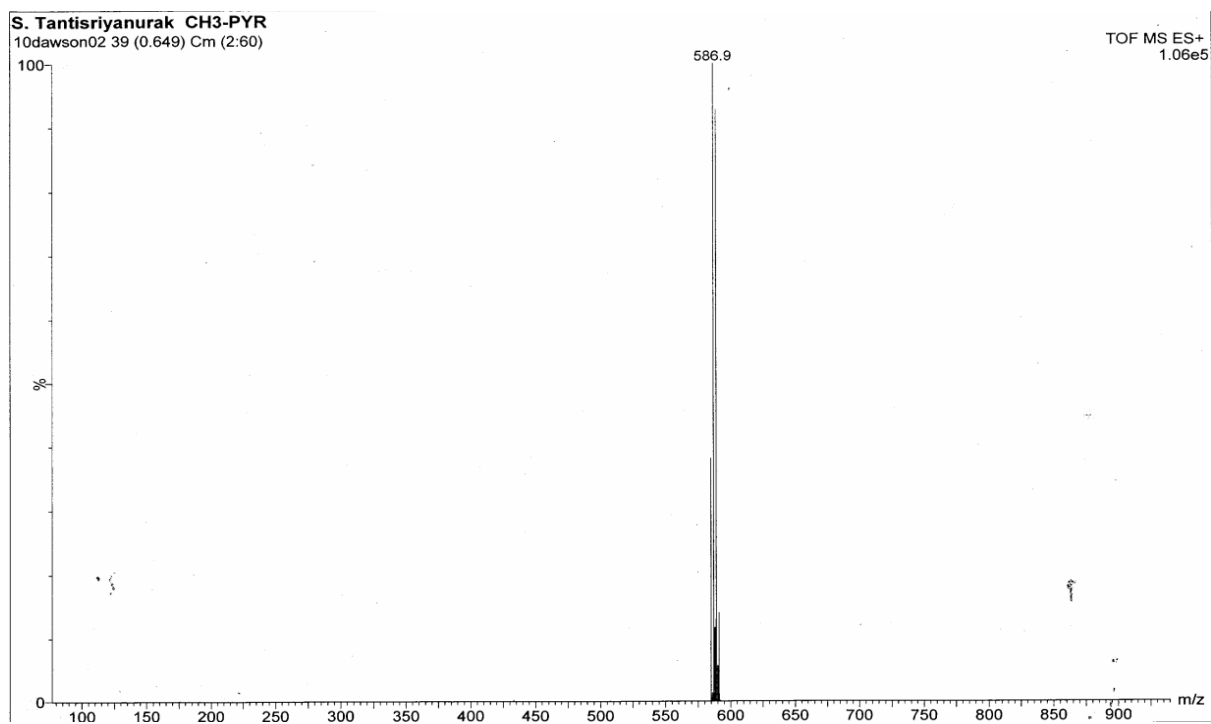


**Figure A3.30** Mass spectrum of 2,4,6-tris(3-bromo, 4-methylphenyl) pyrylium tetrafluoroborate (wide).

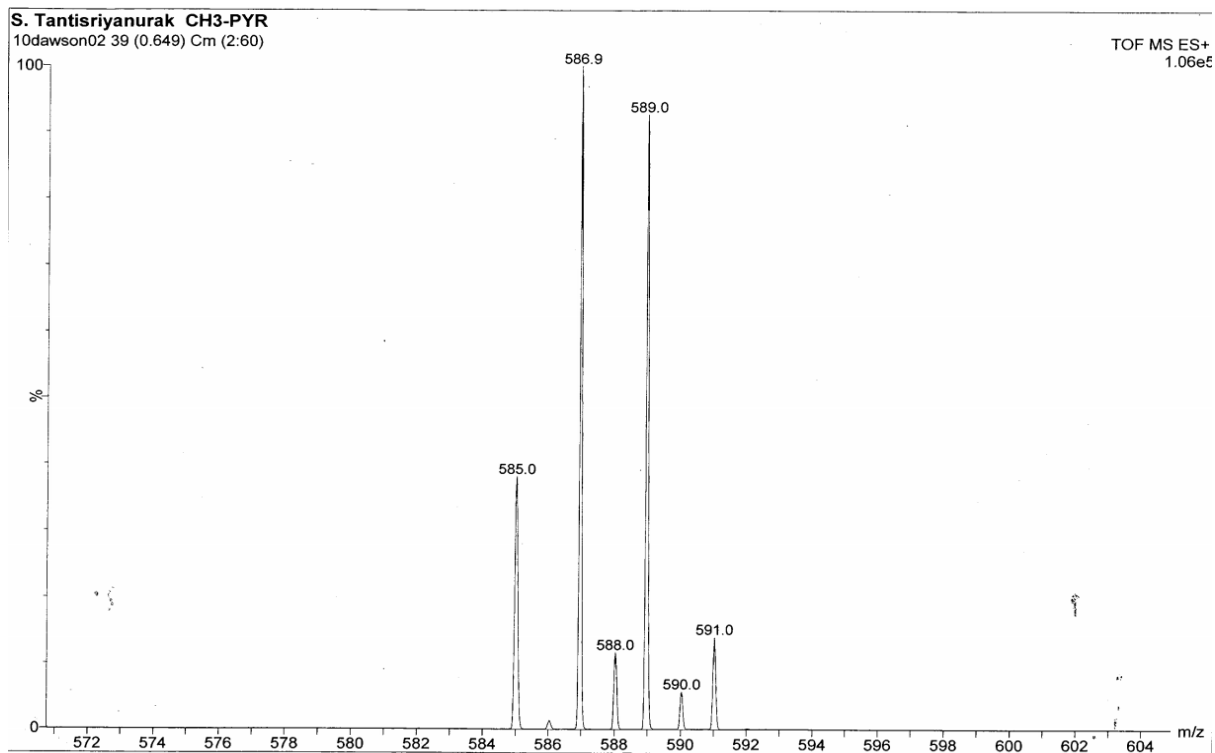


**Figure A3.31** Mass spectrum of 2,4,6-tris(3-bromo, 4-methylphenyl) pyrylium tetrafluoroborate (zoom in).



**Figure A3.32** Mass spectrum of 2,4,6-tris(3-bromo, 4-methoxyphenyl) pyrylium tetrafluoroborate (wide).

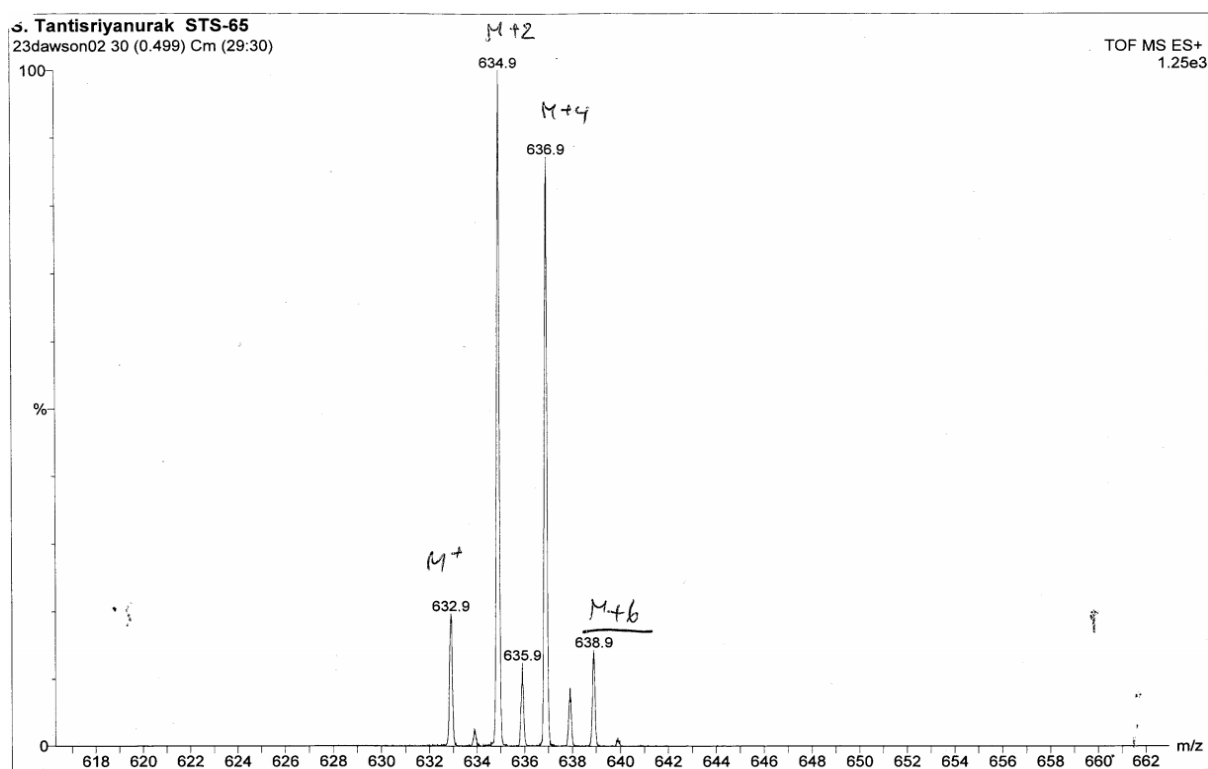


**Figure A3.33** Mass spectrum of 2,4,6-tris(3-bromo, 4-methoxyphenyl) pyrylium tetrafluoroborate (zoom in).

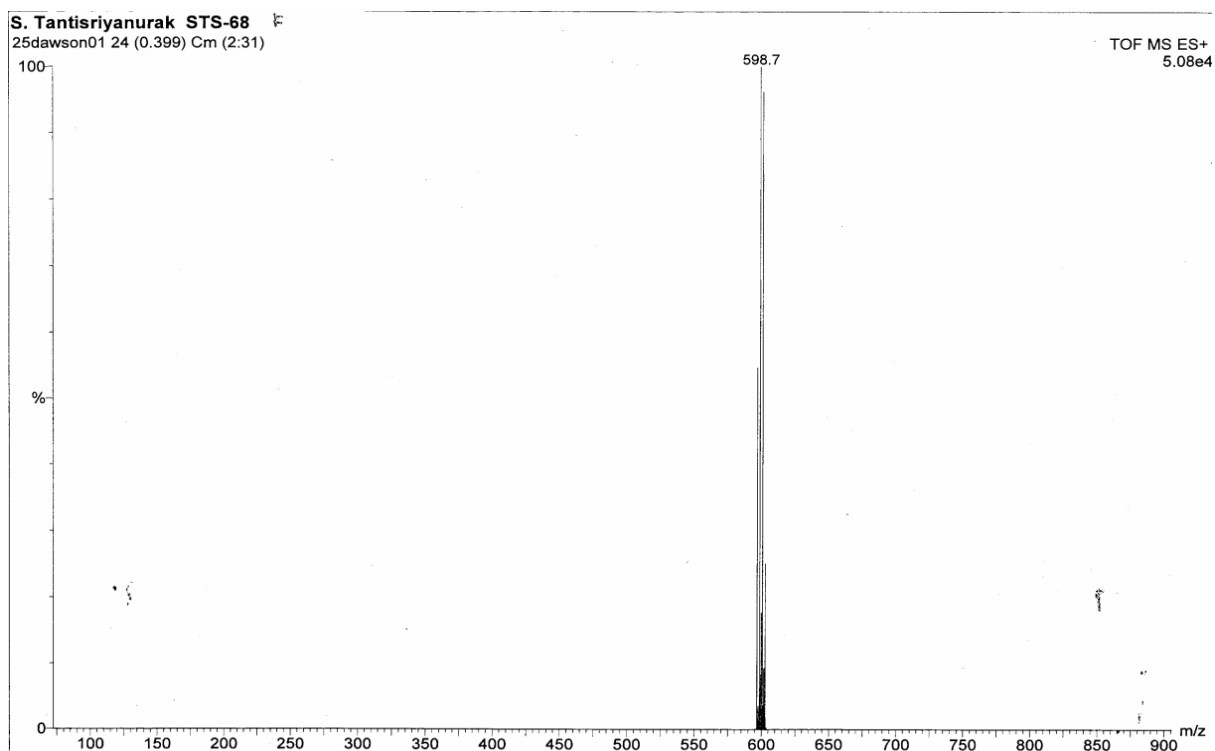


**Figure A3.34** Mass spectrum of 2,4,6-tris(3-bromo, 4-fluorophenyl) pyrylium tetrafluoroborate (wide).

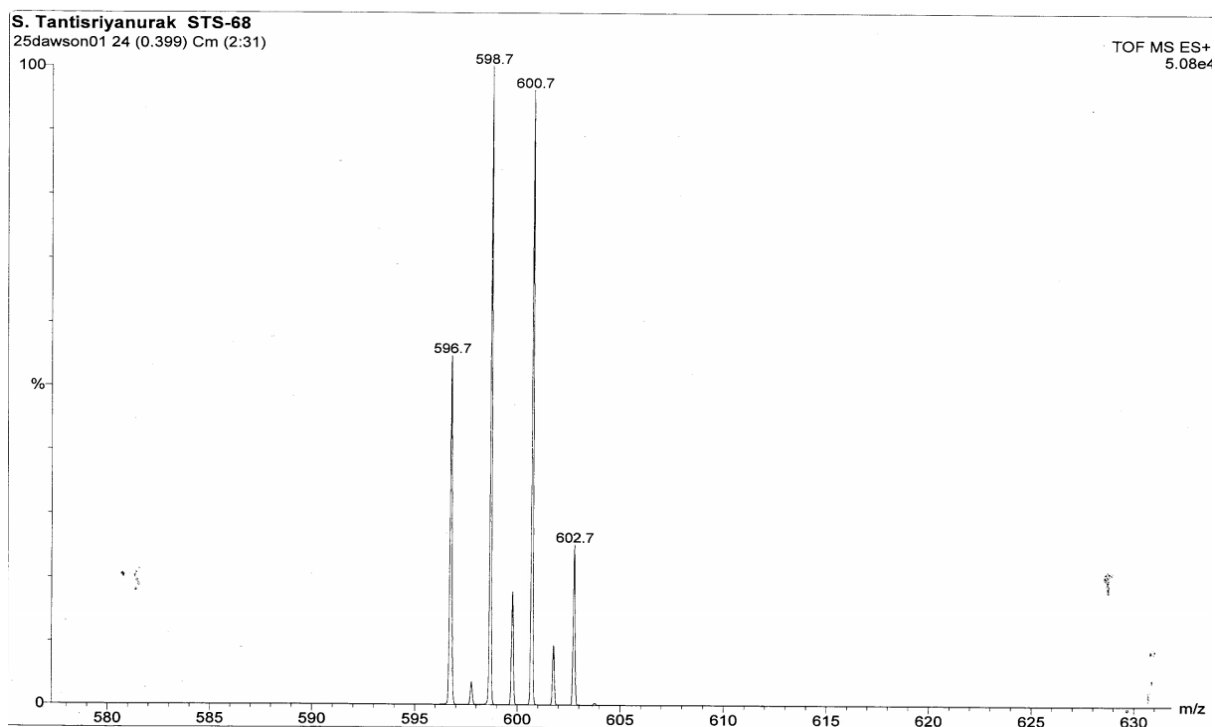


**Figure A3.35** Mass spectrum of 2,4,6-tris(3-bromo, 4-fluorophenyl) pyrylium tetrafluoroborate (zoom in).

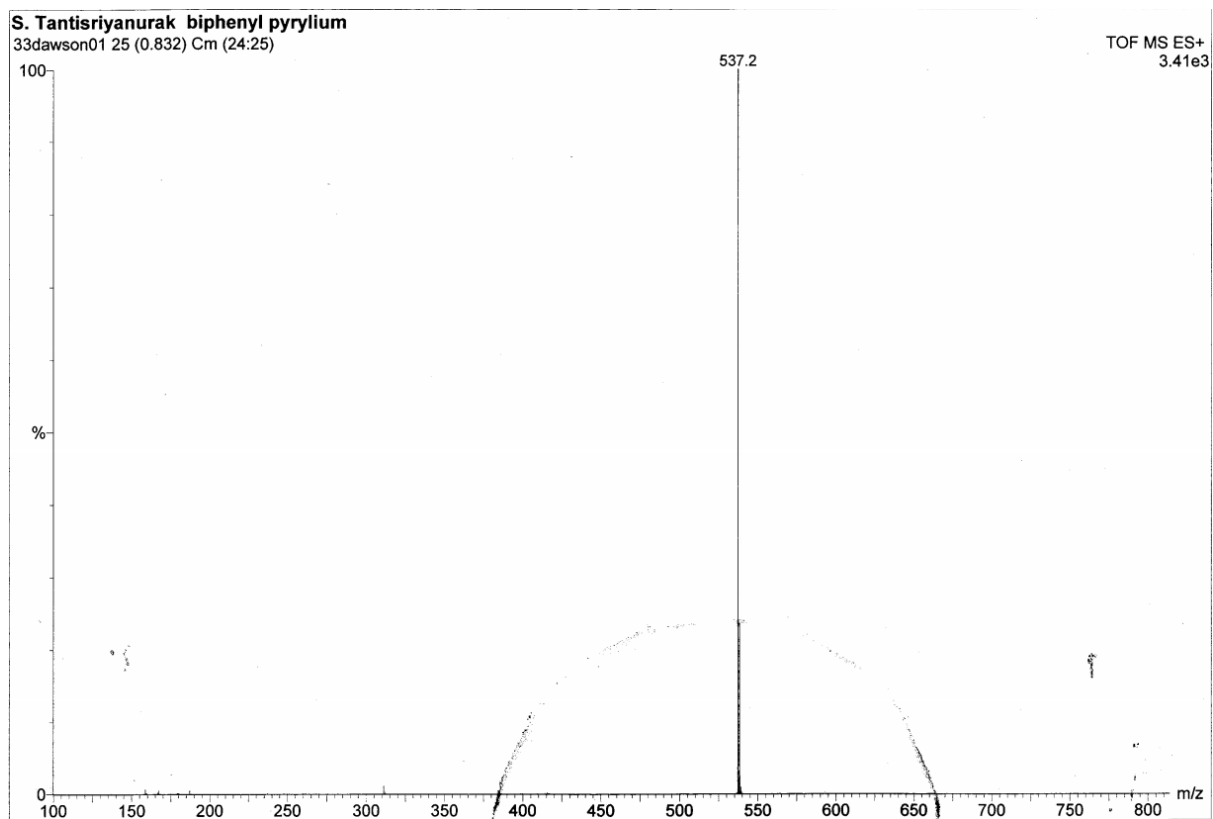


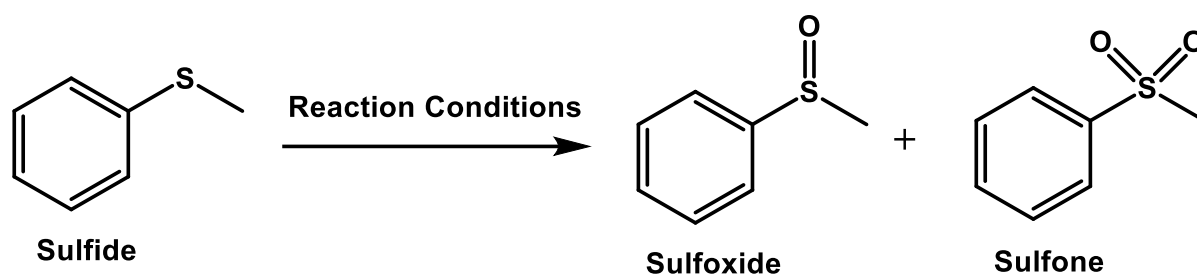
**Figure A3.36** Mass spectrum of 2,4,6-tris(biphenyl) pyrylium tetrafluoroborate.

## Chapter 4

# Pyrylium Based Conjugated Microporous Polymers for Catalytic Oxidation of Thioanisole Using Hydrogen Peroxide as an Oxidant

### 4.1 Introduction

Thioether or sulfide oxidation (Scheme 4.1) is one of the most important organic reactions due to the valuable reaction products including sulfoxide and sulfone which are extensively used in agrochemicals, pharmaceuticals, and as synthetic intermediates.<sup>1</sup> The oxidation of thioethers to the sulfoxide product requires mild and highly selective conditions while over oxidation to the sulfone is much easier to achieve.<sup>2</sup> Organic sulphides can be oxidised using a wide range of oxidising agents, such as hydrogen peroxide ( $\text{H}_2\text{O}_2$ )<sup>1,3-5</sup>, halogen derivatives<sup>6,7</sup>, nitrogen oxide derivatives<sup>8</sup>, molecular oxygen and its derivatives<sup>9,10</sup>, inorganic salts and inorganic acids.<sup>11,12</sup> Among the various oxidants,  $\text{H}_2\text{O}_2$  is cheap, green and environmentally friendly because of the non-toxic by-product water. Other oxidants such as nitric acid and  $\text{KMNO}_4$  have several disadvantages including low yields and extreme reaction conditions while halogen derivatives e.g. *m*-chlorobenzoic acid,  $\text{NaIO}_4$ ,  $\text{NaClO}_4$  are expensive, require long reaction times, high temperatures and are difficult to handle.<sup>13,14</sup>



**Scheme 4.1** Oxidation of sulfide to sulfoxide and sulfone products.

Many heterogeneous catalysts have been developed for sulfide oxidation using  $\text{H}_2\text{O}_2$  as an oxidising agent including metal oxides<sup>15</sup>, metal loaded inorganic and organic supports<sup>5,16–18</sup>, metal organic frameworks<sup>19–21</sup>, and organic materials.<sup>22,23</sup> Microporous polymers especially conjugated microporous polymers (CMPs) have been widely studied as heterogeneous photocatalysts for the photocatalytic oxidation of organic sulfides due to being metal free, having high efficiencies and good reusability. Su and co-workers reported carbazolic conjugated microporous polymers for aerobic oxidation reactions using molecular oxygen and visible light. The synthesised CMPs, which have surface areas up to  $1137 \text{ m}^2/\text{g}$  and lower bandgaps than the monomer, showed high % conversion of more than 99% with high selectivity for the sulfoxide product (up to 95%). The CMPs were also able to be reused up to 7 times without significant loss in catalytic activity.<sup>24</sup> Similar work has also been reported by Zhang *et.al.*,<sup>25</sup> who synthesised benzodithiophenedione (BDD) CMP networks *via* Sonogashira cross-coupling which yielded high surface area materials ( $605 \text{ m}^2/\text{g}$ ) with low bangaps of 2.06 eV. The CMPs also had HOMO at 1.35 eV and LUMO at -0.71 eV vs Saturated Calomel Electrode (SCE), and were used to reduce molecular oxygen to  $\text{O}_2^{\bullet-}$  ( $E_{\text{red}} = -0.56 \text{ eV}$  vs SCE). The BDD-CMPs were used as a photocatalyst for sulfide oxidation and they exhibited a high conversion (up to 99%) with a high

selectivity of sulfoxide of 99%. The BDD-CMP also showed excellent stability and could be reused up to 5 cycles.

However, CMPs for oxidation of sulfide using  $\text{H}_2\text{O}_2$  as an oxidant have not been widely studied. So, in this work, oxidation of sulfide mediated by  $\text{H}_2\text{O}_2$  has been investigated using pyrylium based CMPs as heterogeneous catalysts. The reaction parameters such as structure of catalysts, mole ratios of reactants, reaction time and temperature are studied in order to obtain the optimum reaction conditions as well as reusability tests of the synthesised catalysts.

## 4.2 Aims of the chapter

- To utilise pyrylium based CMPs as heterogeneous catalysts for oxidation of thioanisole.
- To study effect of polymer structures on oxidation of thioanisole.
- To optimize reaction conditions such as temperature, time and  $\text{H}_2\text{O}_2$  amounts.
- To study reusability of the catalysts.
- To investigate reaction mechanism of thioanisole oxidation.

## 4.3 Experimental

### 4.3.1 Materials

Chlorobenzene, sodium pyruvate and thioanisole were purchased from Sigma-Aldrich. 30%W/V  $\text{H}_2\text{O}_2$ , acetonitrile and methanol were obtained from Fischer Scientific. *p*-Benzoquinone and  $\alpha$ -tocopherol were purchased from Fluorochem and *t*-butanol was obtained from Acros.

### **4.3.2 Thioanisole oxidation using H<sub>2</sub>O<sub>2</sub> as an oxidant and pyrylium CMPs as catalysts**

To a solution of thioanisole (1 mmol) in acetonitrile (3 mL) in a 10 mL reaction tube was added 30 mg of catalyst. The mixture was heated to the target temperature and the required amount of H<sub>2</sub>O<sub>2</sub> was added. The reaction was then stirred for desired time. After cooling down, 10 μL of the reaction mixture was diluted with 990 μL of methanol and 5 μL of chlorobenzene was added as internal standard. The mixture was filtered using 0.2 μm syringe filter and analysed by GC-MS.

$$\% \text{ Conversion} = (n_0 - n_t) / n_0 \times 100 \quad (\text{eq. 4.1})$$

Where  $n_0$  is mole of thioanisole at time = 0.

$n_t$  is mole of thioanisole at time = t.

$$\% \text{ Selectivity of sulfoxide} = n_{\text{sulfoxide}} / (n_{\text{sulfoxide}} + n_{\text{sulfone}}) \times 100 \quad (\text{eq. 4.2})$$

$$\% \text{ Selectivity of sulfone} = n_{\text{sulfone}} / (n_{\text{sulfoxide}} + n_{\text{sulfone}}) \times 100 \quad (\text{eq. 4.3})$$

Where  $n_{\text{sulfoxide}}$  is mole of sulfoxide.

$n_{\text{sulfone}}$  is mole of sulfone.

## **4.4 Results and Discussion**

### **4.4.1 Effect of polymer structure on thioanisole oxidation using H<sub>2</sub>O<sub>2</sub> as an oxidant.**

Pyrylium based CMPs bearing different functional groups and structures (Scheme 4.2) were prepared *via* Sonogashira-Hagihara cross-coupling as discussed in Chapter 3 in order to investigate the effect of polymer structure on the oxidation reaction. 30 mg of polymer was used as a catalyst using 1.5 mmol of H<sub>2</sub>O<sub>2</sub> as an

oxidant at 50 °C for 24 h as shown in Figure 4.1. The % conversion was small when the catalyst was used without H<sub>2</sub>O<sub>2</sub>. This indicated that H<sub>2</sub>O<sub>2</sub> was crucial for this reaction. With H<sub>2</sub>O<sub>2</sub> but without the catalyst, it showed a low conversion of 60% while the catalyst conversions were improved to more than 80%, demonstrating that the catalyst can improve the catalytic activity. The pyrylium polymers with DEB linker showed higher conversions than the TEB. This is likely due to the ability of *para* linkage to facilitate electron delocalisation (as opposed to the *meta* 1,3,5 substitution pattern of TEB) in the polymer networks leading to the higher catalytic activity. The Pyr+TEB showed the highest conversion among the TEB incorporated polymers due to *para* linkage of pyrylium monomer with TEB resulting in better electron delocalisation than the *meta* linkage *m*-Pyr+TEB. The additional *para* substituted electron donating group slightly improved % conversion. Likewise, Pyr+DEB showed greater conversion than *m*-Pyr+DEB but the *para* substituted group significantly increased % conversion when compared to the TEB versions due to better delocalisation of electrons in DEB derived polymers. MeO-Pyr+DEB, Me-Pyr+DEB, and F-Pyr+DEB showed lower % selectivity of sulfoxide product than other polymers because they are more active catalysts resulting in over oxidation of sulfoxide to the sulfone product. Thus, the optimum reaction time needed to be investigated to obtain both high % conversion and % selectivity of sulfoxide product. The particle sizes of the synthesised CMPs were determined using an optical microscope to determine the effect of particle size on the catalytic activity. Generally, smaller particle catalysts give a higher catalytic activity due to the higher surface area compared to the same volume of the catalysts with larger particle sizes.<sup>26-28</sup> The synthesised CMPs showed the main particle size distribution at 1-10 micron combined with aggregate particles as shown in Figure A4.1. The DEB derived materials showed the averaged particle sizes from 23.7 to 40.5



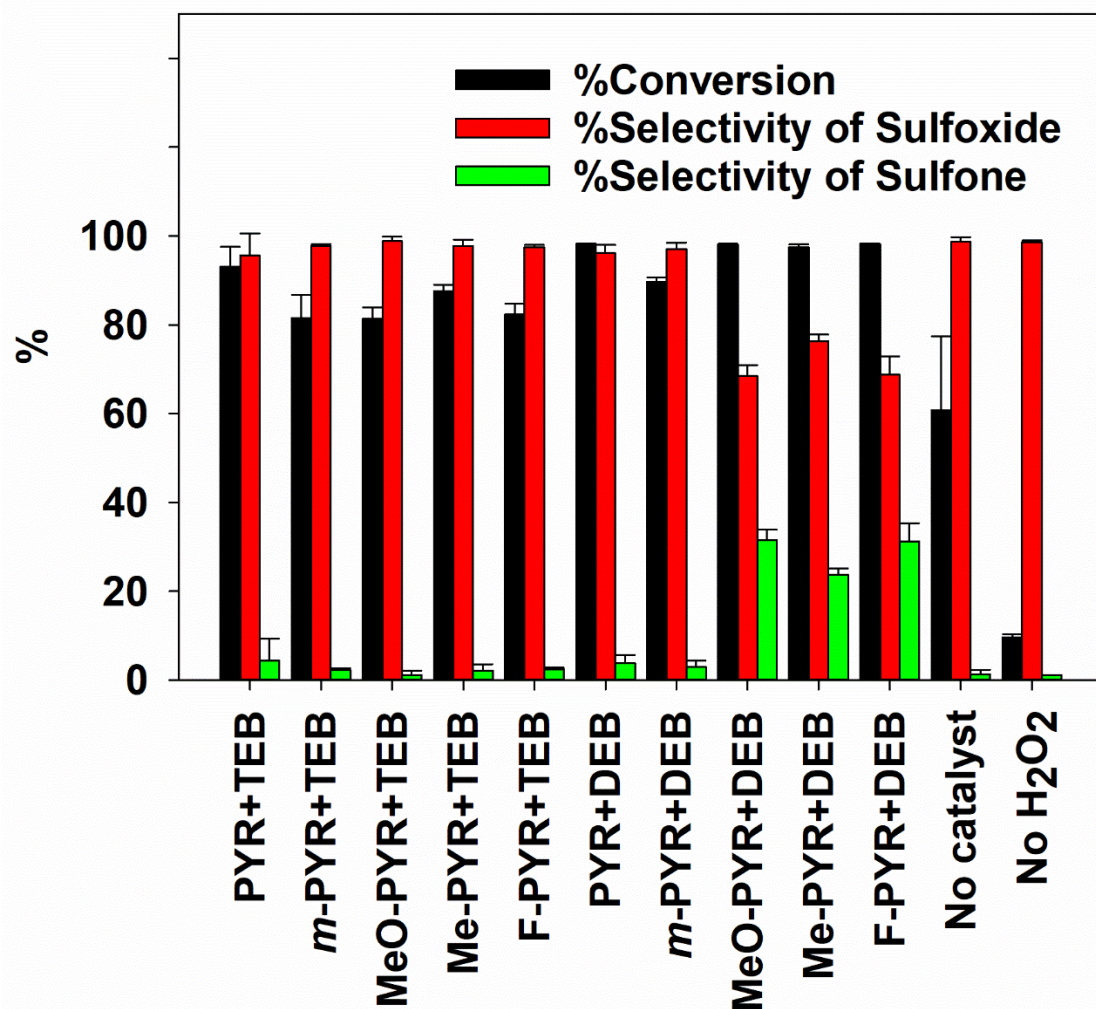


**Figure 4.1** Effect of different polymer structure on thioanisole oxidation using H<sub>2</sub>O<sub>2</sub> as an oxidant. (Condition: 1 mmol of thioanisole, 1.5 mmol of H<sub>2</sub>O<sub>2</sub> and 3 mL of acetonitrile using 30 mg of catalyst at 50 °C for 24h). (The results are an average of 3 experiments)

**4.4.2 Effect of reaction time on thioanisole oxidation using H<sub>2</sub>O<sub>2</sub> as an oxidant.**

DEB polymers were chosen for kinetic study due to the higher conversion at 50 °C using 1.5 mmol of H<sub>2</sub>O<sub>2</sub> and 30 mg of catalyst. The % conversion increased when the reaction time was longer while % selectivity of sulfoxide slightly decreased as shown in Figure 4.2 and 4.3. The no catalyst condition showed the slowest reaction due to lack of catalytic sites. This could confirm that catalyst improved the conversion of the reaction. The F-Pyr+DEB was the fastest catalyst which reached the highest conversion of almost 100 % after 10 h with selectivity of sulfoxide of 96%, so it was chosen as the best catalyst and was used for the next parameter studies. Even though fluoro group are electron donating group *via* the resonance effect but it also has high electronegativity and can withdraw electron *via* the inductive effect which can increase reactivity of pyrylium group leading to the highest catalytic activity.<sup>29</sup>

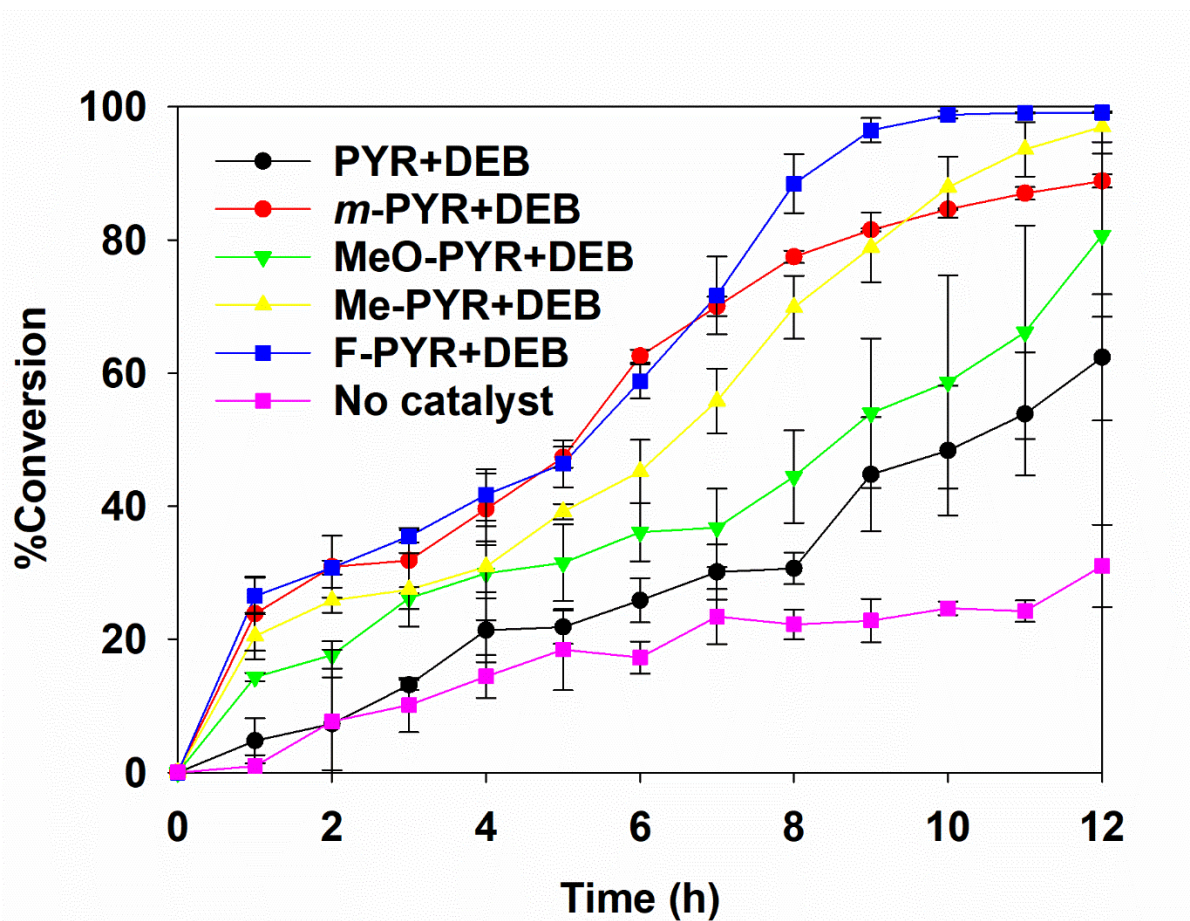


**Figure 4.2** % Conversion of thioanisole oxidation with different polymers at different reaction times. (Condition: 1 mmol of thioanisole, 1.5 mmol of H<sub>2</sub>O<sub>2</sub> and 3 mL of acetonitrile using 30 mg of catalyst at 50 °C). (The results are an average of 3 experiments)

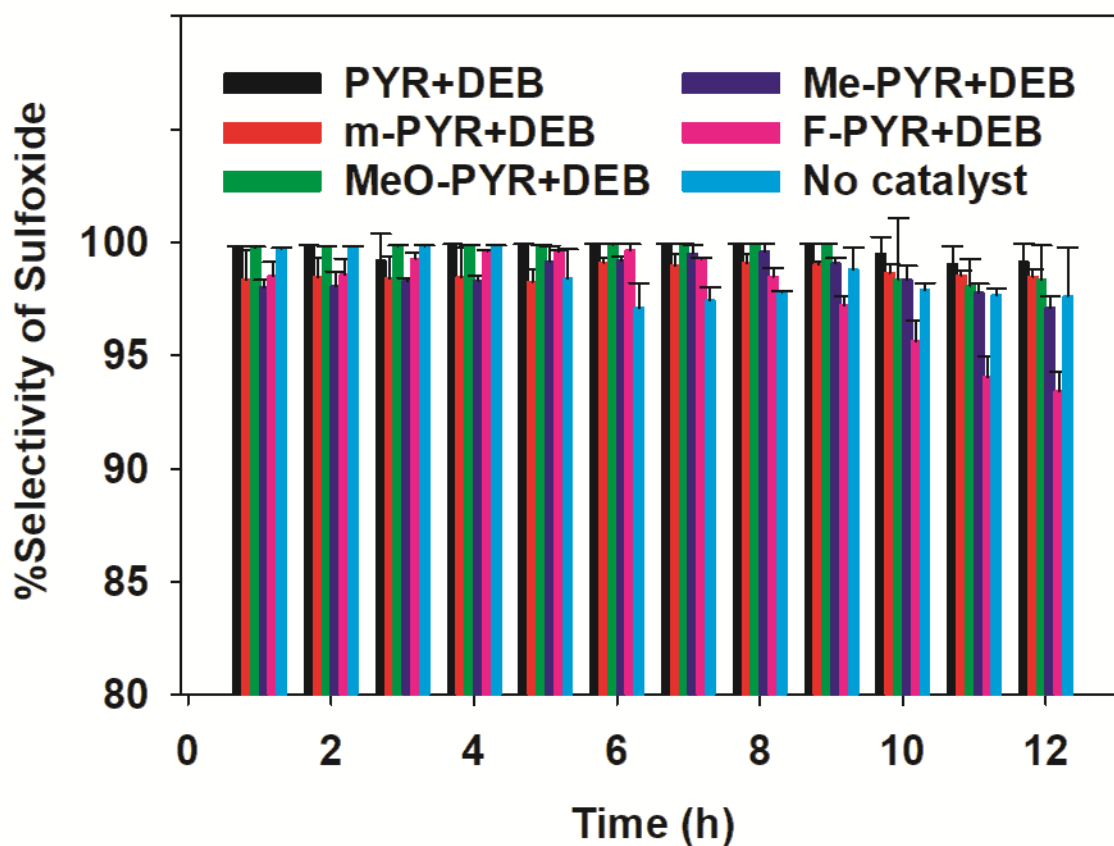


**Figure 4.3** Selectivity of sulfoxide product using different polymers at different times.

(Condition: 1 mmol of thioanisole, 1.5 mmol of  $H_2O_2$  and 3 mL of acetonitrile using 30 mg of catalyst at 50 °C). (The results are an average of 3 experiments)

#### **4.4.3 Effect of amount of $H_2O_2$ on thioanisole oxidation**

The effect of the amount of oxidising agent was studied using 1 mmol of thioanisole, 30 mg of F-Pyr+DEB catalyst in 3 mL of acetonitrile at 50 °C. The results shown in Figure 4.4 and 4.5 suggest that a higher concentration of hydrogen peroxide gives a faster reaction due to more oxidising species. 3.0 mmol of  $H_2O_2$  gave the maximum conversion after 4 h with the selectivity of sulfoxide of 97%. However, when the reaction time was prolonged, the selectivity for the sulfoxide product dropped, especially at high concentration of  $H_2O_2$  because the excess amount of the oxidising

agent can further oxidise sulfoxide to sulfone product.<sup>22</sup> Thus the optimum concentration of  $\text{H}_2\text{O}_2$  was 3.0 mmol at 4 h.

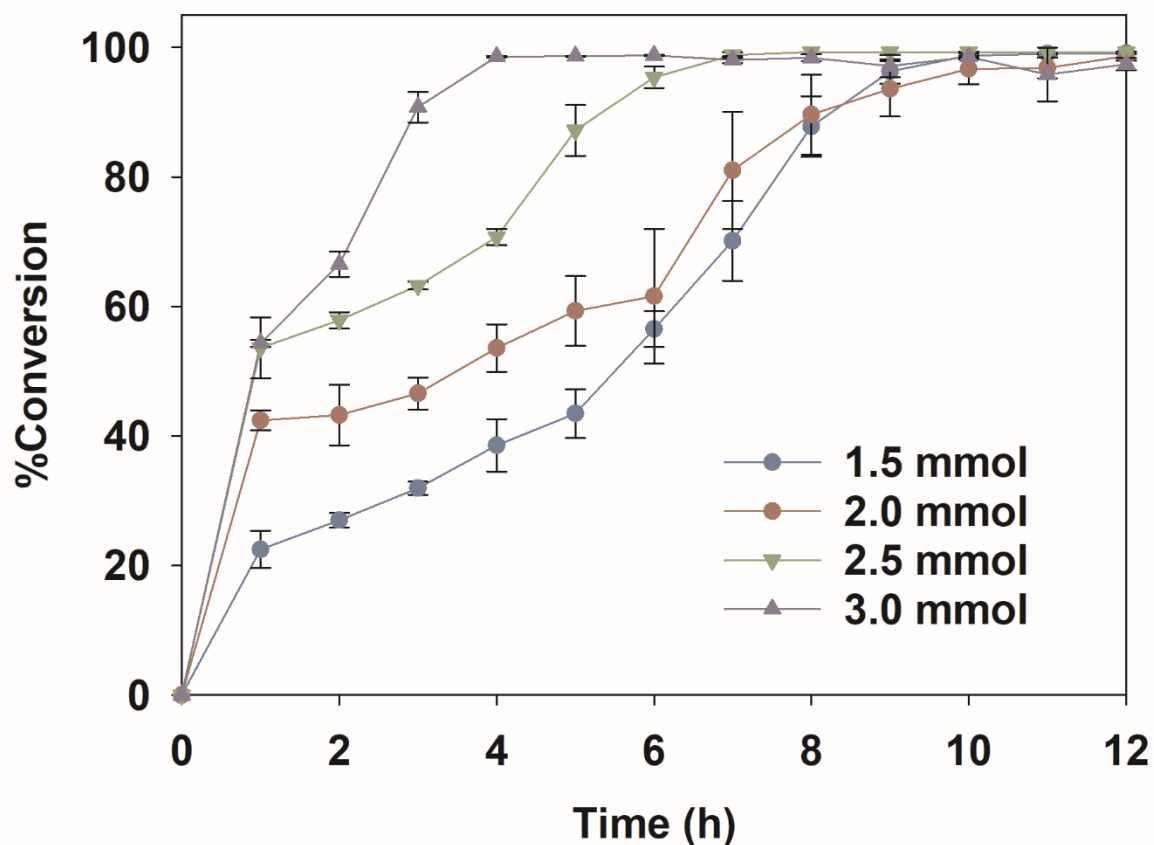


**Figure 4.4** Effect of  $\text{H}_2\text{O}_2$  concentration on conversion of thioanisole oxidation (Condition: 1 mmol of thioanisole and 3 mL of acetonitrile using 30 mg of F-PYR+DEB at 50 °C). (The results are an average of 3 experiments)

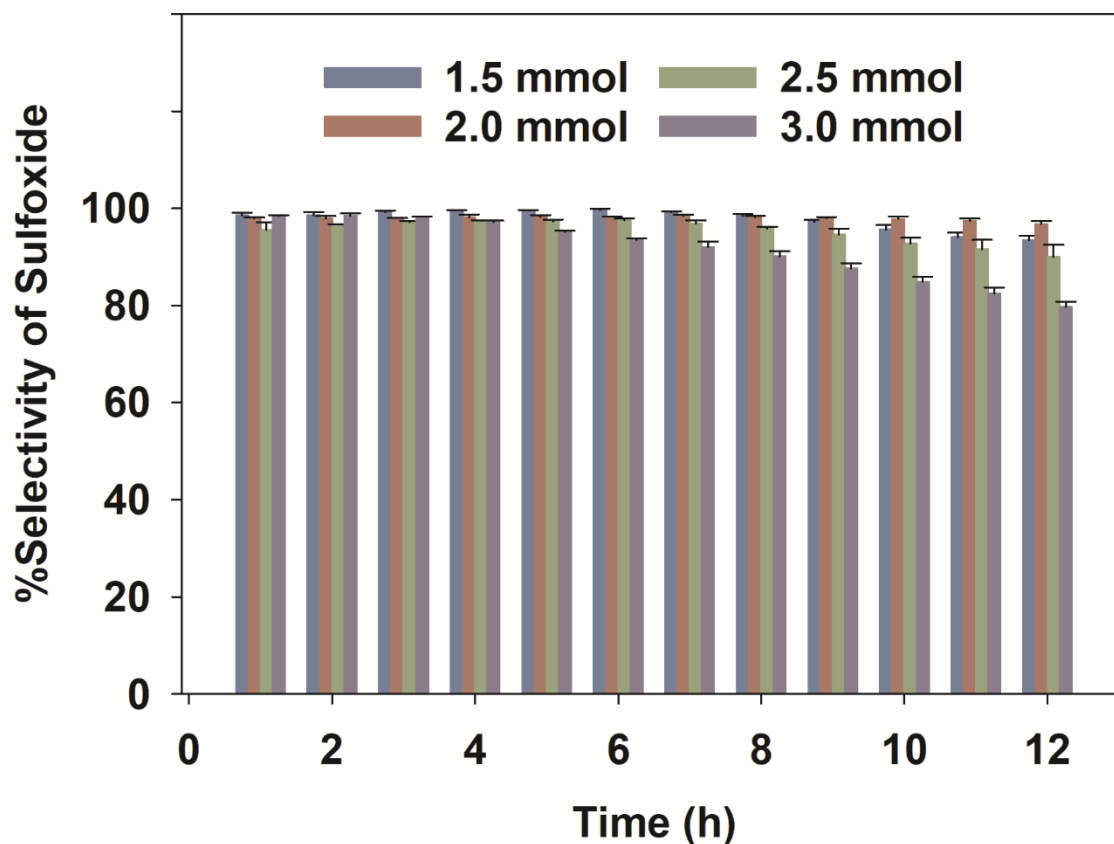


**Figure 4.5** Effect of  $\text{H}_2\text{O}_2$  concentration on selectivity of sulfoxide product (Condition: 1 mmol of thioanisole and 3 mL of acetonitrile using 30 mg of F-PYR+DEB at 50 °C). (The results are an average of 3 experiments)

#### **4.4.4 Effect of reaction temperature on thioanisole oxidation using $\text{H}_2\text{O}_2$ as an oxidant.**

The effect of temperature was determined using 1 mmol of thioanisole, 3 mmol of  $\text{H}_2\text{O}_2$  and 30 mg of F-Pyr+DEB catalyst at 40 to 60 °C as shown in Figure 4.6 and 4.7. The higher temperature resulted in faster reaction but lower selectivity of sulfoxide due to an increase in kinetic energy of the molecules leading to more over oxidation of the sulfoxide to sulfone product.<sup>22</sup> The reactions reached the maximum conversion

at 8, 4, and 2 h for 40 °C, 50 °C and 60 °C, respectively. So, the optimum condition for this reaction was at 60 °C for 2 h which gave 99% conversion with 94% selectivity of sulfoxide product.

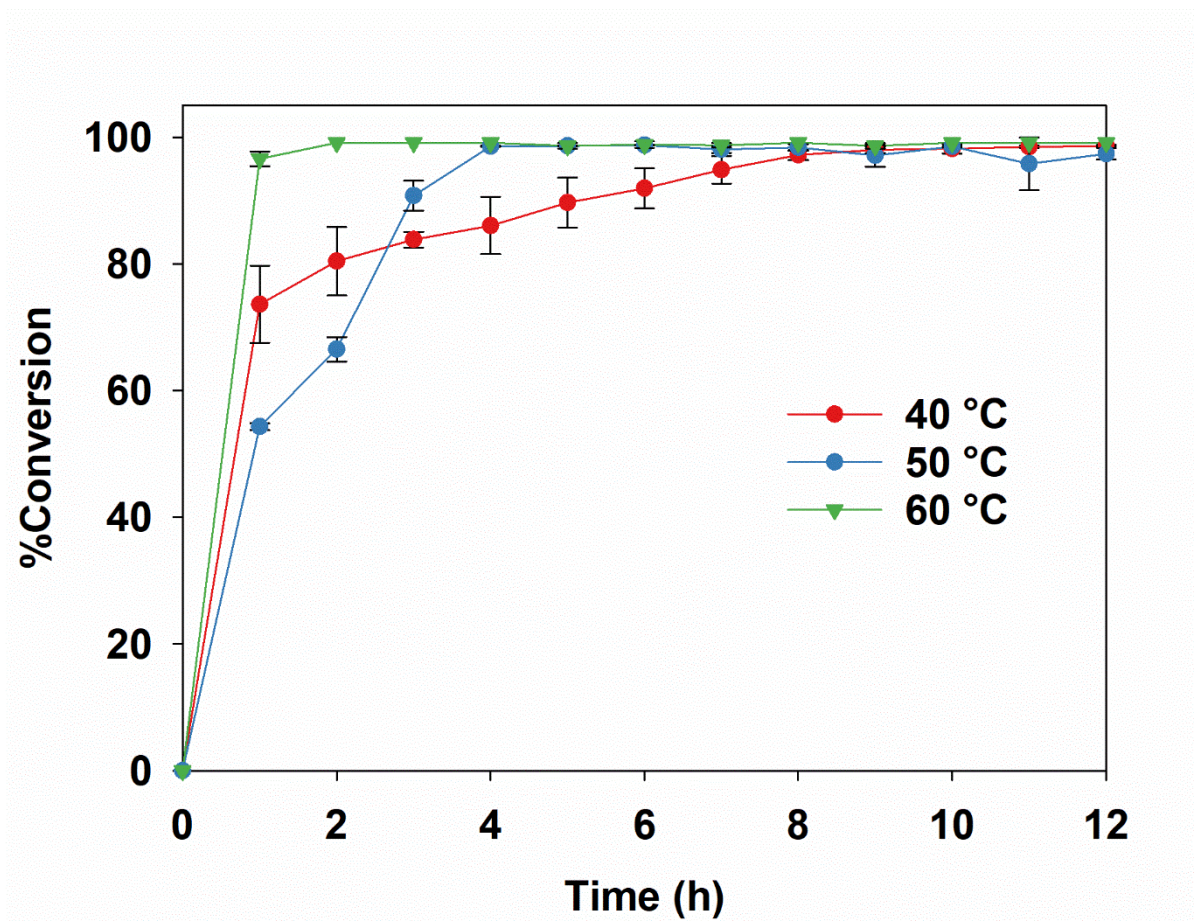


**Figure 4.6** Effect of temperature on the conversion of thioanisole oxidation

(Condition: 1 mmol of thioanisole, 3 mmol of  $\text{H}_2\text{O}_2$  and 3 mL of acetonitrile using 30 mg of F-PYR+DEB). (The results are an average of 3 experiments)

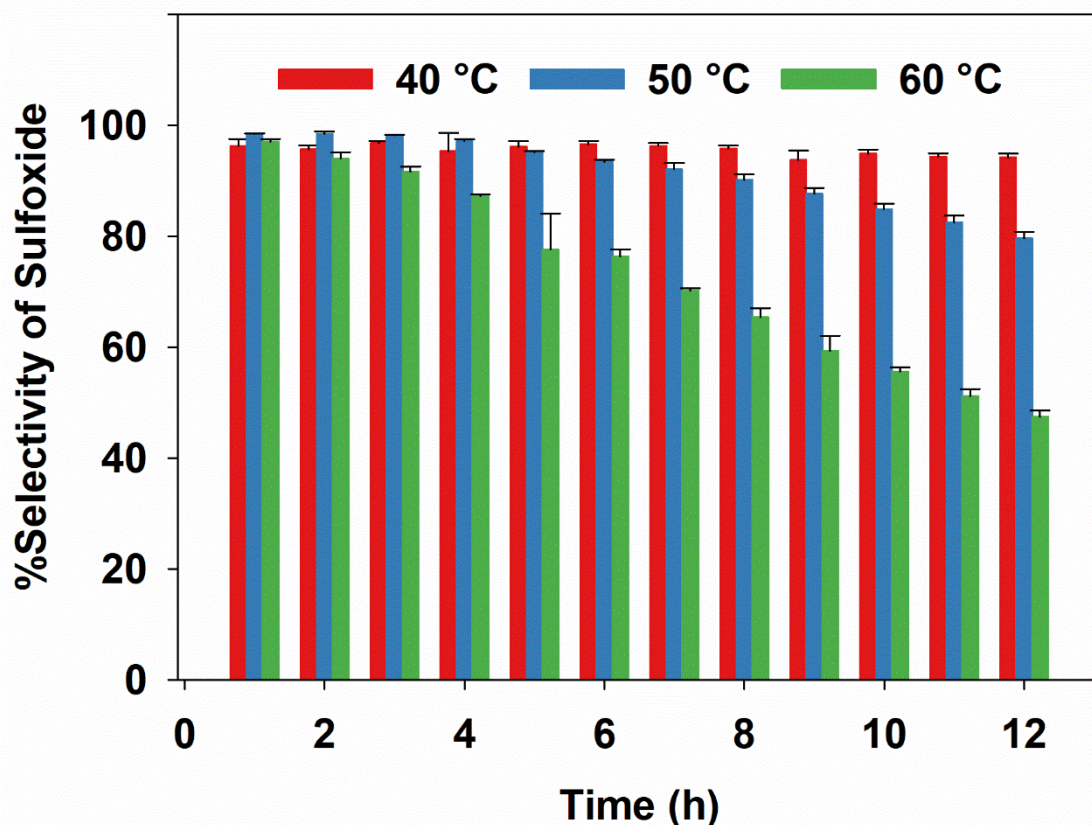


**Figure 4.7** Effect of temperature on the selectivity of sulfoxide product. (Condition: 1 mmol of thioanisole, 3 mmol of  $\text{H}_2\text{O}_2$  and 3 mL of acetonitrile using 30 mg of F-PYR+DEB). (The results are an average of 3 experiments)

#### **4.4.5 Control reactions**

The control reactions were performed using 30 mg of *m*-Br, *p*-F-pyrylium monomer as a homogeneous catalyst and using no catalyst at the optimum reaction conditions which were 1 mmol of thioanisole, 3 mmol of  $\text{H}_2\text{O}_2$ , 60 °C, and 2 h as shown in Table 4.1. The monomer showed a high conversion up to 99.7% which was similar to the heterogeneous catalyst counterpart, but the % selectivity of sulfoxide was 89.8 which was lower than the heterogeneous catalyst. This can be explained that the more

catalytic active sites in the monomer can result in more over oxidation product. Moreover, the catalyst bleaching was observed after the reaction indicating of the low stability of the monomer. The no catalyst condition showed a low conversion of 64.8% due to lack of catalytic active sites. The addition of sodium pyruvate which is H<sub>2</sub>O<sub>2</sub> scavenger resulted in no conversion and no product was observed. This indicates that H<sub>2</sub>O<sub>2</sub> was the important reactive specie for this reaction.

**Table 4.1** Controls reactions of thioanisole oxidation

Condition	Conversion	Selectivity of Sulfoxide
F-Pyr+DEB	99.1	94.1
<i>m</i> -Br, <i>p</i> -F-Pyrylium (momomer)	99.7	89.8
No catalyst	64.8	95.5
F-Pyr+DEB*	0.0	0.0

(Condition: 1 mmol of thioanisole, 3 mmol of H<sub>2</sub>O<sub>2</sub> and 3 mL of acetonitrile using 30 mg of catalyst at 60 °C for 2 h).

\*3 mmol of sodium pyruvate was added.

#### **4.4.6 Reusability test**

The F-Pyr+DEB catalyst was filtered and washed with methanol after the reaction and dried in the vacuum oven at 60 °C. The F-Pyr+DEB was reused 6 times and the conversion dropped to 81.26 and 70.19% after 2<sup>nd</sup> and 3<sup>rd</sup> cycles, respectively as shown in Table 4.2. The conversion was stable after 4<sup>th</sup> cycle which was almost 70%. A decrease in % conversion probably came from pore blocking by residual reactant and product or catalyst degradation under strong oxidising and high temperature reaction.<sup>30</sup> The used catalyst was characterised by TGA to compare with

the fresh catalyst as shown in Figure 4.8. The result showed that the used catalyst had lower decomposition temperature  $T_{dec}$  (onset) and weight loss of 372 °C and 28.3% when compared to the fresh catalyst which have  $T_{dec}$  and weight loss of 432 °C and 37.2%. This indicated that catalyst has been partially degraded during the reaction. The  $S_{BET}$  of the polymer also dropped significantly from 289 to  $\sim 0$  m<sup>2</sup>/g after being reused for 6 cycles indicating of the structure collapse. 30 mg of F-PYR+DEB was stirred with 3 mmol of hydrogen peroxide and 3 mL of acetonitrile at 60 °C for 2 h without thioanisole in order to investigate the stability of the catalyst under strong oxidising conditions. The  $S_{BET}$  of the catalyst decreased dramatically to 2.8 m<sup>2</sup>/g suggesting a low stability of the catalyst in a strong oxidising media. The FTIR spectra of 6<sup>th</sup> time reused and H<sub>2</sub>O<sub>2</sub> treated F-PYR+DEB were shown in Figure 4.9. The peak at 1676 and 1738 cm<sup>-1</sup> corresponded to pyrylium and carbonyl functional groups. The carbonyl peak showed that the pyrylium group was partially oxidised by H<sub>2</sub>O<sub>2</sub> to form ring opening 1,5-dione structure.

**Table 4.2** Reusability test (The results are an average of 3 experiments)

Cycle number	Conversion	Selectivity of Sulfoxide	Remark
1	99.2±0.3	94.2±1.1	
2	81.3±5.8	95.9±0.6	
3	70.2±1.5	96.3±0.4	
4	68.9±3.6	96.2±0.4	
5	64.0±3.3	95.1±0.3	
6	69.3±2.4	94.7±0.2	*Soxhlet

**Conditions:** F-Pyr+DEB 30 mg, 3 mmol of H<sub>2</sub>O<sub>2</sub>, 60 °C, 2 h in 3 mL of acetonitrile

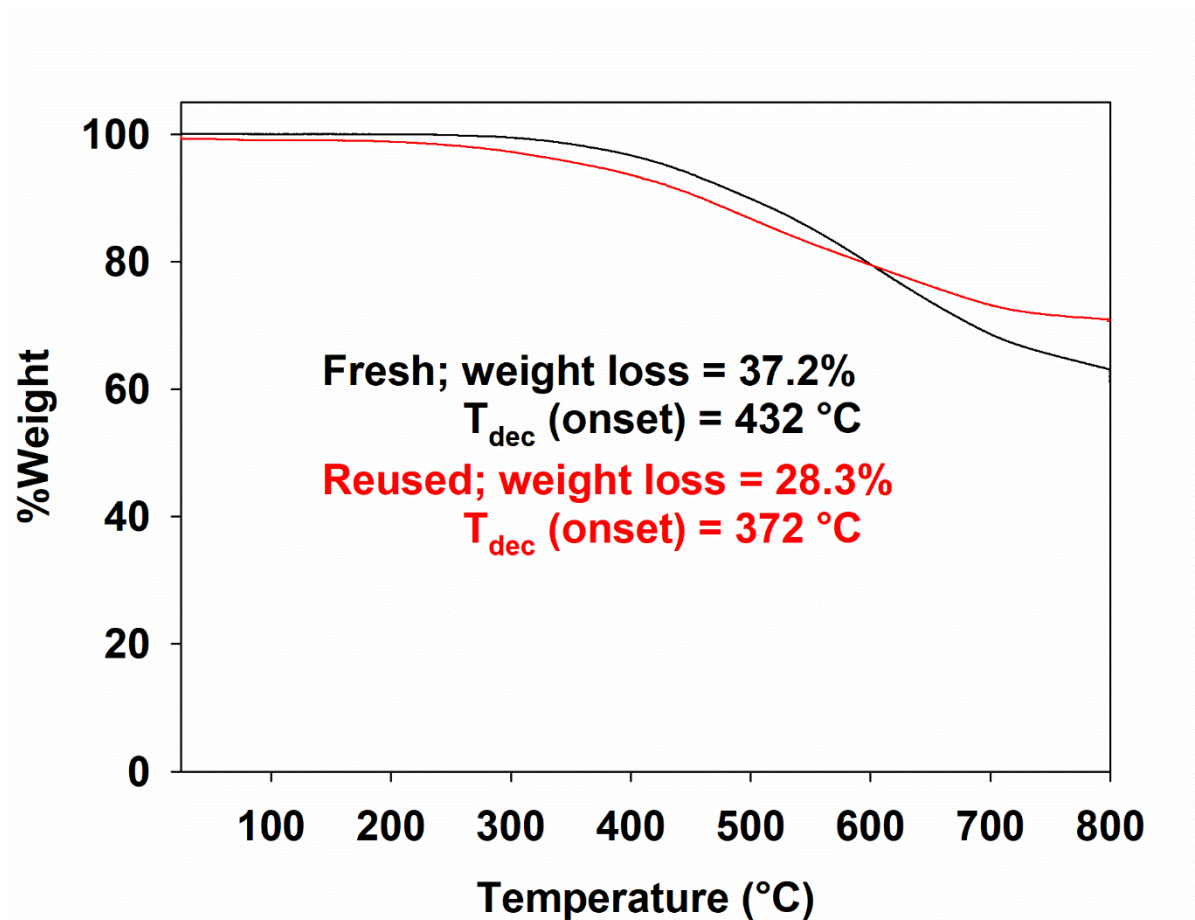


**Figure 4.8** TGA of fresh and 6 time reused F-Pyr+DEB catalysts.

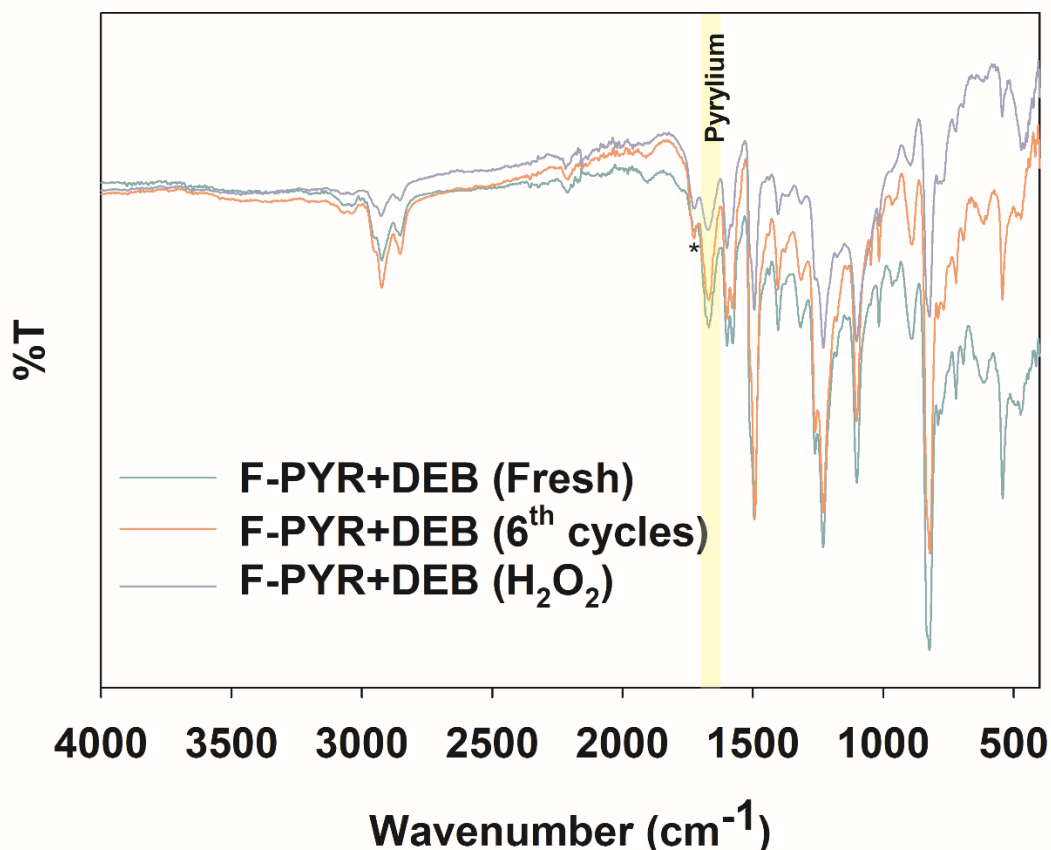
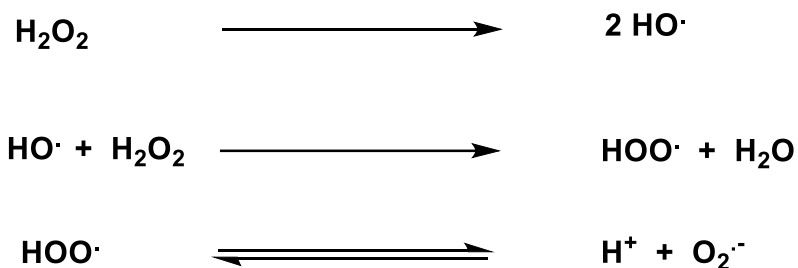


**Figure 4.9** FTIR spectra of fresh, 6<sup>th</sup> time reused and H<sub>2</sub>O<sub>2</sub> treated F-Pyr+DEB. (\* denotes carbonyl peak at 1738 cm<sup>-1</sup>).

#### **4.4.7 Plausible reaction mechanism**

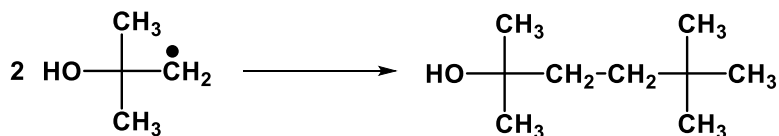
H<sub>2</sub>O<sub>2</sub> can dissociate and form more reactive oxygen species (ROSs) including HO•, HOO• and O<sub>2</sub><sup>•-</sup> as shown in Scheme 4.2.<sup>31</sup> To investigate influence of the ROSs, chemicals namely *t*-butanol,  $\alpha$ -tocopherol, and *p*-benzoquinone were used as a scavenger for HO•, HOO• and O<sub>2</sub><sup>•-</sup>, respectively. The formation of ROSs and scavenging processes of ROSs are shown in Scheme 4.3 and 4.4, respectively as they were discussed in the previous works.<sup>32-34</sup> The effect of ROSs was studied using 1 mmol of sulphide, 3 mmol of H<sub>2</sub>O<sub>2</sub>, 3 mL of acetonitrile at 60 °C for 32 h and the same molar ratio of scavenger to H<sub>2</sub>O<sub>2</sub> was added as shown in Figure 4.10. All

scavenger added condition showed the similar conversion. However, the scavengers affected the selectivity of the products. Without scavenger, the sulfoxide product was over oxidised to sulfone product (70.7%) due to the excess reactive species over long reaction time. The adding of scavengers can reduce over oxidation product as the reactive species were deactivated by the scavengers. The scavengers of  $\text{HOO}\cdot$  and  $\text{O}_2^{\cdot-}$  showed similar selectivity of the products due to the co-existence of these species *via*  $\text{H}^+$  exchange equilibrium (Scheme 4.3) and they retarded over oxidation more than that of  $\text{HO}\cdot$  indicating that the reaction mechanism occurred mainly *via* a perhydroxyl radical transfer pathway as shown in Scheme 4.5. A similar mechanism was also reported in previous work.<sup>35</sup>

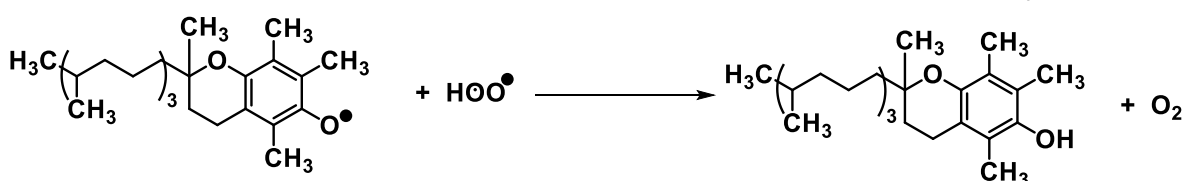
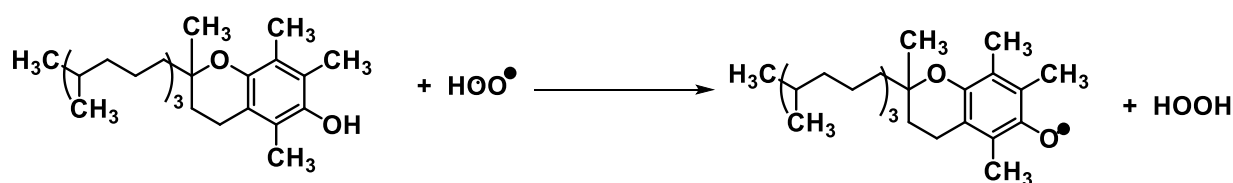


**Scheme 4.3** Formation of reactive oxygen species from  $\text{H}_2\text{O}_2$ .<sup>31</sup>

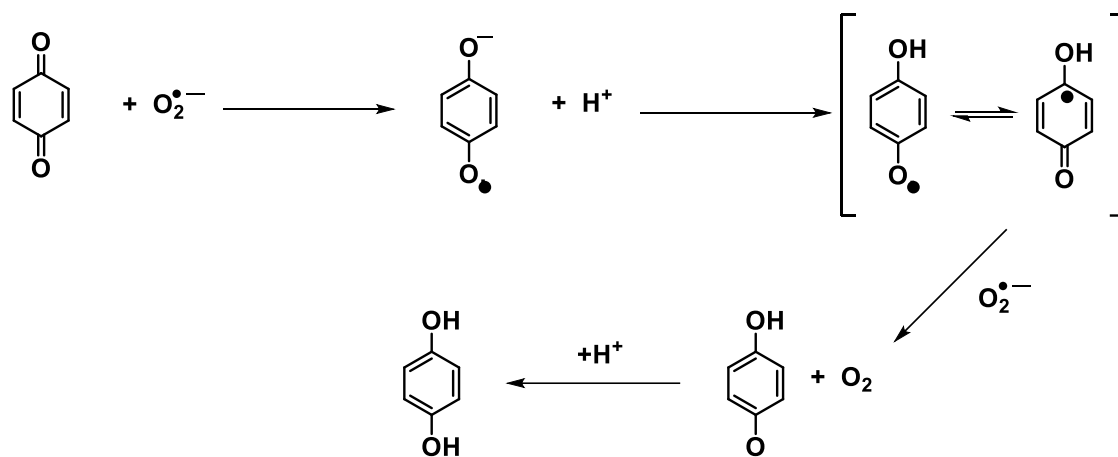
(a)



(b)



(c)



**Scheme 4.4** Scavenging processes of ROSs by (a) t-butanol, (b)  $\alpha$ -tocopherol and (c) *p*-benzoquinone.<sup>32–34</sup>

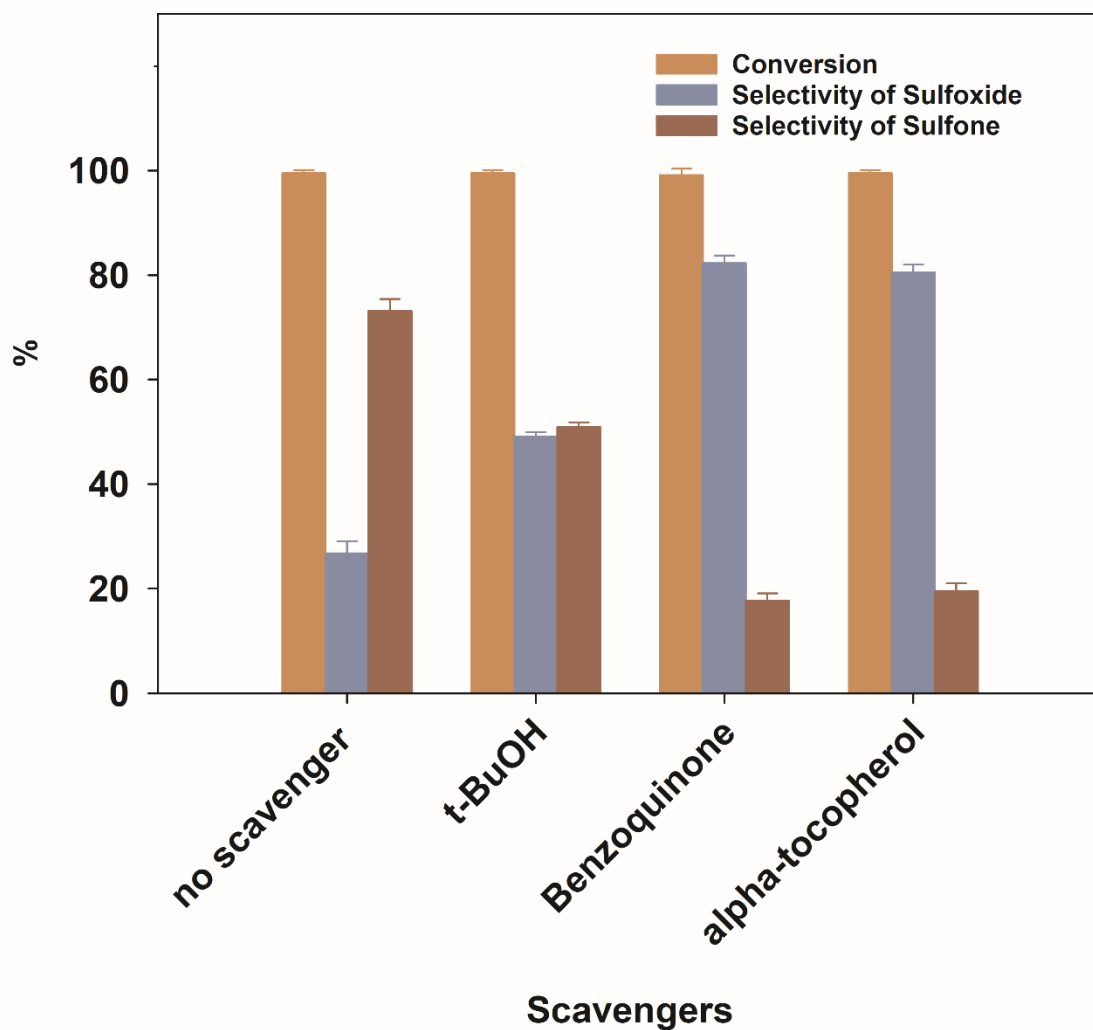
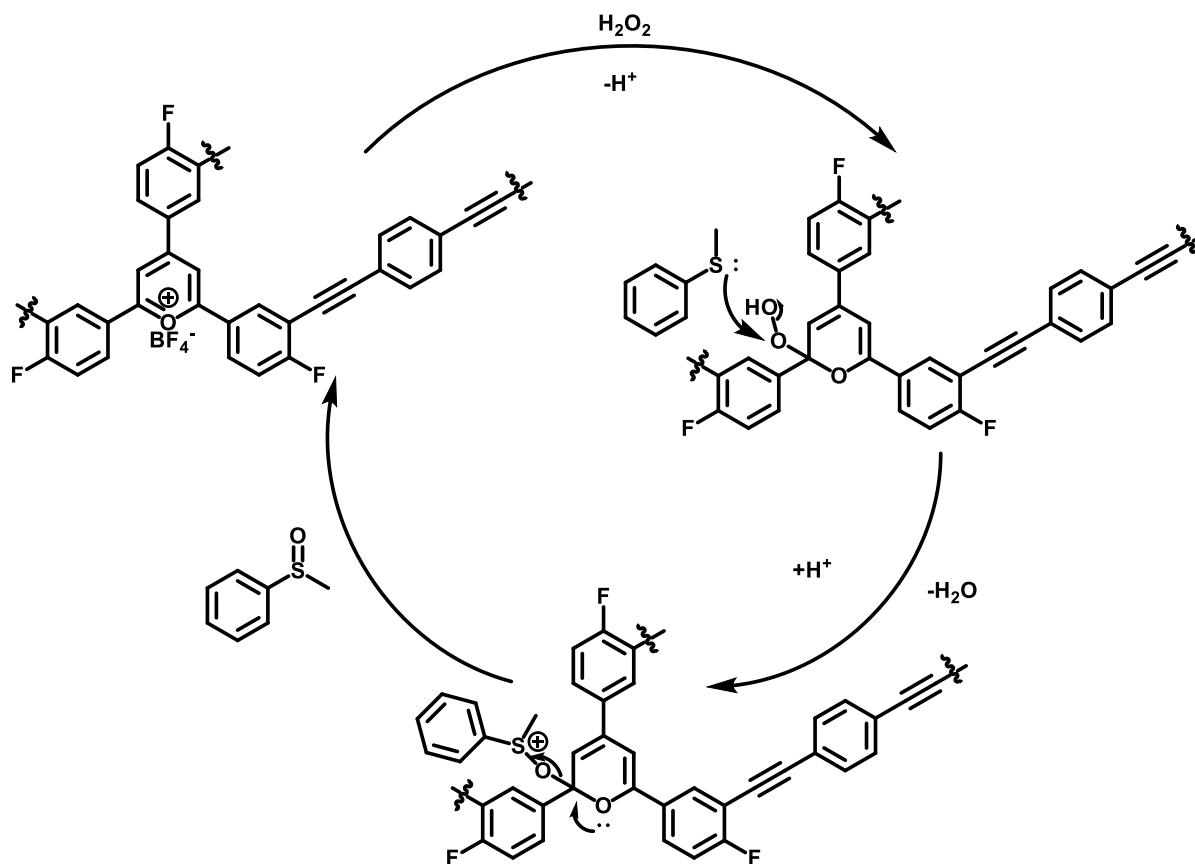


**Figure 4.10** Effect of reactive oxygen scavengers on thioanisole oxidation (Condition: 1 mmol of thioanisole, 3 mmol of  $\text{H}_2\text{O}_2$ , 3 mmol of scavenger, 3 mL of acetonitrile at  $60^\circ\text{C}$  for 32 h). (The results are an average of 3 experiments)



**Scheme 4.5** The plausible mechanism of thioanisole oxidation catalysed by pyrylium CMPs *via* a perhydroxyl radical transfer pathway.

Pyrylium CMPs catalysts showed a high conversion of 99% and selectivity of 94% at the optimum conditions (60 °C, 2 h and 3 mmol of  $\text{H}_2\text{O}_2$  using 30 mg of F-PYR+DEB). The synthesised CMPs are compared with other catalysts on thioanisole oxidation. Tshentu *et al.*, reported chloromethylated polystyrene-anchored oxovanadium (IV) complex for oxidation of thioanisole and the catalyst reached maximum conversion of 99% after 100 minutes using 35 mg of catalyst at 60 °C. However, the catalyst showed a poor selectivity of sulfoxide product even at room temperature at just below 60%. Moreover, the %conversion dropped to 80% after 3<sup>rd</sup> time reuse at 250 minutes and room temperature.<sup>16</sup> Mesoporous niobosilicates (Niobium (Nb) incorporated porous silica) with high surface areas up to 970  $\text{m}^2/\text{g}$  were

used as catalysts for thioanisole oxidation and they showed the maximum conversion at 90% and a high selectivity of sulfoxide at 90% after 12 h at 50 °C using 1 mmol of H<sub>2</sub>O<sub>2</sub> and 40 mg of catalyst.<sup>36</sup> High surface area modified Ta loaded mesoporous silicas (MCM-41) were prepared and they showed high surface areas up to 804 m<sup>2</sup>/g. The materials were utilised as catalysts for thioanisole oxidation. The optimum catalyst showed a relatively high conversion at 80% and more than 95% of selectivity of sulfoxide after 40h using 1 mmol of thioanisole and H<sub>2</sub>O<sub>2</sub>, 0.012 mmol of Ta at 25 °C.<sup>37</sup> Xie *et al.*, reported thioanisole oxidation with H<sub>2</sub>O<sub>2</sub> by 8-quinolinolato manganese(III) complexes. The catalysts showed a high conversion up to 93% with 71% selectivity of sulfoxide product using 0.2 mol% of catalyst, 1.3 mmol of H<sub>2</sub>O<sub>2</sub> at 10 °C for 2 h.<sup>1</sup> These showed that metal free pyrylium CMP catalysts showed comparable or even higher conversions and selectivity of sulfoxide as well as faster reaction rates when compared with other metal loaded porous materials and homogeneous metal complexes.

#### 4.5 Conclusions

The functionalised pyrylium CMPs have been used as heterogeneous catalysts for thioanisole oxidation using H<sub>2</sub>O<sub>2</sub> as an oxidising agent. The optimum condition for thioanisole oxidation was 2 h at 60 °C using 30 mg of F-Pyr+DEB, 3.0 mmol of H<sub>2</sub>O<sub>2</sub> in acetonitrile, which gave a high conversion up to 99% with high selectivity of sulfoxide (94%). The catalytic activity of F-Pyr+DEB decreased over multiple reuses due to pore blocking and structure collapse under strong oxidising and high temperature conditions. The mechanism was investigated by scavenger method and the catalyst catalysed the reaction *via* a perhydroxyl radical transfer pathway. Even though the pyrylium CMPs showed poor reusability, the materials showed a high conversion of thioanisole and high selectivity of sulfoxide product using a short

reaction time. Furthermore, the materials also exhibited comparable or higher catalytic activity compared to previous studies.

#### 4.6 References

- 1 F. Xie, Z. Fu, S. Zhong, Z. Ye, X. Zhou, F. Liu, C. Rong, L. Mao and D. Yin, *J. Mol. Catal. A Chem.*, 2009, **307**, 93–97.
- 2 M. Madesclaire, *Tetrahedron*, 1986, **42**, 5459–5495.
- 3 L. Postigo, M. Ventura, T. Cuenca, G. Jiménez and B. Royo, *Catal. Sci. Technol.*, 2015, **5**, 320–324.
- 4 C. A. Bunton and N. D. Gillitt, *J. Phys. Org. Chem.*, 2002, **15**, 29–35.
- 5 S. Yamaguchi, A. Suzuki, M. Togawa, M. Nishibori and H. Yahiro, *ACS Catal.*, 2018, **8**, 2645–2650.
- 6 V. Mirkhani, S. Tangestaninejad, M. Moghadam, I. Mohammadpoor-Baltork and H. Kargar, *J. Mol. Catal. A Chem.*, 2005, **242**, 251–255.
- 7 N. J. Leonard and C. R. Johnson, *J. Org. Chem.*, 1962, **27**, 282–284.
- 8 Y. Ogata and T. Kamei, *Tetrahedron*, 1970, **26**, 5667–5674.
- 9 C. Schöneich, A. Aced and K. D. Asmus, *J. Am. Chem. Soc.*, 1993, **115**, 11376–11383.
- 10 R. S. Srivastava, *Appl. Organomet. Chem.*, 2001, **15**, 769–771.
- 11 A. Jayaraman and A. L. L. East, *J. Org. Chem.*, 2012, **77**, 351–356.
- 12 S. T. Purrington and A. G. Glenn, *Org. Prep. Proced. Int.*, 1985, **17**, 227–230.
- 13 A. Goti and F. Cardona, in *Green Chemical Reactions*, Springer Netherlands,

- 2008, pp. 191–212.
- 14 S. Doherty, J. G. Knight, M. A. Carroll, J. R. Ellison, S. J. Hobson, S. Stevens, C. Hardacre and P. Goodrich, *Green Chem.*, 2015, **17**, 1559–1571.
  - 15 W. Al-Maksoud, S. Daniele and A. B. Sorokin, *Green Chem.*, 2008, **10**, 447–451.
  - 16 Z. R. Tshentu, C. Togo and R. S. Walmsley, *J. Mol. Catal. A Chem.*, 2010, **318**, 30–35.
  - 17 P. Cruz, M. Fajardo, I. Del Hierro and Y. Pérez, *Catal. Sci. Technol.*, 2019, **9**, 620–633.
  - 18 S. Alavi, H. Hosseini-Monfared and P. Aleshkevych, *RSC Adv.*, 2014, **4**, 48827–48835.
  - 19 K. Tanaka, K. Kubo, K. Iida, K. Otani, T. Murase, D. Yanamoto and M. Shiro, *Asian J. Org. Chem.*, 2013, **2**, 1055–1060.
  - 20 H. Haddadi, S. M. Hafshejani and M. R. Farsani, *Catal. Letters*, 2015, **145**, 1984–1990.
  - 21 A. L. Nuzhdin, D. N. Dybtsev, V. P. Fedin and G. A. Bukhtiyarova, *J. Chem. Soc. Dalt. Trans.*, 2009, 10481–10485.
  - 22 V. R. Tumula, S. Bondwal, P. Bisht, C. Pendem and J. Kumar, *React. Kinet. Mech. Catal.*, 2012, **107**, 449–466.
  - 23 G. A. B. Gonçalves, S. M. G. Pires, M. M. Q. Simões, M. G. P. M. S. Neves and P. A. A. P. Marques, *Chem. Commun.*, 2014, **50**, 7673–7676.
  - 24 C. Su, R. Tandiana, B. Tian, A. Sengupta, W. Tang, J. Su and K. P. Loh, ,

DOI:10.1021/acscatal.6b00443.

- 25 H. Zhang, Q. Huang, W. Zhang, C. Pan, J. Wang, C. Ai, J. Tang and G. Yu, *ChemPhotoChem*, 2019, **3**, cptc.201900095.
- 26 C. Sui, L. Xing, X. Cai, Y. Wang, Q. Zhou and M. Li, *Catalysts*, 2020, **10**, 243.
- 27 R. J. Isaifan, S. Ntais and E. A. Baranova, *Appl. Catal. A Gen.*, 2013, **464–465**, 87–94.
- 28 E. W. Thiele, *Ind. Eng. Chem.*, 1939, **31**, 916–920.
- 29 K. Wang, L. G. Meng and L. Wang, *Org. Lett.*, 2017, **19**, 1958–1961.
- 30 K. Huang, Y. Xu, L. Wang and D. Wu, *RSC Adv.*, 2015, **5**, 32795–32803.
- 31 B. H. J. Bielski, D. E. Cabelli, R. L. Arudi and A. B. Ross, *J. Phys. Chem. Ref. Data*, 1985, **14**, 1041–1100.
- 32 E. L. Jenner, *Org. Synth.*, 1960, **40**, 90.
- 33 J. Cedrowski, G. Litwinienko, A. Baschieri and R. Amorati, *Chem. - A Eur. J.*, 2016, **22**, 16441–16445.
- 34 M. Zhu, J. Lu, Y. Hu, Y. Liu, S. Hu and C. Zhu, *Environ. Sci. Pollut. Res.*, 2020, **27**, 31289–31299.
- 35 B. K. Kundu, M. Das, R. Ganguly, P. A. Bhoje and S. Mukhopadhyay, *J. Catal.*, 2020, **389**, 305–316.
- 36 A. Feliczyk-Guzik, A. Wawrzyńczak and I. Nowak, *Microporous Mesoporous Mater.*, 2015, **202**, 80–89.
- 37 M. Fadhli, I. Khedher and J. M. Fraile, *J. Mol. Catal. A Chem.*, 2015, **410**, 140–148.

## 4.7 Appendices

### **4.7.1 Particle size analysis of the synthesised CMPs**

**Table A4.1** The particle sizes of the synthesised pyrlium based CMPs

Polymers	Particle size (micron)	
	TEB	DEB
Pyrylium	43.3	40.5
m-Pyrylium	50.1	38.1
Me-Pyrylium	28.6	27.3
MeO-Pyrylium	25.7	30.9
F-Pyrylium	42.6	23.7

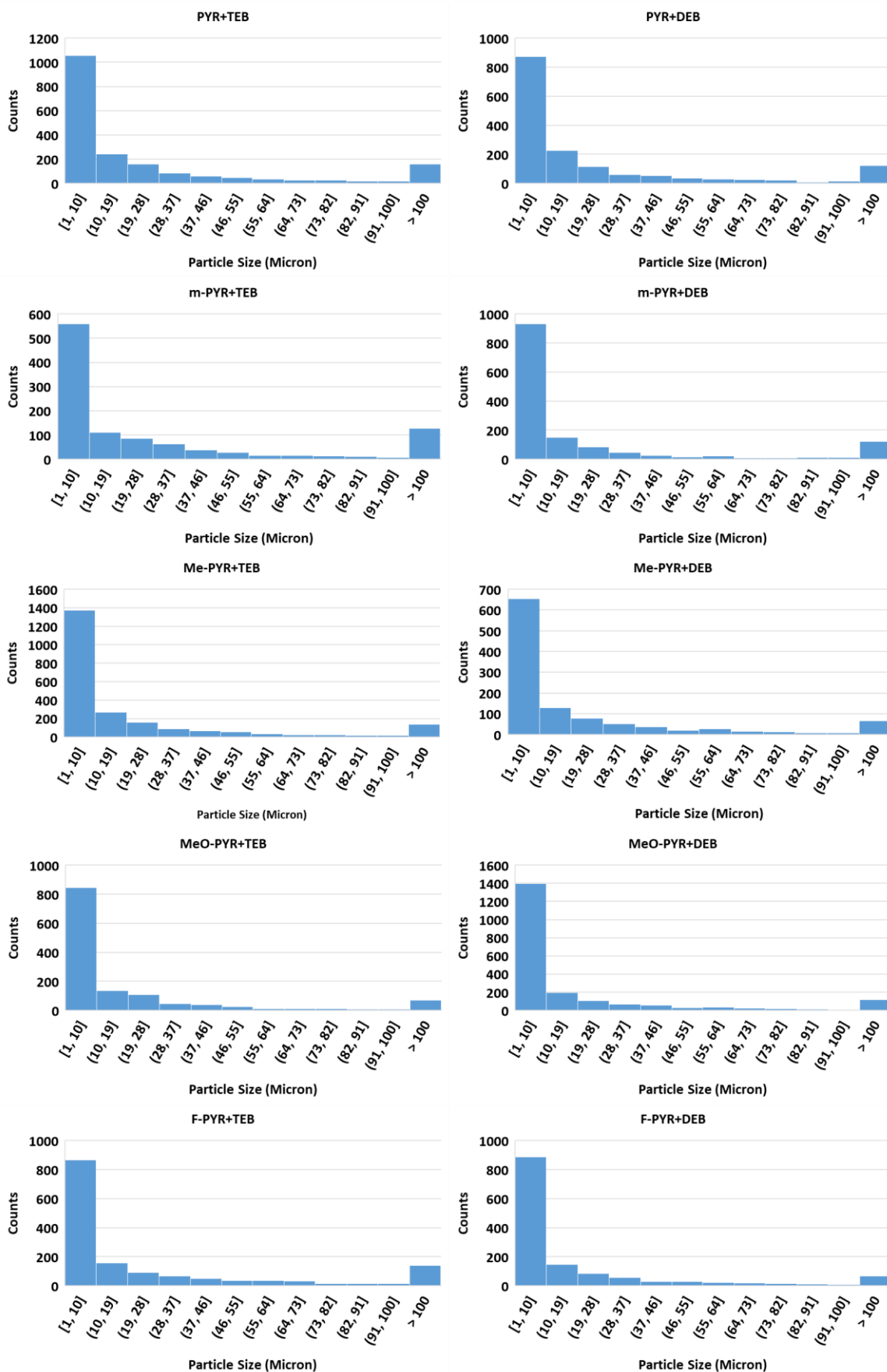


**Figure A4.1** The particle size distributions of the synthesised pyrlium CMPs.

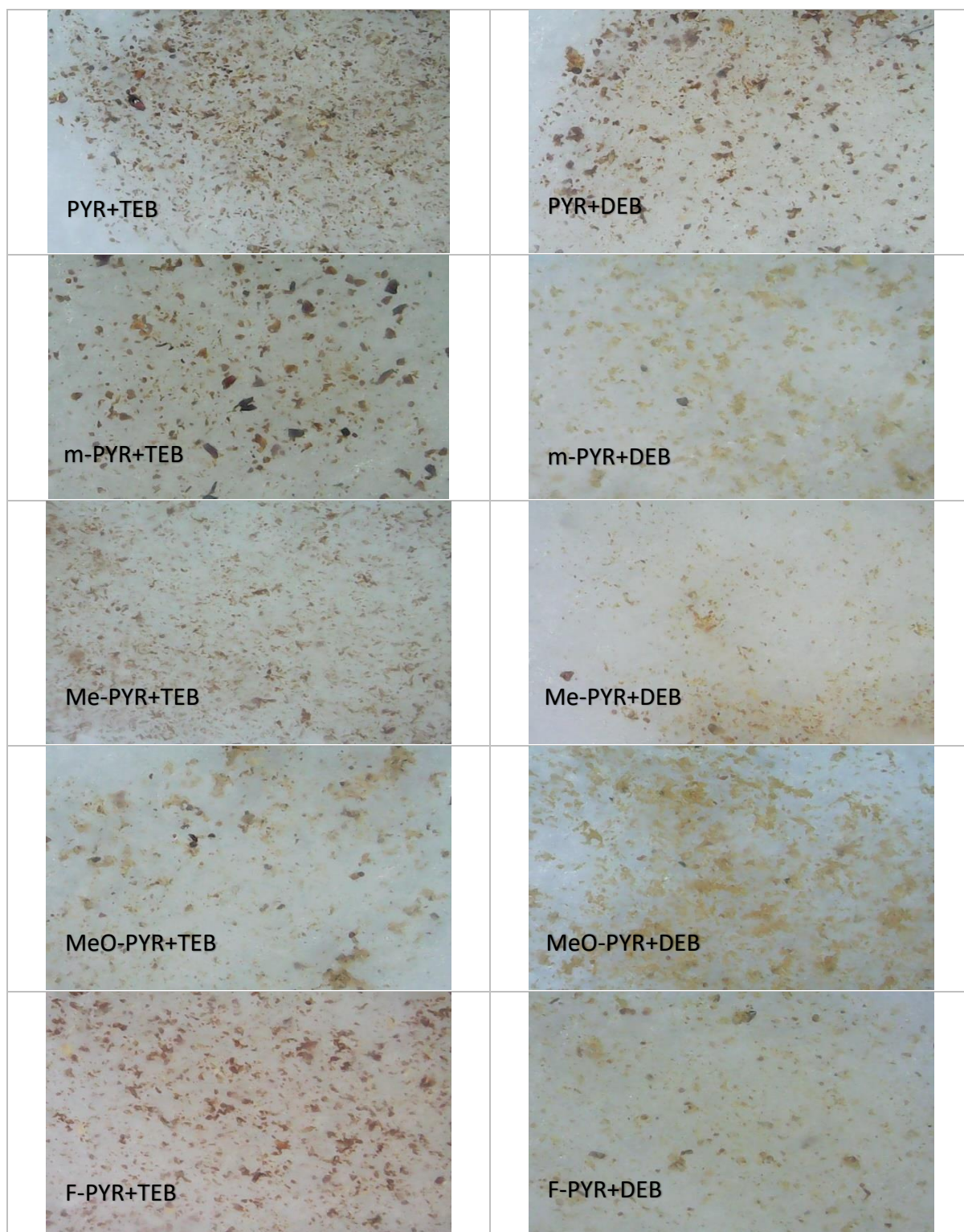


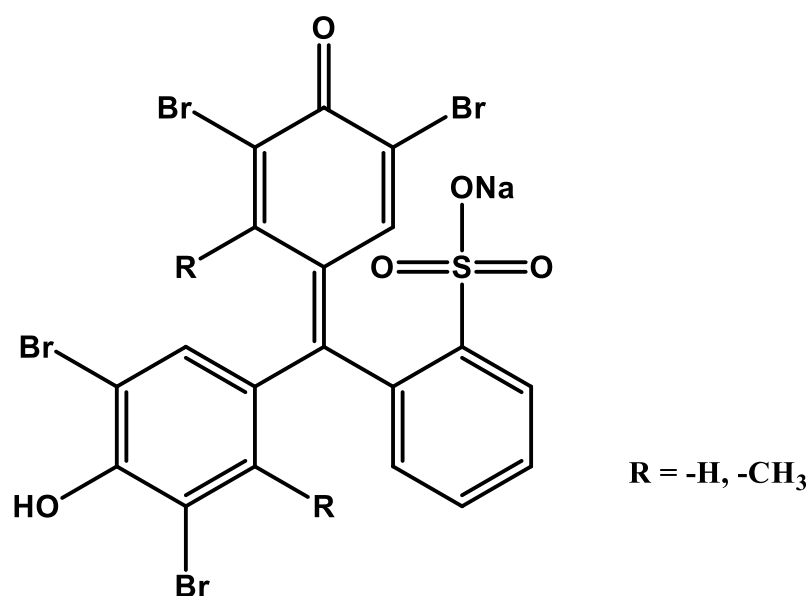
**Figure A4.2** The optical micrographs of the obtained pyrylium CMPs.

# Chapter 5

## Synthesis and Characterisation of Bromophenol Blue and Bromocresol Green Dyes Incorporated Conjugated Microporous Polymers

### 5.1 Introduction

Bromophenol blue (3',3'',5',5''-tetrabromophenolsulfonphthalein) (**BB**) and bromocresol green (3,3',5,5'-tetrabromo-*m*-cresolsulfonphthalein) (**BG**) are synthetic compounds belonging to a class of dyes named sulfonephthaleins which are sulfonic acids derived from phthaleins (Scheme 5.1).<sup>1</sup> They are important dyes that can be used as pH indicators<sup>1,2</sup>, electrophoretic colour marker<sup>3-5</sup> and colorants for printing and textile industrial.<sup>6</sup>



**Scheme 5.1** Structure of bromophenol blue sodium salt (R = H) and bromocresol green sodium salt (R = CH<sub>3</sub>).

The sulfonic acid groups in the molecules make it possible to use them as Brønsted acid catalysts for various organic reactions such as hydrolysis, esterification and transesterification. Organic dyes with halogen functional groups have been incorporated in-to porous polymer networks and the synthesised materials possessed a high surface area with high thermal and chemical stability.<sup>7-14</sup> They have been used for photocatalytic organic reactions showing a high catalytic activity and excellent reusability.<sup>7-12</sup> Both bromophenol blue and bromocresol green contain 4 bromo groups in their structures which can be reacted to form a porous polymer by using cross-coupling reactions such as Sonogashira-Hagihara and Suzuki-Miyaura as well as Yamamoto homocoupling to produce a stable, high surface area reusable heterogeneous acid catalyst.

According to previous reports, acid functionalised porous polymers have been used as acid catalysts for esterification of free fatty acids and transesterification of vegetable oils with alcohols due to their large surface area, excellent stability and high acidity.<sup>15-22</sup> A sulfonated HCP synthesised from carbazole was applied as an acid catalyst for the esterification of different free fatty acids (FFAs) at room temperature showing high %yield of product as well as reusability in up to 4 cycles.<sup>15</sup> Likewise, sulfonated phenol and bisphenol A based HCPs were synthesised and used as acid catalysts for both esterification of FFAs and transesterification of various vegetable oils. The materials showed excellent catalytic activity at room temperature and 60 °C with excellent reusability up to 6 cycles.<sup>17</sup> Acid functionalised CMP networks derived from 1,3 and 1,4-diethynyl benzene (DEB) showed high surface areas up to 550 m<sup>2</sup>/g and high %conversion of FFAs to fatty acid methyl esters (FAMEs) at 60 °C for 24 h. However, the reusability study of these materials for biodiesel production was not reported.<sup>22</sup>

Functionalised HCPs have been widely studied for biodiesel production due to a high surface area as well as high thermal and chemical stability. However, HCPs are usually synthesised *via* Friedel Crafts alkylation required stoichiometric amounts of Lewis acid catalysts such as  $\text{FeCl}_3$ ,  $\text{AlCl}_3$  and  $\text{SnCl}_4$  as well as toxic solvents such as 1,2-dichloroethane. Moreover, the reaction only works with an alkyl halide but not occurs when aryl halide or vinyl halide are utilised due to unstable carbocation intermediate, thus the formation of BB and BG based HCPs *via* Friedel Crafts alkylation are impossible.<sup>23</sup> Sonogashira cross coupling requiring catalytic amount of Pd and Cu catalysts is more suitable method for BB and BG monomers to form porous polymers as this reaction can be promoted by electron deficient aryl halides.<sup>24</sup>

In this work, the bromophenol blue and bromocresol green based conjugated microporous polymers have been synthesised using Sonogashira-Hagihara cross-coupling reaction to yield high surface area polymers and then they were post functionalised with chlorosulfonic acid to yield high acidic porous polymers. The synthesis and characterisation of these polymers will be discussed in this chapter.

## 5.2 Aims of the chapter

- To synthesise bromophenol blue (BB) and bromocresol green (BG) incorporated into CMPs *via* Sonogashira-Hagihara cross-coupling.
- To chemically post modify the obtained CMPs with chlorosulfonic acid to form acid functionalised BB and BG CMPs (s-CMPs)
- To characterise the as-synthesised CMPs and acid functionalised CMPs using elemental analysis (EA), FTIR,  $^{13}\text{C}$  CP MAS NMR, acid determination and thermogravimetric analysis (TGA).

## 5.3 Experimental

### **5.3.1 Materials**

Bromophenol blue (BB), bromocresol green (BG), 1,3,5-triethynylbenzene (TEB) and copper (I) iodide (CuI) were obtained from Alfa Aesar. 1,4-diethynylbenzene (DEB) was purchased from Acros Organics. Pd(PPh<sub>3</sub>)<sub>4</sub>, anhydrous dimethylformamide (DMF), and anhydrous triethylamine (Et<sub>3</sub>N) were bought from Sigma-Aldrich. Methanol, acetone and chloroform were obtained from Fisher Scientific. Nitrogen gas (oxygen free) was purchased from BOC. All chemicals have a purity over 95% and were used as received.

### **5.3.2 Synthesis of BB and BG based CMPs via Sonogashira – Hagihara cross coupling**

The procedure was adapted from the previous reports in which they fixed the ratio of halogen and alkyne at 1:1.5 because this ratio gave the highest surface area.<sup>25–27</sup> BB or BG (0.5 mmol), TEB (2 equivalent) or DEB (3 equivalent) and CuI (0.16 equivalent, 15 mg) were introduced into a two-neck round bottom flask and which was evacuated and backfilled with nitrogen gas 3 times. Anhydrous DMF (5 mL) and Et<sub>3</sub>N (5 mL) were added and the reaction mixture was stirred and heated to 100 °C under a nitrogen atmosphere. Tetrakis(triphenylphosphine)palladium(0) (0.086 equivalent, 50 mg) was mixed with 2 mL of anhydrous DMF and the mixture was added as a slurry to the reaction. The reaction was left for 24 h. The solid product was filtered by vacuum filtration and washed with methanol, chloroform and acetone, respectively. The solid product was then further purified by Soxhlet extraction using methanol for 16 h and the obtained solid was dried under vacuum at 80 °C. Yields were 120, 120, 99 and 114% for BB+TEB, BG+TEB, BB+DEB and BG+DEB, respectively.

### **5.3.3 Sulfonation of BB and BG CMPs**

The sulfonation reaction was adapted from the procedure as reported by Kalla *et al.*<sup>17</sup> 0.4 g of BB- or BG-CMP was suspended and stirred in 10 mL of dichloromethane (DCM). A mixture of 4 mL of chlorosulfonic acid and 10 mL of DCM was slowly added into the polymer suspension and the reaction was stirred for 48 h at 25 °C. After that, the reaction mixture was diluted with 50 mL of DCM and was vacuum filtered and washed with water until the filtrate was neutral. The solid product was dried under vacuum at 80 °C. For comparison, BB- and BG-CMPs were also treated with hydrochloric acid using the same procedure.

### **5.3.4 Determination of acidity of the synthesised materials**

100 mg of the synthesised CMP was added into 10 mL of 0.13 M NaOH and then the mixture was stirred at 40 °C for overnight. After cool down, the polymer was removed and washed with water. The filtrate was titrated by 0.337 M HCl solution using phenolphthalein as an indicator.

## **5.4 Results and Discussion**

The BB and BG were polymerised with either TEB or DEB *via* a Sonogashira-Hagihara cross-coupling reaction using Pd(PPh<sub>3</sub>)<sub>4</sub> and CuI at 100 °C for 24 h to yield four networks: BB-TEB, BB+DEB, BG+TEB and BG+DEB CMPs (Scheme 5.2). The yields of the synthesised polymers were from 99 to 120%. Yields exceeding 100% are common for CMP networks and are often attributed to a combination of unreacted bromo end groups, residual (trapped) monomers, solvents and adsorbed gases (water vapour, carbon dioxide etc.) as reported previously.<sup>26</sup> A quantity of the BB and BG CMPs were post-functionalised with chlorosulfonic acid to increase acidity of the materials. The as-synthesised and the sulfonated CMPs were characterised by

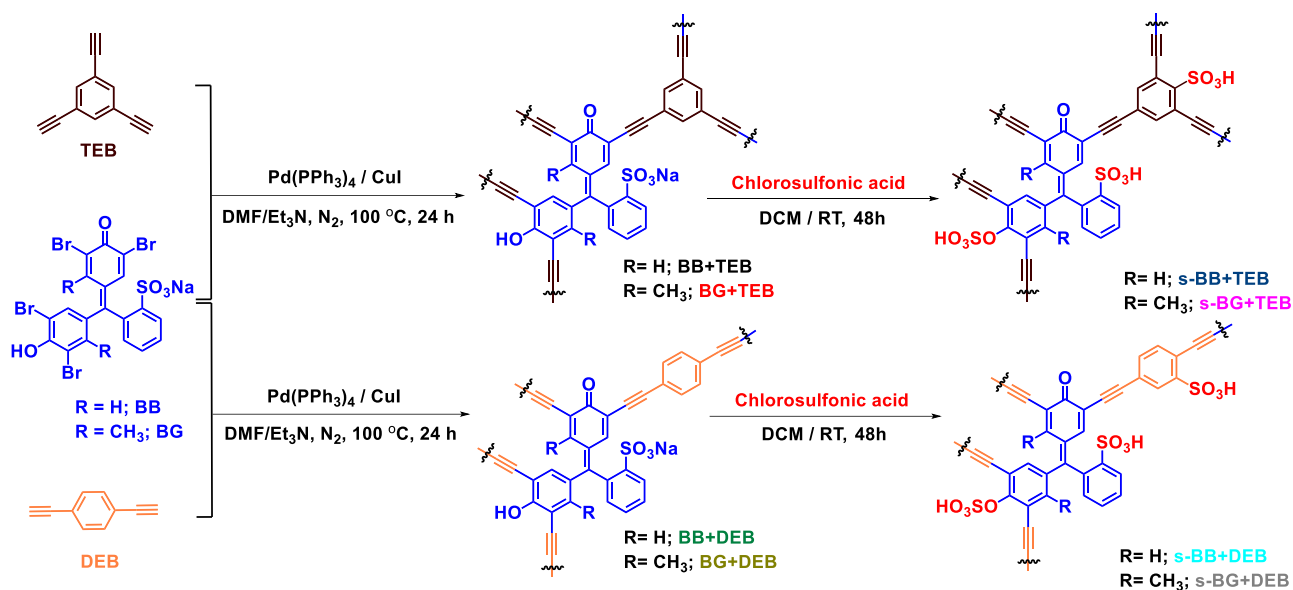
various solid-state methods to determine the chemical structures, porosity and thermal stability of the synthesised materials.

#### **5.4.1 Elemental analysis (EA)**

Elemental analysis results of all synthesised polymers are shown in Table 5.1. Sulphur was observed in elemental analysis of the as-synthesised polymers confirming the successful incorporation of BB and BG monomers. The found values of carbon and sulphur contents were lower than expected due to the residual bromine end groups while hydrogen was higher than the theory because of moisture adsorbed or trapped in the pores of hydrophilic networks as discussed in the previous work.<sup>26</sup> This was consistent with over 100% yield of the synthesised polymers. The sulphur content of sulfonated CMPs (s-CMPs) was significantly higher than the as-synthesised and HCl-treated CMPs due to the incorporation of sulfonic groups into the sulfonated polymers. The sulfonated BB+DEB showed the highest sulphur content due to the incorporation of more sulfonic group as benzene in the DEB alkyne unit having less steric hindrance than TEB. An increase in halogen contents after protonation and sulfonation might cause from the interference from residual chloride ion.

**Table 5.1** Elemental analysis of the synthesised polymers.

Sample	Theoretical				Found			
	C	H	S	Halogen	C	H	S	Halogen
BB+TEB	77.47	2.27	4.81	0	65.96	5.02	2.41	1.39
BB+DEB	79.02	2.84	4.31	0	69.11	4.80	2.75	0
BG+TEB	77.80	2.76	4.62	0	64.79	4.94	2.23	1.92
BG+DEB	79.26	3.26	4.15	0	67.03	5.08	2.34	3.05
HCl-BB+TEB	80.11	2.50	4.97	0	64.01	4.14	3.78	5.65
HCl-BB+DEB	81.43	3.07	4.44	0	70.26	4.08	3.31	4.47
HCl-BG+TEB	80.34	3.00	4.77	0	62.86	4.10	2.79	8.38
HCl-BG+DEB	81.58	3.49	4.27	0	64.88	4.21	2.73	9.14
s-BB+TEB	72.87	2.28	9.05	0	42.35	4.28	8.67	5.76
s-BB+DEB	57.30	2.16	15.61	0	49.01	4.10	10.24	11.37
s-BG+TEB	73.36	2.74	8.70	0	46.51	4.38	9.15	11.36
s-BG+DEB	58.06	2.48	15.19	0	50.83	4.21	9.11	11.13



**Scheme 5.2** Synthesis of BB and BG based CMPs via Sonogashira reaction and post modification of the synthesised CMPs with chlorosulfonic acid.

### 5.4.2 FTIR

The as-synthesised polymers were characterised by FTIR as shown in Figure 5.1 showing the peaks at 1595, 3035 and 1735  $\text{cm}^{-1}$  assigned to C=C, C-H stretching in aromatic and C=O in tetrabromo monomers, respectively as well as the peaks at 624, 1020, and 1170-1233  $\text{cm}^{-1}$  corresponded to C-S stretching, S=O symmetric and asymmetric stretching in -SO<sub>3</sub>Na.<sup>16,28</sup> According to Figure A5.1, the disappearance of peaks at 457, 461 and 3278  $\text{cm}^{-1}$  relating to C<sub>Ar</sub>-Br in BB and BG and C-H in terminal alkyne of TEB and DEB monomers, respectively confirmed the successfully incorporation of all monomers into the obtained polymer networks. The C≡C peak in internal alkyne was observed at 2150  $\text{cm}^{-1}$  further proved the formation of CMP networks.<sup>29</sup> The HCl treated CMPs showed similar spectra with the as-synthesised CMPs as shown in Figure A5.2 while the IR spectra of the polymers treated with chlorosulfonic acid shown in Figure 5.1 illustrate an increase in intensity of sulfonic peaks and the broad OH peak at 3400  $\text{cm}^{-1}$  confirming the more incorporation of

sulfonic groups in the polymer networks. The sulfonated polymers also showed the additional peaks at 890 and 1040 $\text{cm}^{-1}$  assigned as S-O stretching and O=S=O symmetric stretching in  $-\text{OSO}_3\text{H}$ , respectively due to esterification of hydroxyl group with chlorosulfonic acid.<sup>17</sup> The peaks at 2293 and 2362  $\text{cm}^{-1}$  were assigned as C=O stretching associated from the adsorbed carbon dioxide in the synthesised CMPs containing polar groups.<sup>30</sup>

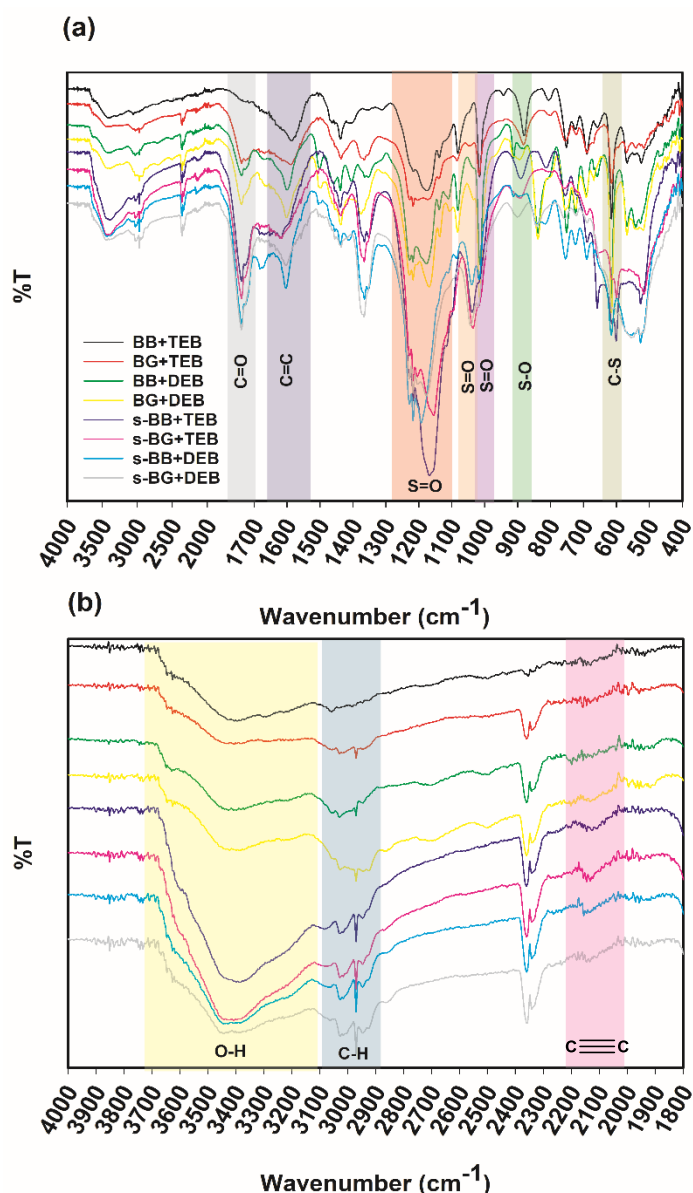


**Figure 5.1** IR spectra of as-synthesised and sulfonated CMPs ((a) from 400-4000  $\text{cm}^{-1}$  and (b) 1800-4000  $\text{cm}^{-1}$ ).

### **5.4.3 $^{13}\text{C}$ CP/MAS NMR Spectroscopy**

Structural characterisation of the BB and BG based CMPs and the sulfonated CMPs was determined by  $^{13}\text{C}$  CP/MAS NMR spectra (Figure 5.2). Due to the amorphous structure of the networks, the spectra were broad, so it is difficult to locate the exact position of each carbon. The peaks at 117-137, 144, and 154 ppm are related to ( $\text{C}_{\text{Ar}}\text{-H}$ ) or ( $\text{C}_{\text{Ar}}\text{-C}$ ) in bromo and alkyne units as labelled in Figure 5.2, ( $\text{C}_{\text{Ar}}\text{-SO}_3^-$ ), and ( $\text{C}_{\text{Ar}}\text{-OH}$ ), respectively. The results are consistent with solution  $^{13}\text{C}$  NMR of BB and BG (Figure A5.3). The small peak at 100 ppm was assigned to  $\text{-}\overset{\color{red}{\text{C}}}{\equiv}\text{C-}$  in internal alkynes while the peaks at 81.1 and 96.5 ppm were labelled as  $\text{C}\equiv\overset{\color{red}{\text{C}}}{\text{-H}}$  and  $\overset{\color{red}{\text{C}}}{\equiv}\text{C-H}$  in terminal alkynes, respectively. The peaks in solid state NMR of alkyne units are also similar with solution NMR of alkyne monomers (Figure A5.4). The presence of peaks from both monomers is indicative of successful formation of CMP networks. The additional peak at 16 ppm is assigned to the methyl group in the BG CMPs. After the BB and BG CMPs were treated with chlorosulfonic acid, the intensity of the 123 ppm peak ( $\text{C}_{\text{Ar}}\text{-H}$ ) decreased while that at 144 ppm ( $\text{C}_{\text{Ar}}\text{-SO}_3^-$ ) increased due to the substitution of sulfonic acid groups on the aromatic ring. The broadening of the peak at 154 ppm corroborates the esterification of hydroxyl group ( $\text{C}_{\text{Ar}}\text{-OH}$ ) to sulphuric acid ( $\text{C}_{\text{Ar}}\text{-OSO}_3\text{H}$ ) which is in agreement with the FTIR.

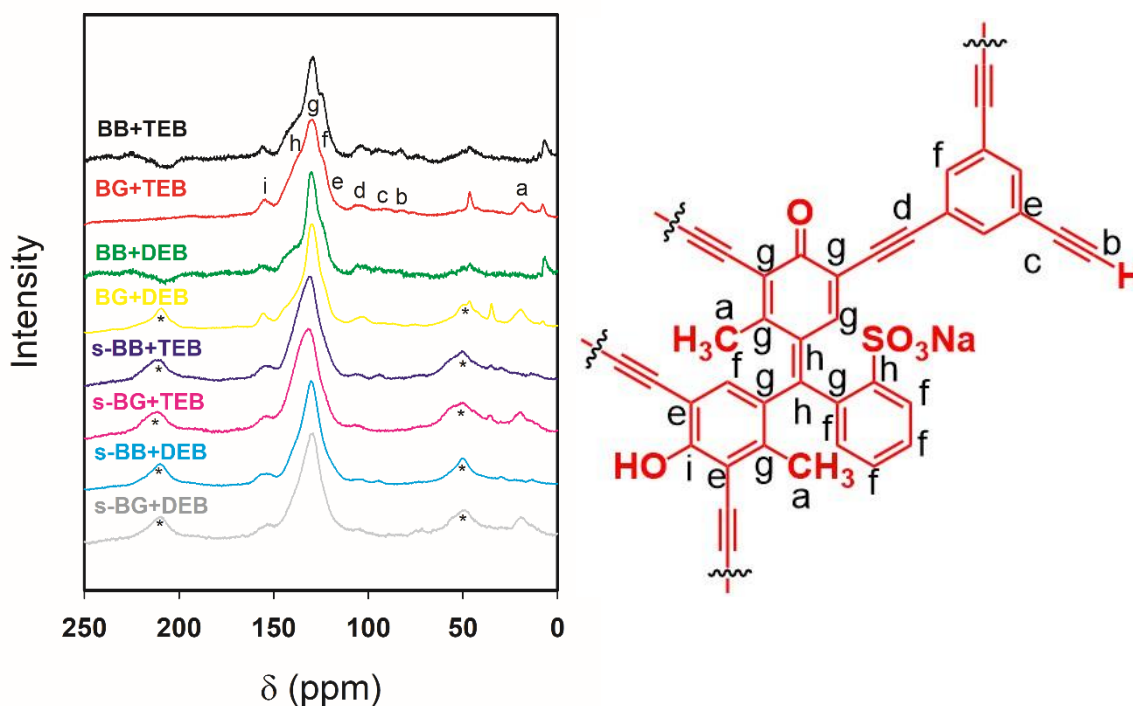


**Figure 5.2**  $^{13}\text{C}$  CP/MAS spectra of the as-synthesised CMPs and sulfonated CMPs.

(\* is spinning sideband)

#### **5.4.4 Nitrogen adsorption and desorption isotherms**

The surface properties of the synthesised materials were characterised by nitrogen adsorption/desorption isotherms. The as-synthesised BB and BG CMPs showed high BET surface areas in a range of 373 to 747  $\text{m}^2/\text{g}$  with total pore volumes from 0.22 to 0.38  $\text{cm}^3/\text{g}$  (see Table 5.2). According to Figure 5.3(a), the as-synthesised CMPs illustrated steep uptake at very low pressure which is a characteristic of Type I isotherms belonging to microporous materials. This is consistent with pore size distribution in Figure 5.3(c) which shows the main peaks centred around a pore width smaller than 2 nm indicative of mainly micropores in the materials. BB+TEB and BG+TEB showed higher surface areas than the DEB derived polymers due to the greater connectivity of the TEB linkers compared to the linear linker of DEB.<sup>31</sup> The BG

polymers showed lower surface areas than BB analogues. This could be due to the methyl group partially filling the pores,<sup>32</sup> or due to the steric hindrance and aryl bromide deactivation causing from the adjacent electron donor methyl group hindering the network formation and resulting in a lower degree of condensation.<sup>24</sup> This is consistent with the higher bromine contents of these networks as seen in the elemental analysis (Table 5.1). After the as-synthesised CMPs were treated with chlorosulfonic acid (s-CMPs), the BET surface areas and pore volumes dropped dramatically, this may be due to pore blocking caused by the incorporation of sulfonic groups into the materials. This is in agreement with type II isotherms exhibited by these networks indicative of non-porous (Figure 5.3(b)). The pore size distribution after sulfonation indicated the filling of the pores with sulfonic groups as the main peaks with the width less than 2 nm have disappeared (Figure 5.3(d)). Again the DEB derived s-CMPs showed much lower BET surface areas than the TEB analogues due to the lower steric hindrance of DEB than TEB leading to the higher degree of substitution of sulfonic group. The nitrogen adsorption and desorption isotherm results were also similar to the previous reports as the BET surface areas and pore volumes decreased after acid functionalisation.<sup>15-17</sup> The as-synthesised CMPs were also treated with HCl in order to exchange the sodium ion at sulfonate groups with protons in the polymer networks. The results showed that the HCl treated CMPs still maintained high surface areas and pore volumes and the isotherms and pore size distribution were almost identical with as-synthesised CMPs after treatment as shown in Table 5.2 and Figure 5.4(a) and (b). The small drop of the surface areas and pore volumes of HCl treated CMPs might be from residual Cl<sup>-</sup>.

**Table 5.2** BET surface areas, total pore volumes, sulphur contents and acidity of the synthesised CMPs.

Sample	S <sub>BET</sub> (m <sup>2</sup> /g)	V <sub>t</sub> (cm <sup>3</sup> /g)	S Content (%)	Acidity (mmol/g)
BB+TEB	747 ± 3	0.38	2.41	1.54
BB+DEB	580 ± 2	0.35	2.75	1.55
BG+TEB	566 ± 2	0.34	2.23	1.83
BG+DEB	373 ± 1	0.22	2.34	1.89
HCl-BB+TEB	688 ± 3	0.34	3.78	1.72
HCl-BB+DEB	511 ± 3	0.26	3.31	1.69
HCl-BG+TEB	532 ± 2	0.29	2.79	1.89
HCl-BG+DEB	463 ± 2	0.27	2.73	1.84
s-BB+TEB	349 ± 1	0.22	8.67	3.53
s-BB+DEB	12 ± 0	0.01	10.24	7.67
s-BG+TEB	303 ± 1	0.29	9.15	4.39
s-BG+DEB	60 ± 0	0.003	9.11	4.04

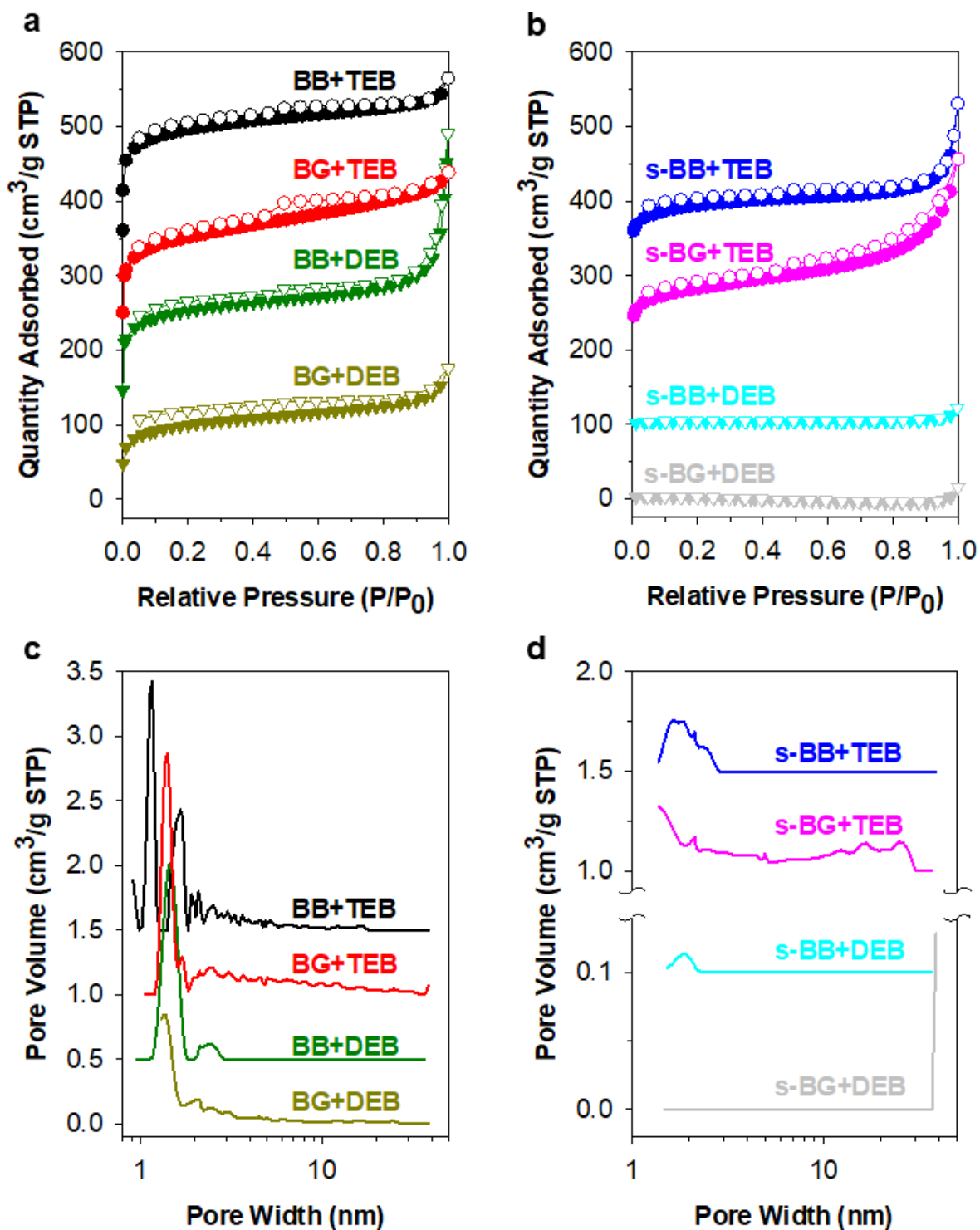


**Figure 5.3** (a) Nitrogen gas sorption isotherms (filled is adsorption and emptied is desorption) of the synthesised CMPs and (b) the sulfonated CMPs, (c) pore size distribution of the synthesised CMPs and (d) the sulfonated CMPs. The isotherms were offset by  $100 \text{ cm}^3/\text{g}$  and  $0.5 \text{ cm}^3/\text{g}$  for pore size distribution.

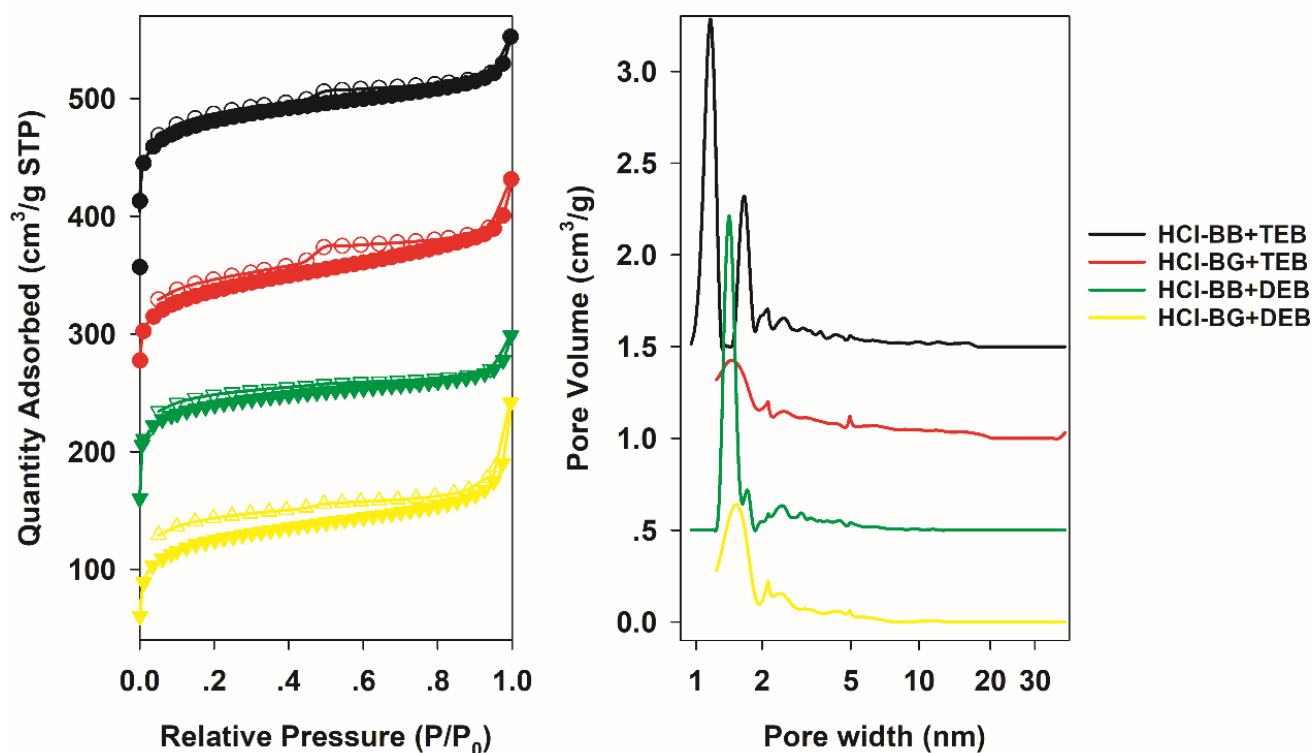


**Figure 5.4** (a) Nitrogen sorption isotherms (filled is adsorption and emptied is desorption) of HCl treated CMPs and (b) pore size distributions of HCl treated CMPs. The isotherms were offset by 100 cm<sup>3</sup>/g and 0.5 cm<sup>3</sup>/g for pore size distribution.

#### **5.4.5 Thermogravimetric analysis (TGA)**

All obtained polymers were characterised by TGA under nitrogen atmosphere as shown in Figure 5.5. All synthesised CMPs exhibited high thermal stability with onset decomposition temperature between 200 and 300 °C. BB based CMPs showed higher degradation temperature (ca. 300 °C) than the BG based CMPs (ca. 250 °C) due to the loss of methyl group in the BG based polymers. The HCl treated CMPs showed similar profiles of thermogram and degradation temperature with as-synthesised CMPs. All sulfonated CMPs showed lower decomposition temperature at approximately 200 °C because of the loss of more sulfonic group in the materials.<sup>22</sup>

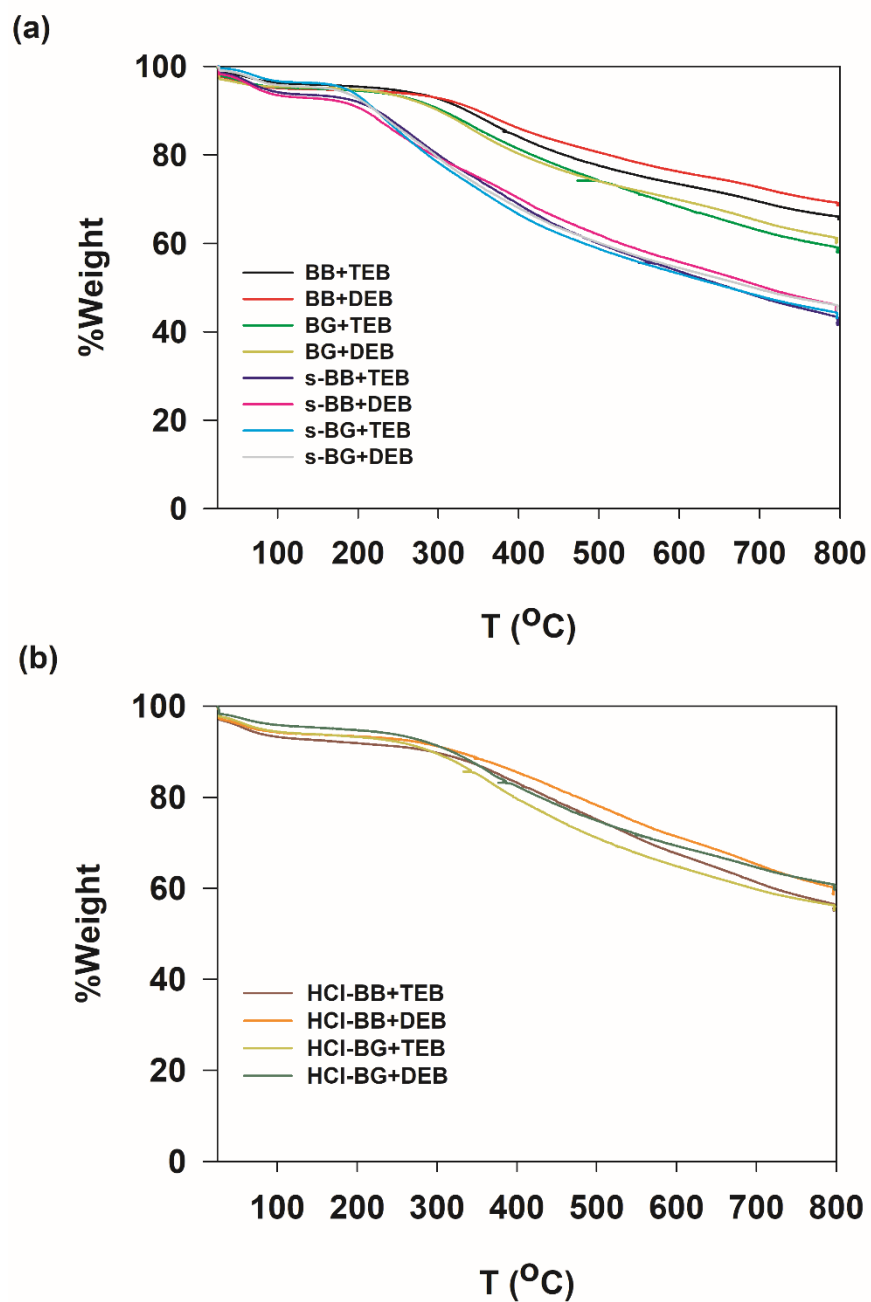


**Figure 5.5** TGA graphs of (a) non-functionalised CMPs and sulfonated CMPs and (b) HCl treated CMPs.

#### **5.4.6 Determination of acidity of the synthesised materials**

The results presented in Table 5.2 show the acidity of all polymers which were from 1.54 to 7.67 mmol/g and the results were consistent with sulphur contents from elemental analysis. After treated with HCl acid, the small increase in acidity was observed while the acidity increased significantly after treated with chlorosulfonic acid as shown in Figure 5.6. s-BB+DEB exhibited the highest acidity and it exceeded the reported results from other acid functionalised porous polymers.<sup>15-17</sup>

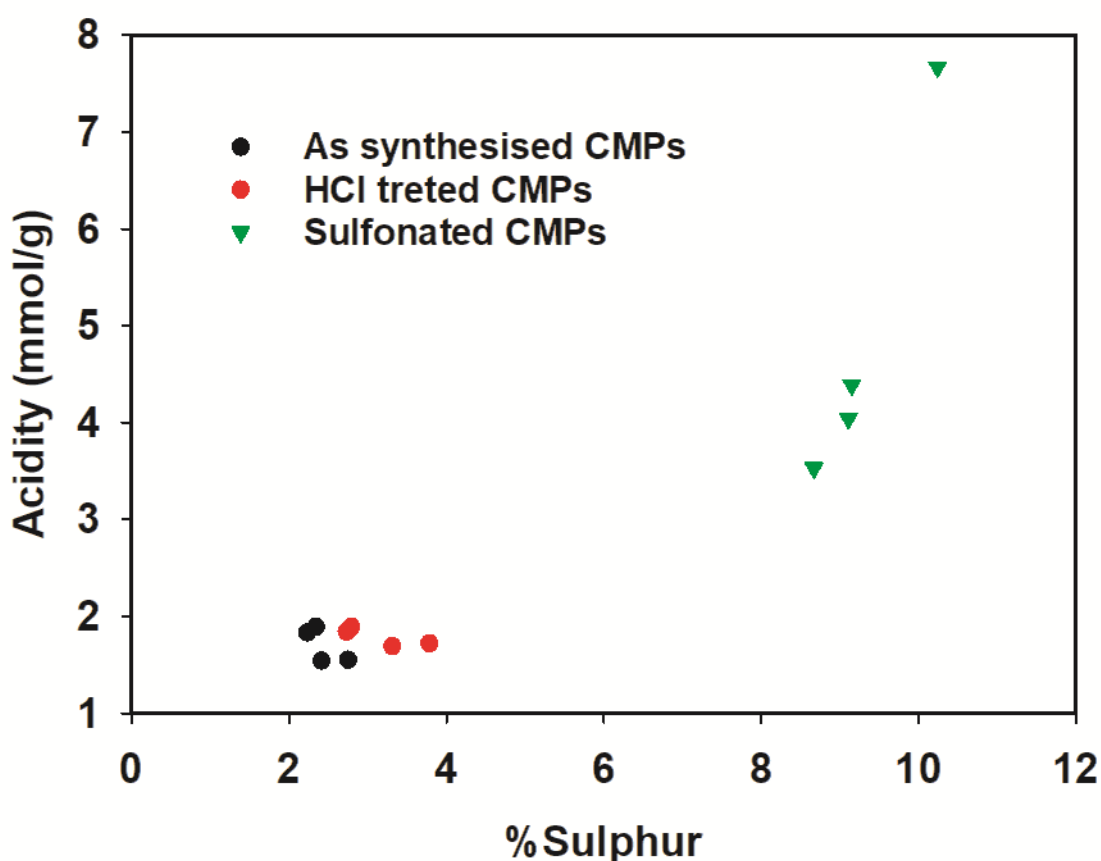


**Figure 5.6** Relationship between acidity and sulphur contents of the synthesised CMPs.

## 5.5 Conclusions

Novel BB and BG based CMPs have been successfully synthesised by Sonogashira coupling method. The synthesised materials showed high surface areas up to 747 m<sup>2</sup>/g with high thermal stability. The obtained CMPs were chemically modified by chlorosulfonic acid to increase an acidity of the polymers. The sulfonated CMPs showed a high acidity up to 7.67 mmol/g which was higher than the previous reports, thus the sulfonated CMPs can potentially be applied as an acid catalyst for organic reactions. In this work, we have applied the synthesised polymers as a catalyst for esterification of fatty acids and transesterification of vegetable oils to produce biodiesel and the result has been discussed in the next chapter.

## 5.6 References

- 1 R. W. Sabnis, *Handbook of acid-base indicators*, CRC Press, 2007.
- 2 K. A. Cockell, *Encycl. Food Sci. Nutr.*, 2003, 765–771.
- 3 D. Gadella, *Lab. Tech. Biochem. Mol. Biol.*, 2009, 33.
- 4 E. J. Thompson, *Proteins of the Cerebrospinal Fluid*, Elsevier Ltd, 2005.
- 5 T. T. M. Tan, Z. Y. Tan, W. L. Tan and P. F. P. Lee, *Biochem. Mol. Biol. Educ.*, 2007, **35**, 342–349.
- 6 P. Magee, in *Side Effects of Drugs Annual*, Elsevier, 2005, vol. 28, pp. 261–264.
- 7 J. X. Jiang, Y. Li, X. Wu, J. Xiao, D. J. Adams and A. I. Cooper, *Macromolecules*, 2013, **46**, 8779–8783.
- 8 C. A. Wang, Y. W. Li, X. L. Cheng, J. P. Zhang and Y. F. Han, *RSC Adv.*,

- 2017, **7**, 408–414.
- 9 X. Yu, Z. Yang, B. Qiu, S. Guo, P. Yang, B. Yu, H. Zhang, Y. Zhao, X. Yang, B. Han and Z. Liu, *Angew. Chemie Int. Ed.*, 2019, **58**, 632–636.
- 10 S. Bandyopadhyay, A. G. Anil, A. James and A. Patra, *ACS Appl. Mater. Interfaces*, 2016, **8**, 27669–27678.
- 11 M. Liras, M. Iglesias and F. Sánchez, *Macromolecules*, 2016, **49**, 1666–1673.
- 12 J. M. Tobin, J. Liu, H. Hayes, M. Demleitner, D. Ellis, V. Arrighi, Z. Xu and F. Vilela, *Polym. Chem.*, 2016, **7**, 6662–6670.
- 13 Y. Zhu, Y.-J. Ji, D.-G. Wang, Y. Zhang, H. Tang, X.-R. Jia, M. Song, G. Yu and G.-C. Kuang, *J. Mater. Chem. A*, 2017, **5**, 6622–6629.
- 14 C. P. Sen, R. G. Shrestha, L. K. Shrestha, K. Ariga and S. Valiyaveetil, *Chem. - A Eur. J.*, 2015, **21**, 17344–17354.
- 15 S. Bhunia, B. Banerjee and A. Bhaumik, *Chem. Commun.*, 2015, **51**, 5020–5023.
- 16 S. K. Kundu and A. Bhaumik, *ACS Sustain. Chem. Eng.*, 2015, **3**, 1715–1723.
- 17 R. M. N. Kalla, M.-R. Kim and I. Kim, *Ind. Eng. Chem. Res.*, 2018, **57**, 11583–11591.
- 18 R. Gomes, P. Bhanja and A. Bhaumik, *J. Mol. Catal. A Chem.*, 2016, **411**, 110–116.
- 19 J. Guadalupe, A. M. Ray, E. M. Maya, B. Gómez-Lor and M. Iglesias, *Polym. Chem.*, 2018, **9**, 4585–4595.
- 20 R. M. N. Kalla, S. S. Reddy and I. Kim, *Catal. Letters*, 2019, **149**, 2696–2705.

- 21 J. Fu, L. Chen, P. Lv, L. Yang and Z. Yuan, *Fuel*, 2015, **154**, 1–8.
- 22 L. Sekerová, P. Březinová, T. T. Do, E. Vyskočilová, J. Krupka, L. Červený, L. Havelková, B. Bashta and J. Sedláček, *ChemCatChem*, 2020, **12**, 1075–1084.
- 23 Z. Wang, in *Comprehensive Organic Name Reactions and Reagents*, John Wiley & Sons, Inc., Hoboken, NJ, USA, 2010, pp. 1131–1136.
- 24 M. Schilz and H. Plenio, *J. Org. Chem.*, 2012, **77**, 2798–2807.
- 25 A. Laybourn, R. Dawson, R. Clowes, T. Hasell, A. I. Cooper, Y. Z. Khimyak and D. J. Adams, *Polym. Chem.*, 2014, **5**, 6325–6333.
- 26 R. Dawson, A. Laybourn, Y. Z. Khimyak, D. J. Adams and A. I. Cooper, *Macromolecules*, 2010, **43**, 8524–8530.
- 27 J. X. Jiang, F. Su, A. Trewin, C. D. Wood, H. Niu, J. T. A. Jones, Y. Z. Khimyak and A. I. Cooper, *J. Am. Chem. Soc.*, 2008, **130**, 7710–7720.
- 28 T. M. Geng, S. N. Ye, Y. Wang, H. Zhu, X. Wang and X. Liu, *Talanta*, 2017, **165**, 282–288.
- 29 R. Dawson, A. Laybourn, R. Clowes, Y. Z. Khimyak, D. J. Adams and A. I. Cooper, *Macromolecules*, 2009, **42**, 8809–8816.
- 30 B. Li, Z. Guan, X. Yang, W. D. Wang, W. D. Wang, I. Hussain, K. Song, B. Tan and T. Li, *J. Mater. Chem. A*, 2014, **2**, 11930–11939.
- 31 Y. Xu and D. Jiang, *Chem. Commun.*, 2014, **50**, 2781–2783.
- 32 L. Leay and F. R. Siperstein, *Adsorpt. Sci. Technol.*, 2013, **31**, 99–112.

## 5.7 Appendices

### 5.7.1 FTIR Spectra of monomers and HCl-CMPs

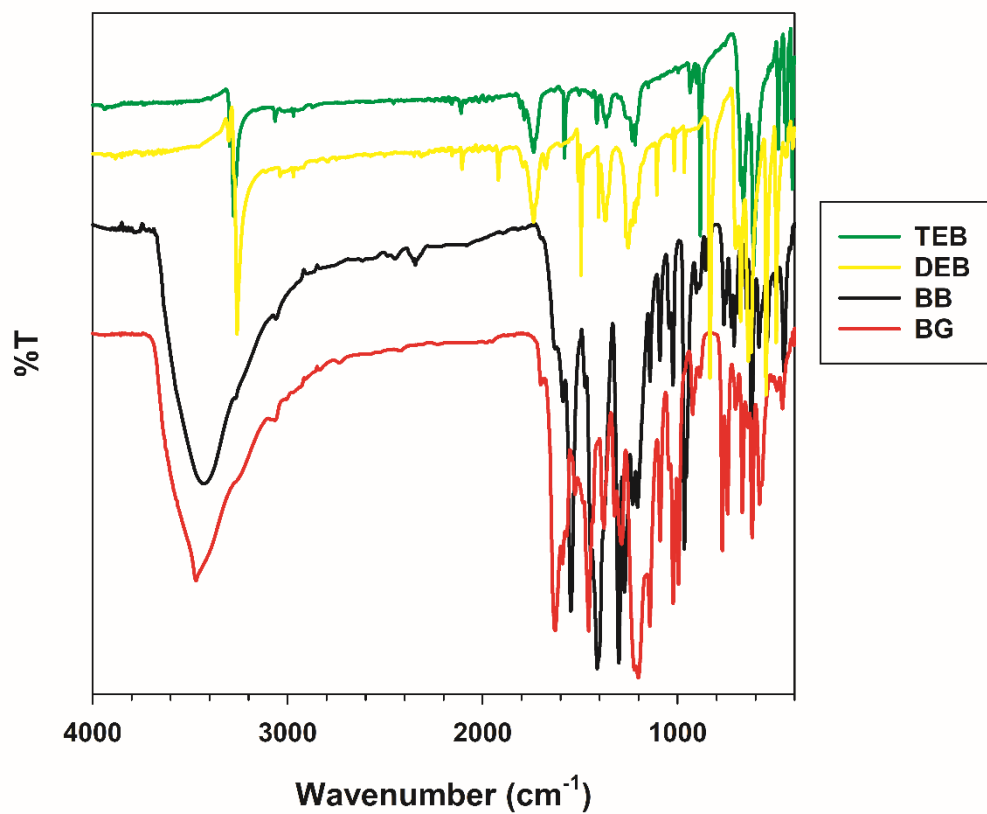
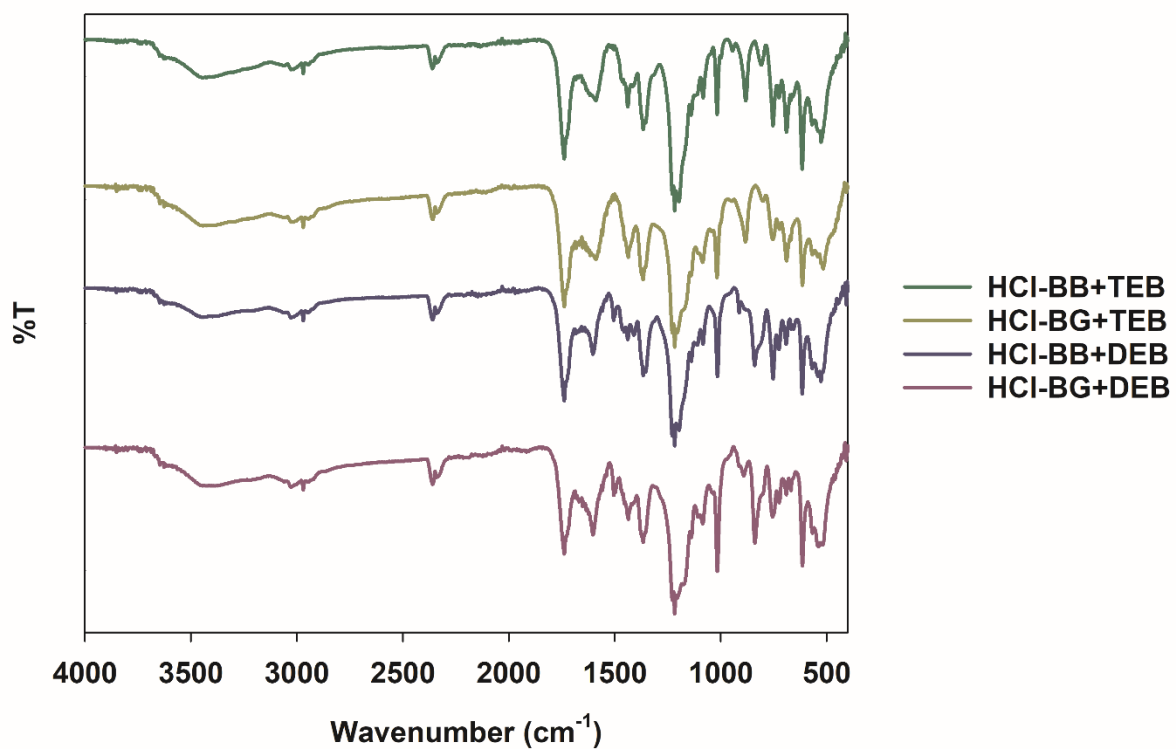
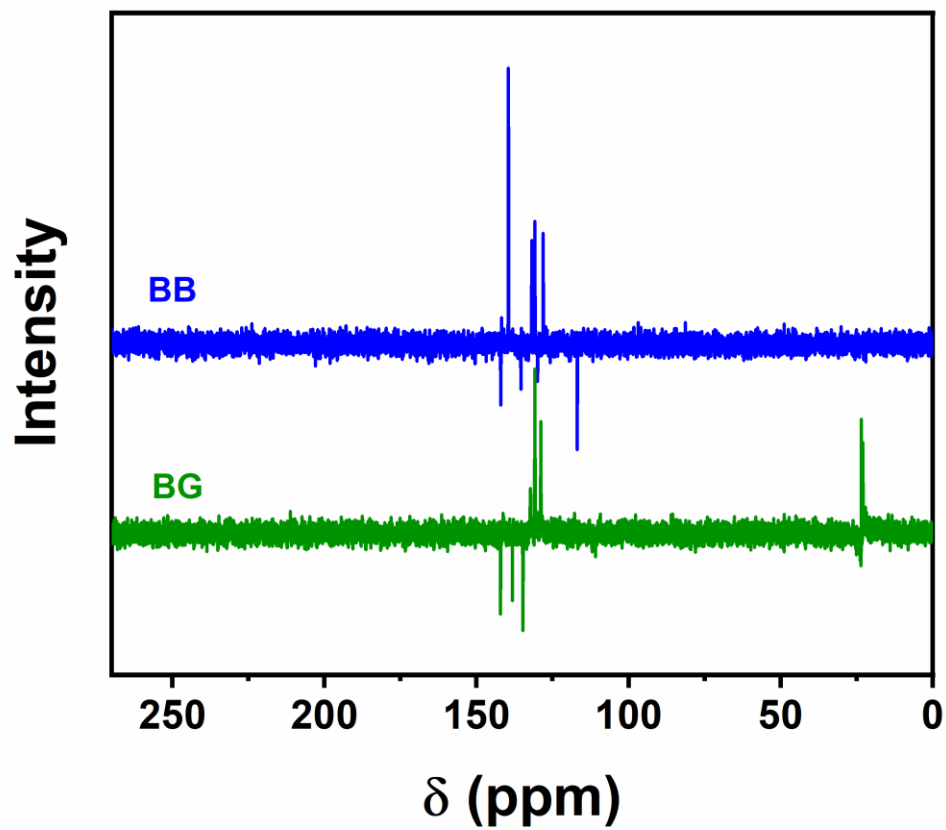


Figure A5.1 IR spectra of the monomers used in this study.



**Figure A5.2** IR spectra of HCl treated BB and BG CMPs.

**5.7.2  $^{13}\text{C}$  NMR of monomers used in this work**

**Figure A5.3**  $^{13}\text{C}$  NMR of bromophenol blue (BB) and bromocresol green (BG) in  $\text{D}_2\text{O}$ .

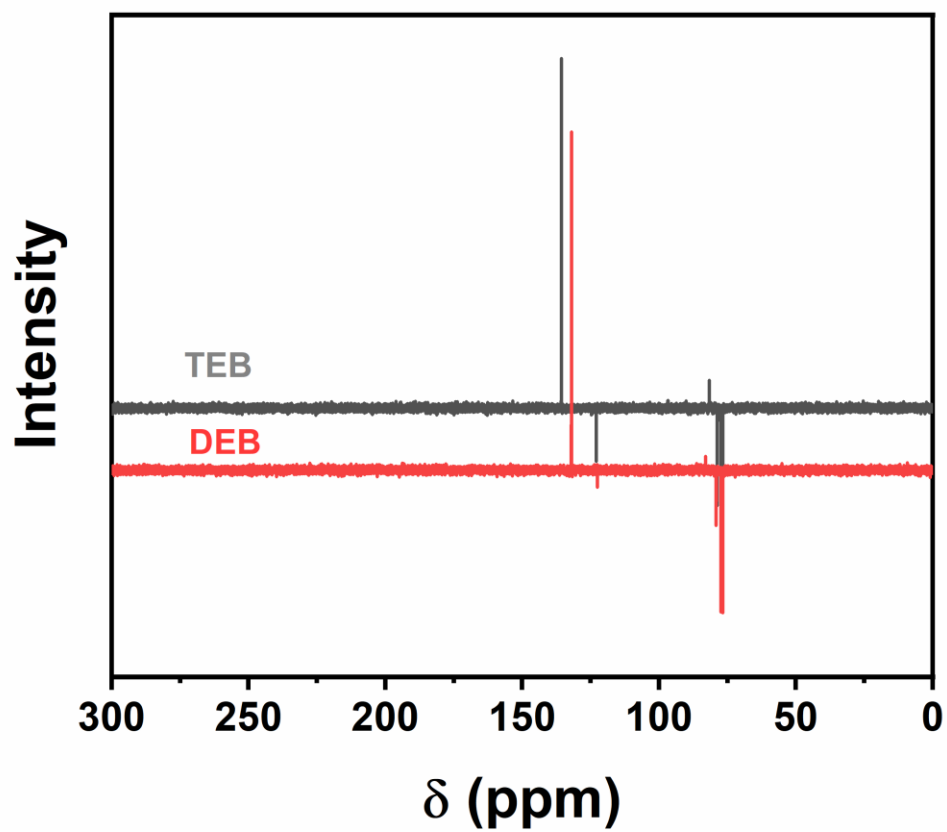


**Figure A5.4**  $^{13}\text{C}$  NMR of 1,3,5-triethynylbenzene (TEB) and 1,4-diethynylbenzene (DEB) in *d*-chloroform.

## Chapter 6

# Biodiesel Production from Free Fatty Acids and Vegetable Oils Using Acid Functionalised CMPs

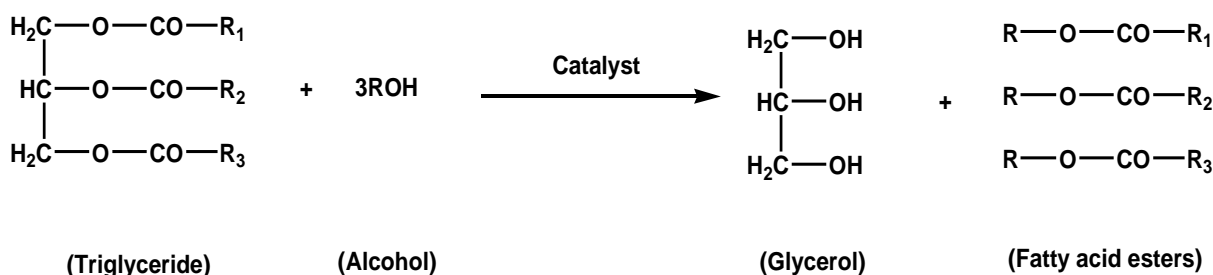
### 6.1 Introduction

Fossil fuels such as coal, petroleum, and natural gas have been massively used as main energy supplies for industrialised societies. However, fossil fuels are non-renewable and an increase in utilisation of fossil fuels causes rapid depletion of the natural fuels. Moreover, they are also main contributors to serious environmental problems such as global warming and pollutions. To resolve these problems, numerous energy industries and researchers have invested and studied in renewable and sustainable energies.<sup>1-3</sup> Fossil fuels can be replaced by several alternative energies including bioenergy, nuclear power, solar energy, geothermal energy, hydropower, wind and ocean energy.<sup>4,5</sup> Biodiesel is one of renewable energy which can be made from biological sources such as cheap vegetable oils and animal fats. The advantages of biodiesel are its biodegradable, non-toxic and low carbon emission, thus it is environmentally friendly.<sup>6</sup> Moreover, biodiesel has higher combustion efficiency than the diesel fuel.<sup>1</sup> The production of biodiesel are continuously growing as the annual biodiesel consumption in the United States was 15 billion litres in 2006.<sup>4</sup> According to department for transport, biodiesel is contributed to 53% of verified renewable fuel and 83% of biodiesel was produced from wasted cook oil.<sup>7</sup> According to Wang and co-workers, approximately 5 million tonnes of waste cooking oil were produced in China resulting in serious environmental problems, so the use of waste oil for biodiesel production not only provides us clean energy sources but also reduce

the causes of environmental pollutions.<sup>8</sup> Moreover, the price of waste cooking oil is much cheaper than food grade vegetable oil, so the use of the waste oil for biodiesel production is efficient and economical. A substantial amount of biodiesel fuel from waste cooking oil can partly reduce the dependency on petroleum-based fuel.<sup>9</sup>

Biodiesel can be produced by 4 main methods including direct use and blending of raw oils, microemulsion, thermal cracking and transesterification.<sup>1</sup> The transesterification is the most commonly used method to convert vegetable oils and animal fats by reacting with alcohol to form biodiesel product due to renewability, higher cetane number, lower emissions, and higher combustion efficiency.<sup>1</sup>

Vegetable oils and animal fats are ester compounds (triglycerides) of saturated and unsaturated monocarboxylic acids with triglycerol. They can be reacted with alcohols *via* transesterification to form fatty acid ester products as shown in Scheme 6.1.

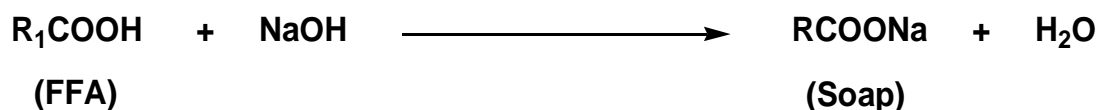


**Scheme 6.1** Biodiesel production *via* transesterification of triglyceride and alcohol.

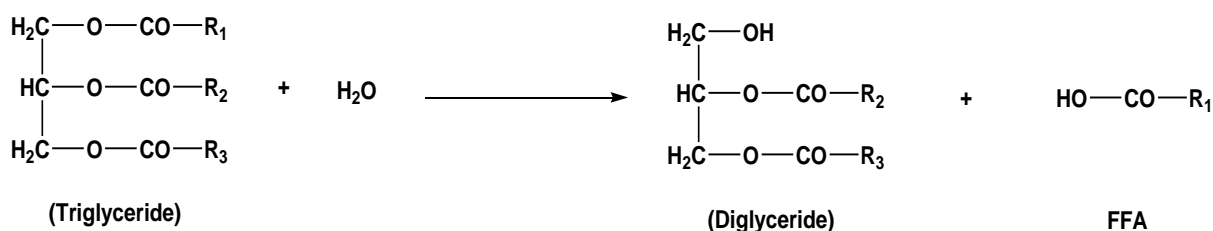
R<sub>1</sub>, R<sub>2</sub> and R<sub>3</sub> represent long-chain hydrocarbons. There are five kinds of chains that are found in vegetable oils and animal fats including saturated chains; palmitic (CH<sub>3</sub>(CH<sub>2</sub>)<sub>14</sub>COOH) and stearic (CH<sub>3</sub>C<sub>16</sub>H<sub>32</sub>COOH) and unsaturated chains; oleic (CH<sub>3</sub>(CH<sub>2</sub>)<sub>7</sub>CH=CH(CH<sub>2</sub>)<sub>7</sub>COOH), linoleic (CH<sub>3</sub>(CH<sub>2</sub>)<sub>4</sub>(CH=CHCH<sub>2</sub>)<sub>2</sub>(CH<sub>2</sub>)<sub>6</sub>COOH), α-

linolenic (omega-3) ( $\text{CH}_3\text{CH}_2\text{CH}=\text{CHCH}_2\text{CH}=\text{CHCH}_2\text{CH}=\text{CH}(\text{CH}_2)_7\text{COOH}$ ) and  $\gamma$ -linolenic acids (omega-6) ( $\text{CH}_3(\text{CH}_2)_4\text{CH}=\text{CHCH}_2\text{CH}=\text{CHCH}_2\text{CH}=\text{CH}(\text{CH}_2)_4\text{COOH}$ ). Methanol is normally used to make biodiesel due to its low cost. The triglyceride is converted stepwise to diglyceride, then monoglyceride, and finally to glycerol. 1 mole of fatty acid ester is produced in each step.<sup>1</sup>

Vegetable oils and animal fats contain small amounts of water and free fatty acids (FFAs) which have an effect on the yield of biodiesel product, thus the selection of types of catalysts is crucial for this reaction. The catalysts for transesterification can be either acids or bases. However, when alkaline catalysts are used, there are several drawbacks especially for the oils and fats with high water and FFA contents including the saponification of the base catalysts with FFA and hydrolysis of triglyceride to form FFA as shown in Scheme 6.2 and 6.3.<sup>1</sup>



**Scheme 6.2** Saponification of FFA with alkaline catalyst.

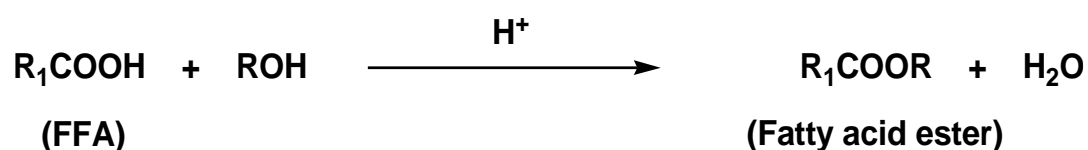


**Scheme 6.3** Hydrolysis of triglyceride to diglyceride and FFA.

Soap formed during saponification reaction can bind with the catalyst, thus reducing the efficiency of the catalyst and hence decreasing the yield of the biodiesel

product. In addition, it also inhibits the separation of ester products from glycerol. Water from crude oils or the saponification reaction causes hydrolysis of triglyceride, consequently it retards the transesterification of triglyceride to fatty acid esters.<sup>1</sup>

Instead of base catalysts, acid catalysts (normally sulphuric acid) can avoid formation of soap and can be used with vegetable oils and animal fats with high FFA contents. They can catalyse the esterification of FFA with alcohol to fatty acid esters as illustrated in Scheme 6.4.<sup>1</sup>

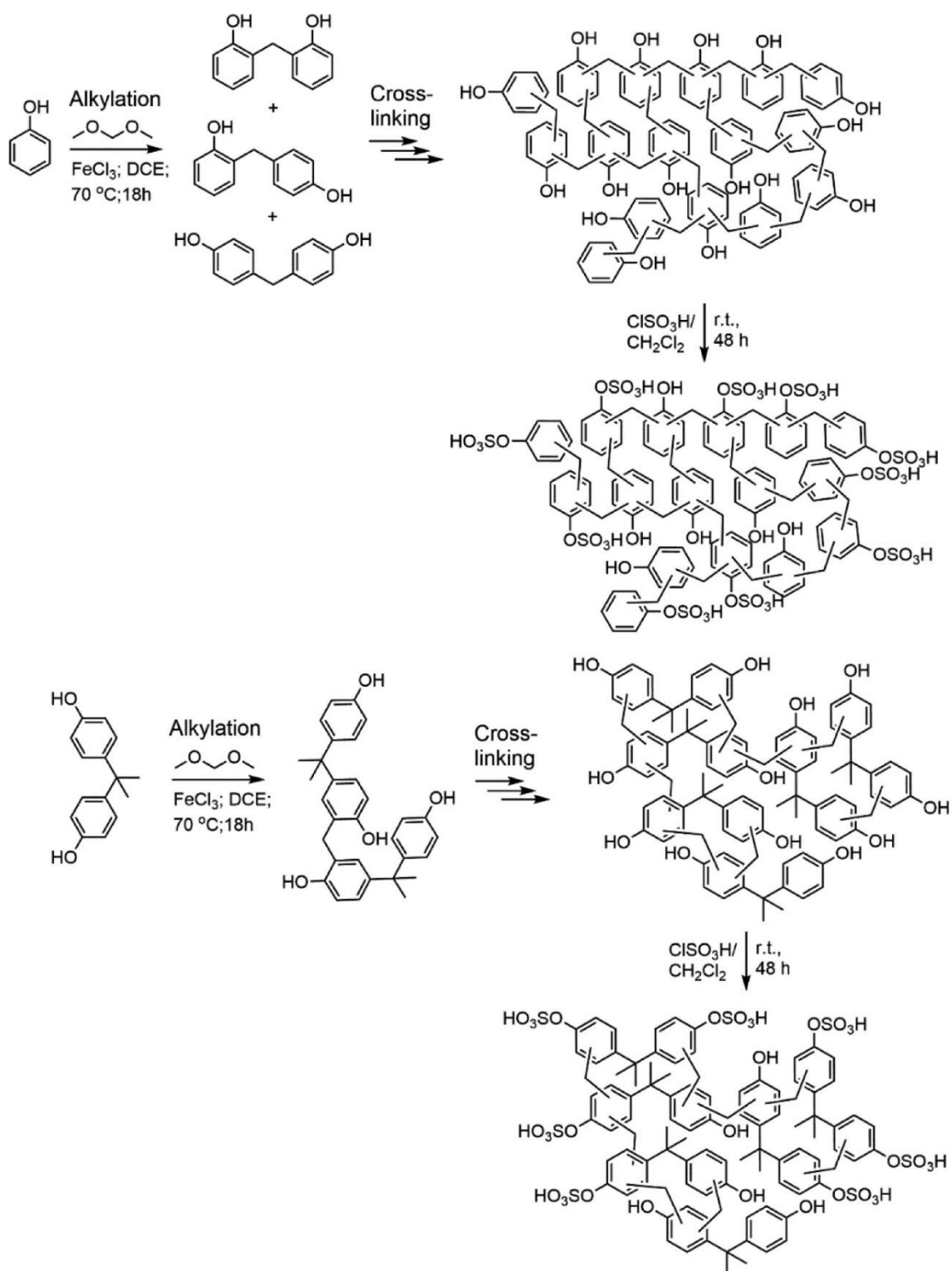


**Scheme 6.4** Esterification of FFA to fatty acid ester using acid catalyst.

Due to the mentioned advantages of acid catalysed transesterification and esterification of oils and FFAs, acid catalysts have been studied in this work. Although homogeneous acid catalysts have been widely used in the biodiesel production due to their high reaction rates, the process for purification and separation of homogeneous catalyst from biodiesel is problematic and energy intensive as well as the catalyst cannot be reused, which is not cost effective.<sup>10,11</sup> From this point of view, solid acid catalysts have gained more attention for biodiesel production because they can be easily separated from biodiesel product and then be recycled for multiple times which is more environmentally friendly and economical. Solid acid catalysts can be divided into 2 main types; Lewis acids such as the mixed and sulfonated metal oxides and Brønsted acids including sulfonic acid containing materials.<sup>10</sup> Most of the acid metal oxides are expensive and synthesised by complicated methods.<sup>12</sup> The development of metal free acidic organic porous materials with high surface areas and

reactive functional groups have been recently explored by numerous researchers.<sup>12-</sup>

15



**Scheme 6.5** Synthesis of phenol and bisphenol A based HCPs via Friedel-Craft alkylation and post-functionalisation with chlorosulfonic acid.<sup>14</sup>

Kalla and co-workers reported sulfonic acid functionalised hyper-cross-linked polymers (HCPs) derived from phenol and bisphenol A. The phenol and bisphenol A were incorporated into polymer networks by Friedel-Crafts alkylation using dimethoxymethane as an external crosslinker as shown in Scheme 6.5. The synthesised materials showed high surface areas of 440 and 635 m<sup>2</sup>/g for phenol and bisphenol A based HCPs, respectively. The synthesised HCPs were then post-functionalised with chlorosulfonic acid to introduce sulfonic groups into the polymer networks. The surface areas dropped significantly to 210 and 324 m<sup>2</sup>/g confirming the incorporation of sulfonic groups in the materials. The acidities of the functionalised of sulfonated phenol and bisphenol A polymers were 0.85 and 1.60 mmol/g, respectively. They showed excellent catalytic activity on esterification of free fatty acids and transesterification of vegetable oils at room temperature and the catalysts can be reused up to 6 cycles without significant loss in the activity.<sup>14</sup> Similar works have also been reported including sulfonic acid functionalised carbazole based HCPs and pyrene based HCPs. The synthesised materials showed high surface areas with excellent catalytic activity and reusability on biodiesel production.<sup>13,15</sup>

In this work, bromophenol blue (BB) and bromocresol green (BG) containing sulfonate groups in their structures were incorporated into CMP networks *via* a Sonogashira-Hagihara reaction and then post-functionalised by chlorosulfonic acid. The synthesis and characterisation have been discussed in Chapter 5. Biodiesel production from esterification of free fatty acids (FFAs), vegetable oils and waste cooking oil using the sulfonated BB and BG based CMPs are discussed in this chapter as well as the optimisation of reaction parameters to obtain the highest activity and reusability of the synthesised catalysts.

## 6.2 Aims of the chapter

- To investigate catalytic activity of the acid functionalised BB and BG based CMPs on biodiesel production *via* esterification of free fatty acids (FFAs) and transesterification of vegetable oils.
- To optimise the reaction conditions of biodiesel production such as type of FFAs, catalyst structures, catalyst amounts, reaction temperatures and times.
- To study reusability of the acid functionalised CMPs.

## 6.3 Experimental

### 6.3.1 Materials

Myristic acid and palmitic acid were obtained from Acros Organics. Oleic acid was bought from Fluorochem. All other fatty acids were purchased from Sigma Aldrich. Methanol and chloroform were obtained from Fisher Scientific. All chemicals were used as received and had a purity over 95%. Commercially available vegetable oils were purchased from supermarkets and used as received.

### 6.3.2 Esterification of free fatty acids (FFAs) and transesterification of different vegetable oils with methanol.

The method was adapted from previous research.<sup>14</sup> Fatty acid (1 mmol), 10 mg of acid catalyst and 2 mL of methanol (50 mmol) were added into a reaction vessel and stirred at 25 °C or 60 °C. The catalyst was doubled if dicarboxylic fatty acids were utilised. For transesterification, 100 mg of vegetable oil, different amounts of acid catalyst and 5.7 mL of methanol were mixed together in a reaction flask and stirred at 60 °C for 24 h. The catalyst was removed by vacuum filtration and washed with chloroform. The filtrate was evaporated under vacuum and the product was dried using

vacuum oven at 60 °C. Yield of fatty acid methyl ester (FAME) and conversion of oil to FAME were calculated by <sup>1</sup>H NMR by following equations<sup>14,16</sup>;

$$\text{Yield}(\%) \text{ for esterification} = \frac{I_{\text{ME}}}{I_{\text{CH}_2}} \times 100$$

$$\text{Yield}(\%) \text{ for transesterification} = \frac{2 \times I_{\text{ME}}}{3 \times I_{\alpha\text{-CH}_2}} \times 100$$

$$\text{Conversion}(\%) = \frac{4 \times I_{\text{ME}}}{(4 \times I_{\text{ME}}) + (9 \times I_{\text{TG}})} \times 100$$

Where  $I_{\text{ME}}$  is peak area of single proton of methyl ester protons at 3.6 ppm

$I_{\text{CH}_2}$  is peak area of single proton methylene protons at 2.25 ppm

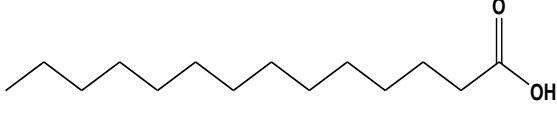
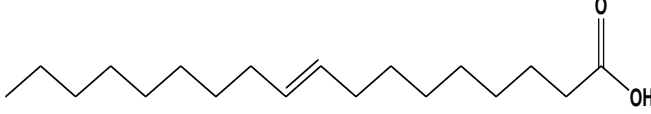
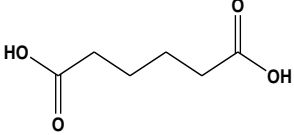
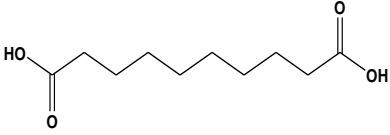
$I_{\alpha\text{-CH}_2}$  is peak area of  $\alpha$ -carbonyl methylene protons at 2.3

$I_{\text{TG}}$  is peak area of glyceridic protons at 4.15 ppm

### **6.3.3 Reusability study**

Recyclability was studied using 10 mg of s-BB+DEB catalyst, 1 mmol of myristic acid and 2 mL of methanol at 60 °C for 6h. After cooling, the catalyst was removed from reaction mixture by vacuum filtration and washed with methanol and chloroform, respectively. The catalyst was further washed using chloroform by Soxhlet extraction method for 16 h and the catalyst was dried under vacuum at 60 °C before 10 mg of the used catalyst was utilised for the next cycle.

**Table 6.1** Chemical formula and structure of free fatty acids (FFAs) used in this work.

Fatty acid	Formula	Structure
Lauric	$C_{12}H_{24}O_2$	
Myristic	$C_{14}H_{28}O_2$	
Palmitic	$C_{16}H_{32}O_2$	
Stearic	$C_{18}H_{36}O_2$	
Oleic	$C_{18}H_{34}O_2$	
Adipic	$C_6H_{10}O_4$	
Sebacic	$C_{10}H_{18}O_4$	

## 6.4 Results and Discussion

### **6.4.1 Effect of polymer structures on esterification of free fatty acids (FFAs)**

The esterification of FFAs with different polymer catalysts was studied at 60 °C using 10 mg of catalyst, 1 mmol of fatty acids and 2 mL of methanol as shown in Table 6.2. The esterification of lauric acid without catalysts showed very low %yield of fatty acid methyl ester (FAME) product due to no acid active species to catalyse the reaction. When the non-functionalised BB and BG CMPs were used as catalysts, they exhibited very low %yields of the biodiesel product because lack of acidity of the catalysts. After the as synthesised CMPs were treated with HCl, the %yield improved but it still gave low to moderate yields from 16 to 75% for lauric acid and 24 to 78% for myristic acid. The sulfonated CMPs; s-BB+TEB, s-BB+DEB, s-BG+TEB and s-BG+DEB showed higher catalytic activity and they gave the high yield of FAME product more than 89% for lauric acid because the sulfonated CMPs possessed higher acidity than HCl treated CMPs and as synthesised CMPs as it was discussed in section 5.4.6 in Chapter 5. s-BB+TEB, the lowest acidity sulfonated catalyst still showed a high % yield of the product which was similar to other sulfonated polymers. This indicated that the acidity of the sulfonated polymer is high enough to catalyse the esterification of FFAs. Moreover, the porosity of the sulfonated polymers (Chapter 5, Table 5.2) have small effect on catalytic activity as all sulfonated catalysts which have different  $S_{BET}$  showed similar catalytic activity. This can imply that the internal catalysis (catalysis inside pores of catalysts) has a less important role than the acidity of the materials. After acid modification, the acid modified polymers showed smaller particle sizes compared to as synthesised CMPs as shown in Table A6.1. The as made polymers exhibited particle sizes from 23.3-27.3 micron. The HCl treated CMPs showed smaller particle sizes from 15.2-21.9 micron while the sulfonated CMPs

possessed particle sizes between 16.3-22.2 micron. The acidities of the HCl modified polymers were in the range of 1.69-1.89 mmol/g which slightly increased when compared to those unmodified (1.54-1.89 mmol/g). However, the catalytic activity of HCl treated CMPs increased significantly (6 to 12 times higher than the as synthesised polymers). This may indicate that the particle sizes might play an important role as the smaller particles can enhance catalytic performance due to the larger external catalytic surface area.<sup>17,18</sup>

**Table 6.2** Effect of different catalysts on esterification of FFAs.

Entry	Fatty acid	Catalyst	Time (h)	Yield (%)
1 (Control)	Lauric acid	No catalyst	24	2.6
2	Lauric acid	BB+TEB	24	2.7
3	Lauric acid	BB+DEB	24	2.2
4	Lauric acid	BG+TEB	24	4.3
5	Lauric acid	BG+DEB	24	1.9
6	Lauric acid	HCl-BB+TEB	24	16.2
7	Lauric acid	HCl-BB+DEB	24	64.2
8	Lauric acid	HCl-BG+TEB	24	75.3
9	Lauric acid	HCl-BG+DEB	24	15.1
10	Lauric acid	s-BB+TEB	24	<b>93.7</b>
11	Lauric acid	s-BB+DEB	24	89.3
12	Lauric acid	s-BG+TEB	24	92.6
13	Lauric acid	s-BG+DEB	24	93.6
14	Myristic acid	HCl-BB+TEB	24	24.0
15	Myristic acid	HCl-BB+DEB	24	63.5
16	Myristic acid	HCl-BG+TEB	24	66.7
17	Myristic acid	HCl-BG+DEB	24	77.9
18	Adipic acid	s-BB+DEB	6	91.3 (91.3)*
19	Sebacic acid	s-BB+DEB	6	95.2 (92.6)*

The reactions were at 60 °C using 10 mg of catalyst, 1mmol of FFA and 2 mL of methanol and the catalyst was doubled for dicarboxylic acids (\* The number in brackets is %yield when 10 mg of the catalyst was used.)

### **6.4.2 Effect of reaction time on esterification of FFAs**

The effect of reaction time was studied using 1 mmol of myristic acid with 2 mL of methanol and 10 mg of different sulfonated BB and BG CMPs at 60 °C. The homogeneous catalyst (chlorosulfonic acid) with the same mole of sulfonic acid in s-BB+DEB; the highest acidic materials in this study, was used to compare with heterogeneous catalysts. All CMPs showed high % product yield and they also showed comparable catalytic activity with the homogeneous catalyst (Figure 6.1). The s-BB+DEB catalyst showed the highest initial reaction rate reaching 80% yield of the product when compared with other CMPs due to the highest acidity in the material as discussed in 5.4.6 (Chapter 5). s-BG+DEB and s-BB+DEB reached a plateau at 3 and 4 h, respectively while the other polymers levelled off at 6 h.

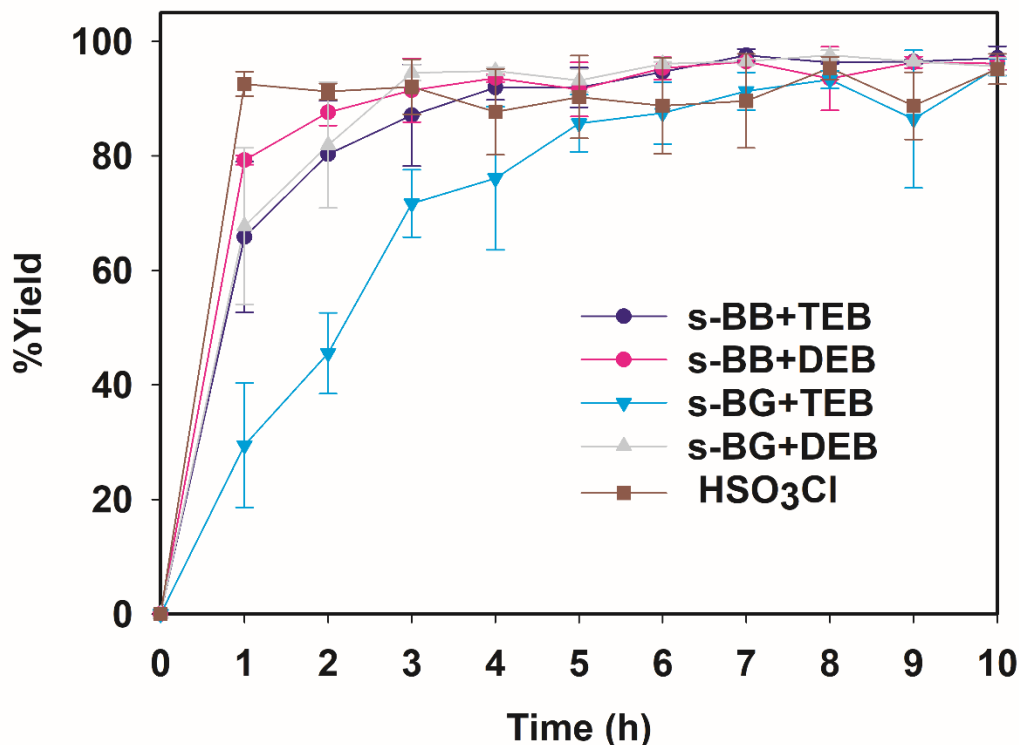


**Figure 6.1** Effect of reaction time on esterification of FFAs using different catalysts.

(The results are an average of 3 experiments)

### **6.4.3 Effect of different FFAs and reaction temperature on biodiesel production**

The different FFAs were applied in this work including monocarboxylic acids; lauric, myristic, palmitic, stearic, and oleic acids and dicarboxylic acids; adipic and sebacic acids as shown in Table 6.1. 10 mg of catalyst was used for monocarboxylic acid and the catalyst was doubled when dicarboxylic acid was used. The reaction was also investigated under 2 different conditions; 25 °C for 24 h and 60 °C for 6 h as shown in Figure 6.2 (a) and (b), respectively. The polymers produced from DEB exhibited higher catalytic activity than those synthesised from TEB due to more sulfonic group in DEB version of polymers as discussed in section 5.4.6 of Chapter 5. All synthesised catalysts showed yields more than 80% for both room temperature and 60 °C for all FFAs except for stearic acid at 25 °C. Stearic acid which was the longest FFA in this study was poorly dissolved in methanol at room temperature giving the %biodiesel yield just up to 68%. However, the %yields were improved significantly at higher temperature due to the better solubility leading to higher catalytic activity. From previous studies, the catalyst was doubled to 20 mg when dicarboxylic acid was used due to low acidity of the synthesised catalysts.<sup>14,15</sup> It is worth noting that s-BB+DEB still showed very high yield of 91.3 and 92.6 % for the dicarboxylic acids; adipic and sebacic acids, respectively even 10 mg of the catalyst was used at 60 °C for 6 h. This indicates that our synthesised catalysts possessed high acidity in the materials leading to excellent catalytic activity even at a lower amount of catalyst loading. The results indicate that sulfonated polymers synthesised in this work have similarly high catalytic activity for esterification of FFAs at either room temperature or 60 °C compared with the previous reported sulfonated HCPs and CMPs.<sup>13–15,19</sup> Sulfonated HCPs derived from phenol and bisphenol A exhibited high %yield of 78.5–96.6% for esterification of different FFAs at room temperature from 6–24 h.<sup>14</sup>

Sulfonated carbazole incorporated HCPs also gave high %yield of 93-99% at room temperature using 0.5 mmol of FFA and 6 mg of catalysts.<sup>15</sup> Sulfonated pyrene based HCPs showed high %yield of 88-94% for esterification of FFAs at room temperature for 10h, but higher amount of catalysts (17-25 mg) was utilised for 1 mmol of FFA.<sup>13</sup> Sulfonated CMPs derived from 1,3 and 1,4-diethynyl benzene (DEB) yielded up to 99% of FAME product obtained from various FFAs using 1 wt% of catalyst. However, a high temperature and long reaction time (60 °C for 24h) was needed.<sup>19</sup>

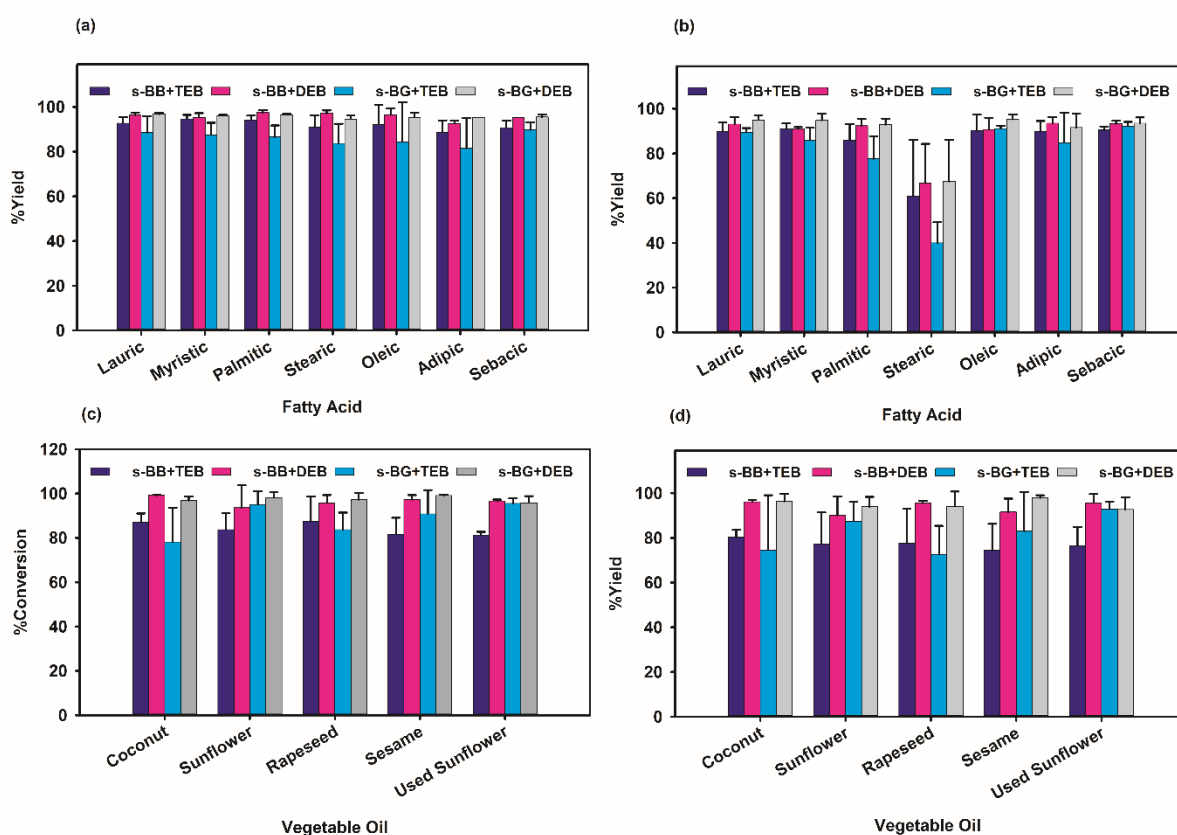


**Figure 6.2** Esterification of different FFAs using different polymers at (a) 60 °C for 6h and (b) 25 °C for 24h, (c) %conversion and (d) %yield of transesterification of various vegetable oils using different polymers. (The results are an average of 3 experiments)

#### **6.4.4 Transesterification of vegetable oil using different polymers as an acid catalyst**

The effect of different polymers was investigated using 10 mg of polymer catalyst and 100 mg of coconut oil in methanol at 60 °C for 24 h as illustrated in Table 6.3. The non-functionalised and HCl treated polymers showed very low conversion due to the low acidity in the materials. The conversions were improved when the sulfonated polymers which possessed higher acidity were used. The acidity study which was discussed in 5.4.6 in Chapter 5 showed that s-BB+DEB had the highest acidity up to 7.67 mmol/g. The result was consistent with catalytic activity test as s-BB+DEB showed the highest conversion at 49%. This indicates that acidity of the catalyst plays an important role in the biodiesel production.

**Table 6.3** Transesterification of coconut oil with methanol using various catalysts.

Entry	Oil	Catalyst	Catalyst amount (mg)	%Conversion
1	Coconut	BB+TEB	10	0.9
2	Coconut	BB+DEB	10	0.0
3	Coconut	BG+TEB	10	0.9
4	Coconut	BG+DEB	10	0.4
5	Coconut	HCl-BB+TEB	10	0.0
6	Coconut	HCl-BB+DEB	10	0.9
7	Coconut	HCl-BG+TEB	10	1.3
8	Coconut	HCl-BG+DEB	10	0.9
9	Coconut	s-BB+TEB	10	12.3
10	Coconut	s-BB+DEB	10	49.0
11	Coconut	s-BG+TEB	10	30.3
12	Coconut	s-BG+DEB	10	47.9

#### **6.4.5 Effect of catalyst loading on transesterification of vegetable oil**

The catalyst amount was varied from 10 mg to 70 mg in order to find the optimum catalyst loading. Different amounts of s-BB+TEB and s-BB+DEB were used as a catalyst for transesterification of coconut oil at 60 °C for 24 h and the results were shown in Figure 6.3. The results showed that when the amount of the catalyst increased, the %conversion also increased due to higher amount of acid active sites. There was no further increase in catalytic activity when more than 60 mg of catalyst was used for both s-BB+TEB and s-BB+DEB, so the optimum catalyst loading was 60 mg.

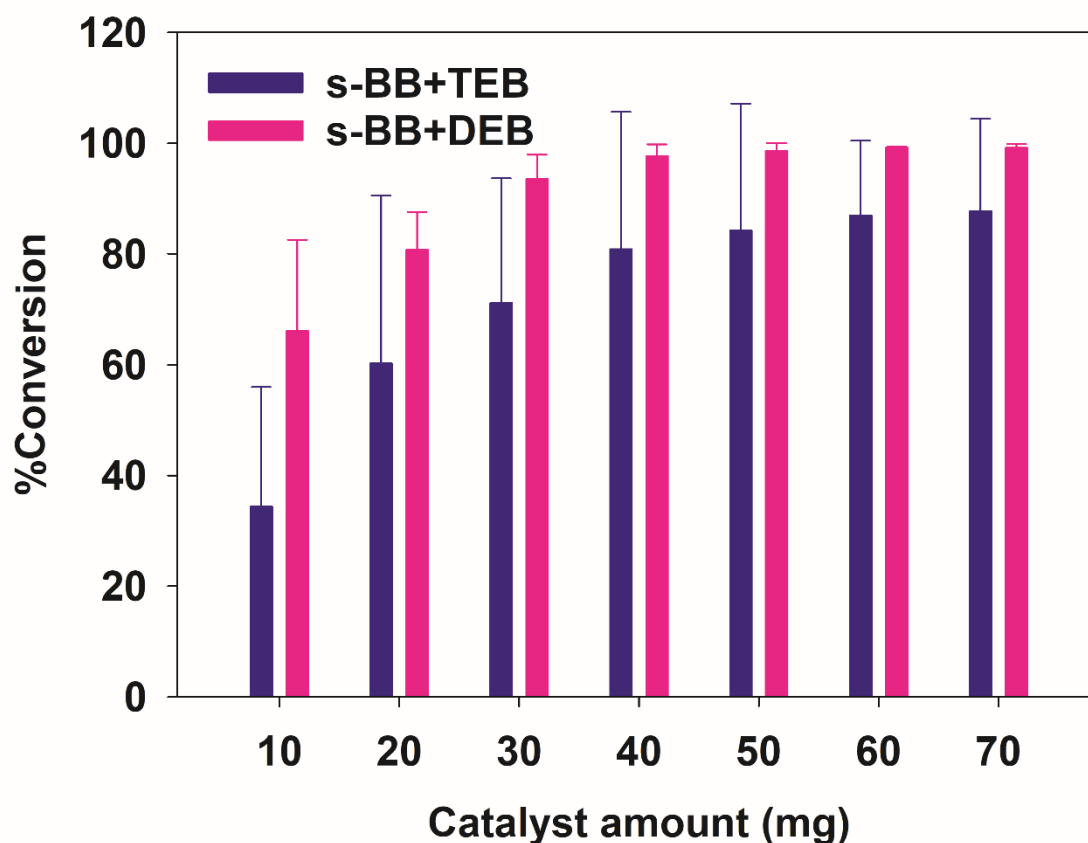


**Figure 6.3** Effect of catalyst loading on transesterification of vegetable oil. (The results are an average of 3 experiments)

#### **6.4.6 Transesterification of various vegetable oils using different sulfonated polymers as a catalyst**

Different vegetable oils such as coconut, sunflower, rapeseed and sesame oil as well as the waste cooking sunflower oil were studied at 60 °C for 24 h using different acid polymers as catalysts as shown in Figure 6.2 (c) and (d). The sulfonated catalysts (s-CMPs) showed the high conversions of transesterification of various vegetable oils up to 87, 99, 96 and 99% and high yields up to 80, 96, 93, 98% for s-BB+TEB, s-BB+DEB, s-BG+TEB and s-BG+DEB, respectively. The s-CMPs derived from DEB linker showed higher conversions and yields than those synthesised from TEB due to

the more acidity of the catalysts as discussed before in section 5.4.6 of the previous chapter. Interestingly, our synthesised sulfonated CMPs also showed a high conversion up to 97% for the cooked sunflower oil indicating that the acid functionalised CMPs can be used as catalysts for biodiesel production from waste cooking oil.

#### **6.4.7 Reusability study**

s-BB+DEB was selected as a catalyst to study reusability for esterification of 1 mmol of myristic acid with methanol at 60 °C for 6 h as illustrated in Figure 6.4. After a run, the catalyst was washed with chloroform and dried before 10 mg of the reused catalyst was applied for the next cycle. The catalyst showed excellent reusability and can be reused up to 4 times with just around 10% loss in catalytic activity. The main reason why the catalytic activity dropped after reuse for multiple times was the leaching of acid sites from the catalyst as elemental analysis showed a decrease in sulphur content to 4.16%. In addition, the pore blocking from residual fatty acid and its product might also reduce catalytic activity of the catalyst.<sup>20</sup> According to Figure 6.5, the used catalyst was also characterised by TGA and the catalyst show slightly decrease in residual to 40% indicating of high thermal stability of the material. However, the reused catalyst showed sharp mass loss after 300 °C which was higher than the fresh catalyst due to the loss of sulfonic groups after reuse for multiple times. The FTIR spectra in Figure 6.6 illustrate that the used catalyst still showed characteristic peaks of internal alkyne linkage at 2150  $\text{cm}^{-1}$  and sulfonic group at 624, 890, 1020-1040 and 1170-1233  $\text{cm}^{-1}$ . However, the disappearance of a peak at 1735  $\text{cm}^{-1}$  which is assigned to C=O stretching in carbonyl group of bromophenol blue indicates of partial collapse of polymer structure.

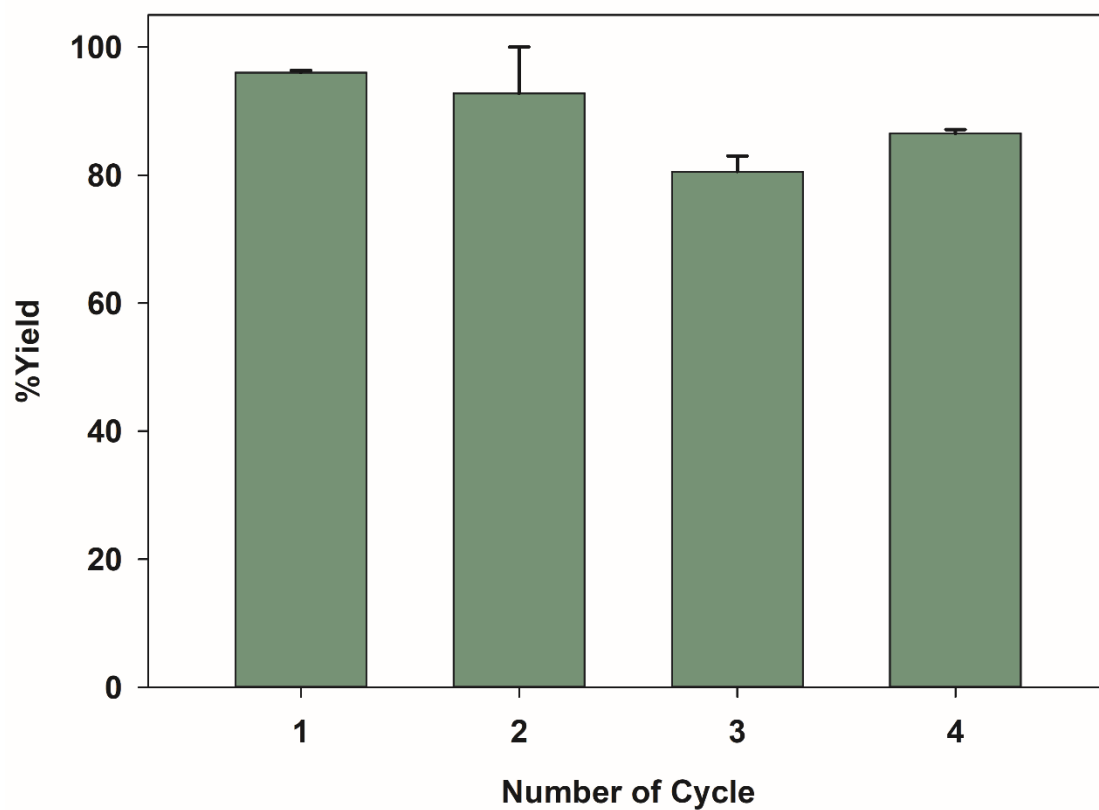


**Figure 6.4** Reusability test of s-BB+DEB catalyst. (The results are an average of 3 experiments)

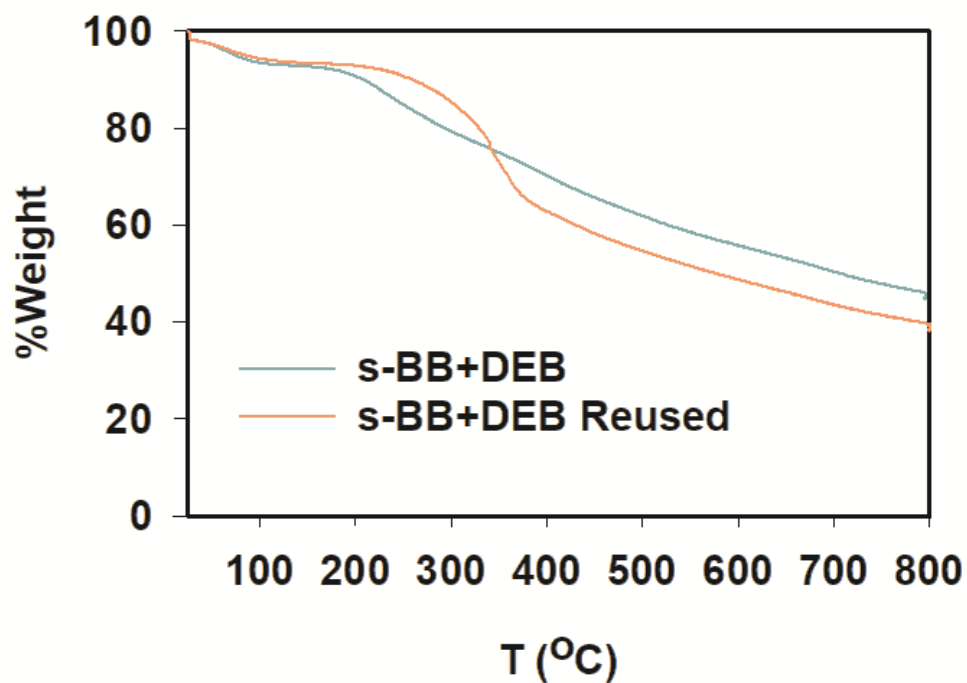


Figure 6.5 TGA of the fresh s-BB+DEB catalyst and reused s-BB+DEB.

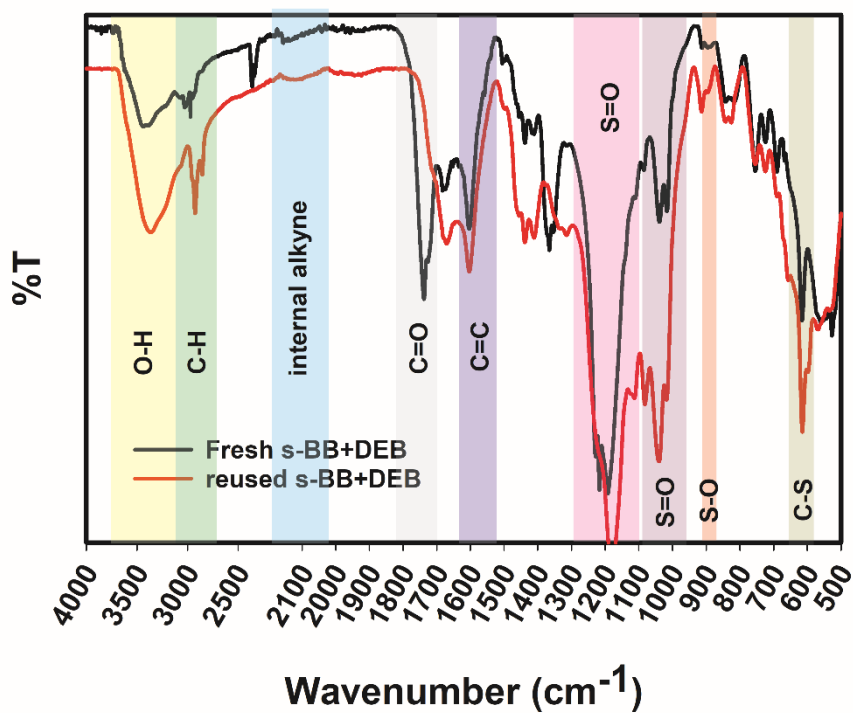


Figure 6.6 FTIR spectra of the fresh s-BB+DEB catalyst and reused s-BB+DEB.

## 6.5 Conclusions

Sulfonated BB and BG CMPs were excellent acid catalysts for biodiesel production as they showed high %yield of the product for esterification of various FFAs and high %conversion and yield for transesterification of various vegetable oils. The catalysts also exhibited high activity for biodiesel production from waste cooking oil which not only provides a clean renewable energy but also reduces the pollutions caused from the used oil. The catalyst can be reused up to 4 times without significant loss of activity which makes it an excellent catalyst for biodiesel production.

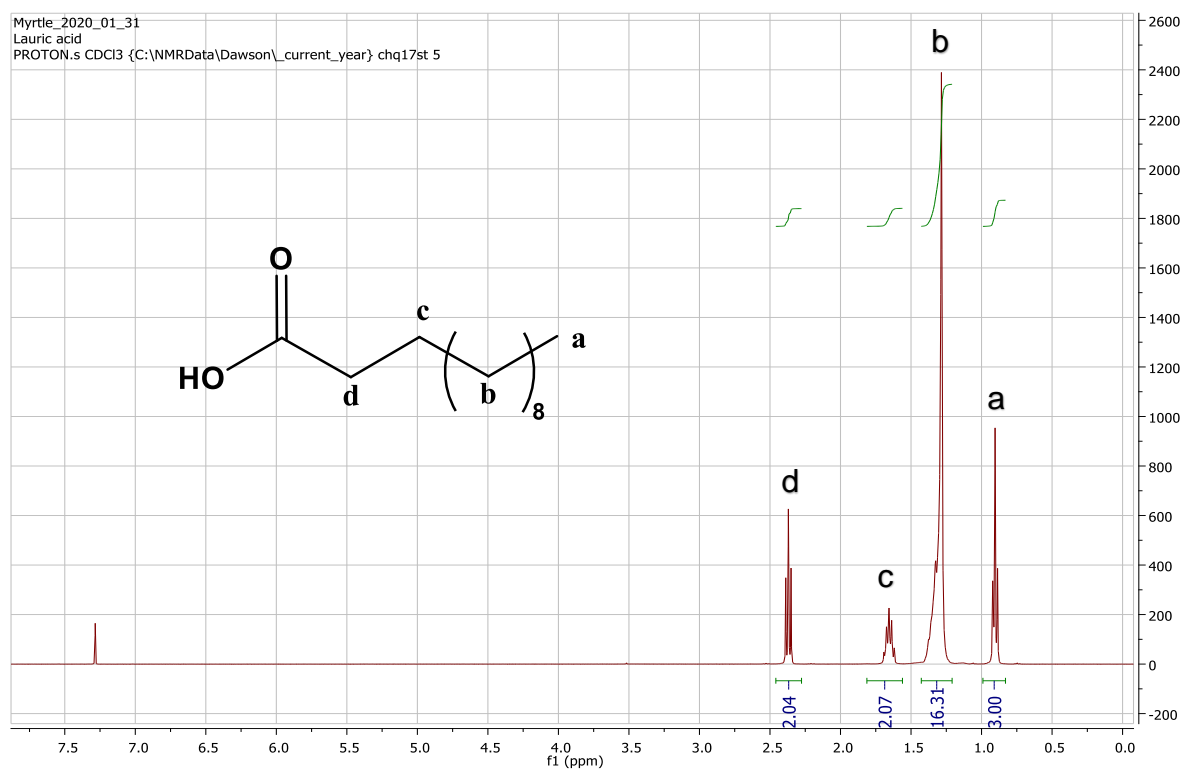
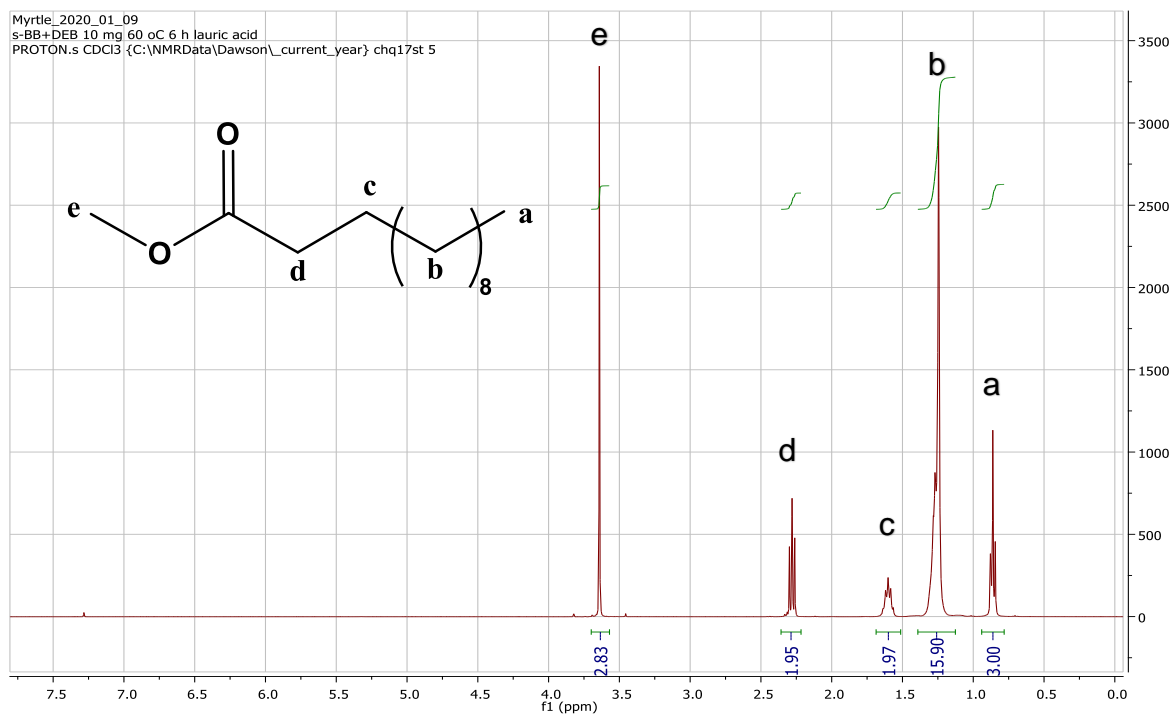
## 6.6 References

- 1 D. Y. C. Leung, X. Wu and M. K. H. Leung, *Appl. Energy*, 2010, 87, 1083–1095.
- 2 V. K. Mishra and R. Goswami, *Biofuels*, 2018, 9, 273–289.
- 3 A. Gashaw, T. Getachew and A. Mohammed, *J. For. Prod. Ind.*, 2015, 4, 80–85.
- 4 P. A. Owusu and S. Asumadu-Sarkodie, *A review of renewable energy sources, sustainability issues and climate change mitigation*, Cogent OA, 2016, vol. 3.
- 5 M. Ho, E. Obbard, P. A. Burr and G. Yeoh, in *Energy Procedia*, Elsevier Ltd, 2019, vol. 160, pp. 459–466.
- 6 F. Ma and M. A. Hanna, *Bioresour. Technol.*, 1999, 70, 1–15.
- 7 *Renewable Fuel Statistics 2019 Second Provisional Report Statistical Release*, 2019.

- 8 M. Wang, J. Ma, H. Liu, N. Luo, Z. Zhao and F. Wang, *ACS Catal.*, 2018, **8**, 2129–2165.
- 9 M. G. Kulkarni and A. K. Dalai, *Ind. Eng. Chem. Res.*, 2006, **45**, 2901–2913.
- 10 Y. M. Sani, W. M. A. W. Daud and A. R. Abdul Aziz, *Appl. Catal. A Gen.*, 2014, **470**, 140–161.
- 11 A. F. Lee, J. A. Bennett, J. C. Manayil and K. Wilson, *Chem. Soc. Rev.*, 2014, **43**, 7887–7916.
- 12 A. Varyambath, M. R. Kim and I. Kim, *New J. Chem.*, 2018, **42**, 12745–12753.
- 13 S. K. Kundu and A. Bhaumik, *ACS Sustain. Chem. Eng.*, 2015, **3**, 1715–1723.
- 14 R. M. N. Kalla, M.-R. Kim and I. Kim, *Ind. Eng. Chem. Res.*, 2018, **57**, 11583–11591.
- 15 S. Bhunia, B. Banerjee and A. Bhaumik, *Chem. Commun.*, 2015, **51**, 5020–5023.
- 16 R. Naureen, M. Tariq, I. Yusoff, A. J. K. Chowdhury and M. A. Ashraf, *Saudi J. Biol. Sci.*, 2014, **22**, 332–339.
- 17 R. S. Sprick, Y. Bai, A. A. Y. Guilbert, M. Zbiri, C. M. Aitchison, L. Wilbraham, Y. Yan, D. J. Woods, M. A. Zwijnenburg and A. I. Cooper, *Chem. Mater.*, 2019, **31**, 305–313.
- 18 J. S. M. Lee and A. I. Cooper, *Chem. Rev.*, 2020, **120**, 2171–2214.
- 19 L. Sekerová, P. Březinová, T. T. Do, E. Vyskočilová, J. Krupka, L. Červený, L. Havelková, B. Bashta and J. Sedláček, *ChemCatChem*, 2020, **12**, 1075–1084.
- 20 J. Dantas, E. Leal, D. R. Cornejo, R. H. G. A. Kiminami and A. C. F. M. Costa,

*Arab. J. Chem.*, 2020, **13**, 3026–3042.

## 6.7 Appendices

**6.7.1 <sup>1</sup>H NMR spectra of FFAs, vegetable oils and methyl ester products**Figure A6.1 <sup>1</sup>H-NMR spectrum of lauric acid in CDCl<sub>3</sub>.Figure A6.2 <sup>1</sup>H-NMR spectrum of methyl ester of lauric acid in CDCl<sub>3</sub>.

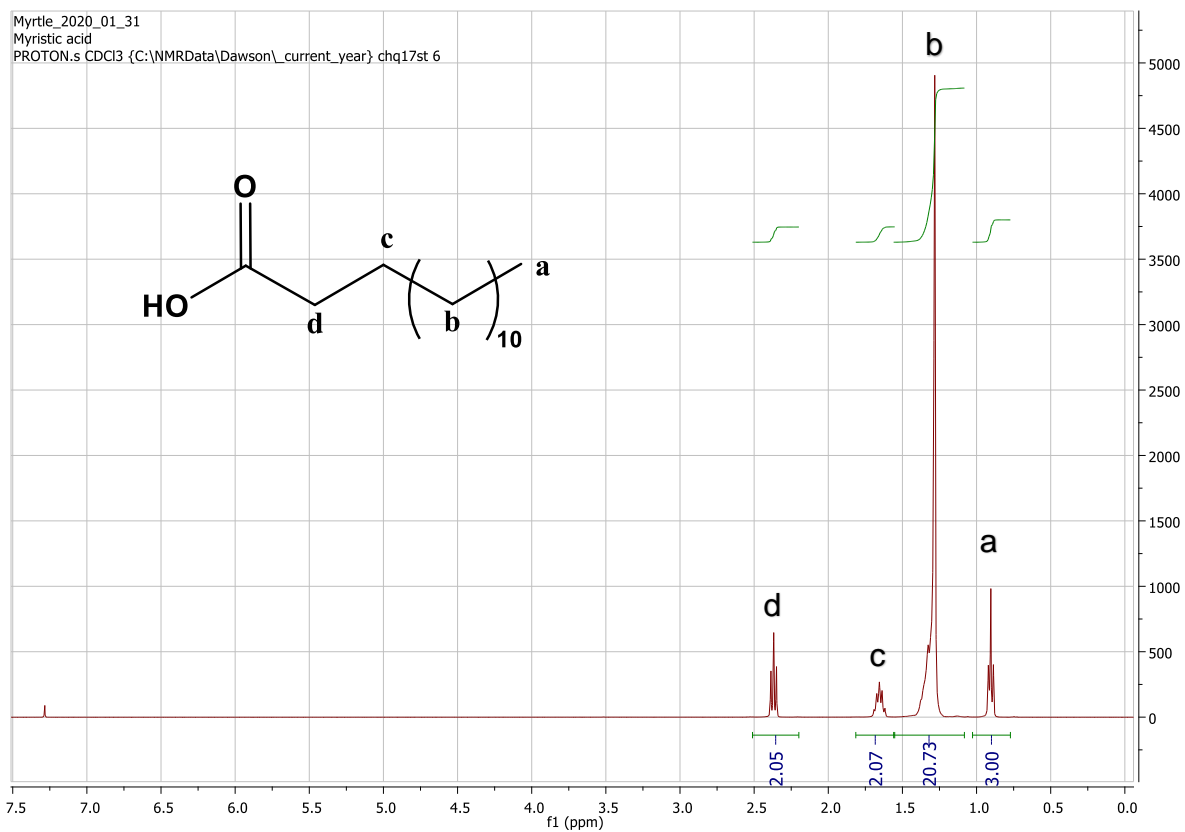


**Figure A6.3**  $^1\text{H-NMR}$  spectrum of myristic acid in  $\text{CDCl}_3$ .

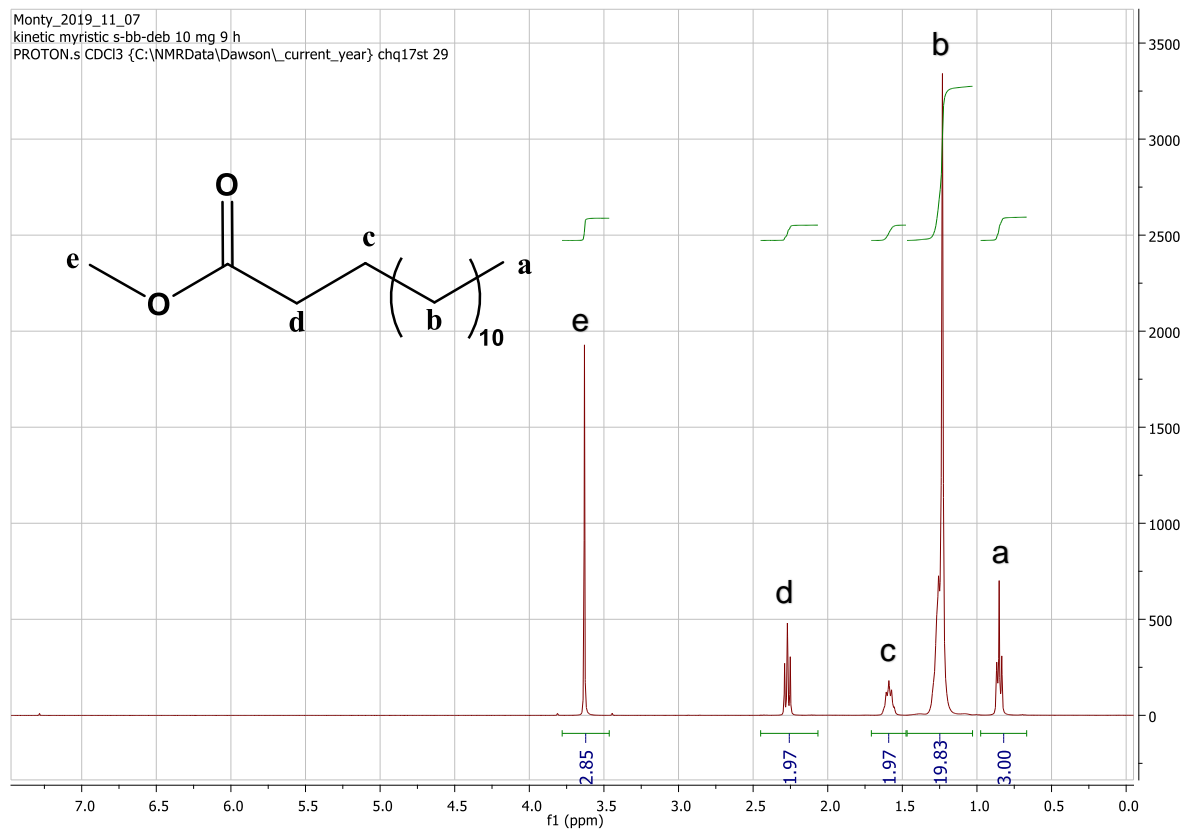


**Figure A6.4**  $^1\text{H-NMR}$  spectrum of methyl ester of myristic acid in  $\text{CDCl}_3$ .

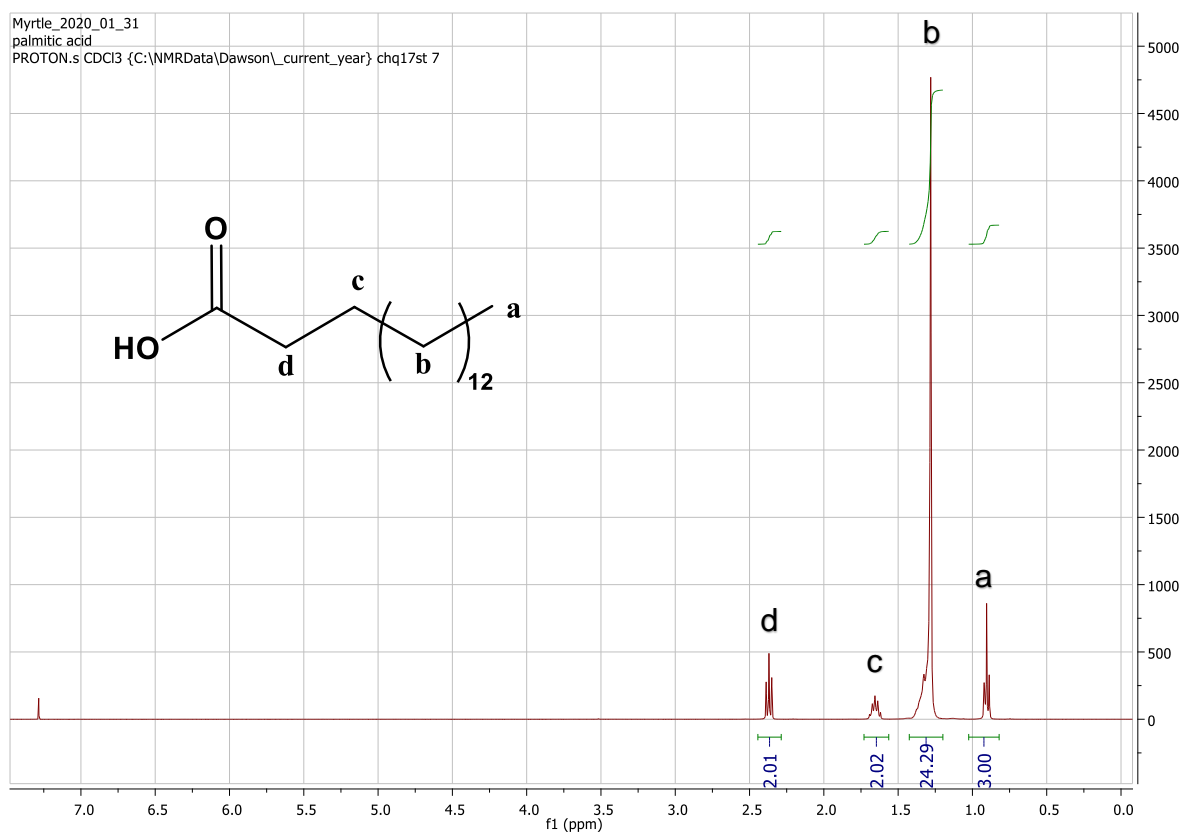


**Figure A6.5**  $^1\text{H-NMR}$  spectrum of palmitic acid in  $\text{CDCl}_3$ .

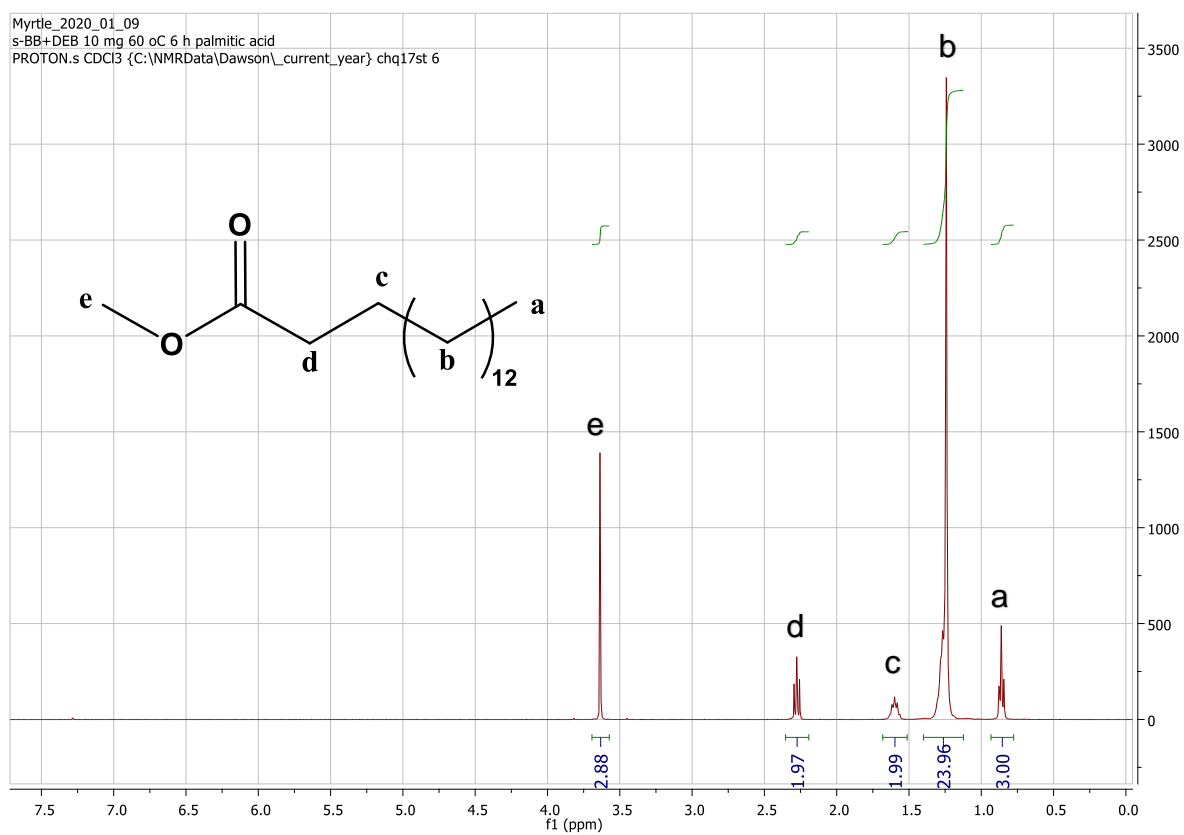


**Figure A6.6**  $^1\text{H-NMR}$  spectrum of methyl ester of palmitic acid in  $\text{CDCl}_3$ .

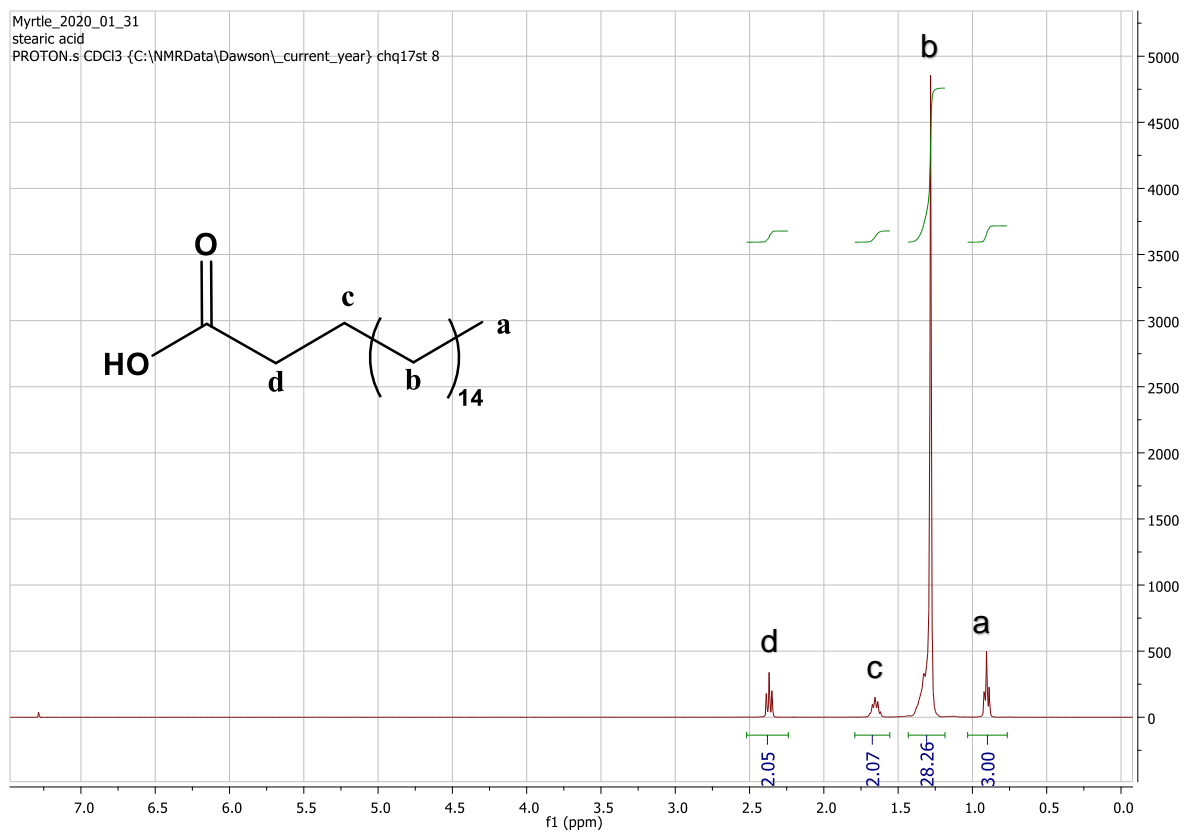


**Figure A6.7**  $^1\text{H-NMR}$  spectrum of stearic acid in  $\text{CDCl}_3$ .

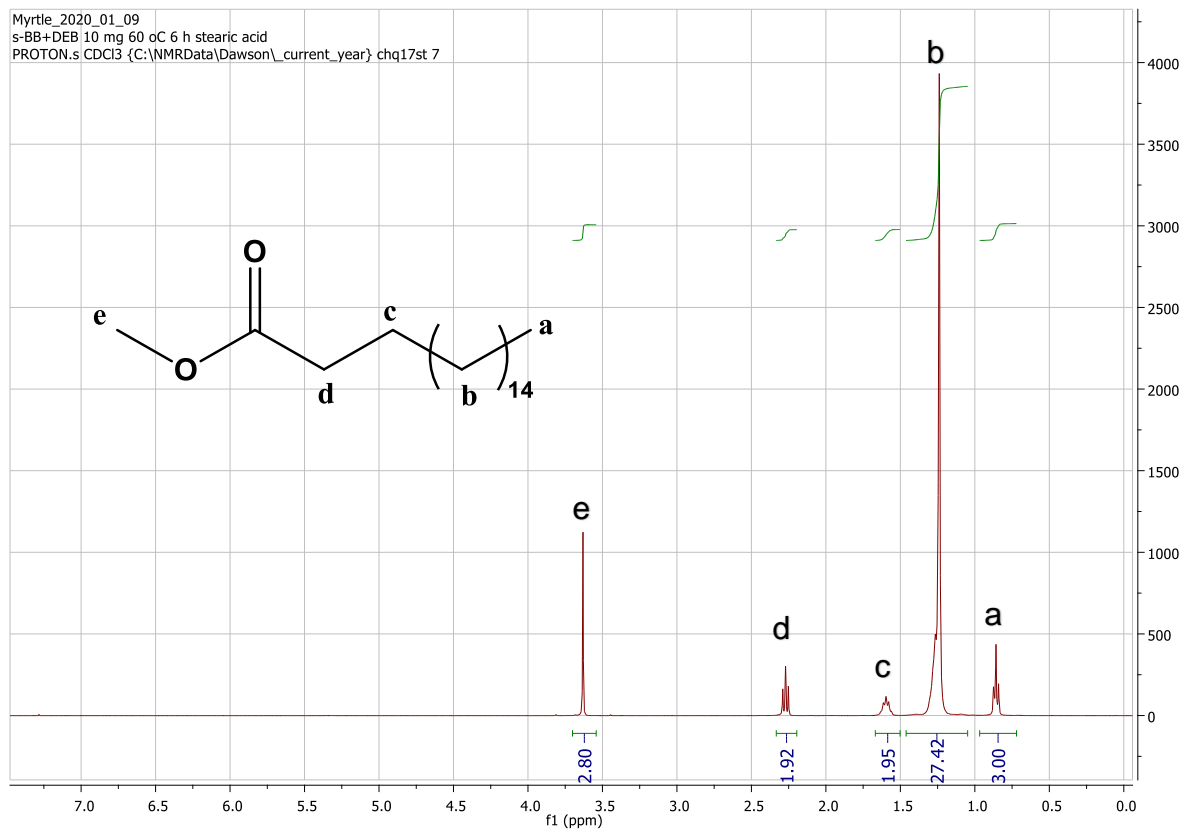


**Figure A6.8**  $^1\text{H-NMR}$  spectrum of methyl ester of stearic acid in  $\text{CDCl}_3$ .

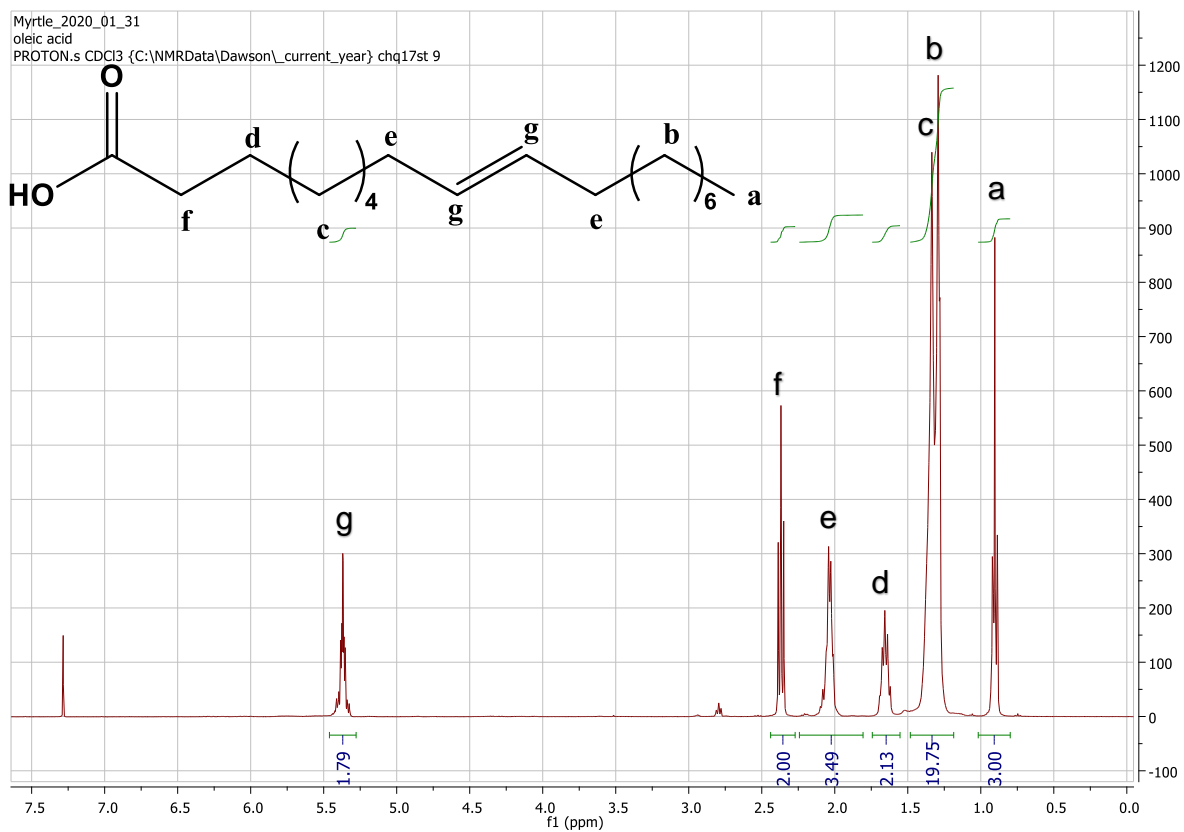


Figure A6.9 <sup>1</sup>H-NMR spectrum of oleic acid in CDCl<sub>3</sub>.

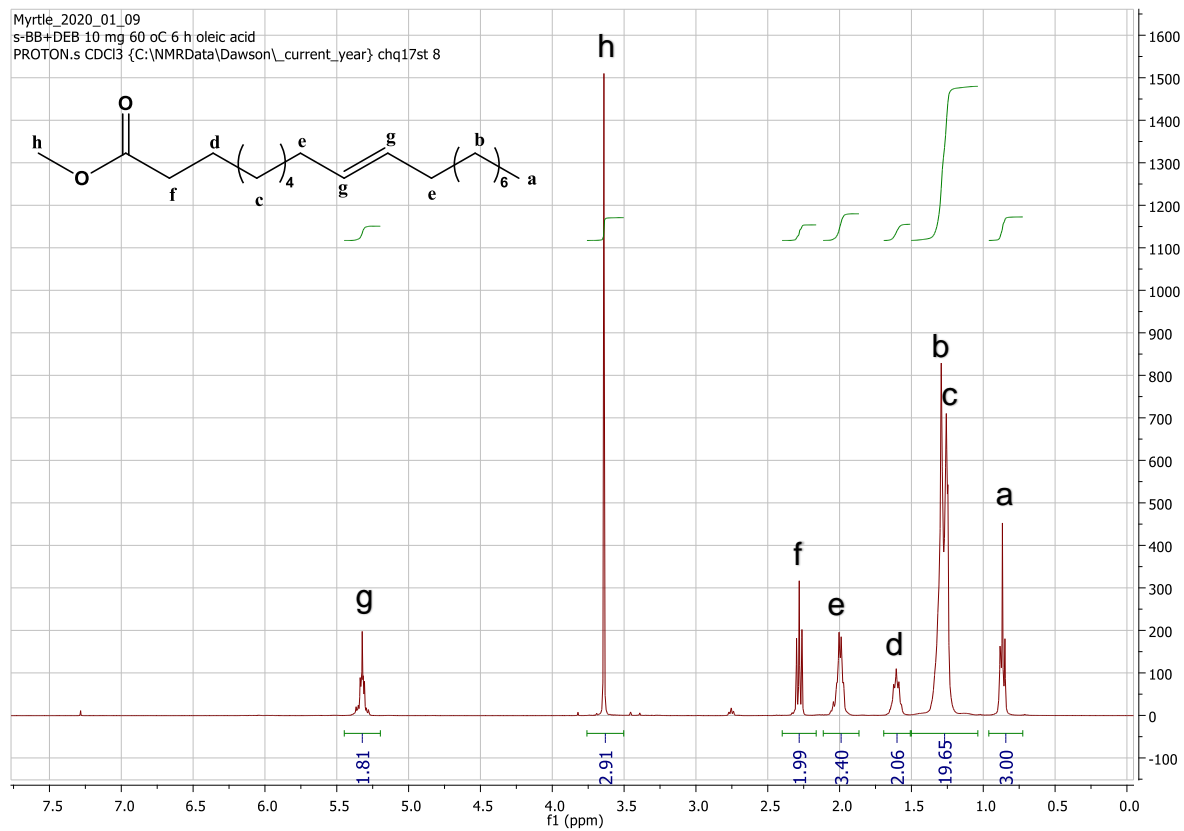
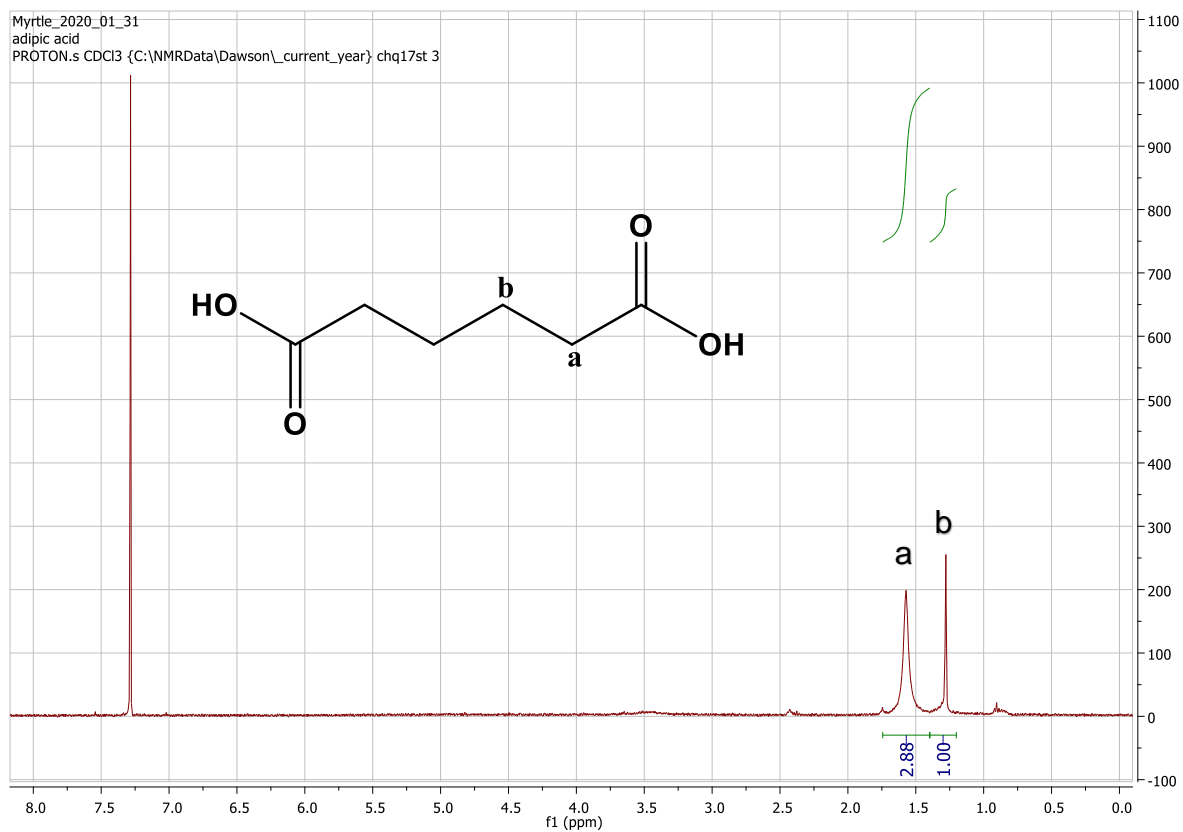
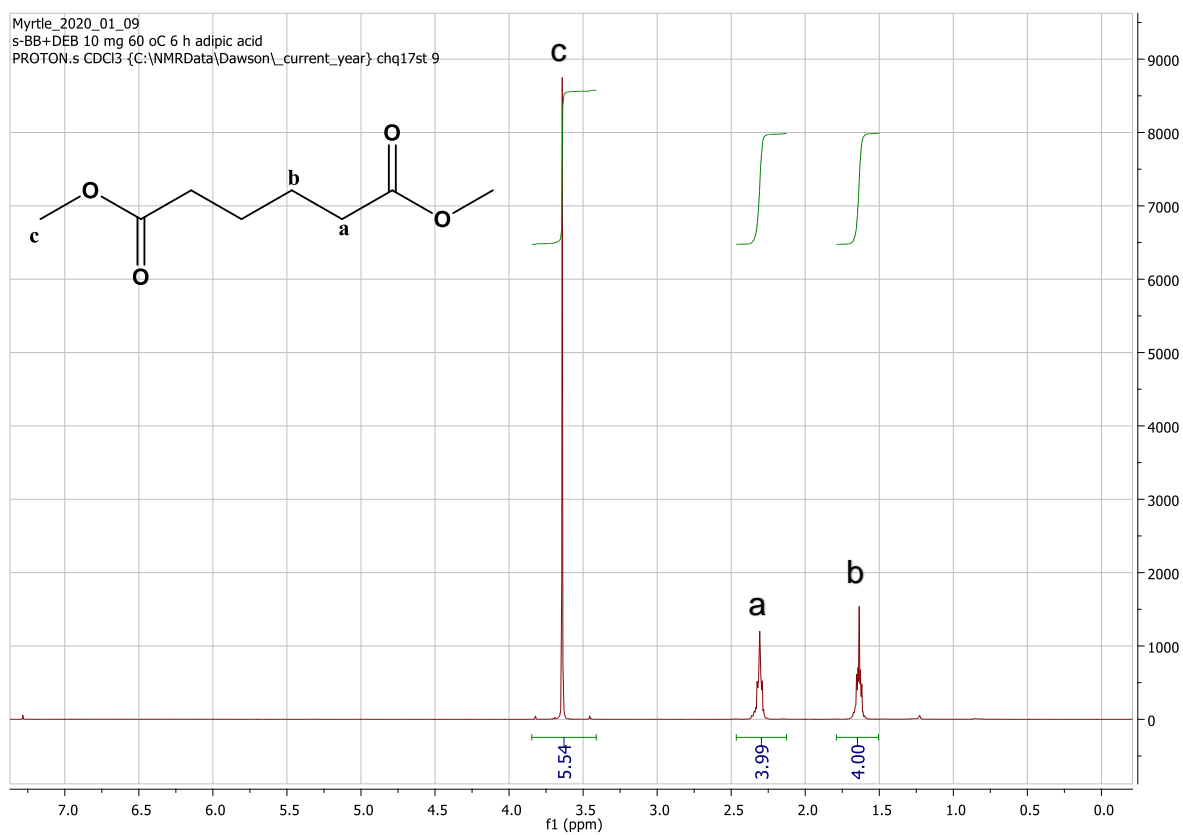


Figure A6.10 <sup>1</sup>H-NMR spectrum of methyl ester of oleic acid in CDCl<sub>3</sub>.



**Figure A6.11**  $^1\text{H-NMR}$  spectrum of adipic acid in  $\text{CDCl}_3$ .



**Figure A6.12**  $^1\text{H-NMR}$  spectrum of methyl ester of adipic acid in  $\text{CDCl}_3$ .

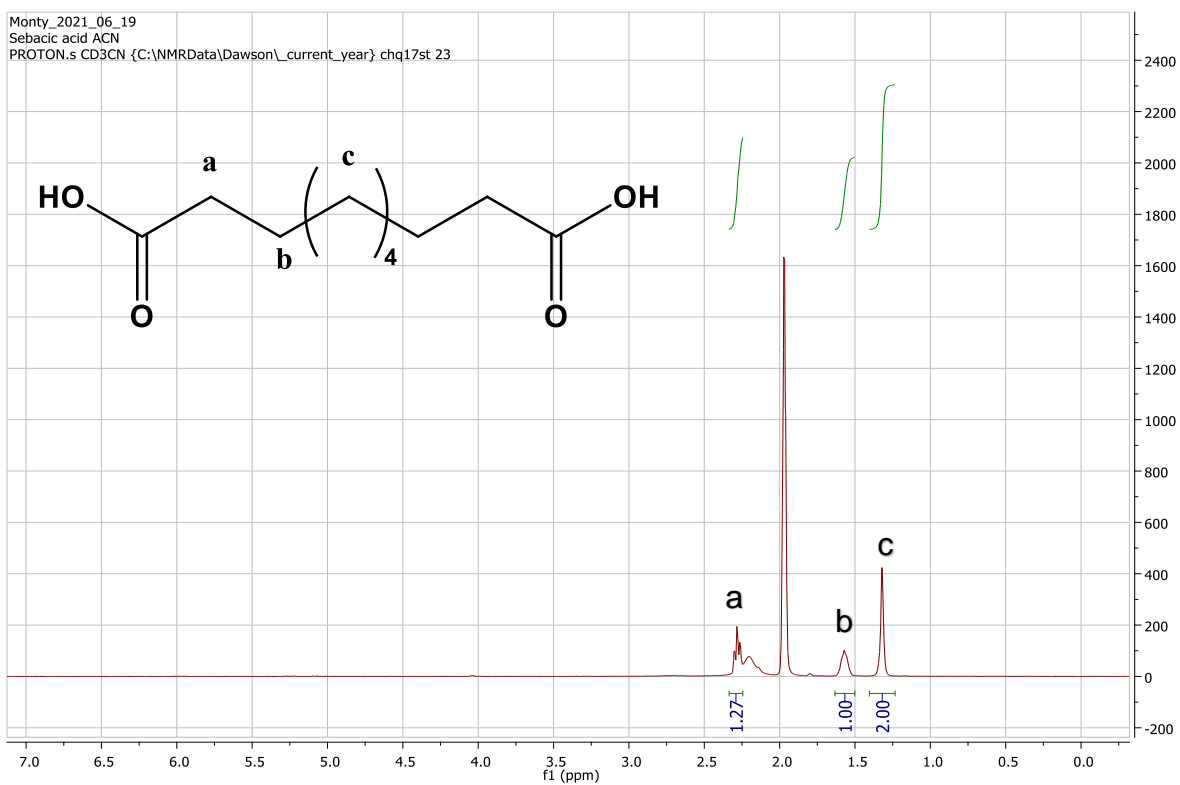


Figure A6.13  $^1\text{H-NMR}$  spectrum of sebacic acid in  $\text{CD}_3\text{CN}$ .

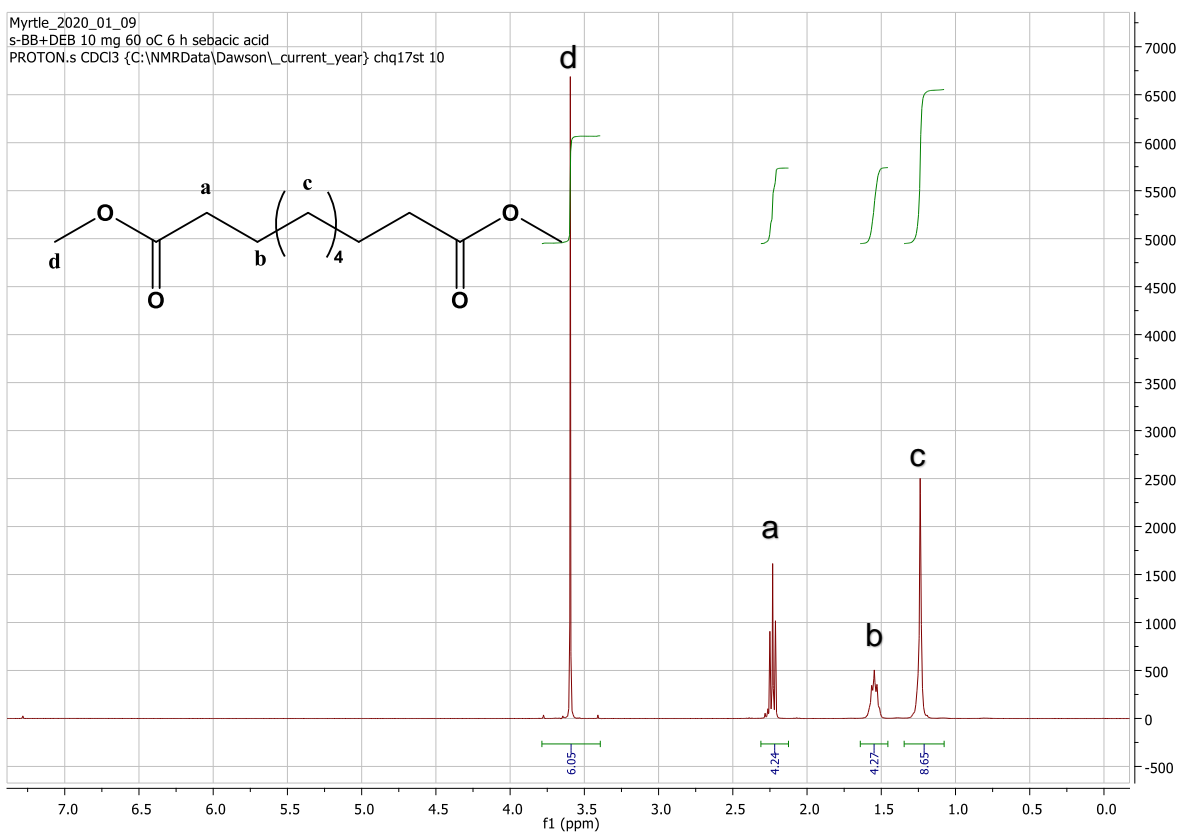
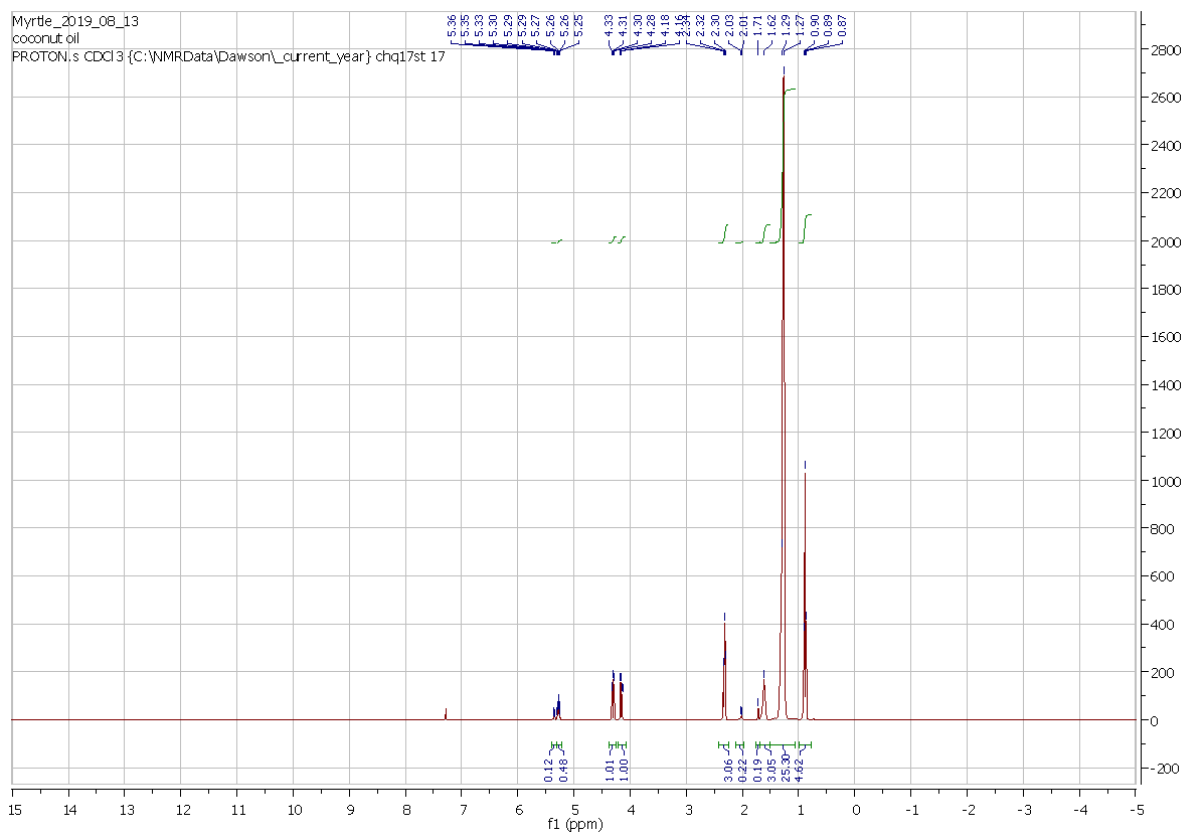
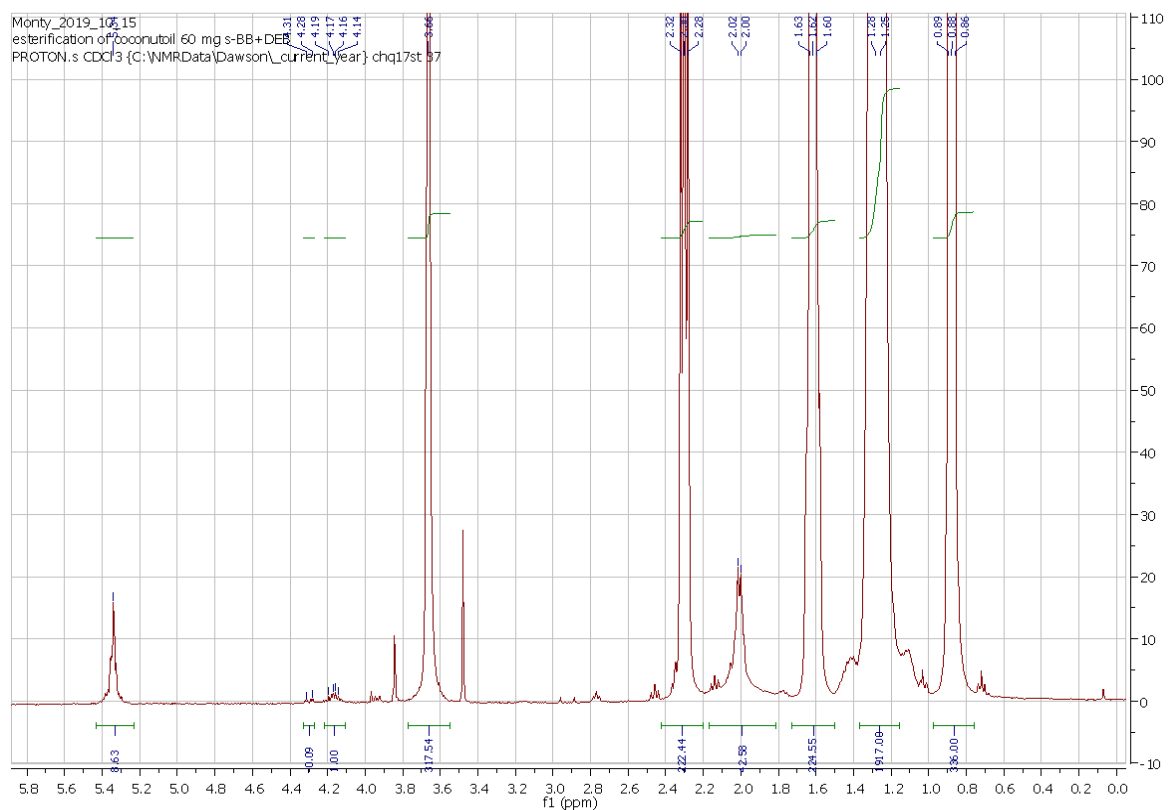


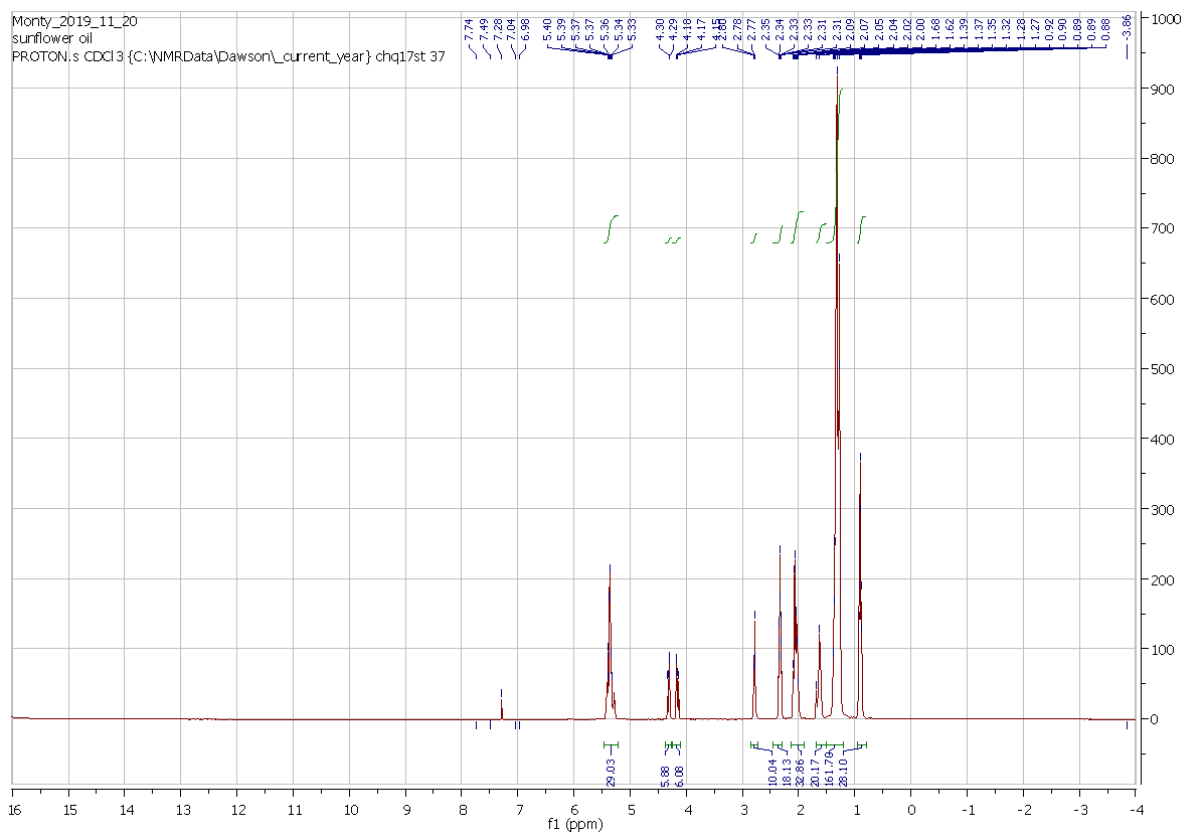
Figure A6.14  $^1\text{H-NMR}$  spectrum of methyl ester of sebacic acid in  $\text{CDCl}_3$ .



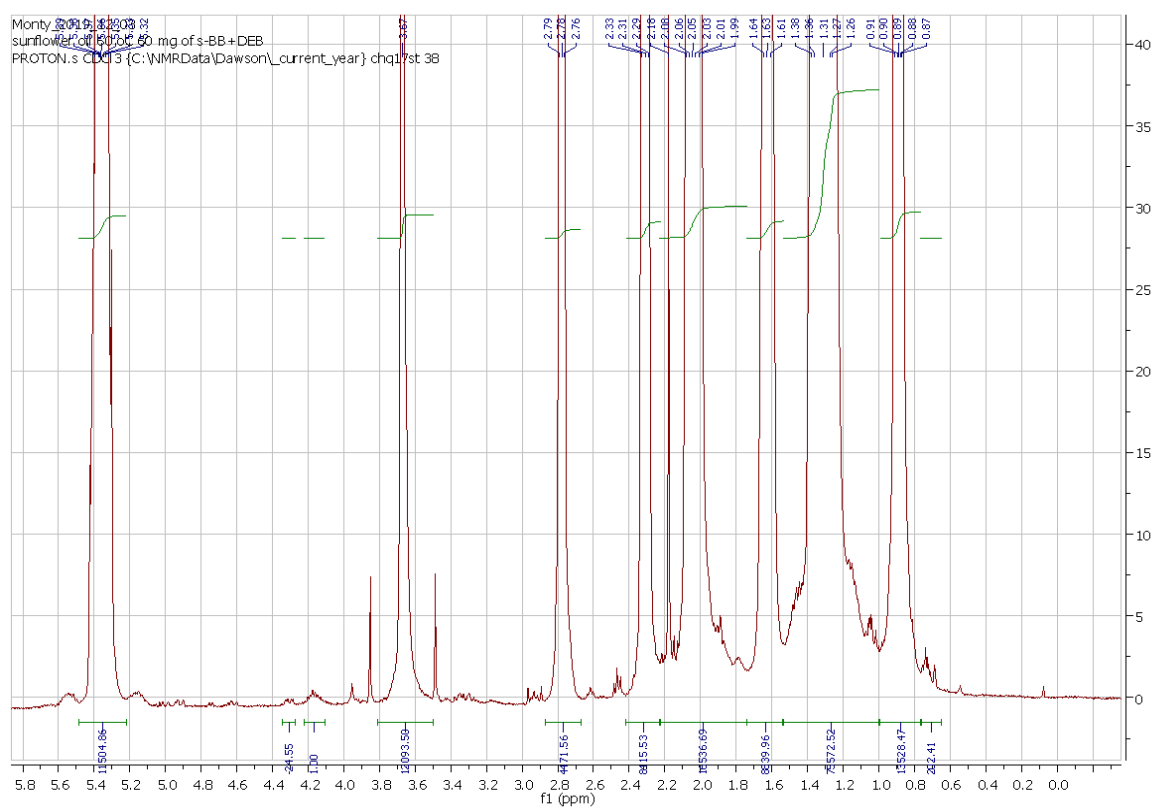
**Figure A6.15**  $^1\text{H-NMR}$  spectrum of coconut oil in  $\text{CDCl}_3$ .



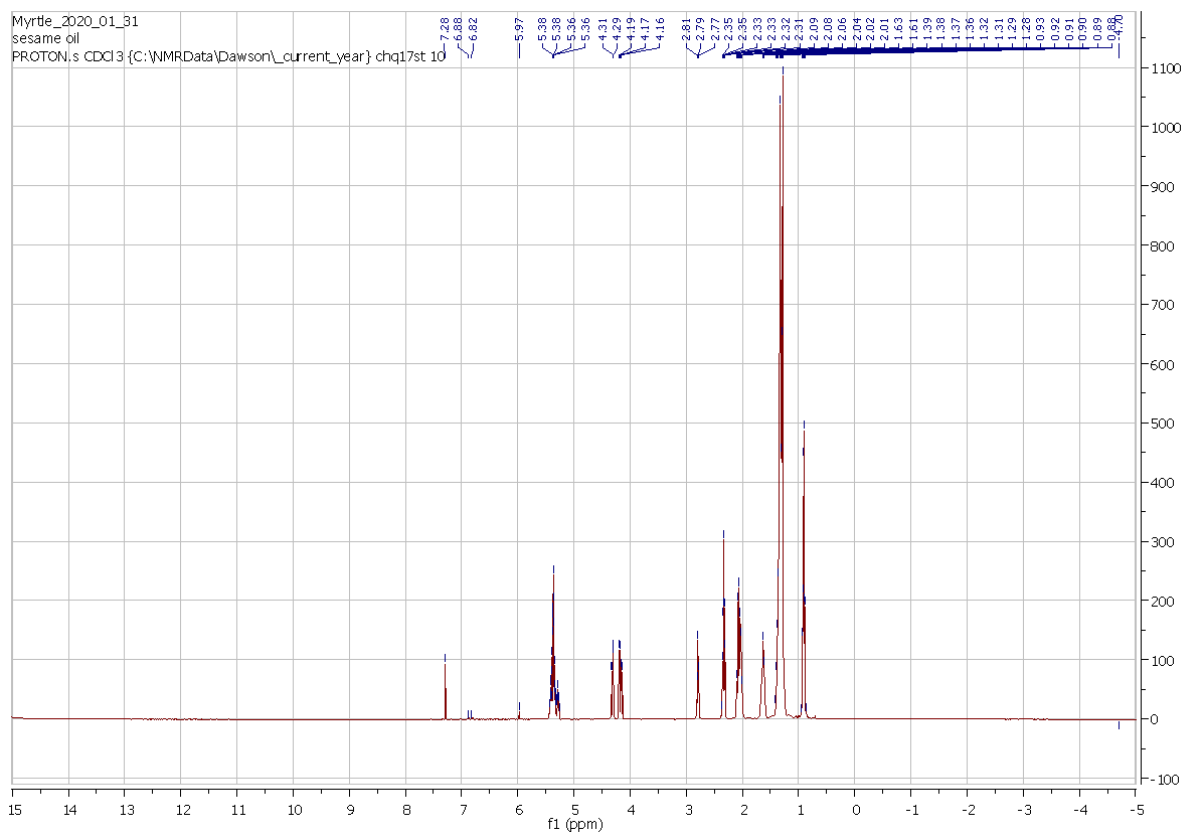
**Figure A6.16**  $^1\text{H-NMR}$  spectrum of transesterification of coconut oil using s-BB+DEB at  $60\text{ }^\circ\text{C}$  for 24 h in  $\text{CDCl}_3$ .



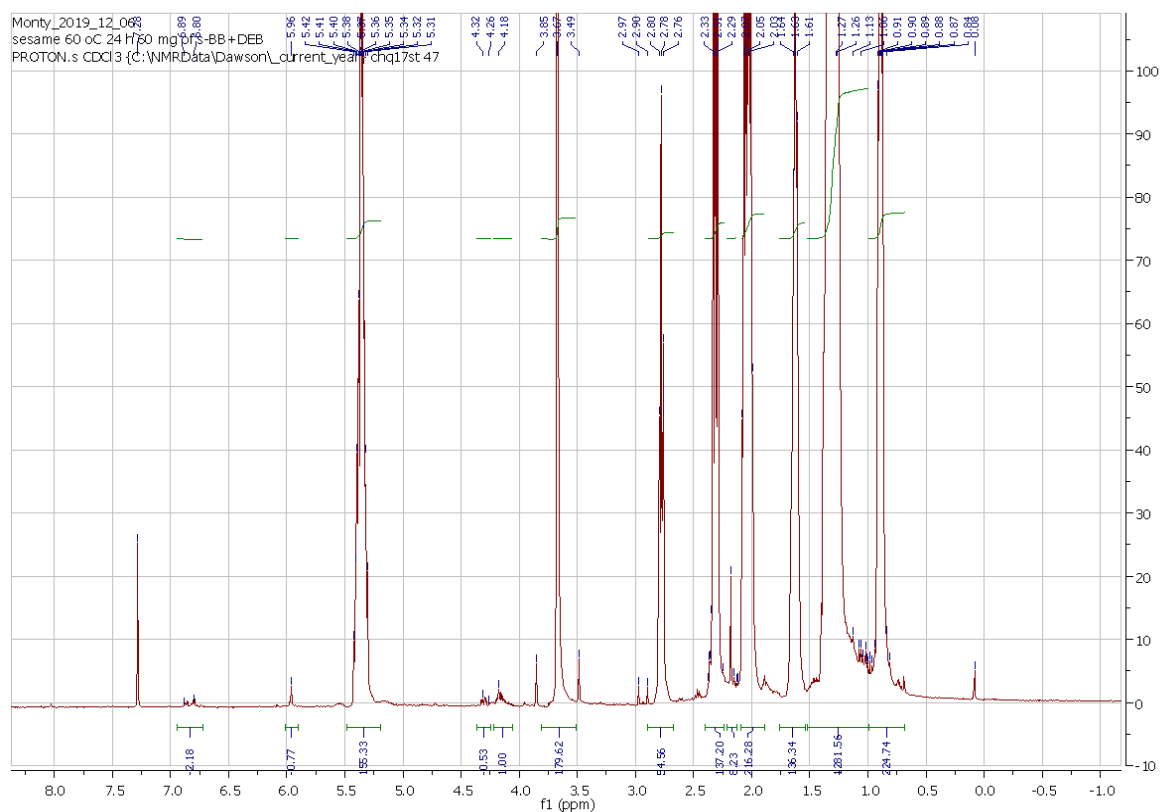
**Figure A6.17**  $^1\text{H}$ -NMR spectrum of sunflower oil in  $\text{CDCl}_3$ .



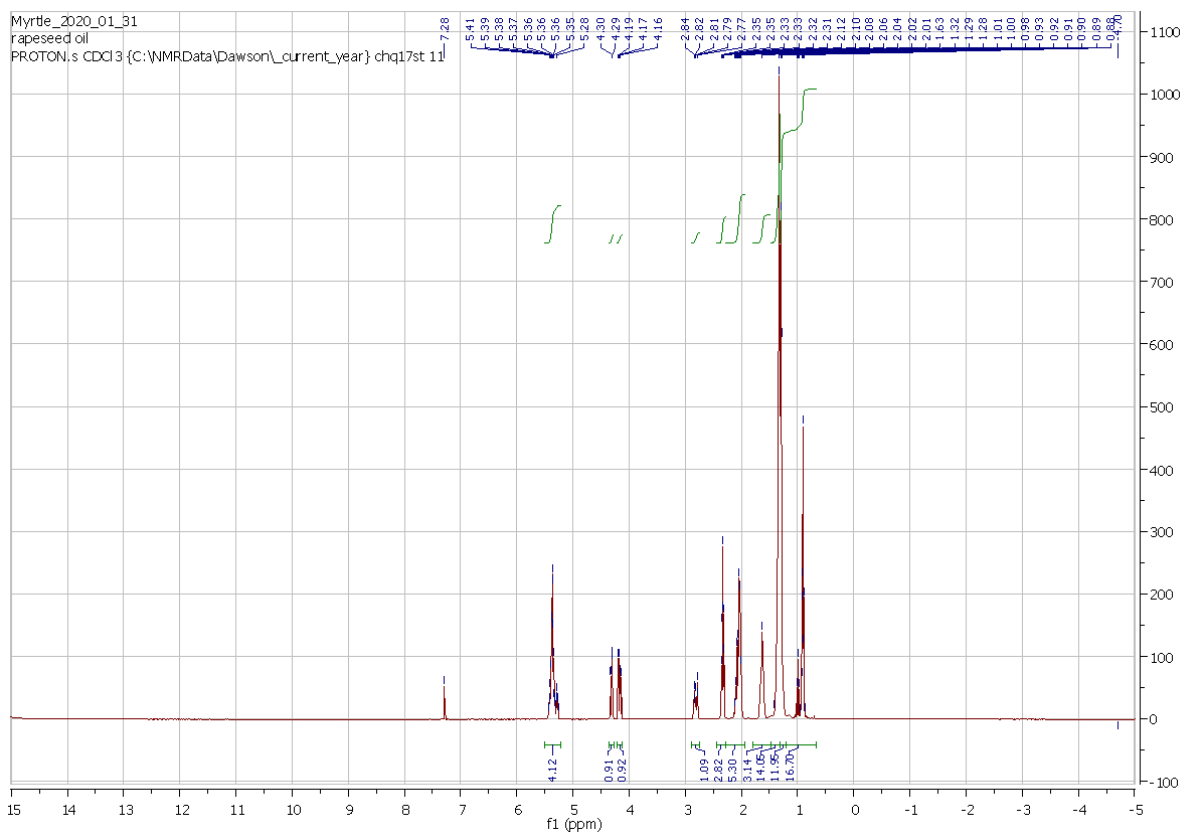
**Figure A6.18**  $^1\text{H}$ -NMR spectrum of transesterification of sunflower oil using s-BB+DEB at  $60\text{ }^\circ\text{C}$  for 24 h in  $\text{CDCl}_3$ .



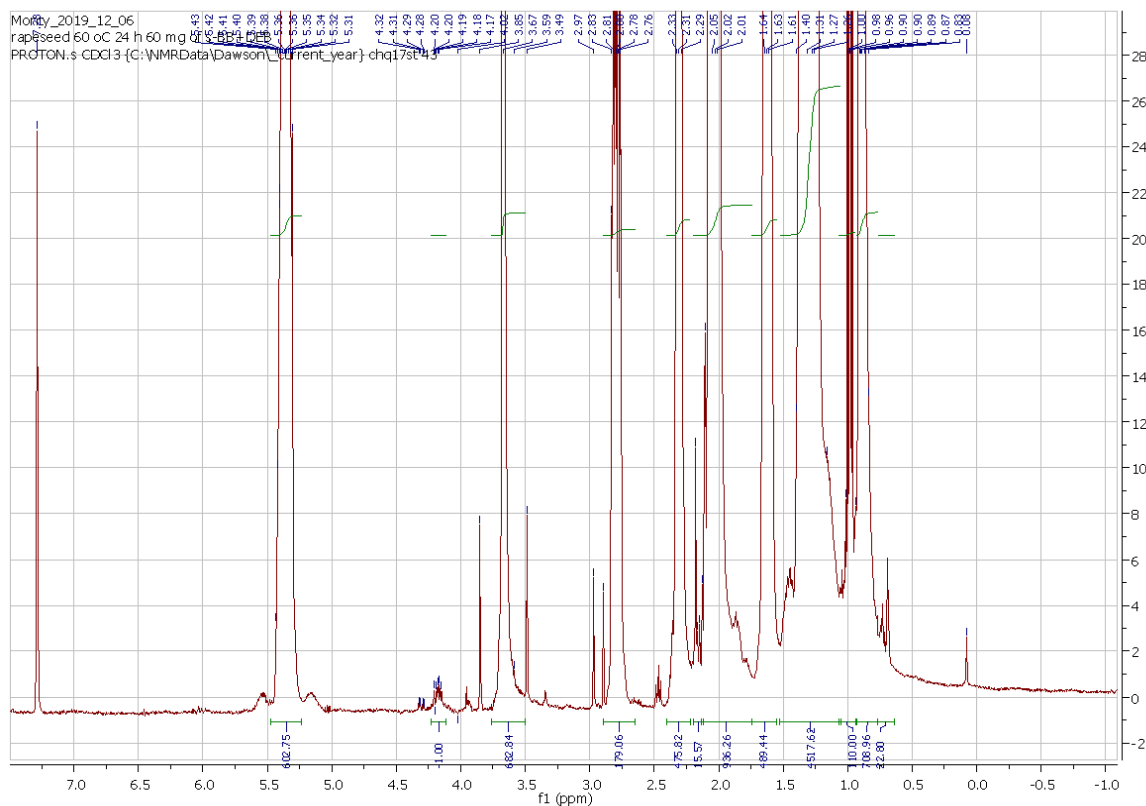
**Figure A6.19**  $^1\text{H-NMR}$  spectrum of sesame oil in  $\text{CDCl}_3$ .



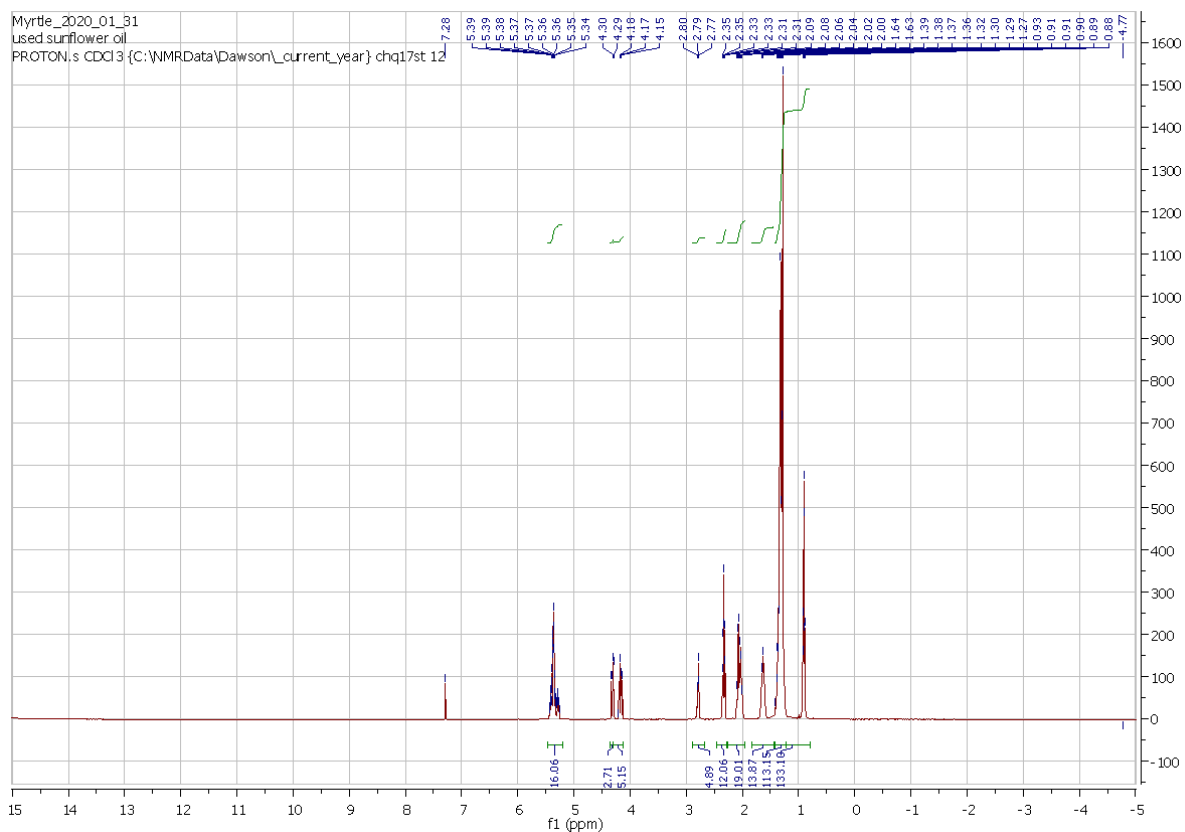
**Figure A6.20**  $^1\text{H-NMR}$  spectrum of transesterification of sesame oil using s-BB+DEB at 60 °C for 24 h in  $\text{CDCl}_3$ .



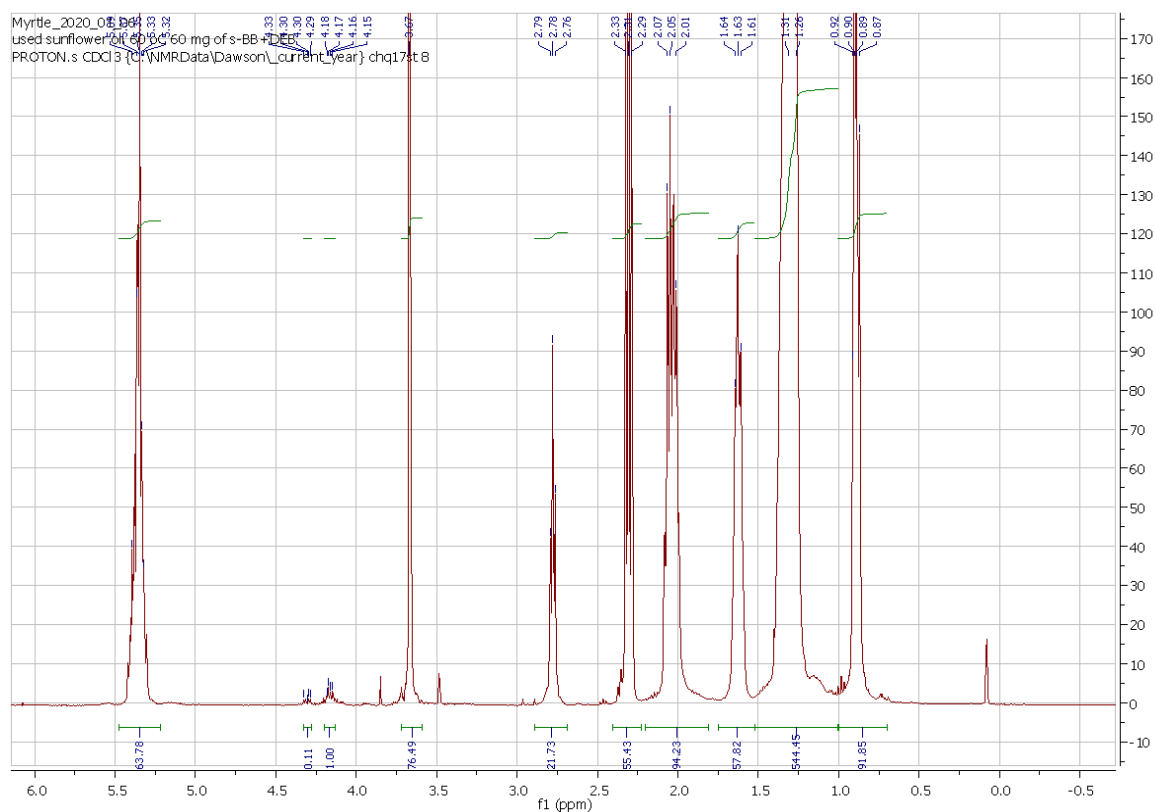
**Figure A6.21**  $^1\text{H-NMR}$  spectrum of rapeseed oil in  $\text{CDCl}_3$ .



**Figure A6.22**  $^1\text{H-NMR}$  spectrum of transesterification of rapeseed oil using s-BB+DEB at  $60\text{ }^\circ\text{C}$  for 24 h in  $\text{CDCl}_3$ .



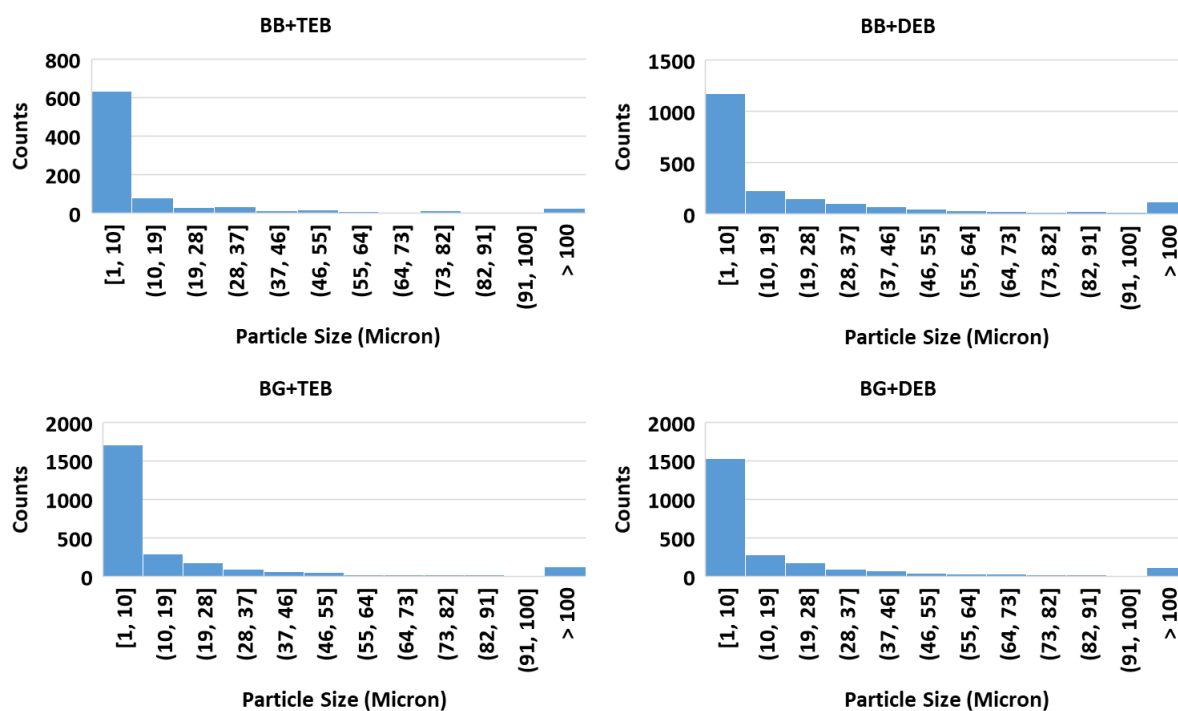
**Figure A6.23**  $^1\text{H-NMR}$  spectrum of used sunflower oil in  $\text{CDCl}_3$ .



**Figure A6.24**  $^1\text{H-NMR}$  spectrum of transesterification of used sunflower oil using s-BB+DEB at  $60\text{ }^\circ\text{C}$  for 24 h in  $\text{CDCl}_3$ .

**6.7.2 Particle size analysis of the synthesised polymers****Table A6.1** The particle size of the synthesised polymers

Polymers	Particle Size (Micron)	
	TEB	DEB
<b>BB</b>	24.6	27.3
<b>BG</b>	23.3	26.0
<b>HCI-BB</b>	15.2	19.4
<b>HCI-BG</b>	21.9	18.7
<b>s-BB</b>	19.1	16.3
<b>s-BG</b>	22.2	19.6

**Figure A6.25** The particle size distributions of the as synthesised polymers.

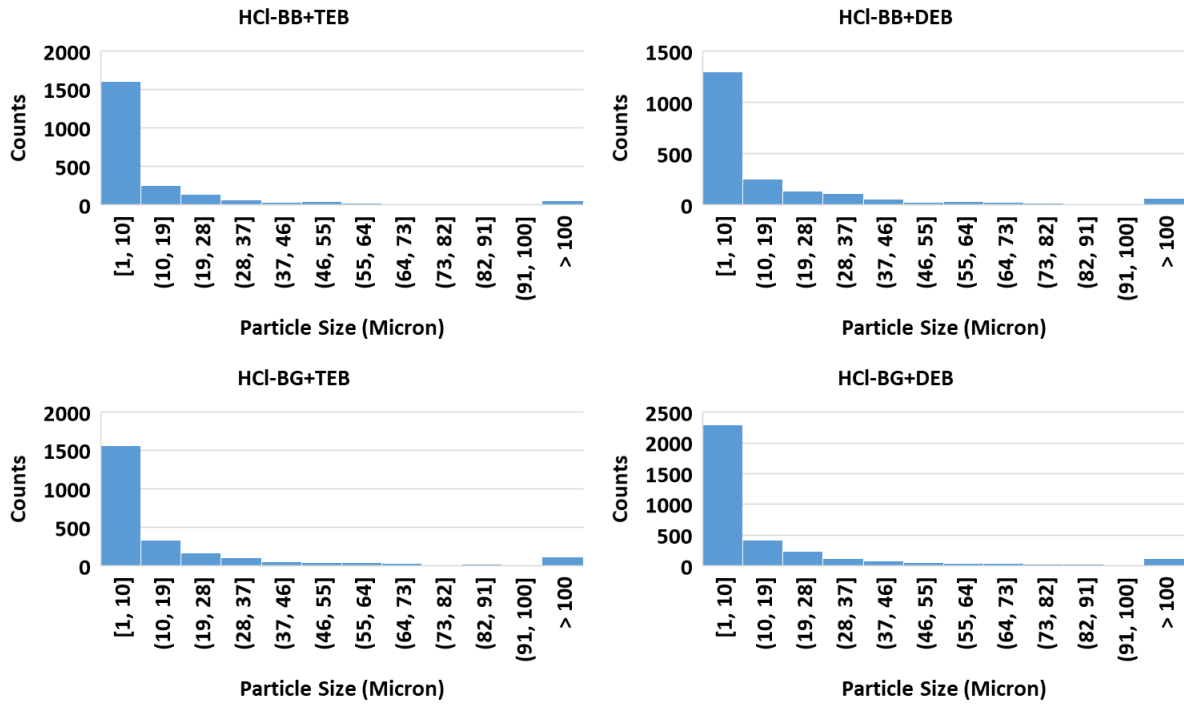


Figure A6.26 The particle size distributions of the HCl treated polymers.

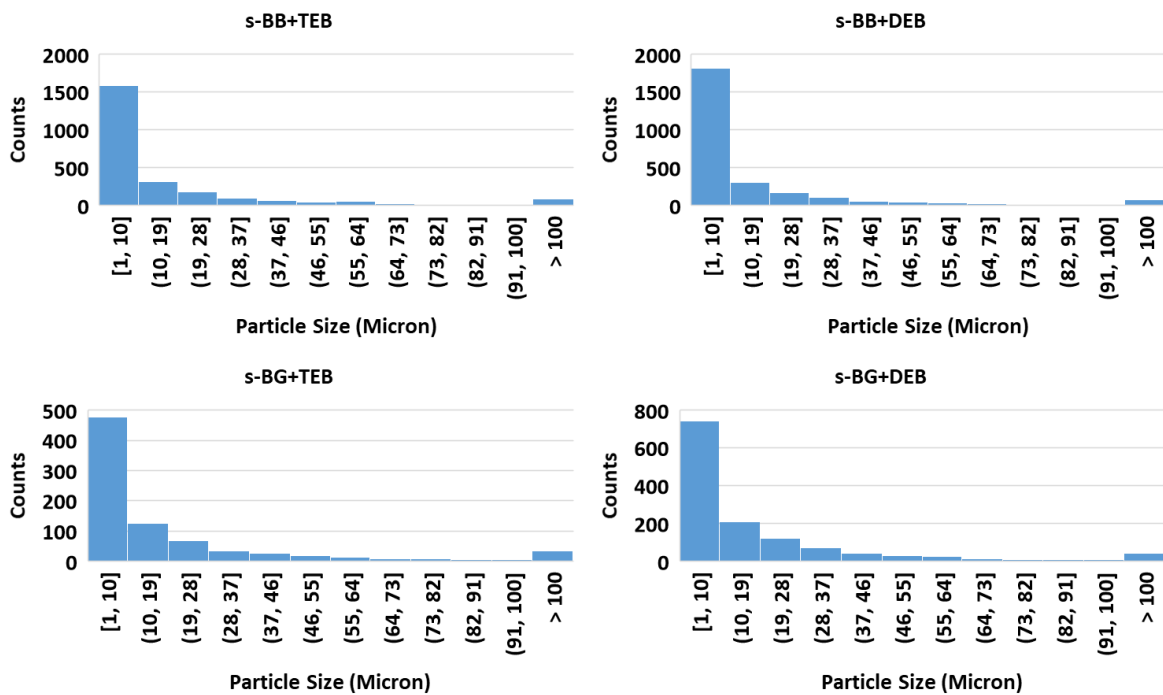
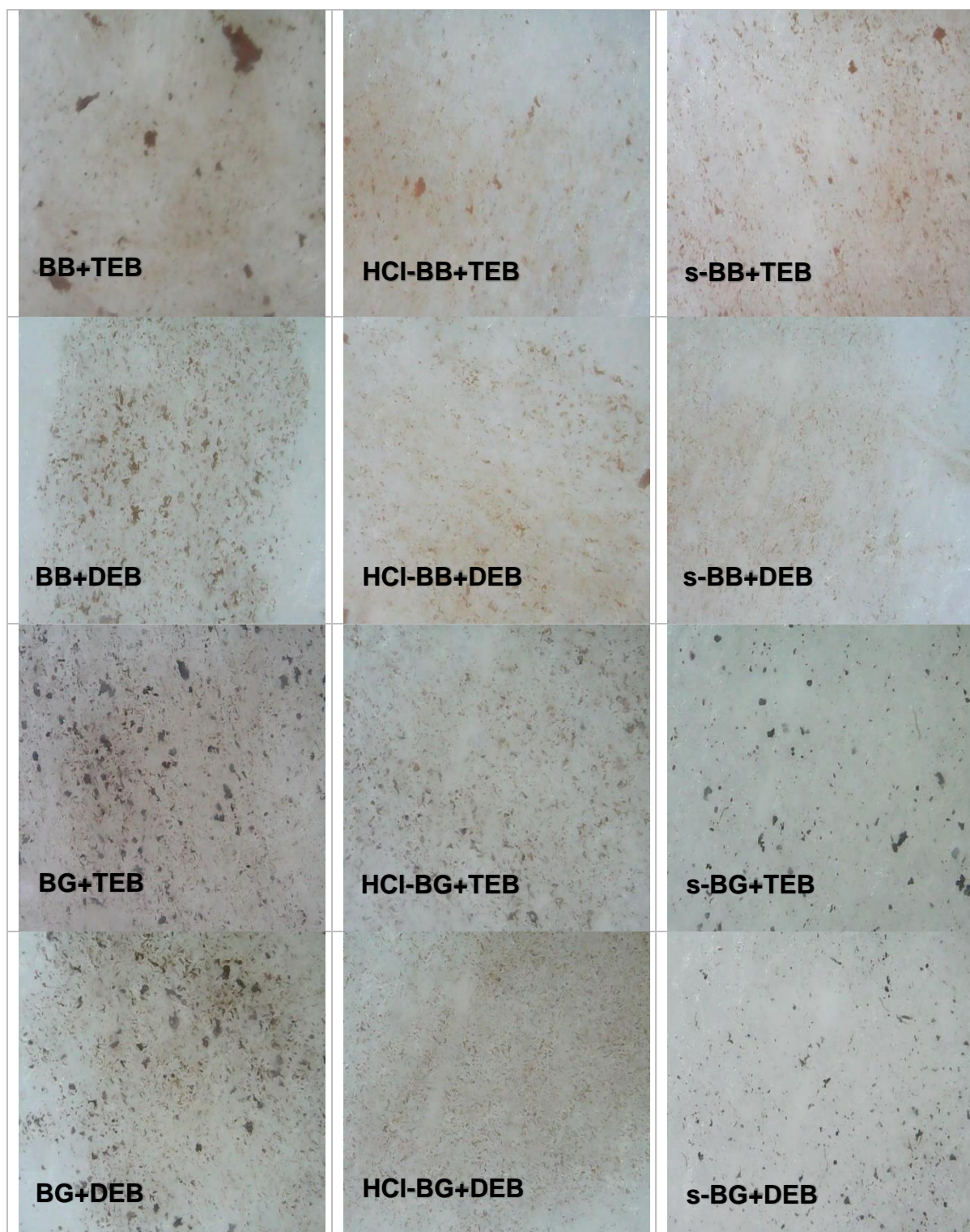


Figure A6.27 The particle size distributions of the sulfonated polymers.



**Figure A6.28** The optical micrographs of the synthesised polymers.

## Chapter 7

### Conclusions and Future Work

#### 7.1 Conclusions

A variety of conjugated microporous polymers (CMPs) were synthesised and characterised in this work. As described in Chapter 3, pyrylium based CMPs were synthesised by various synthetic methods such as Sonogashira cross coupling, oxidative and Yamamoto homocouplings giving various structures and porosities of the materials. The formation of polymer networks was confirmed by  $^{13}\text{C}$  CP/MAS and FTIR. The porosity of the materials, characterised by nitrogen gas sorption, can be tuned by varying crosslinkers e.g. TEB and DEB, pyrylium structures such as bromo groups at *para* and *meta* positions and substituted groups at *para* position e.g. methyl, methoxy and fluoro groups. The pyrylium based CMPs showed broad UV-Vis adsorption profiles due to extended conjugation systems resulting in low band gap energies. Due to the covalent bonded structures, the materials showed high thermal stability.

The synthesised pyrylium based CMPs were used as heterogeneous catalysts for oxidation of thioanisole using hydrogen peroxide as an oxidising agent. The structure of the materials showed significant effect on the catalytic activity as DEB linkage polymers displayed higher catalytic activity than TEB version due to the better delocalisation of electron in DEB derived materials. The substituents also improved catalytic activity as the fluoro substituted polymer showed the fastest reaction rate because the higher electronegativity of the fluoro group increased the reactivity of the pyrylium group. The selectivity of the products can be altered by the structure of

polymers and reaction time, temperature and amount of oxidant. At the optimum condition, the pyrylium based CMPs showed a high conversion and high selectivity toward sulfoxide product. The optimum catalyst could be reused 6 times; however, the %conversion decreased over multiple utilisation due to the pore blocking by residual reactants and products and the collapsed of polymer structure under strong oxidising condition as confirmed by the significant loss of the BET surface area of the material. The reaction mechanism was studied by adding different reactive oxygen scavengers and the results showed that the reaction occurred *via* a perhydroxyl radical transfer pathway as discussed in Chapter 4.

In Chapter 5, tetrabromo monomers; bromophenol blue and bromocresol green were polymerised with either TEB or DEB *via* Sonogashira coupling to produce 4 different structures of polymers. The polymers were characterised by  $^{13}\text{C}$  CP/MAS and FTIR confirming formation of the CMP networks. The synthesised materials showed high surface areas up to  $747\text{ m}^2/\text{g}$  and showed the main pore sizes at less than 2 nm confirming the microporous structure. The synthesised CMPs were chemically post modified by chlorosulfonic acid to increase acidity of the materials. The incorporation of acid groups can be confirmed by a significant decrease in surface area of the materials, an increase in sulphur content from elemental analysis and the higher acidity of the materials compared with as synthesised materials. The high acidity of the materials up to  $7.67\text{ mmol/g}$  made them suitable as an acid catalyst for biodiesel production.

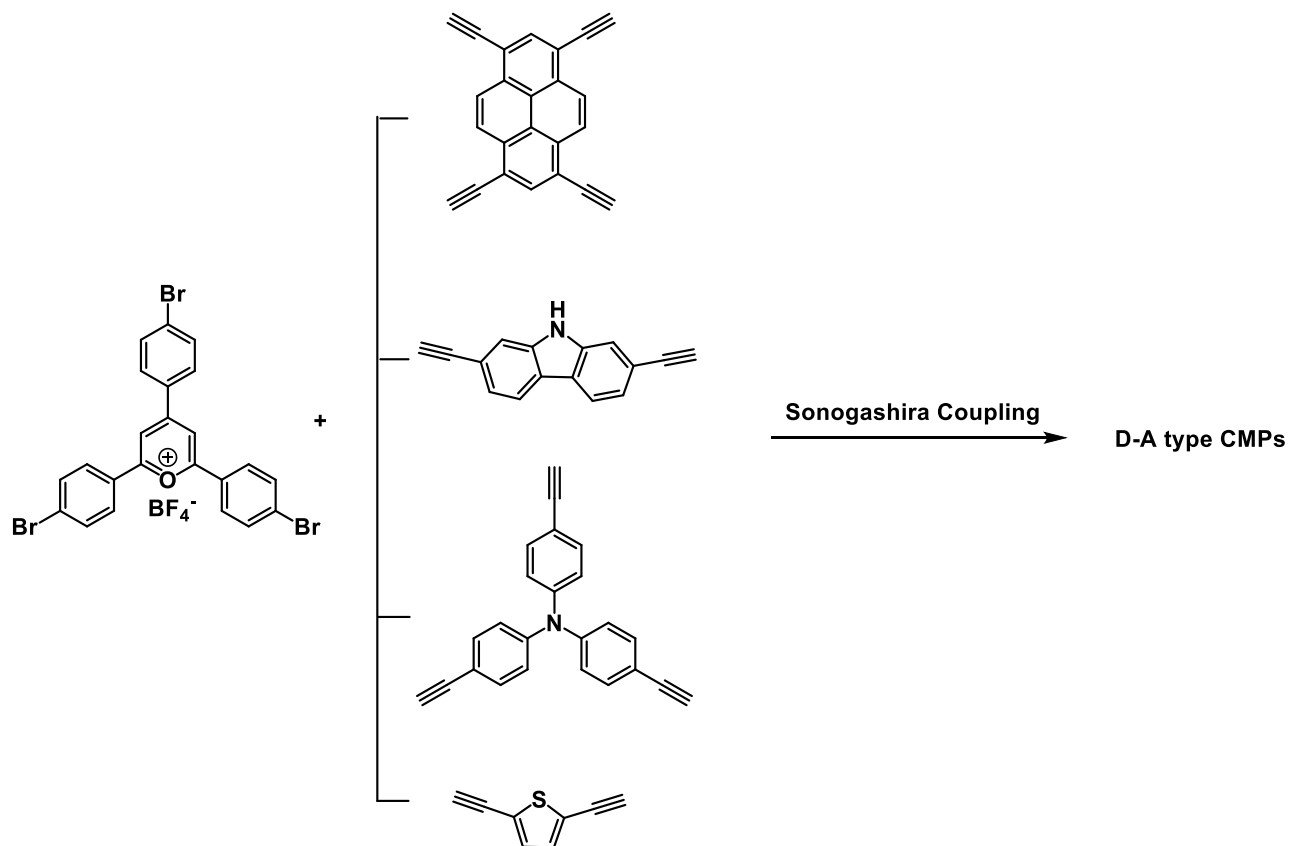
In Chapter 6, the synthesised CMPs were utilised as an acid catalyst for esterification of free fatty acids (FFAs) and transesterification of vegetable oils. The no catalyst and non-functionalised CMPs showed very low %yield of product while the sulfonated CMPs showed higher %yield due to the higher acidity of the materials. The

acid functionalised CMPs showed comparable activity with homogeneous catalyst and can produce high yields of the products at room temperature. The functionalised materials can also produce high % yield of biodiesel product from waste sunflower oil indicating that the synthesised materials can not only use for production of renewable energy but also reduce the environmental problems caused from the excessive waste cooking oils. The optimum catalyst showed an excellent reusability and can be reused up to 4 cycles with just 10% activity loss.

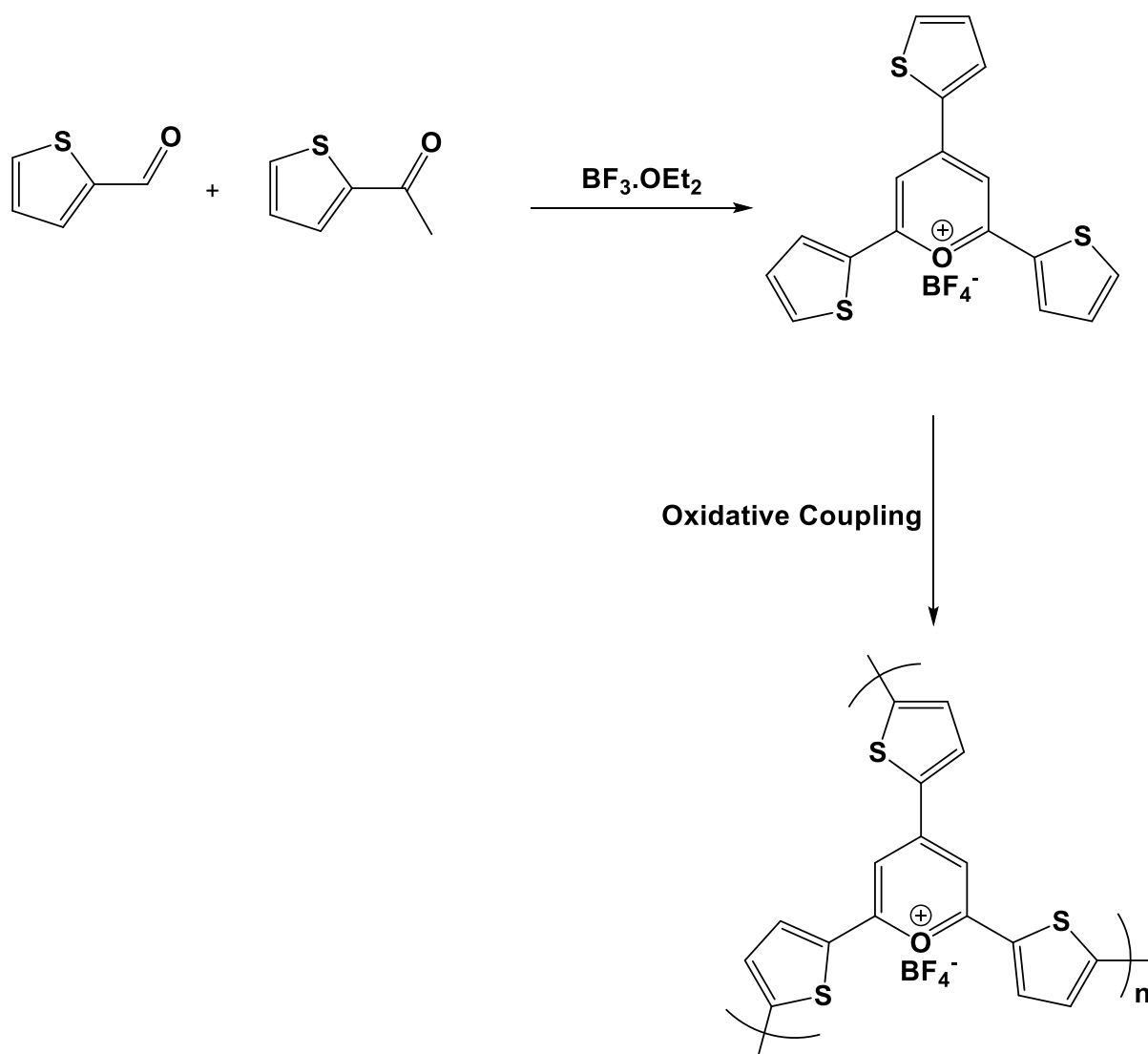
## 7.2 Future work

According to previous works, electron donor (D) and electron acceptor (A) type conjugate microporous polymers (CMPs) have been widely studied due to strong push–pull intramolecular charge transfer (ICT) combining with extended conjugated structure leading to the strong absorption ability in the visible and near-infrared region. The alternation of D and A monomers can tune the band gap as well as the highest occupied molecular orbital (HOMO) and the lowest unoccupied molecular orbital (LUMO) for specific applications such as organic solar cells and photocatalysis.<sup>1–5</sup> Pyrylium is well known electron acceptor.<sup>6</sup> This work showed that pyrylium functional groups can be incorporated into CMPs using various synthetic methods such as Sonogashira, Yamamoto and oxidative couplings. However, the pyrylium based CMPs still showed a low activity toward photocatalysis using visible light. The incorporation of strong electron donor such as pyrene<sup>2</sup>, carbazole<sup>3</sup>, triphenylamine<sup>4</sup> and thiophene<sup>5</sup> into pyrylium based networks in order to form D-A type CMPs can improve photophysical properties of the materials such as lower band gap energy and adjustment of HOMO and LUMO for specific photocatalysis reaction. Moreover, the crosslinked structure of CMPs provides a high thermal stability and insolubility in the common solvents making them as an excellent choice for a reusable heterogeneous

catalyst for photochemical reactions. The proposed synthetic methods of D-A type CMPs are shown in Scheme 7.1 and 7.2.



**Scheme 7.1** Synthesis of D-A type CMPs *via* Sonogashira-Hagihara coupling.



**Scheme 7.2** Synthesis of D-A molecule and oxidative coupling of the D-A molecule to form D-A type CMP.

### 7.3 References

- 1 F. Yu, Z. Zhu, S. Wang, Y. Peng, Z. Xu, Y. Tao, J. Xiong, Q. Fan and F. Luo, *Chem. Eng. J.*, 2020, 127558.
- 2 Y. Xu, N. Mao, C. Zhang, X. Wang, J. Zeng, Y. Chen, F. Wang and J. X. Jiang, *Appl. Catal. B Environ.*, 2018, **228**, 1–9.
- 3 Y. Zhi, S. Ma, H. Xia, Y. Zhang, Z. Shi, Y. Mu and X. Liu, *Appl. Catal. B Environ.*, 2019, **244**, 36–44.
- 4 W. J. Xiao, Y. Wang, W. R. Wang, J. Li, J. Wang, Z. W. Xu, J. Li, J. Yao and W. S. Li, *Macromolecules*, 2020, **53**, 2454–2463.
- 5 K. Zhang, B. Tieke, J. C. Forgie, F. Vilela and P. J. Skabara, *Macromolecules*, 2012, **45**, 743–750.
- 6 M. Vondenhof and J. Mattay, in *Organic Free Radicals*, Springer Berlin Heidelberg, 1988, pp. 227–228.